Poznan University of Technology

Faculty of Mechanical Engineering

Division of Strength of Materials and Structures

Doctoral dissertation

Analysis and optimization of stress distribution in complex shell structures

Krzysztof SOWIŃSKI, MSc, Eng.

Supervisor: Paweł JASION, DSc, Eng.

Co-supervisor: Dariusz KURPISZ, PhD

Poznan, 2022

Podziękowania

Serdecznie dziękuję mojemu Promotorowi dr hab. inż. Pawłowi Jasionowi oraz Promotorowi pomocniczemu dr Dariuszowi Kurpiszowi za cenne pomysły, uwagi i wskazówki, które przyczyniły się do powstania tej pracy.

Dziękuję prof. dr hab. inż. Krzysztofowi Magnuckiemu za udzieloną naukę oraz za zainteresowanie mnie zagadnieniami z obszaru konstrukcji powłokowych.

Dziękuję dr inż. Piotrowi Wasilewiczowi za wprowadzenie mnie do tematyki badań eksperymentalnych oraz wiele ciekawych pomysłów, które miały istotne znaczenie dla przeprowadzonych w pracy analiz.

Dziękuję Panu Leszkowi Paetzowi za pomoc przy pracach laboratoryjnych.

Podziękowania składam również całemu Zakładowi Wytrzymałości Materiałów i Konstrukcji za udzieloną pomoc oraz miłą i koleżeńską atmosferę.

Podziękowania

Dziękuję moim rodzicom Barbarze i Krzysztofowi oraz narzeczonej Joannie
za ciągłe wsparcie oraz wiarę w obraną przeze mnie drogę zawodową.

Niniejszą pracę dedykuję najbliższym mi osobom

Narzeczonej, Tacie oraz Mamie

List of publications

I declare that the folowing papers are an integral part of my doctoral dissertation.

Appendix A1

K. Sowiński, The Ritz method application for stress and deformation analyses of standard orthotropic pressure vessels, Thin-Walled Structures 162 (2021) 107585

Appendix A2

K. Sowiński, K. Magnucki, Shaping of dished heads of the cylindrical pressure vessel for diminishing of the edge effect, Thin-Walled Structures 131 (2018) 746-754

Appendix A3

K. Sowiński, Stress distribution optimization in dished ends of cylindrical pressure vessels, Thin-Walled Structures 171 (2022) 108808

Contents

Abstract

Human activity in engineering is dated back to antiquity. The achievements in this field of science directly contributed to the immensely far-reaching civilizational development. Nowadays, the expansion of technology is focused on advanced solutions in the aspect of designing structures to enhance their broadly defined properties.

The primary determinant in structural design is undoubtedly the load-carrying capacity, ensuring safe operation and preventing economically undesired underutilization of a mechanical system. It is necessary to provide specific methods or tools to give insight into their mechanical behaviour to address this issue. The presented work is devoted to the analysis and optimization of stress distribution in complex shell structures. Those serve as structural members of numerous relevant structures in the industry. The provided considerations are narrowed to problems of cylindrical pressure vessels; however, a similar methodology can be adapted to nearly any linear shell problem. Analytical, semi-analytical, numerical and experimental studies are considered to expand the knowledge and propose improvements to the investigated topic.

The first phase of the study is based on the theories and methods available in the literature. The stress and deformations in the cylindrical pressure vessel with standard ellipsoidal and torispherical dished ends are analyzed using membrane theory (MT) and the edge effect theory (EET). Two formulations of the EET are discussed, applied, and compared. The derivation is provided for the linear, orthotropic material model. The obtained results show that the superposition of MT and EET can result in unsatisfactory results due to simplifications in MT and neglection of the effect of surface loads on bending.

The same structures were investigated in a semi-analytical manner using the Ritz method in a subsequent study. The elastic strain energy and the work of the external forces were described according to linear shell theory. The functions describing displacements in the Ritz method are in the form of polynomials, trigonometric series, and functions similar to those derived from EET. The influence of the degree of these functions on the obtained results was taken into account. The achieved outcome agrees with the finite element method (FEM) for a relatively large range of thicknesses, proven by almost identical values of stress, displacements and strain energy.

In the conducted analyses of cylindrical pressure vessels, attention was drawn to the unfavourable stress distribution. Their maximum values in standard dished ends significantly exceed the stress in cylindrical shells, making them unsatisfactory solutions. Significant edge loads in the junctions of shell segments cause such an issue, leading to the appearance of significant bending phenomena. The shapes of dished ends described by three analytical curves, i.e. Cassini and Booth's oval and generalized clothoid, were formulated in further analyses. Specific conditions were defined to diminish the edge effect. They led to the intended effect of improving the stress distribution in the junction area but caused its maximum value to be shifted beyond this region. Therefore, the proposed shapes of shells do not constitute a significant advancement compared to the standard solutions, although their analysis provided important conclusions for further research.

The ability to carry relatively high loads by shell structures comes from their geometrical form. It is necessary to refer to optimization methods to seek the desired improvements in stress distribution. It comes from general reasoning that choosing some arbitrary geometries from an infinite set of possible solutions usually leads to poor results. In this work, the optimization is carried out in two separate processes. A parametric curve is developed to describe the shape of the dished end. Initially, the fitness function is evaluated according to MT, and the deterministic algorithm performs the optimization procedure. Due to the simplified nature of MT, the approach is then modified. The fitness function is calculated using the FEM, and the optimization is carried out by a genetic algorithm (GA). The obtained enhancement in the stress distribution is compelling while maintaining manufacturability and standard general dimensions.

Finally, the optimization results are verified in an experimental study. The pressure vessel with the optimized dished end is manufactured using Multi Jet Fusion – a 3D printing technology. Optical scanner measurements are conducted to verify geometrical deviations and to recreate the CAD model of the imperfect shape. Such a geometry is then considered in the FEM analysis. Ultimately the structure is tested on a designed test bench, enabling pressurizing of the vessel. The strain gauge measurements are performed to evaluate the stress distribution. The results are then compared for ideal and imperfect geometry by the FEM and juxtaposed with the experimental study. A good agreement is achieved, confirming the advantageous characteristics of the developed dished ends.

1. Introduction

The structural members in the form of shells are highly involved in numerous branches of the industry, including military industry, mechanical, civil, marine engineering, transportation, aeronautics and astronautics. Such load-carrying structures in the mentioned areas can be found in roofings, pipelines, pressure vessels, silos, aircraft, submersible vehicles and space ships. Those examples are only a fraction of the possible applications. Their widespread utilization in engineering is justified by exceptional resistance to some external loads under specific boundary conditions. Compared to other structural members, shells are characterized by a relatively high ratio of load-carrying capacity to mass, which constitutes a critical factor in technological advancement due to the desired mass minimization. In numerous cases, the deformations of shells are comparably modest because of their significant stiffness. Additionally, shells usually constitute materially continuous geometries which ensure their integrity and ability to pressurize. The application of shells can also become vital where space limitation becomes an issue, as those can take nearly any possible shape.

Currently, the industry strives for the most robust solutions in terms of structural design. It is based on achieving the highest functionality and optimal load-carrying capacity while considering economic factors. In the case of shell structures, obtaining the desired solutions can be generally achieved in two ways. The first one is the improvement of mechanical properties of a structure, e.g. by increasing the wall thickness or using materials with higher strength parameters. This method is simple, minimal and may cause a significant deterioration of other aspects of the structure.

The second way is to modify the geometry of shells. It should be noted here that the mentioned advantages of shells are connected with their geometric form. This method allows for a much broader modification of their properties while maintaining some of their original properties, e.g. general dimensions, mass or volume. Within this work, only the latter method is taken into consideration.

The research of this thesis is focused on the analysis and optimization of stress distribution in complex shell structures. The adopted in the thesis term "complex shells" refers to shell structures consisting of segments with various shapes and integral geometry. In most cases, the difference in shape leads to discontinuous curvature. Such a problem is vital in real-world engineering problems, where variously shaped shells are joined together. There are numerous examples of complex

shells, and for that reason, the research is narrowed to cylindrical pressure vessels loaded with uniform internal pressure.

The theory of shells is widely described in the literature. Particularly noteworthy is the work of Mazurkiewicz and Nagórski [1], where the authors show the solutions to numerous static and dynamic shell problems. Ventsel and Krauthammer [2] formulated the theories of plates and shells concerning static and buckling problems with some examples of their application. Gol'Denveizer [3] described the thin elastic shells theory and emphasised the analysis of typical geometries. Calladine [4], in his work, considered the stress and stability of shells, including elastic and plastic deformations as well as vibrations. Zingoni [5] explained the theories of membrane and bending phenomena of shell structures and applied them to multiple practical engineering cases.

Cylindrical pressure vessels are designed with the use of the shell theory. Magnucki [6] devoted his work to structural analysis and optimization of isotropic shells, including cylindrical pressure vessels with hemispherical and ellipsoidal dished ends. Spence and Tooth [7] described concepts and principles for designing pressure vessels. Magnucki et al. [8] prepared a review of strength and buckling problems of dished ends of cylindrical pressure vessels. Ziółko [9] focused on the practical aspects of numerous industrial vessels, including a reference to technical standards. Such a connection is critical as the design of those structures, their shapes and operating conditions are described within consistent European and American standards, i.e. EN 13445 [10] and ASME Section VIII, Division 1, 2 [11], [12]. Seipp et al. [12] compared the stress distributions between ellipsoidal dished end and equivalent torispherical shells proposed by the technical standards.

The edge effect theory (EET) constitutes the only known formulation that enables for analytical solution of bending phenomena in shells. The foundation to the theory was provided by Reissner [14], referring to spherical structures. Meissner [15] generalized the theory for an optional shape of a shell and formulated the governing differential equations of the EET. The first solution to those equations was proposed by Blumenthal [16] using the asymptotic integration method. Geckeler [17] introduced certain simplifications to the EET, enabling to rewrite of the governing differential equations to a single, elementary differential equation. Steuermann [18], [19] focused on developing the asymptotic integration method application in the EET.

Despite the EET being well established, solving the problems of complex shell structures remains vital. Pietraszkiewicz and Konopińska [20] provided substancial input to this topic. Vullo [21] presented the solution to numerous practical problems of junctures in shells, especially for pressure vessels. Zingoni [22] prepared a review

4

of recent studies on strength, stability and dynamics, including the problems of complex shell structures. Zingoni investigated the discontinuity effect in the shells junctions considering sludge digesters [23], [24], conical [25], elliptic toroidal [26] and multi-segmented spherical shells [27]. Zingoni [28] also simplified the derivation of influence coefficients for symmetric frusta of shells of revolution. Following the problems studied in the presented work, the stress and deformations in standard pressure vessels are resolved as a superposition of the membrane theory (MT) solution and the EET analysis. The latter refers to both Geckeler [17] as well as Blumenthal [16] and Steuermann [18], [19] approach for solving the governing differential equations of the EET formulated by Meissner [15].

The analytical formulation of the analysed problems of shell structures is generally inconvenient and adopts numerous simplifications, potentially impairing the solution. For that reason, semi-analytical or numerical methods can be considered beneficial. Among many, the Ritz method constitutes a universal and widely used method in structural mechanics, which is confirmed by various papers and monographs. Kumar [29] presented a comprehensive review of the Ritz method to analyse beams, shells and plates vibration, static and buckling characteristics. In the case of shell structures, the Ritz method is rarely used to analyse stress and deformation. Shahgholian-Ghahfarokhi et al. [30] investigated torsional buckling analysis of functionally graded graphene-platelets reinforced composite porous cylindrical shells using the Ritz method. Qin et al. [31] presented a unified Fourier series solution to solve the vibration problem of functionally graded carbon nanotube-reinforcement composite cylindrical shells, conical shells and annular plates. Lopatin and Morozov [32] considered a problem of axisymmetric vibrations of composite orthotropic cylindrical shells with rigid weightless disks attached to their ends. Qin et al. [33] provided a general approach for the free vibration analysis of rotating functionally graded carbon nanotube-reinforced composite cylindrical shells. Pang et al. [34] used a semi-analytical method to investigate the free vibration of doubly-curved shells of revolution with arbitrary boundary conditions. Senjanovic et al. [35] developed a finite strip method for vibration analysis of rotating toroidal shells subjected to internal pressure. On the higher-order shear deformation theory, Choe et al. [36] established an analysis model for dynamic analysis of composite laminated doubly-curved revolution shells. The solution of stress and deformation for standard orthotropic pressure vessels using the Ritz method was described by Sowiński [37] (A1). This work is an integral part of the presented thesis.

Due to the constantly increasing need for technological development, the optimization of shell structures became another vital research area. The theory of

optimization, fundamental deterministic and heuristic algorithms and their application are discussed by Kochenderfer and Wheeler [38] and Ostwald [39]. Nocedal and Wright [40] focused on numerical aspects of optimization. Ugray et al. [41] presented robust NLP solvers embedded in current, commercial computational software. Arabas [42] discussed the characteristics and application of evolutionary optimization algorithms. Bochenek and Krużelecki [43] described and solved the optimization problems of stability in structural mechanics. Magnucki and Ostwald [44] referred to the stability and optimization of three-layered sandwich structures.

Currently, there is a significant emphasis on developing highly efficient pressure vessels due to increased interest in hydrogen energy [45], where the gas must be stored at immense pressure to maintain sufficient energy density. This trend implies the need for improving the known technical solutions. Ortega and Robles [46] investigated a methodology of finding optimal forms of shells of revolution, which enables obtaining approximately bending-free geometries. Banichuk [47] presented shape and thickness optimization of the shell of revolution. Błachut and Magnucki [48] presented a review work of selected problems concerning strength, buckling and optimization of cylindrical pressure vessels.

The stability analysis of shells is of great importance, as those are prone to buckling, manifested by collapse when loaded with external pressure. Prediction of such a destructive circumstance implies the necessity of determining the post-buckling behaviour. Bochenek [49] presented a new optimization concept referring to this undesirable phenomenon. Numerous interesting studies on buckling and post-buckling have been conducted by Jasion [50], [51], Jasion and Magnucki [52] - [55] for a variety of shapes, including the shells with positive and negative Gaussian curvature. Similar studies were conducted by Sowiński and Jasion [56] and Sowiński [57] for shells based on Booth lemniscate and corrugated cylindrical, barrelled, and pseudo-barrelled structures. Paczos and Zielnica [58] investigated the stability of orthotropic elastic-plastic open conical shells. Zhang et al. [59] - [61] devoted their work to analysing shells whose shapes are inspired by nature.

As the stress distribution in standard dished ends of cylindrical pressure vessels can be considered unsatisfactory [12], [37] (A1), striving to improve it is crucial. Sowiński and Magncki [62] (A2) developed untypical shapes of dished ends with the intent to diminish the edge effect phenomenon. Lewiński [63] discussed the topic of optimal shaping of the dished ends, including step-wise thickness changes. Magnucki et al. [64] analysed the stress concentration factor minimization in cylindrical pressure vessels with ellipsoidal heads. Lewiński and Magnucki [65] developed the shape of the dished end described by the trigonometric series and

optimized its geometry by applying the condition of continuity of the curvatures in the joint. Kruželecki and Proszowski [66] proposed the two- and one-arc dished ends described by different functions, including Bézier polynomial and optimized their shapes using a simulated annealing algorithm. Kisigolu et al. [67] studied the minimum material design of the end closure of propane cylinders. Magnucki et al. [68] focused on reducing the peak stress in a cylindrical pressure vessel by introducing the dished end based on a composite curve of a circular arc and a polynomial of the fifth degree.

The primary issue with the optimization procedure is the lack of accurate analytical methods for solving the structural problems of shells. The optimization research provided in the previously mentioned studies [63]-[68] is based on the MT. Despite a significant reduction of the stress concentration factor due to optimization, the verification using the finite element method (FEM) resulted in an elevated peak stress value compared to the membrane state solution [66], [68]. That is the result of neglecting the bending phenomenon in the analysed shell structures. It is necessary to consider more accurate theories or methods to achieve a better optimization outcome.

Carbonari et al. [69] studied shape sequential linear programming optimization of axisymmetric pressure vessel, intending to reduce von Mises stress. The fitness function was obtained within the study framework utilizing FEM, where the pressure vessel was modelled using 2D-axisymmetric shell finite elements. Błachut and Ramachandra [70] considered the problem of internally pressurised torispherical domes and proposed to optimize their shape using genetic algorithms (GAs) and FEM.

The application of evolutionary algorithms, as the derivative-free methods, gained significant attention throughout recent years in structural optimization [71]. It is most likely connected with their ability to operate on discontinuous fitness functions present throughout any numerical analysis, where the relationship between input parameters and output result is undeterminable. There are numerous lately developed papers to justify the given statement. Firlik et al. [72] focused on tram wheel profile optimization using a biologically-inspired optimization algorithm. Yang et al. [73] designed the novel corrugated hierarchical truncated conical shells by adopting a surrogate model and GA. Kumar et al. [74] presented an isogeometric shape optimization to design 2D auxetic structures with a prescribed Poisson's ratio. Liang and Li [75] developed an optimization scheme to design the postbuckling behaviour of composite laminates. Imran et al. [76] carried out design optimization of composite submerged pressure hull under hydrostatic pressure. The authors analysed the effect of orientation angles and the number of layers on the load-

carrying capacity of a submersible. Eshani and Dalir [77] focused on optimum design to maximize the critical buckling load and minimize the structural weight of an angle grid plate. Zhu et al. [78] investigated the optimal shapes of reticulated shell structures with the intent to maximize nonlinear buckling load. Dias and Mahendran [79] optimized cold-formed steel-framed wall studs with sheathing restraints. Karimi and Kani [80] studied finding the worst imperfection pattern in shallow lattice domes using GAs.

The optimization in this work is based on the parametric shape of the dished end, described using a Bézier curve (BC) of arbitrary order. This part of the thesis has been already published [81] (A3). Some particular restrains are proposed and applied on its control points to satisfy numerous geometrical conditions, including non-negative curvature. The shape optimization of the dished end aims to minimize maximum equivalent von Mises stress in a cylindrical vessel loaded with uniform internal pressure.

The procedure is performed using two methods. Initially, equivalent stress is solved analytically according to the MT, while the sequential quadratic programming (SQP) algorithm seeks the maximum stress along the meridian of the dished end and attempts to minimize it. Further, numerical FEM calculations are conducted to validate the outcome of the analysis. Realizing the simplified character of the MT and the impact of the bending phenomena on shell structures, the procedure is further changed. The stress distribution is resolved using FEM in ANSYS software, where its peak value constitutes the fitness function. Due to its discontinuous character, the optimization is performed using GA in MATLAB software. A significant improvement in the maximum stress over the standard dished ends is achieved.

The last part of the research is focused on the experimental study of stress distribution in the cylindrical pressure vessel with the optimized dished end referring to [81] (A3). A suitable additive manufacturing method (AMM) is selected by performing static tensile tests according to ISO527 [82]. The topics of different AMMs, fundamental concepts and their application were covered by Gibson et al. [83]. The shell structure with the optimized dished end is manufactured in Multi Jet Fusion (MJF) technology. A test bench is designed to pressurize the vessel internally. During the test, the strains are measured using strain gauges.

Among many, Hoffman [84] described the practical basics of strain gauge measurements. Plentiful experimental beam and column studies were conducted by Paczos [85], Paczos et al. [86], Paczos and Wasilewicz [87], Jasion et al. [88]. These include the simultaneous strength test and strain gauge measurements. Zhang et al.

[89]-[90] performed experimental buckling studies of untypical steel shells. The experimental investigation of non-metallic shell structures remains somewhat an unpopular topic. Zhang et al. [91] considered a collapse performance of externally pressurized resin egg-shaped shell with corrosion thinning. Tang et al. [93] conducted an experimental buckling study over corrugated cylindrical shells made of resin. Lebans and Bisagni [94] described a similar topic, but the cylinders were 3D-printed. Sharifi et al. [95] considered a numerical and experimental study on the strength of internally pressurized laminated woven composite shells. To measure the strain, the authors used surface-bounded sensors.

According to the literature review, the problems of experimental stress distribution analyses are not well established in shell structures. Numerous papers are referring to this problem analytically and numerically. In the case of structures with applicational potential, those should be verified experimentally to prove their load-carrying capacity or other functional characteristics. The conventional methods of manufacturing shell structures are significantly limited, making such a process complicated and economically inefficient. The recent development of additive manufacturing enables the reproduction of actual structures with nearly any geometry. Although they are limited to plastics, usually characterized by nonlinear behaviour and creep phenomenon, in some cases, they can be successfully used in experimental tests of structures that are ultimately manufactured from steel. This observation is proven by the promising outcome of the experimental study in this dissertation.

As the result of the literature review, the following theses of the presented work are formulated.

> *(1) The analytical, theory-based solutions to stress and deformation problems in shell structures can lead to inaccurate results.*
> *(2) The stress distributions in the standard dished ends of cylindrical pressure vessels are unfavourable.*

The two hypotheses are introduced to address the current state of the art issues in shell structures.

> *(1) Applying the Ritz method to solve the stress and deformation problems of shell structures may lead to more accurate results than the analytical solutions.*
> *(2) The shape optimization of the dished end of the cylindrical pressure vessel could lead to substantial improvement in stress distribution while maintaining their general dimensions and manufacturability.*

2. Linear theory of shells

2.1. Definition of a shell

The term shell is applied to bodies limited by two curved surfaces, where the distance between the surfaces is small compared to other body dimensions (Fig. 2.1). The middle surface is defined by the locus of points that lie at equal distances from internal and external surfaces. The length of a perpendicular to the middle surface segment between those two surfaces corresponds to the thickness of a shell, denoted as t. Such a definition enables characterising the shell by providing the geometrical form of its middle surface and its thickness.
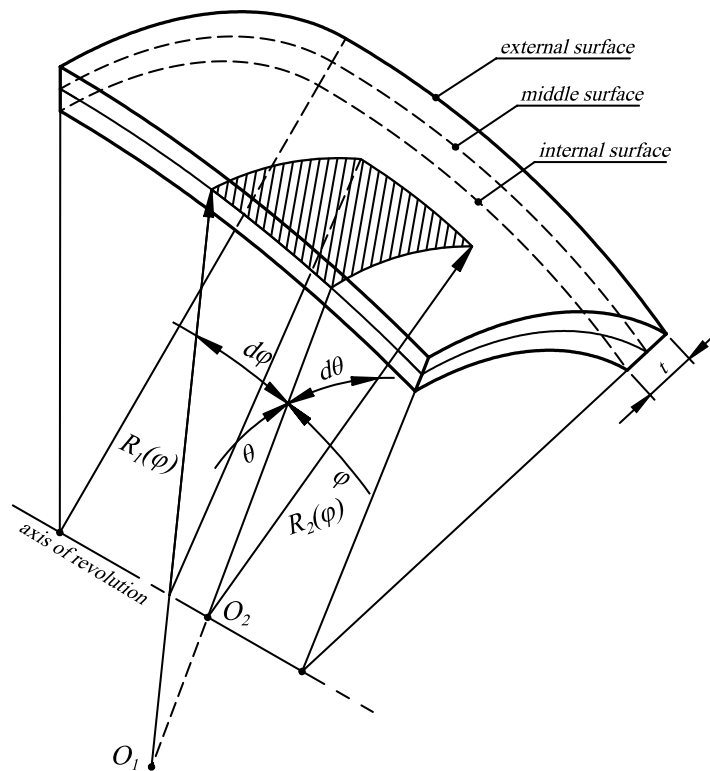

Fig. 2.1. A segment of a shell of revolution

The middle surface of an arbitrary shell structure is described by the principal radii of curvature, namely R_1, R_2 (Fig. 2.1), specified towards two mutually orthogonal and curvilinear directions φ, θ. Usually, those are refered to as meridional and circumferential directions. Shells can have vastly diversified shapes depending on the radii of curvature R_1, R_2 which can be either constant or variable in the given directions. The most common group of shell structures are shells of revolution, for which the principal radii of curvature are variable only towards one direction, i.e. the meridional angle φ, thus $R_1(\varphi), \ R_2(\varphi)$. The geometries of revolution are defined by the revolution of an arbitrary generator (meridian) over an axis. The generator can be described as a function expressed in an optional coordinate system.

The shells of revolution constitute a group of meaningful structures in industrial applications, while shells without such a property are less common, as they are challenging to design and manufacture using conventional methods. Most of the shell structures serving as real-world engineering objects are characterised by variable thickness. The source of this feature is usually a side effect of the manufacturing processes involved in forming those structures. In most cases, the variation of the thickness can be considered negligible.

Depending on the thickness t, shells can be divided into two groups ([1]-[6]), namely thick and thin-walled structures. The latter term is referred to geometries for which the ratio $t/\min(R_1, R_2)$ is relatively small compared to unity. The exact value distinguishing the thick and thin-walled structures is difficult to specify; however, the literature suggests that thin shells satisfy the following condition

$$\frac{t}{\min[R_1(\varphi),\ R_2(\varphi)]} \leq \frac{1}{20}. \tag{2.1}$$

Referring to the provided description of shells, this work is focused on shells of revolution with constant thickness. Definition of those geometries can be limited to a plane intersecting with the axis of revolution, as shown in Fig. 2.2.
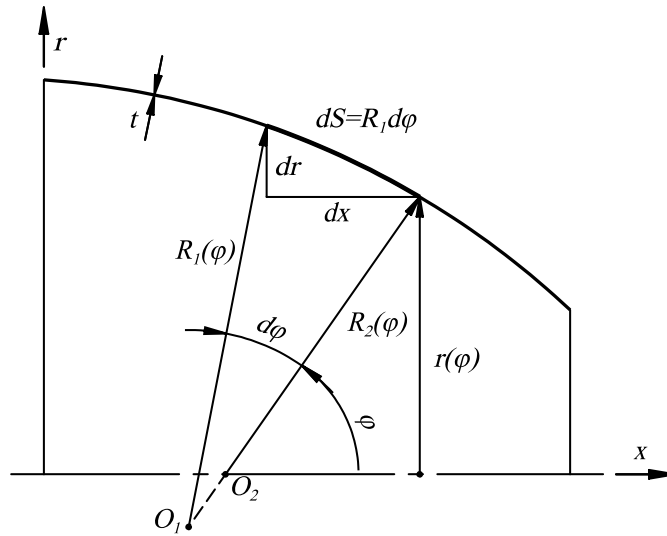

Fig. 2.2. Axial section of a surface of revolution

The geometrical relation for the surface of revolution is as follows

$$\frac{\mathrm{d}}{\mathrm{d}\varphi}(R_1 \sin\varphi) = R_1 \cos\varphi. \tag{2.2}$$

The arc length can be resolved according to integral

$$S = \int_{\underline{\varphi}}^{\overline{\varphi}} R_1 \,\mathrm{d}\varphi, \tag{2.3}$$

where $\underline{\varphi}$, $\overline{\varphi}$ are the coordinates over which the meridian length S is determined. Denoted in Fig. 2.2 coordinate $r(\varphi)$ is referred to as parallel radius, being related to the circumferential radius of curvature in the following manner

$$r = R_2 \sin\varphi. \tag{2.4}$$

2.2. Linear shell theory for axisymmetric shell problems

Within the framework of this research, the analyses are restricted to axisymmetrical loads acting upon the middle surface of a shell of revolution. Such an assumption implies that the problem description can be narrowed to meridional angle φ, while all the physical quantities remain constant towards circumferential direction θ (Fig. 2.1). The further theoretical description is based on Kirchoff-Love linear shell theory discussed in [1]-[4]. As such a formulation is well established in the literature, its explanation is kept to a minimum within this dissertation. A section of a shell structure undergoing deformation is presented in Fig. 2.3.
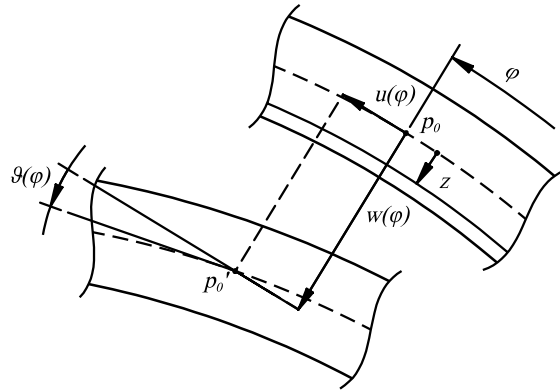

Fig. 2.3. A section of axisymmetrically loaded shell of revolution undergoing deformation

As shown in Fig. 2.3, the deformation state is described by three quantities, i.e. u - tangent displacements, w – normal displacements, ϑ – rotation of a line tangent to the middle surface. Notably, only two of those can be considered independent, as displacements can define the rotation by the following relation

$$\vartheta = \frac{1}{R_1}\left(u + \frac{dw}{d\varphi}\right). \tag{2.5}$$

It is often convenient to additionally define a vertical component of displacements. Assuming it is consistent with the axis r in Fig. 2.2, one obtains

$$d_v = u \cos\varphi - w \sin\varphi. \tag{2.6}$$

In further consideration, the quantities referring to the meridional and circumferential directions are distinguished by their subscripts ($_1$, $_2$) just as

principal radii of curvature. The linear strains in the middle surface towards principal directions expressed with the use of displacements are:

$$\varepsilon_1 = \frac{1}{R_1}\left(\frac{du}{d\varphi} - w\right), \qquad \varepsilon_2 = \frac{1}{R_2}\left(u\cot\varphi - w\right), \tag{2.7}$$

while the changes of curvatures:

$$\chi_1 = -\frac{1}{R_1}\frac{d\vartheta_1}{d\varphi}, \qquad \chi_2 = -\frac{1}{R_2}\vartheta_1\cot\varphi. \tag{2.8}$$

Considering the relations in Eq. (2.7), (2.8), one can express the linear strains across the thickness according to coordinate z (Fig. 2.3):

$$\varepsilon_{1z} = \frac{1}{1 - \dfrac{z}{R_1}}(\varepsilon_1 + z\chi_1), \qquad \varepsilon_{1z} = \frac{1}{1 - \dfrac{z}{R_1}}(\varepsilon_2 + z\chi_2), \tag{2.9}$$

where

$$-\frac{t}{2} \le z \le \frac{t}{2}. \tag{2.10}$$

The material in the study is considered to be perfectly elastic and orthotropic, aligned with the principal directions φ, θ, where E_1, E_2 – Young's moduli, v_1, v_2 – Poisson's ratios. The internal loads in the form of normal forces and moments are expressed as follows:

$$N_1 = C_1(\varepsilon_1 + v_2\varepsilon_2), \qquad N_2 = C_2(\varepsilon_2 + v_1\varepsilon_1), \tag{2.11}$$

$$M_1 = D_1(\chi_1 + v_2\chi_2), \qquad M_2 = D_2(\chi_2 + v_1\chi_1), \tag{2.12}$$

while:

$$C_1 = \frac{E_1 t}{1 - v_1 v_2}, \qquad C_2 = \frac{E_2 t}{1 - v_1 v_2}, \tag{2.13}$$

$$D_1 = \frac{E_1 t^3}{12(1 - v_1 v_2)}, \qquad D_2 = \frac{E_2 t^3}{12(1 - v_1 v_2)}. \tag{2.14}$$

To derive the shear forces, it is necessary to refer to the equilibrium equations of a shell element [1]. The principal stresses are defined as follows:

$$\sigma_1 = \frac{C_1}{t}(\varepsilon_1 + v_2\varepsilon_2), \qquad \sigma_2 = \frac{C_2}{t}(\varepsilon_2 + v_1\varepsilon_1), \tag{2.15}$$

and their change across the thickness of a shell:

$$\sigma_{1z} = \frac{C_1}{t}(\varepsilon_{1z} + v_2\varepsilon_{2z}), \qquad \sigma_{2z} = \frac{C_2}{t}(\varepsilon_{2z} + v_1\varepsilon_{1z}). \tag{2.16}$$

3. Analytical study

3.1. Membrane state analysis

3.1.1. General theory

For some practical cases of shell structures, one can consider that the bending phenomena can be inexistent or marginal, implying they do not contribute significantly to stresses and deformations. The neglection of bending moments M_1, M_2 assumes that only normal forces N_1, N_2 are present in a shell. This constitutes the desired simplification of the linear shell theory, which is difficult to solve problems with for numerous practical analyses. Such an approach is referred to as membrane theory (MT). As a result of its simplified nature, the authors of [1], [2] suggest the following conditions of the MT applicability.

1) The middle surface of a shell has smoothly varying and continuous geometry.
2) The thickness of a shell must be sufficiently small, constant or slightly varying.
3) Applied surface loads must be distributed in a continuous and possibly uniform manner.
4) The edges of a shell can be loaded solely by the forces tangent to a middle surface, i.e. only normal forces are included. Similarly, the applied boundary conditions can be imposed only on tangent displacements u to remain valid reaction forces.

Importantly, the given conditions are based on non-definitive terms when referring to thickness, radii of curvature and surface loads. The MT can undoubtedly be successfully adopted for the problems considering uniformly loaded shells with small, constant thickness and radii of curvature. The first two conditions are usually consistent with practical cases of shell structures, especially by referring to Eq. (2.1). Unfortunately, the assumption of constant radii of curvature limits the applicability of MT to spherical and cylindrical shells. The allowance of potential variations implies difficulties in determining whether the MT application is justified and, if so, what is the expected magnitude of inaccuracies.

Let us consider a shell of revolution with an arbitrary shape described within the range $\varphi_1 \leq \varphi \leq \varphi_2$ (Fig. 3.1). In the presented thesis, the coordinate φ_1 describes the first edge, while φ_2 corresponds to second edge of a shell. The external forces in the MT are limited to pressure p and normal force P_0 applied at the first edge, i.e. $\varphi = \varphi_1$. As the introduced forces do not include all possible external loads, the MT cannot be used alone to analyse stress in complex shell structures.
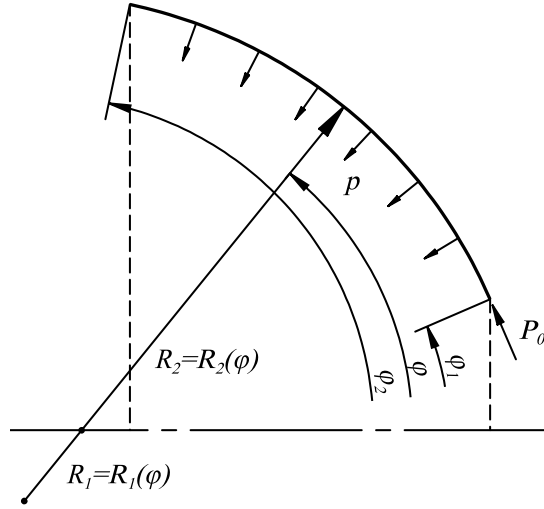
Fig. 3.1. An arbitrary shell loaded with external forces

The normal internal forces resulting from the applied external loads are as follows:

$$N_1 = pR_0\tilde{N}_1, \qquad \tilde{N}_1 = -\frac{\tilde{P}}{\tilde{R}_2\sin^2\varphi},$$

$$N_2 = pR_0\tilde{N}_2, \qquad \tilde{N}_2 = \frac{\tilde{P}}{\tilde{R}_1\sin^2\varphi} - \tilde{R}_2,$$

(3.1)

where:

$$P = pR_0{}^2\tilde{P}, \qquad P_0 = pR_0{}^2\tilde{P}_0,$$

$$\tilde{P} = \tilde{P}_0\tilde{R}_2(\varphi_1)\sin^2\varphi_1 + \frac{1}{2}\left(\tilde{R}_2{}^2\sin^2\varphi - \tilde{R}_2(\varphi_1)^2\sin^2\varphi_1\right),$$

(3.2)

$$\frac{d\tilde{P}}{d\varphi} = \tilde{R}_2\sin\varphi\left(\tilde{R}_2\cos\varphi + \frac{d\tilde{R}_2}{d\varphi}\sin\varphi\right).$$

The coefficient $\tilde{P}_0$ is a dimensionless normal force applied at the first edge of a shell. The principal strains occurring in the meridional and circumferential directions:

$$\varepsilon_1 = \frac{pR_0}{E_1t}\left(\tilde{N}_1 - v_1\tilde{N}_2\right), \qquad \varepsilon_2 = \frac{pR_0}{E_2t}\left(\tilde{N}_2 - v_2\tilde{N}_1\right)$$

(3.3)

Tangent and normal displacements are expressed in the following manner:

$$u = \frac{pR_0{}^2}{E_2t}\tilde{u}, \qquad \tilde{u} = \sin\varphi\,(f + c_1),$$

(3.4)

$$w = \frac{pR_0{}^2}{E_2t}\tilde{w}, \qquad \tilde{w} = \cos\varphi\,(f + c_1) - \left(\frac{\tilde{R}_2}{\tilde{R}_1} + v_2\right)\frac{\tilde{P}}{\sin^2\varphi} + \tilde{R}_2{}^2.$$

(3.5)

For the sake of further derivation, it is useful to refer to the vertical displacement component from Eq. (2.6):

$$d_v = \frac{pR_0{}^2}{E_2h}\tilde{d}_v, \qquad \tilde{d}_v = \sin\varphi\left[\left(\frac{\tilde{R}_2}{\tilde{R}_1} + v_2\right)\frac{\tilde{P}}{\sin^2\varphi} - \tilde{R}_2{}^2\right].$$

(3.6)

The rotation of the line tangent to the meridian of a shell is defined as:

$$\vartheta_1 = \frac{pR_0}{E_2 t}\tilde{\vartheta}_1, \qquad \tilde{\vartheta}_1 = \frac{1}{\tilde{R}_1}\left(\tilde{u} + \frac{d\tilde{w}}{d\varphi}\right), \tag{3.7}$$

where derivative of the dimensionless normal displacements

$$\frac{d\tilde{w}}{d\varphi} = \frac{df}{d\varphi}\cos\varphi - (f + c_1)\sin\varphi + \frac{1}{\tilde{R}_1^{\,2}\sin^2\varphi}\left[\tilde{R}_1\left(v_2\tilde{R}_1 + \tilde{R}_2\right)\left(2\cot\varphi\,\tilde{P} - \frac{d\tilde{P}}{d\varphi}\right) + \tilde{P}\tilde{R}_2\frac{d\tilde{R}_1}{d\varphi}\right] +$$

$$+ \frac{1}{\tilde{R}_1}\frac{d\tilde{R}_2}{d\varphi}\left(2\tilde{R}_1\tilde{R}_2 - \frac{\tilde{P}}{\sin^2\varphi}\right), \tag{3.8}$$

and the derivative of the expression $\tilde{P}$

$$\frac{d\tilde{P}}{d\varphi} = \tilde{R}_2\sin\varphi\left(\tilde{R}_2\cos\varphi + \frac{d\tilde{R}_2}{d\varphi}\sin\varphi\right). \tag{3.9}$$

The function f defined in the above formulae is expressed as

$$f = \int_{\varphi_1}^{\varphi} \frac{1}{\sin\varphi}\left[\left(\frac{\tilde{R}_2}{\tilde{R}_1} + v_2\right)\tilde{R}_1\tilde{R}_2 - \left(\frac{\tilde{R}_2}{\tilde{R}_1} + 2v_2 + \alpha\frac{\tilde{R}_2}{\tilde{R}_1}\right)\frac{\tilde{P}}{\sin^2\varphi}\right]d\varphi, \tag{3.10}$$

where α is an orthotropy coefficient defined as

$$\alpha = \frac{E_2}{E_1} = \frac{v_2}{v_1}. \tag{3.11}$$

The function f and its first derivative can be written in a more convenient form:

$$f = \left[\left(-\frac{1}{2}\alpha + v_2\right)f_1 + (1 - v_2)f_2 - \frac{1}{2}f_3 + \tilde{R}_2(\varphi_1)^2\sin^2\varphi_1\left(v_2 f_4 + \frac{1}{2}\alpha f_5 + \frac{1}{2}f_6\right)\right] -$$

$$- \tilde{P}_0\tilde{R}_2(\varphi_1)\sin^2\varphi_1(2v_2 f_4 + \alpha f_5 + f_6) \tag{3.12}$$

$$\frac{df}{d\varphi} = \left[\left(-\frac{1}{2}\alpha + v_2\right)\psi_1 + (1 - v_2)\psi_2 - \frac{1}{2}\psi_3 + \tilde{R}_2(\varphi_1)^2\sin^2\varphi_1\left(v_2\psi_4 + \frac{1}{2}\alpha\psi_5 + \frac{1}{2}\psi_6\right)\right] \tag{3.13}$$

where:

$$f_1 = \int_{\varphi_1}^{\varphi}\psi_1 d\varphi, \qquad f_2 = \int_{\varphi_1}^{\varphi}\psi_2 d\varphi, \qquad f_3 = \int_{\varphi_1}^{\varphi}\psi_3 d\varphi,$$

$$f_4 = \int_{\varphi_1}^{\varphi}\psi_4 d\varphi, \qquad f_5 = \int_{\varphi_1}^{\varphi}\psi_5 d\varphi, \qquad f_6 = \int_{\varphi_1}^{\varphi}\psi_6 d\varphi, \tag{3.14}$$

$$\psi_1 = \tilde{R}_1\tilde{R}_2\frac{1}{\sin\varphi}, \qquad \psi_2 = \tilde{R}_2^{\,2}\frac{1}{\sin\varphi}, \qquad \psi_3 = \frac{\tilde{R}_2^{\,3}}{\tilde{R}_1}\frac{1}{\sin\varphi},$$

$$\psi_4 = \frac{1}{\sin^3\varphi}, \qquad \psi_5 = \frac{\tilde{R}_1}{\tilde{R}_2}\frac{1}{\sin^3\varphi}, \qquad \psi_6 = \frac{\tilde{R}_2}{\tilde{R}_1}\frac{1}{\sin^3\varphi}. \tag{3.15}$$

16

The displacements and rotations can be further resolved by assuming appropriate boundary condition and calculating the constant c_1. In the presented paper, tangent displacement is restrained at the second edge ($\varphi = \varphi_2$) of a shell

$$\tilde{u}(\varphi_2) = 0. \tag{3.16}$$

A significant simplification of the above expressions can be achieved for the closed apex shells, i.e. when $\varphi_1 = 0$:

$$\tilde{P}_0 = 0, \qquad \tilde{P} = \frac{1}{2}\tilde{R}_2{}^2 \sin^2\varphi. \tag{3.17}$$

The components containing the edge load $\tilde{P}_0$ then disappear, which enables to rewrite the expressions for internal forces:

$$\widetilde{N}_1 = -\frac{1}{2}\tilde{R}_2, \qquad \widetilde{N}_2 = -\frac{1}{2}\tilde{R}_2\left(2 - \frac{\tilde{R}_2}{\tilde{R}_1}\right). \tag{3.18}$$

Further, the f function and its derivative can be expressed as follows:

$$f = \left(-\frac{1}{2}\alpha + \nu_2\right)f_1 + (1 - \nu_2)f_2 - \frac{1}{2}f_3,$$
$$\frac{\mathrm{d}f}{\mathrm{d}\varphi} = \left(-\frac{1}{2}\alpha + \nu_2\right)\psi_1 + (1 - \nu_2)\psi_2 - \frac{1}{2}\psi_3. \tag{3.19}$$

3.1.2. Cylindrical pressure vessels

Cylindrical pressure vessels constitute an essential structure in the industrial applications, enabling for storage and transportation of gases and liquids. They consist of a cylindrical shell enclosed by two convex dished ends. The general geometry of the introduced structure is shown in Fig. 3.2.

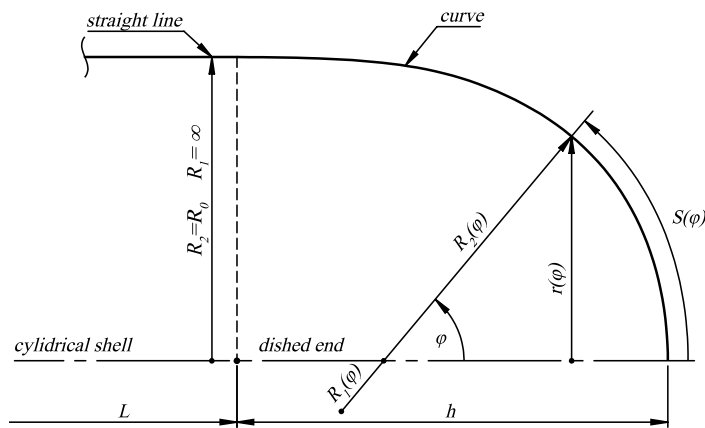*Fig. 3.2. The general geometry of the cylindrical pressure vessel*

Most of the pressure vessels are thin-walled shell structures which can be described by the parameters referred to their middle surface (Fig. 3.2), i.e. φ - meridional angle, R_1, R_2 – meridional and circumferential radii of curvature, r - parallel radius, S - meridian length, L – cylindrical shell length, R_0 – cylindrical

shell radius, h - dished end height, and thickness t. The relative depth of a dished end is defined as

$$\beta = \frac{h}{R_0}. \tag{3.20}$$

The standard dished ends are ellipsoidal, torispherical and hemispherical, as shown in Fig. 3.3. Those are described and manufactured according to coherent European and American standards, i.e. EN 13445 [10] and ASME Section VIII, Division 1, 2 [11], [12].
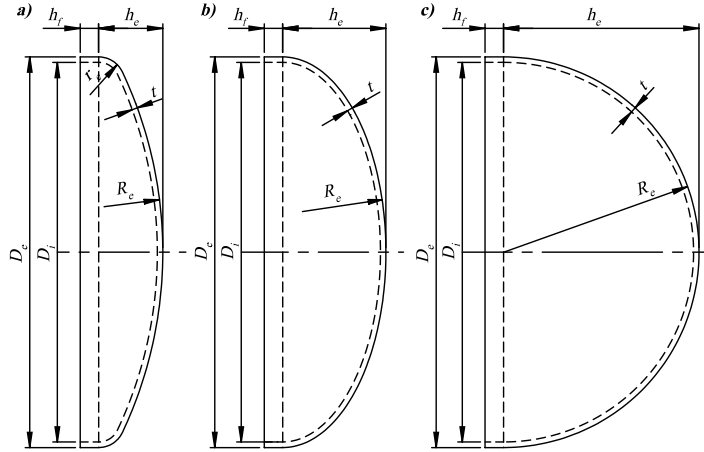

Fig. 3.3. Dished ends according to EN 13445; a) - torispherical, b) - ellipsoidal, c) – hemispherical

Calculation methods provided in technical standards are based on a simplified and not necessarily insightful approach. The presented study aims to provide an analytical solution to deformation and stress problems of pressure vessels using shell theories. As the solutions considering hemispherical geometries are known, the research is narrowed to torispherical and ellipsoidal geometries. To investigate the stress distribution in those, it is convenient to formulate relative equivalent stress

$$\tilde{\sigma}_r = \frac{\sigma_r}{\sigma_r^{(cyl)}}, \tag{3.21}$$

where: σ_r – von Mises stress in a pressure vessel, $\sigma_r^{(cyl)}$ – maximum von Mises stress in a cylindrical shell beyond any stress disturbance caused by the edge loads. Such formulation enables to define of the stress concentration factor k, which is the maximum value of $\tilde{\sigma}_r$:

$$k = \frac{\sigma_r^{(max)}}{\sigma_r^{(cyl)}}, \tag{3.22}$$

where: $\sigma_r^{(max)}$ – maximum von Mises stress in a pressure vessel.

To proceed with the derivation employing MT, one must refer to separate geometries of pressure vessels, for which principal radii of curvature constitute continuous functions.

18

3.1.3. Toroidal shell

The further subsections in this chapter refer to the derivation of the necessary formulae to analyse standard orthotropic pressure vessels according to the MT. A more detailed description of the selected shells is provided in [37] (A1). Each of the considered geometries is described by a unique symbol, i.e. s – spherical, c - cylindrical, t - toroidal and e – ellipsoidal, which appear in the bottom indices of the previously derived expressions. In the case of the toroidal shell (Fig. 3.1):

$$\varphi_{1t} = \frac{3}{20}\pi, \qquad \varphi_{2t} = \frac{\pi}{2}.$$

(3.23)

For the sake of clarity, the value of φ_{1t} is not substituted for the derivation of the selected expressions. Meridional and circumferential radii of curvatures are given as:

$$R_{1t} = R_0 \tilde{R}_t, \qquad R_{2t} = R_0 \left[\tilde{R}_t + \frac{1}{\sin\varphi}(1 - \tilde{R}_t)\right], \qquad \tilde{R}_t = \frac{\beta \cot\frac{\varphi_{t1}}{2} - 1}{\cot\frac{\varphi_{t1}}{2} - 1},$$

(3.24)

and their first derivatives:

$$\frac{d\tilde{R}_{1t}}{d\varphi} = 0, \qquad \frac{d\tilde{R}_{2t}}{d\varphi} = (\tilde{R}_t - 1)\frac{\cos\varphi}{\sin^2\varphi}.$$

(3.25)

To calculate the internal forces, the normal edge load must be defined, which in the case of the torispherical shell results from the interaction with the spherical segment:

$$\tilde{P}_{0t} = -\tilde{N}_{1s}(\varphi_{t1}) = \frac{1}{2}\tilde{R}_s.$$

(3.26)

The components of f function in Eq. (3.14) for the analysed shell are:

$$f_{1t} = \tilde{R}_t^2 f_t^{(a)} - \tilde{R}_t(\tilde{R}_t - 1)f_t^{(b)},$$

$$f_{2t} = \tilde{R}_t^2 f_t^{(a)} - 2\tilde{R}_t(\tilde{R}_t - 1)f_t^{(b)} + (\tilde{R}_t - 1)^2 f_t^{(c)}$$

$$f_{3t} = \tilde{R}_t^2 f_t^{(a)} - 3\tilde{R}_t(\tilde{R}_t - 1)f_t^{(b)} + 3(\tilde{R}_t - 1)^2 f_t^{(c)} - \frac{(\tilde{R}_t - 1)^3}{\tilde{R}_t}f_t^{(d)}$$

(3.27)

$$f_{4t} = f_t^{(c)}, \qquad f_{5t} = \tilde{R}_t f_t^{(e)}, \qquad f_{6t} = f_t^{(c)} + \left(\frac{1}{\tilde{R}_t} - 1\right)f_t^{(d)},$$

where:

$$f_t^{(a)} = \ln\left(\tan\frac{\varphi}{2}\right), \qquad f_t^{(b)} = -\cot\varphi,$$

$$f_t^{(c)} = \frac{1}{8}\left[\frac{2}{\cos\varphi - 1} + \ln\left(\tan^4\frac{\varphi}{2}\right) + \frac{1}{\cos^2\frac{\varphi}{2}}\right], \qquad f_t^{(d)} = -\frac{1}{3}\left(2 + \frac{1}{\sin^2\varphi}\right)\cot\varphi,$$

(3.28)

$$f_t^{(e)} = \frac{1}{(\tilde{R}_t - 1)^2}\left\{\frac{2\tilde{R}_t^2}{\sqrt{1 - 2\tilde{R}_t}}\arctan\left[\frac{\tilde{R}_t - (\tilde{R}_t - 1)\tan\frac{\varphi}{2}}{\sqrt{1 - 2\tilde{R}_t}}\right] + \tilde{R}_t\cot\varphi + \tilde{R}_t\ln\left(\cot\frac{\varphi}{2}\right) - \cot\varphi\right\}.$$

Using Eq. (3.16) results in

$$c_{1t} = 0. \tag{3.29}$$

3.1.4. Spherical shell

The meridional coordinates for the spherical shell of a torispherical dished end depend on the definition of the toroidal shell:

$$\varphi_{1s} = 0, \qquad \varphi_{2s} = \varphi_{1t} = \frac{3}{20}\pi. \tag{3.30}$$

Principal radii of curvature are constant:

$$R_{1s} = R_{2s} = R_0 \tilde{R}_s,$$

$$\tilde{R}_s = \frac{1}{1 - \cos\varphi_{2s}}\left(\beta - \tilde{R}_t \cos\varphi_{2s}\right), \tag{3.31}$$

therefore their derivatives

$$\frac{\mathrm{d}\tilde{R}_{1s}}{\mathrm{d}\varphi} = \frac{\mathrm{d}\tilde{R}_{2s}}{\mathrm{d}\varphi} = 0. \tag{3.32}$$

Using Eq. (3.19), one obtains

$$f_{1s} = f_{2s} = f_{3s} = \tilde{R}_s{}^2 \ln\left(\tan\frac{\varphi}{2}\right), \tag{3.33}$$

therefore

$$f_s = \frac{1}{2}\tilde{R}_s{}^2 (1 - \alpha) \ln\left(\tan\frac{\varphi}{2}\right). \tag{3.34}$$

Applying boundary condition in Eq. (3.16) yields

$$c_{1s} = -\frac{1}{2}\tilde{R}_s{}^2 (1 - \alpha) \ln\left(\tan\frac{\varphi_{2s}}{2}\right). \tag{3.35}$$

It is worth noting that if the material is isotropic ($\alpha = 1$), then:

$$c_{1s} = 0, \qquad f_s = 0, \tag{3.36}$$

which implies the tangent displacements are zero

$$u_s = 0. \tag{3.37}$$

3.1.5. Ellipsoidal shell

The meridional angle boundaries of the ellipsoidal dished end are:

$$\varphi_{1e} = 0, \qquad \varphi_{2e} = \frac{\pi}{2}. \tag{3.38}$$

Unlike the previous shapes, both radii of curvature are variable for the ellipsoidal shell:

$$R_{1e} = R_0 \tilde{R}_{1e}, \qquad \tilde{R}_{1e} = \beta^2 \frac{1}{\sin^3 \varphi} \left(\frac{1}{1 + \beta^2 \cot^2 \varphi} \right)^{3/2},$$

$$R_{2e} = R_0 \tilde{R}_{2e}, \qquad \tilde{R}_{2e} = \frac{1}{\sin \varphi} \left(\frac{1}{1 + \beta^2 \cot^2 \varphi} \right)^{1/2}. \tag{3.39}$$

Their derivatives are as follows:

$$\frac{d\tilde{R}_{1e}}{d\varphi} = 3\beta^2 (\beta^2 - 1) \left(\frac{1}{1 + \beta^2 \cot^2 \varphi} \right)^{5/2} \frac{\cos \varphi}{\sin^4 \varphi},$$

$$\frac{d\tilde{R}_{2e}}{d\varphi} = (\beta^2 - 1) \left(\frac{1}{1 + \beta^2 \cot^2 \varphi} \right)^{3/2} \frac{\cos \varphi}{\sin^2 \varphi}. \tag{3.40}$$

For the closed apex shells i.e. $\varphi_1 = 0$, the internal forces can be calculated according to Eq. (3.18). The components of the f function (Eq. (3.19)) are further resolved:

$$f_{1e} = \frac{1}{4\beta^2} \left[2\sqrt{1 - \beta^2}(2 + \beta^2) \operatorname{arctanh}\left(\frac{2\sqrt{1 - \beta^2}}{\beta^2 \tan^2 \frac{\varphi}{2} - \beta^2 + 2} \right) + \ln\left(\tan^4 \frac{\varphi}{2} \right) \right] -$$

$$- \frac{(\beta^2 - 1) \cos \varphi}{(\beta^2 - 1) \cos 2\varphi + \beta^2 + 1},$$

$$f_{2e} = \frac{1}{2\beta^2} \left[2\sqrt{1 - \beta^2} \operatorname{arctanh}\left(\frac{2\sqrt{1 - \beta^2}}{\beta^2 \tan^2 \frac{\varphi}{2} - \beta^2 + 2} \right) + \ln\left(\tan^2 \frac{\varphi}{2} \right) \right],$$

$$f_{3e} = \frac{1}{2\beta^2} \ln\left(\tan^2 \frac{\varphi}{2} \right). \tag{3.41}$$

Applying an adequate boundary condition (Eq. (3.16)) yields

$$c_{1e} = \frac{\sqrt{1 - \beta^2}}{4\beta^2} [(2 + \beta^2)\alpha - 2\beta^2 \nu_2 - 4] \operatorname{arctanh} \sqrt{1 - \beta^2}. \tag{3.42}$$

3.1.6. Cylindrical shell

To describe the membrane state in a cylindrical shell, it is necessary to transform the description from the meridional angle φ to a linear coordinate ξ. The following substitution is applied:

$$\varphi = \frac{\pi}{2}, \qquad \tilde{R}_1 d\varphi = d\xi, \tag{3.43}$$

where $0 \leq \xi \leq L$. Principal radii of curvature are expressed as:

$$
\begin{aligned}
R_1 &= R_0 \tilde{R}_1, \qquad \tilde{R}_1 \to \infty, \\
R_2 &= R_0 \tilde{R}_2, \qquad \tilde{R}_2 = 1.
\end{aligned}
\tag{3.44}
$$

Assuming the shell is enclosed by a dished end, the horizontal edge load, i.e. the expression for P, $\tilde{P}$ and $\tilde{P}_0$ consequently can be significantly simplified:

$$P_c = pR_0{}^2 \tilde{P}_c, \qquad \tilde{P}_c = \tilde{P}_{0c} = \frac{1}{2}, \qquad \frac{d\tilde{P}_c}{d\xi} = 0, \tag{3.45}$$

which leads to the following form of the internal forces:

$$
\begin{aligned}
N_1 &= pR_0 \tilde{N}_1, \qquad \tilde{N}_1 = -\frac{1}{2}, \\
N_2 &= pR_0 \tilde{N}_2, \qquad \tilde{N}_2 = -1.
\end{aligned}
\tag{3.46}
$$

The components of the f function can be reduced to:

$$f_{1c} = \xi, \qquad f_{2c} = 0, \qquad f_{3c} = 0, \qquad f_{4c} = 0, \qquad f_{5c} = \xi, \qquad f_{6c} = 0, \tag{3.47}$$

therefore

$$f_c = \left(v_2 - \frac{1}{2}\alpha \right)\xi. \tag{3.48}$$

Applying the boundary condition in Eq. (3.16) leads to

$$c_{1c} = 0, \tag{3.49}$$

which results in the following expressions for displacements:

$$\tilde{u}_c = \left(v_2 - \frac{1}{2}\alpha \right)\xi, \qquad \tilde{w}_c = 1 + \frac{1}{2}v_2. \tag{3.50}$$

3.2. The edge effect theory

3.2.1. Doubly curved shells

To consider all possible external loads that can occur in complex shell structures, one must refer to a formulation that includes the bending phenomenon, which is omitted in MT. The edge effect theory (EET) is employed in the presented study to describe bending effects. It constitutes a simplification of the general bending theory of shells. The differential equations of the latter were initially defined by Reissner [14] for spherical shells and further generalized by Meissner [15]. The authors introduced two unknown functions in the derivation:

$$\vartheta = \frac{1}{R_1}\left(u + \frac{dw}{d\varphi}\right), \qquad U = R_2 Q, \tag{3.51}$$

where: Q – shear force, ϑ – rotation of a line tangent to the meridian (Fig. 2.3). The form of the proposed governing differential equations is:

$$L(U) + \nu_2\, U - R_1 E_2 t\vartheta = F,$$

$$L(\vartheta) - \nu_2\vartheta + \frac{R_1}{D_1} U = 0, \tag{3.52}$$

where:

$$L = \frac{R_2}{R_1}\frac{d^2}{d\varphi^2} + \left[\frac{R_2}{R_1}\cot\varphi + \frac{d}{d\varphi}\left(\frac{R_2}{R_1}\right)\right]\frac{d}{d\varphi} - \alpha\frac{R_1}{R_2}\cot^2\varphi, \tag{3.53}$$

$$F = P_0\left\{\frac{d}{d\varphi}\left[\left(\frac{R_2}{R_1} + \nu_2\right)\frac{1}{\sin^2\varphi}\right] + \left(\frac{R_2}{R_1} + 2\nu_2 + \alpha\frac{R_1}{R_2}\right)\frac{1}{\sin^2\varphi}\cot\varphi\right\} - $$
$$-p\left[\frac{d}{d\varphi}\left(R_2{}^2\right) - \left(\frac{R_2}{R_1} + \nu_2\right)R_1 R_2 \cot\varphi\right], \tag{3.54}$$

$$D_1 = \frac{E_1 t^3}{12(1 - \nu_1\nu_2)}, \tag{3.55}$$

The solution of the system of differential equations as expressed in Eq. (3.52) remains unknown. Importantly, they are linear, therefore their general solution has the following form:

$$U = U^e + U^s + U^n,$$

$$\vartheta = \vartheta^e + \vartheta^s + \vartheta^n, \tag{3.56}$$

where U^e, ϑ^e are general integrals of homogenous equations assuming $p = P_0 = 0$, ($F = 0$), U^s, ϑ^s are particular integrals for surface load only ($P_0 = 0$) and finally U^n, ϑ^n are particular integrals for normal edge load P_0 ($p = 0$). The surface load in this paper refers to pressure p.

The EET assumes omitting the bending effects caused by surface loads and normal edge load P_0. The solution of differential equations in homogenous form

($F = 0$) is possible and is referred to as the EET, where the bending phenomenon caused by the normal edge load P_0 and surface loads like pressure p are neglected. Having this in mind, one can rewrite Eq. (3.56) to the following form:

$$U = U^e, \qquad \vartheta = \vartheta^e. \tag{3.57}$$

This approach assumes the bending effect is caused only by the moments and transverse forces applied on the edges of a shell, hence the name of the theory. The omitted load components p, P_0 (Fig. 3.1) might be considered within the MT, and the final solution constitutes then a superposition of both membrane and bending state. The system of differential equations (Eq. (3.52)) can be further rewritten to:

$$L(U) + v_2 U - R_1 \frac{E_2 t}{D_1} \bar{\vartheta} = 0, \tag{3.58}$$

$$L(\bar{\vartheta}) - v_2 \bar{\vartheta} + R_1 U = 0,$$

where

$$\vartheta = \frac{1}{D_1} \bar{\vartheta}. \tag{3.59}$$

There are two methods for solving Eq. (3.58). The solution based on the simplifications proposed by Geckeler [17] is the most widely described in the literature. Those are as follows.

A) Value of the functions $U, \bar{\vartheta}$ (Eq. (3.58)) increase significantly with the order of their derivatives, i.e.

$$\frac{\mathrm{d}^n U}{\mathrm{d}\varphi^n} \gg \frac{\mathrm{d}^{(n-1)} U}{\mathrm{d}\varphi^{(n-1)}}, \qquad \frac{\mathrm{d}^n \bar{\vartheta}}{\mathrm{d}\varphi^n} \gg \frac{\mathrm{d}^{(n-1)} \bar{\vartheta}}{\mathrm{d}\varphi^{(n-1)}}. \tag{3.60}$$

B) The change of radii of curvature near the shells edge, where the disturbance occurs, is negligible; therefore, it can be assumed:

$$R_1, R_2 = \text{const.} \tag{3.61}$$

According to Eq. (3.60), the differential operator in Eq. (3.53) can be expressed as

$$L = \frac{R_2}{R_1} \frac{\mathrm{d}^2}{\mathrm{d}\varphi^2}, \tag{3.62}$$

one can further omit the function U and $\bar{\vartheta}$ in the first and second expression correspondingly in the system of equations Eq. (3.58), which results in:

$$\frac{\mathrm{d}^2 U}{\mathrm{d}\varphi^2} - \frac{R_1{}^2}{R_2} \frac{E_2 t}{D_1} \bar{\vartheta} = 0,$$

$$\frac{\mathrm{d}^2 \bar{\vartheta}}{\mathrm{d}\varphi^2} + \frac{R_1{}^2}{R_2} U = 0. \tag{3.63}$$

The above system can be reduced to a single fourth-order differential equation

$$\frac{d^4 U}{d\varphi^4} + 4\mu^4 U = 0,$$ (3.64)

where:

$$\mu = \varkappa\rho,$$ (3.65)

$$\varkappa = \sqrt[4]{\frac{3\alpha(1 - \nu_1\nu_2)}{t^2}},$$ (3.66)

$$\rho = \frac{R_1}{\sqrt{R_2}}.$$ (3.67)

Replacing meridional angle φ in Eq. (3.64) with a dummy angular coordinate towards the same direction denoted by γ (Fig. 3.4), one obtains

$$\frac{d^4 U}{d\gamma^4} + 4\mu^4 U = 0.$$ (3.68)

The general solution of the differential equation in Eq. (3.68) can be written in the following form:

$$U = 2\varkappa^2 [e^{-\mu\gamma}(A_1 \cos\mu\gamma - A_2 \sin\mu\gamma) + e^{\mu\gamma}(A_3 \cos\mu\gamma + A_4 \sin\mu\gamma)],$$

$$\bar{\vartheta} = e^{-\mu\gamma}(A_1 \sin\mu\gamma + A_2 \cos\mu\gamma) - e^{\mu\gamma}(A_3 \sin\mu\gamma - A_4 \cos\mu\gamma).$$ (3.69)

It is expected that the solution of the Meissner homogenous equations is characterised by the functions that rapidly decay with the increase of the coordinate γ from a shell edge. In the above solution, the component $e^{-\mu\gamma}$ is consistent with this observation, while $e^{\mu\gamma}$ has the exact opposite property. The increase of the values of the functions (Eq. (3.69)) with meridional angle γ can only occur when it is caused by the disturbance on another edge of a shell (Fig. 3.4).
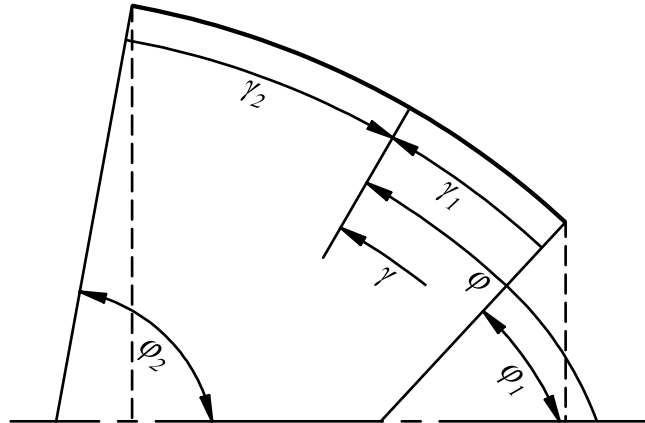

Fig. 3.4. Angular coordinates in the EET

To obtain a convenient form of the presented solution, one may introduce new variables that express the angular distance from each of the shell edges separately, as presented in Fig. 3.4:

$$\gamma = \gamma_1 = \varphi - \varphi_1, \qquad \gamma = -\gamma_2 = -(\varphi_2 - \varphi), \tag{3.70}$$

which results in:

$$U_g = 2\varkappa^2[e^{-\mu\gamma_1}(A_1\cos\mu\gamma_1 - A_2\sin\mu\gamma_1) + e^{-\mu\gamma_2}(A_3\cos\mu\gamma_2 - A_4\sin\mu\gamma_2)],$$
$$\bar{\vartheta}_g = e^{-\mu\gamma_1}(A_1\sin\mu\gamma_1 + A_2\cos\mu\gamma_1) + e^{-\mu\gamma_2}(A_3\sin\mu\gamma_2 + A_4\cos\mu\gamma_2). \tag{3.71}$$

In the presented work, the EET solution U_g, $\bar{\vartheta}_g$ proposed by Geckeler [17] is compared to Blumenthal [16] and Steuermann [18], [19] asymptotic integration solution U_s, $\bar{\vartheta}_s$ (Eq. (3.72)) of homogenous Reissner-Meissner differential equations. The derivation of the latter, unlike the former, assumes the principal radii of curvature are functions of the meridional angle. Such a solution is discussed by Mazurkiewicz and Nagórski [1], and after unifying symbols and adjusting variables, it takes the form:

$$U_s = 2\varkappa^2[e^{-\varkappa\omega_1}(B_1\cos\varkappa\omega_1 - B_2\sin\varkappa\omega_1) + e^{-\varkappa\omega_2}(B_3\cos\varkappa\omega_2 - B_4\sin\varkappa\omega_2)],$$
$$\bar{\vartheta}_s = e^{-\varkappa\omega_1}(B_1\sin\varkappa\omega_1 + B_2\cos\varkappa\omega_1) + e^{-\varkappa\omega_2}(B_3\sin\varkappa\omega_2 + B_4\cos\varkappa\omega_2), \tag{3.72}$$

where:

$$\omega_1 = \int_{\varphi_1}^{\varphi}\rho\,\mathrm{d}\gamma, \qquad \omega_2 = \int_{\varphi}^{\varphi_2}\rho\,\mathrm{d}\gamma. \tag{3.73}$$

Note that in the case of a shell with constant radii of curvature, applying the same constants yields the same form of the solutions in Eq. (3.71) and Eq. (3.72), as:

$$\varkappa\omega_1 = \mu(\varphi - \varphi_1) = \mu\gamma_1, \qquad \varkappa\omega_2 = \mu(\varphi_2 - \varphi) = \mu\gamma_2. \tag{3.74}$$

The solution in Eq. (3.71) can be then written to match the form of Eq. (3.72), which led to:

$$U_g = 2\varkappa^2[e^{-\varkappa\bar{\omega}_1}(A_1\cos\varkappa\bar{\omega}_1 - A_2\sin\varkappa\bar{\omega}_1) + e^{-\varkappa\bar{\omega}_2}(A_3\cos\varkappa\bar{\omega}_2 - A_4\sin\varkappa\bar{\omega}_2)],$$
$$\bar{\vartheta}_g = e^{-\varkappa\bar{\omega}_1}(A_1\sin\varkappa\bar{\omega}_1 + A_2\cos\varkappa\bar{\omega}_1) + e^{-\varkappa\bar{\omega}_2}(A_3\sin\varkappa\bar{\omega}_2 + A_4\cos\varkappa\bar{\omega}_2), \tag{3.75}$$

enabling to introduce the similar functions to Eq. (3.73):

$$\bar{\omega}_1 = \rho\int_{\varphi_1}^{\varphi}\mathrm{d}\gamma, \qquad \bar{\omega}_2 = \rho\int_{\varphi}^{\varphi_2}\mathrm{d}\gamma. \tag{3.76}$$

In the further derivation, it is assumed that the functions $U, \bar{\vartheta}$ can be described by Eq. (3.72) or Eq. (3.75). Following the authors of [1], the internal forces of the EET expressed with the functions $U, \bar{\vartheta}$ are:

$$Q_1 = \frac{1}{R_2} U, \tag{3.77}$$

$$N_1 = -\frac{1}{R_2} U \cot\varphi, \qquad N_2 = -\frac{1}{R_1} \frac{dU}{d\varphi}. \tag{3.78}$$

$$M_1 = -\left(\frac{1}{R_1} \frac{d\bar{\vartheta}}{d\varphi} + \nu_2 \frac{1}{R_2} \bar{\vartheta} \cot\varphi \right), \qquad M_2 = -\alpha \left(\frac{1}{R_2} \bar{\vartheta} \cot\varphi + \nu_1 \frac{1}{R_1} \frac{d\bar{\vartheta}}{d\varphi} \right). \tag{3.79}$$

The rotation of the line tangent to the meridian is proportional to $\bar{\vartheta}$ and can be resolved according to Eq. (3.59). The normal and tangent displacement components are expressed as follows:

$$u = \frac{\sin\varphi \, R_1}{E_2 t} \int \left[\frac{d}{d\varphi} \left(\frac{U}{\sin\varphi} \right) \left(\frac{R_2}{R_1^2} + \nu_2 \frac{1}{R_1} \right) + \left(\frac{R_2}{R_1^2} - \alpha \frac{1}{R_2} \right) \frac{\cos\varphi}{\sin^2\varphi} U \right] d\varphi +$$

$$+ C \sin\varphi, \tag{3.80}$$

$$w = u \cot\varphi + \frac{R_2}{E_2 t} \left(\frac{1}{R_1} \frac{dU}{d\varphi} - \nu_2 \frac{1}{R_2} U \cot\varphi \right).$$

Analytical calculation of these functions can be considered difficult due to cumbersome integrals. Importantly, normal and tangent displacement components are not necessary for further analyses. Instead, one can refer to the vertical displacement component defined in Eq. (2.6), which can be simplified to a very convenient form

$$d_v = -\frac{R_2 \sin\varphi}{E_2 t} \left(\frac{1}{R_1} \frac{dU}{d\varphi} - \nu_2 \frac{1}{R_2} U \cot\varphi \right). \tag{3.81}$$

Remarkably, the functions in Eqs. (3.79), (3.81) are inconsistent with the simplification (Eq. (3.60)) proposed by Geckeler, as the derivatives of functions $U, \bar{\vartheta}$ are not neglected in the presence of those functions themselves like in Eq. (3.63). For such a reason those are usually rewritten ([1], [2]) to:

$$M_1 = -\frac{1}{R_1} \frac{d\bar{\vartheta}}{d\varphi}, \qquad M_2 = -\nu_2 \frac{1}{R_1} \frac{d\bar{\vartheta}}{d\varphi} = \nu_2 M_1, \tag{3.82}$$

$$d_v = -\frac{1}{E_2 t} \frac{R_2 \sin\varphi}{R_1} \frac{dU}{d\varphi}. \tag{3.83}$$

The justification of this simplification is debatable, as it leads to the omission of $\cot\varphi$ component. When the meridional angle φ becomes sufficiently small near a shell edge, the functions in Eqs. (3.79), (3.81) and corresponding Eqs. (3.82), (3.83) may yield considerably different values depending on a studied case.

To simplify the EET approach, it is usually assumed that two edges of a single shell structure can be considered separately. This is valid due to the character of the solutions in Eq. (3.72) or Eq. (3.75), as their values diminish relatively quickly when moving away from the edge, therefore:

$$U_g = U_g^{(1)} + U_g^{(2)}, \quad \bar{\vartheta}_s = \bar{\vartheta}_g^{(1)} + \bar{\vartheta}_g^{(2)},$$

$$U_g^{(1)} = 2\varkappa^2 e^{-\varkappa\bar{\omega}_1}(A_1 \cos\varkappa\bar{\omega}_1 - A_2 \sin\varkappa\bar{\omega}_1), \ U_g^{(2)} = 2\varkappa^2 e^{-\varkappa\bar{\omega}_2}(A_3 \cos\varkappa\bar{\omega}_2 - A_4 \sin\varkappa\bar{\omega}_2), \text{ (3.84)}$$

$$\bar{\vartheta}_g^{(1)} = e^{-\varkappa\bar{\omega}_1}(A_1 \sin\varkappa\bar{\omega}_1 + A_2 \cos\varkappa\bar{\omega}_1), \ \bar{\vartheta}_g^{(2)} = e^{-\varkappa\bar{\omega}_2}(A_3 \sin\varkappa\bar{\omega}_2 + A_4 \cos\varkappa\bar{\omega}_2),$$

$$U_s = U_s^{(1)} + U_s^{(2)}, \quad \bar{\vartheta}_s = \bar{\vartheta}_s^{(1)} + \bar{\vartheta}_s^{(2)},$$

$$U_s^{(1)} = 2\varkappa^2 e^{-\varkappa\omega_1}(B_1 \cos\varkappa\omega_1 - B_2 \sin\varkappa\omega_1), \ U_s^{(2)} = 2\varkappa^2 e^{-\varkappa\omega_2}(B_3 \cos\varkappa\omega_2 - B_4 \sin\varkappa\omega_2), \text{ (3.85)}$$

$$\bar{\vartheta}_s^{(1)} = e^{-\varkappa\omega_1}(B_1 \sin\varkappa\omega_1 + B_2 \cos\varkappa\omega_1), \ \bar{\vartheta}_s^{(2)} = e^{-\varkappa\omega_2}(B_3 \sin\varkappa\omega_2 + B_4 \cos\varkappa\omega_2).$$

Their derivatives are as follows:

$$\frac{dU_g^{(1)}}{d\varphi} = 2\sqrt{2}\varkappa^3\rho e^{-\varkappa\bar{\omega}_1}\left[A_1 \sin\left(\varkappa\bar{\omega}_1 - \frac{3}{4}\pi\right) + A_2 \cos\left(\varkappa\bar{\omega}_1 - \frac{3}{4}\pi\right)\right],$$

$$\frac{dU_g^{(2)}}{d\varphi} = -2\sqrt{2}\varkappa^3\rho e^{-\varkappa\bar{\omega}_2}\left[A_3 \sin\left(\varkappa\bar{\omega}_2 - \frac{3}{4}\pi\right) + A_4 \cos\left(\varkappa\bar{\omega}_2 - \frac{3}{4}\pi\right)\right],$$

$$\frac{d\bar{\vartheta}_g^{(1)}}{d\varphi} = -\sqrt{2}\varkappa\rho e^{-\varkappa\bar{\omega}_1}\left[A_1 \sin\left(\varkappa\bar{\omega}_1 - \frac{1}{4}\pi\right) + A_2 \cos\left(\varkappa\bar{\omega}_1 - \frac{1}{4}\pi\right)\right], \quad \text{(3.86)}$$

$$\frac{d\bar{\vartheta}_g^{(2)}}{d\varphi} = \sqrt{2}\varkappa\rho e^{-\varkappa\bar{\omega}_2}\left[A_3 \sin\left(\varkappa\bar{\omega}_2 - \frac{1}{4}\pi\right) + A_4 \cos\left(\varkappa\bar{\omega}_2 - \frac{1}{4}\pi\right)\right],$$

$$\frac{dU_s^{(1)}}{d\varphi} = 2\sqrt{2}\varkappa^3\rho e^{-\varkappa\omega_1}\left[B_1 \sin\left(\varkappa\omega_1 - \frac{3}{4}\pi\right) + B_2 \cos\left(\varkappa\omega_1 - \frac{3}{4}\pi\right)\right],$$

$$\frac{dU_s^{(2)}}{d\varphi} = -2\sqrt{2}\varkappa^3\rho e^{-\varkappa\omega_2}\left[B_3 \sin\left(\varkappa\omega_2 - \frac{3}{4}\pi\right) + B_4 \cos\left(\varkappa\omega_2 - \frac{3}{4}\pi\right)\right],$$

$$\frac{d\bar{\vartheta}_s^{(1)}}{d\varphi} = -\sqrt{2}\varkappa\rho e^{-\varkappa\omega_1}\left[B_1 \sin\left(\varkappa\omega_1 - \frac{1}{4}\pi\right) + B_2 \cos\left(\varkappa\omega_1 - \frac{1}{4}\pi\right)\right], \quad \text{(3.87)}$$

$$\frac{d\bar{\vartheta}_s^{(2)}}{d\varphi} = \sqrt{2}\varkappa\rho e^{-\varkappa\omega_2}\left[B_3 \sin\left(\varkappa\omega_2 - \frac{1}{4}\pi\right) + B_4 \cos\left(\varkappa\omega_2 - \frac{1}{4}\pi\right)\right].$$

In the further derivation, the edge effect theory formulation proposed by Geckeler is from now on called EETG, while Blumenthal and Steuermann approach

is referred to as EETS. Assuming the functions $U^{(1)}, U^{(2)}, \bar{\vartheta}^{(1)}, \bar{\vartheta}^{(2)}$ are expressed by Eq. (3.84) or Eq. (3.85), normal and shear internal forces can be written in a concise form in EETG and EETS:

$$Q_1 = Q_1^{(1)} + Q_1^{(2)}, \qquad Q_1^{(1)} = \frac{1}{R_2} U^{(1)}, \qquad Q_1^{(2)} = \frac{1}{R_2} U^{(2)}, \tag{3.88}$$

$$N_1 = N_1^{(1)} + N_1^{(2)}, \qquad N_1^{(1)} = -\frac{1}{R_2} U^{(1)} \cot \varphi, \qquad N_1^{(2)} = -\frac{1}{R_2} U^{(2)} \cot \varphi,$$

$$N_2 = N_2^{(1)} + N_2^{(2)}, \qquad N_2^{(1)} = -\frac{1}{R_1} \frac{dU^{(1)}}{d\varphi}, \qquad N_2^{(2)} = -\frac{1}{R_1} \frac{dU^{(2)}}{d\varphi}. \tag{3.89}$$

Meridional and circumferential moments in EETS are described as:

$$M_1 = M_1^{(1)} + M_1^{(2)}, \quad M_2 = M_2^{(1)} + M_2^{(2)},$$

$$M_1^{(1)} = -\left(\frac{1}{R_1} \frac{d\bar{\vartheta}_s^{(1)}}{d\varphi} + v_2 \frac{1}{R_2} \bar{\vartheta}_s^{(1)} \cot \varphi \right), \quad M_1^{(2)} = -\left(\frac{1}{R_1} \frac{d\bar{\vartheta}_s^{(2)}}{d\varphi} + v_2 \frac{1}{R_2} \bar{\vartheta}_s^{(2)} \cot \varphi \right),$$

$$M_2^{(1)} = -\alpha \left(\frac{1}{R_2} \bar{\vartheta}_s^{(1)} \cot \varphi + v_1 \frac{1}{R_1} \frac{d\bar{\vartheta}_s^{(1)}}{d\varphi} \right), \quad M_2^{(2)} = -\alpha \left(\frac{1}{R_2} \bar{\vartheta}_s^{(2)} \cot \varphi + v_1 \frac{1}{R_1} \frac{d\bar{\vartheta}_s^{(2)}}{d\varphi} \right). \tag{3.90}$$

The simplification applied in EETG leads to the following expressions:

$$M_1 = M_1^{(1)} + M_1^{(2)}, \qquad M_1^{(1)} = -\frac{1}{R_1} \frac{d\bar{\vartheta}_g^{(1)}}{d\varphi}, \qquad M_1^{(2)} = -\frac{1}{R_1} \frac{d\bar{\vartheta}_g^{(2)}}{d\varphi},$$

$$M_2 = M_2^{(1)} + M_2^{(2)}, \qquad M_2^{(1)} = v_2 M_1^{(1)}, \qquad M_2^{(2)} = v_2 M_1^{(2)}. \tag{3.91}$$

Vertical displacements in EETS can be written in a convenient form:

$$d_v = d_v^{(1)} + d_v^{(2)},$$

$$d_v^{(1)} = -\frac{R_2 \sin \varphi}{E_2 t} \left(\frac{1}{R_1} \frac{dU_s^{(1)}}{d\varphi} - v_2 \frac{1}{R_2} U_s^{(1)} \cot \varphi \right),$$

$$d_v^{(2)} = -\frac{R_2 \sin \varphi}{E_2 t} \left(\frac{1}{R_1} \frac{dU_s^{(2)}}{d\varphi} - v_2 \frac{1}{R_2} U_s^{(2)} \cot \varphi \right). \tag{3.92}$$

After introducing Geckeler simplification to Eq. (3.92), one obtains:

$$d_v = d_v^{(1)} + d_v^{(2)},$$

$$d_v^{(1)} = -\frac{1}{E_2 t} \frac{R_2 \sin \varphi}{R_1} \frac{dU_g^{(1)}}{d\varphi}, \qquad d_v^{(2)} = -\frac{1}{E_2 t} \frac{R_2 \sin \varphi}{R_1} \frac{dU_g^{(2)}}{d\varphi}. \tag{3.93}$$

To resolve the constants in Eq. (3.84) or Eq. (3.85), the following boundary conditions are assumed:

$$Q_1^{(1)}(\varphi_1) = Q_{e1}, \qquad Q_1^{(2)}(\varphi_2) = Q_{e2},$$

$$M_1^{(1)}(\varphi_1) = M_{e1}, \qquad M_1^{(2)}(\varphi_2) = -M_{e2}.$$

(3.94)

The constants in EETG are calculated according to internal shear forces in Eq. (3.88) and moments in Eq. (3.91):

$$A_1 = Q_{e1}\frac{R_2(\varphi_1)}{2\varkappa^2}, \qquad A_3 = Q_{e2}\frac{R_2(\varphi_2)}{2\varkappa^2},$$

$$A_2 = Q_{e1}\frac{R_2(\varphi_1)}{2\varkappa^2} + M_{e1}\frac{\sqrt{R_2(\varphi_1)}}{\varkappa}, \qquad A_4 = Q_{e2}\frac{R_2(\varphi_2)}{2\varkappa^2} + M_{e2}\frac{\sqrt{R_2(\varphi_2)}}{\varkappa}.$$

(3.95)

Similarly, in EETS, using Eq. (3.88) and Eq. (3.90), the following expressions are derived:

$$B_1 = Q_{e1}\frac{R_2(\varphi_1)}{2\varkappa^2}, \qquad B_3 = Q_{e2}\frac{R_2(\varphi_2)}{2\varkappa^2},$$

$$B_2 = Q_{e1}\frac{R_2(\varphi_1)^{3/2}}{2\varkappa(\varkappa\sqrt{R_2(\varphi_1)} - \nu_2\cot\varphi_1)} + M_{e1}\frac{R_2(\varphi_1)}{\varkappa\sqrt{R_2(\varphi_1)} - \nu_2\cot\varphi_1},$$

(3.96)

$$B_4 = Q_{e2}\frac{R_2(\varphi_2)^{3/2}}{2\varkappa(\varkappa\sqrt{R_2(\varphi_2)} + \nu_2\cot\varphi_2)} + M_{e2}\frac{R_2(\varphi_2)}{\varkappa\sqrt{R_2(\varphi_2)} + \nu_2\cot\varphi_2}.$$

It is important to notice that in the case of closed apex shells, i.e. when $\varphi_1 = 0$, some of the presented equations are characterised by singularity for $\varphi = 0$ caused by the component $\cot\varphi$. This issue is present in the functions expressing meridional, normal force $N_1^{(2)}$ (Eq. (3.89)) and meridional moment $M_1^{(2)}$ (Eq. (3.90)). Despite the same formulation of equivalent functions $N_1^{(1)}, M_1^{(1)}$, those are not considered when $\varphi_1 = 0$. Values of the functions $U^{(2)}$, $\bar{\vartheta}^{(2)}$ as well as their derivatives for $\varphi = 0$ can be considered meager, but importantly never exactly zero, thus $N_1^{(2)}(0) \to \pm\infty$, $M_1^{(2)}(0) \to \pm\infty$. Described characteristics of those functions is unexpected. Applying Geckeler simplification in EETG resolves this problem with the moment $M_1^{(2)}$ (Eq. (3.91)), however the issue persists for the normal force $N_1^{(2)}$. The effect of the component $\cot\varphi$ increases with thickness of a shell as it makes the functions $U^{(2)}$, $\bar{\vartheta}^{(2)}$ diminish at a lower pace with the decrease of meridional angle φ.

3.2.2. Cylindrical shell

Due to the geometrical form of cylindrical shells, a significant simplification over a general case from the previous section can be achieved. Importantly, it is necessary to describe the problem using a linear variable along the shell axis instead of the meridional angle. The following expressions need to be considered:

$$\mathrm{d}\varphi = \frac{L}{R_1}\mathrm{d}\xi, \qquad \mathrm{d}\gamma = \frac{L}{R_1}\mathrm{d}\varsigma \tag{3.97}$$

$$\varphi = \frac{\pi}{2}, \qquad R_1 \rightarrow \infty, \qquad R_2 = R_0, \tag{3.98}$$

where ς is a general, linear coordinate equivalent to the curvilinear coordinate γ (Fig. 3.4). Due to the form of Eqs. (3.97), (3.98), EETS and EETG solutions become identical. The further derivation is based on the EETG due to its convenient form:

$$\bar{\omega}_1 = \rho \int_{\xi_1}^{\xi} \mathrm{d}\varsigma, \qquad \bar{\omega}_2 = \rho \int_{\xi}^{\xi_2} \mathrm{d}\varsigma, \tag{3.99}$$

where ξ_1, ξ_2 are linear coordinates analogous to φ_1, φ_2 (Fig. 3.4), and consequently

$$\rho = \frac{L}{\sqrt{R_0}}. \tag{3.100}$$

The solution of the governing differential equations of EET remains unchanged concerning Eq. (3.84) and derivatives Eq. (3.86). The constants in those expressions can be simplified to:

$$A_1 = Q_{e1}\frac{R_0}{2\varkappa^2}, \qquad A_3 = Q_{e2}\frac{R_0}{2\varkappa^2},$$

$$A_2 = Q_{e1}\frac{R_0}{2\varkappa^2} + M_{e1}\frac{\sqrt{R_0}}{\varkappa}, \qquad A_4 = Q_{e2}\frac{R_0}{2\varkappa^2} + M_{e2}\frac{\sqrt{R_0}}{\varkappa}. \tag{3.101}$$

The internal forces are described as:

$$Q_1^{(1)} = \frac{1}{R_0}U^{(1)}, \qquad Q_1^{(2)} = \frac{1}{R_0}U^{(2)}, \tag{3.102}$$

$$N_1^{(1)} = 0, \qquad N_1^{(2)} = 0,$$

$$N_2^{(1)} = -\frac{1}{L}\frac{\mathrm{d}U^{(1)}}{\mathrm{d}\xi}, \qquad N_2^{(2)} = -\frac{1}{L}\frac{\mathrm{d}U^{(2)}}{\mathrm{d}\xi}, \tag{3.103}$$

$$M_1^{(1)} = -\frac{1}{L}\frac{\mathrm{d}\bar{\vartheta}^{(1)}}{\mathrm{d}\xi}, \qquad M_1^{(2)} = -\frac{1}{L}\frac{\mathrm{d}\bar{\vartheta}^{(2)}}{\mathrm{d}\xi},$$

$$M_2^{(1)} = \nu_2 M_1^{(1)}, \qquad M_2^{(2)} = \nu_2 M_1^{(2)}. \tag{3.104}$$

The rotation of a line tangent to the meridian ϑ can be resolved using Eq. (3.59), while vertical displacements:

$$d_v^{(1)} = -\frac{1}{E_2 t}\frac{R_0}{L}\frac{\mathrm{d}U^{(1)}}{\mathrm{d}\xi}, \qquad d_v^{(2)} = -\frac{1}{E_2 t}\frac{R_0}{L}\frac{\mathrm{d}U^{(2)}}{\mathrm{d}\xi}. \tag{3.105}$$

3.3. Stress and deformation analysis in complex shell structures

The primary, practical purpose of the EET is to take into consideration the problems of shells with discontinuous radii of curvature. In such a case, the shell is virtually divided into segments with continuous radii of curvature and the interaction between them is studied. The solution to this problem aims to achieve the state of continuity of deformations in the form of displacements and rotations using EET and MT by finding the values of transverse forces and moments in the coupled shells. For most analyses, it is necessary to consider the simultaneous interaction between edges of two neighbouring shells in the form of normal and transverse forces X, Y, as well as bending moments Z (Fig. 3.5).
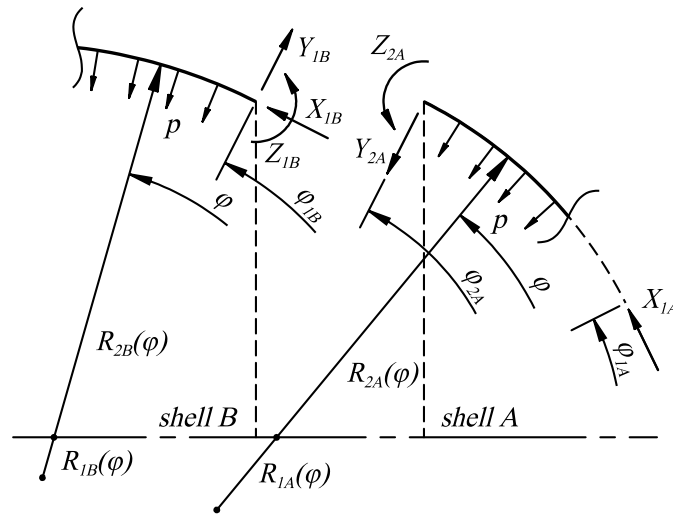

Fig. 3.5. The loads in the junction of a complex shell

In a general case of two shells denoted as A and B (Fig. 3.5), the equations of compatibility can be written as follows:

$$\delta_{XA}{}^{(2)}X_{1A} + \delta_{YA}{}^{(2)}Y_{2A} + \delta_{ZA}{}^{(2)}Z_{2A} + \delta_{pA}{}^{(2)}p = \delta_{XB}{}^{(1)}X_{1B} + \delta_{YB}{}^{(1)}Y_{1B} + \delta_{ZB}{}^{(1)}Z_{1B} + \delta_{pB}{}^{(1)}p,$$

$$(3.106)$$

$$\vartheta_{XA}{}^{(2)}X_{1A} + \vartheta_{YA}{}^{(2)}Y_{2A} + \vartheta_{ZA}{}^{(2)}Z_{2A} + \vartheta_{pA}{}^{(2)}p = \vartheta_{XB}{}^{(1)}X_{1B} + \vartheta^{(1)}Y_{1B} + \vartheta_{ZB}{}^{(1)}Z_{1B} + \vartheta_{pB}{}^{(1)}p,$$

where the corresponding symbols in the above e refer to the vertical displacement δ and rotation ϑ components caused by the loads X, Y, Z and applied pressure p. The indices in those describe the corresponding load, shell, and edge notation. For example $\delta_{XA}{}^{(1)}$ is a displacement component caused by unit normal load $X_{1A} = 1$ on the first edge of the shell denoted as A. Such factors are calculated employing the EET for transverse forces Y and moment Z, while MT is used to resolve the effect of pressure p and normal forces X, analogous to P_0 (Fig. 3.1) and its dimensionless form $\tilde{P}_0$. It is essential to note that MT does not consider the normal edge load X applied to

the second edge of a shell, as it results from the applied external loads relevant for MT (Fig. 3.1). Notably, the load applied on the first edge usually causes deformations on the second edge. For that reason, expressions in Eq. (3.106) are not symmetrical due to the appearance of X_{1A} and X_{1B} on the opposite site.

The subsequent derivation is provided for a general case of a shell structure. Following Eq. (3.6) and applying $\tilde{P}_0 = 0$ and $\varphi = \varphi_1$ or $\varphi = \varphi_2$ the displacement components caused by applied pressure p are:

$$\delta_p{}^{(1)} = -\frac{1}{E_2 h} R_0{}^2 \tilde{R}_2(\varphi_1)^2 \sin \varphi_1,$$

$$\delta_p{}^{(2)} = \frac{1}{E_2 h} R_0{}^2 \sin\varphi_2 \left[\frac{1}{2}\left(\frac{\tilde{R}_2(\varphi_2)}{\tilde{R}_1(\varphi_2)} + v_2 \right) \left(\tilde{R}_2(\varphi_2)^2 - \tilde{R}_2(\varphi_1)^2 \frac{\sin^2\varphi_1}{\sin^2\varphi_2} \right) - \tilde{R}_2(\varphi_2)^2 \right].$$

(3.107)

Considering the relation

$$X_1 = p R_0 \tilde{P}_0,$$

(3.108)

one obtains:

$$\delta_X{}^{(1)} = \frac{1}{E_2 h} R_0 \left(\frac{\tilde{R}_2(\varphi_1)}{\tilde{R}_1(\varphi_1)} + v_2 \right),$$

$$\delta_X{}^{(2)} = \frac{1}{E_2 h} R_0 \frac{\sin \varphi_1}{\sin \varphi_2} \left(\frac{\tilde{R}_2(\varphi_2)}{\tilde{R}_1(\varphi_2)} + v_2 \right)$$

(3.109)

The derivation of the expressions referring to rotations ϑ (Eq. (3.106)) in a general form using MT is omitted, as no significant simplification over Eqs. (3.7), (3.8), (3.12)-(3.15) can be achieved. It is convenient to resolve them specifically for a selected geometry, for which the angular coordinates of edges φ_1, φ_2 are given. In the typical case of a shell, where $\varphi_2 = \pi/2$

$$\vartheta_p{}^{(2)} = 0,$$

(3.110)

which can be shown by proving that the derivative of normal displacements equals zero for $\varphi_2 = \pi/2$ (Eq. (3.8)) as well as employing the applied boundary condition in the membrane theory $\tilde{u}(\varphi_2) = 0$ and substituting those to Eq. (3.7).

Considering the cylindrical shell, the components of displacements and rotations are following:

$$\delta_p{}^{(1)} = \delta_p{}^{(2)} = -\frac{1}{E_2 h} R_0{}^2, \qquad \delta_X{}^{(1)} = \delta_X{}^{(2)} = \frac{v_2}{E_2 h} R_0, \qquad \vartheta_p{}^{(1)} = 0. \qquad (3.111)$$

The rest of the factors from Eq. (3.106) can be derived from EET either using Blumenthal and Steuermann (EETS) or Geckeler (EETG) approach. Both of those

formulations are included in the presented work. The coefficients for the first of those are resolved using Eqs. (3.85), (3.87), (3.92), (3.96), while for the latter, according to Eqs. (3.84), (3.86), (3.93), (3.95) and considering the expressions for corresponding shell edges. The coefficients $\delta_Y{}^{(1)}, \vartheta_Y{}^{(1)}$ are obtained by applying to the afromentioned equations:

$$Q_{e1} = 1, \qquad M_{e1} = 0, \tag{3.112}$$

while in the case of $\delta_Z{}^{(1)}$ and $\vartheta_Z{}^{(1)}$:

$$Q_{e1} = 0, \qquad M_{e1} = 1. \tag{3.113}$$

Analogous substitution is applied for the second edge of a shell. Vertical displacement and rotation components $\delta_Y{}^{(2)}, \vartheta_Y{}^{(2)}$ are derived assuming:

$$Q_{e2} = 1, \qquad M_{e2} = 0, \tag{3.114}$$

and lastly for $\delta_Z{}^{(2)}$ and $\vartheta_Z{}^{(2)}$:

$$Q_{e2} = 0, \qquad M_{e2} = 1. \tag{3.115}$$

The summary of compatibility equations factors is provided in Eq. (3.116) for EETS and Eq. (3.117) for EETG:

$$
\delta_Y{}^{(1)} = \frac{1}{E_2 t} \frac{R_2(\varphi_1)(2\varkappa^2 R_2(\varphi_1) \sin \varphi_1 - v_2{}^2 \cos \varphi_1 \cot \varphi_1)}{\varkappa \sqrt{R_2(\varphi_1)} - v_2 \cot \varphi_1},
$$

$$
\delta_Z{}^{(1)} = 2 \frac{1}{E_2 t} \frac{\varkappa^3 R_2(\varphi_1)^{3/2} \sin \varphi_1}{\varkappa \sqrt{R_2(\varphi_1)} - v_2 \cot \varphi_1},
$$

$$
\vartheta_Y{}^{(1)} = \frac{1}{2 D_1 \varkappa} \frac{R_2(\varphi_1)^{3/2}}{\varkappa \sqrt{R_2(\varphi_1)} - v_2 \cot \varphi_1}, \qquad
\vartheta_Z{}^{(1)} = \frac{1}{D_1} \frac{R_2(\varphi_1)}{\varkappa \sqrt{R_2(\varphi_1)} - v_2 \cot \varphi_1},
$$

$$
\delta_Y{}^{(2)} = -\frac{1}{E_2 t} \frac{R_2(\varphi_2)(2\varkappa^2 R_2(\varphi_2) \sin \varphi_2 - v_2{}^2 \cos \varphi_2 \cot \varphi_2)}{\varkappa \sqrt{R_2(\varphi_2)} + v_2 \cot \varphi_2},
$$

$$
\delta_Z{}^{(2)} = -2 \frac{1}{E_2 t} \frac{\varkappa^3 R_2(\varphi_2)^{\frac{3}{2}} \sin \varphi_2}{\varkappa \sqrt{R_2(\varphi_2)} + v_2 \cot \varphi_2},
$$

$$
\vartheta_Y{}^{(2)} = \frac{1}{2 D_1 \varkappa} \frac{R_2(\varphi_2)^{3/2}}{\varkappa \sqrt{R_2(\varphi_2)} + v_2 \cot \varphi_2}, \qquad
\vartheta_Z{}^{(2)} = \frac{1}{D_1} \frac{R_2(\varphi_2)}{\varkappa \sqrt{R_2(\varphi_2)} + v_2 \cot \varphi_2}.
$$

<div align="right">(3.116)</div>

$$\delta_Y{}^{(1)} = 2\frac{1}{E_2 t}\varkappa R_2(\varphi_1)^{3/2}\sin\varphi_1, \qquad \delta_Z{}^{(1)} = 2\frac{1}{E_2 t}\varkappa^2 R_2(\varphi_1)\sin\varphi_1,$$

$$\vartheta_1{}^{(Y1)} = \frac{1}{2D_1\varkappa^2}R_2(\varphi_1), \qquad \vartheta_1{}^{(Z1)} = \frac{1}{D_1\varkappa}\sqrt{R_2(\varphi_1)},$$

$$\delta_2{}^{(Y2)} = -2\frac{1}{E_2 t}\varkappa R_2(\varphi_2)^{\frac{3}{2}}\sin\varphi_2, \qquad \delta_2{}^{(Z2)} = -2\frac{1}{E_2 t}\varkappa^2 R_2(\varphi_2)\sin\varphi_2,$$

$$\vartheta_2{}^{(Y2)} = \frac{1}{2D_1\varkappa^2}R_2(\varphi_2), \qquad \vartheta_2{}^{(Z2)} = \frac{1}{D_1\varkappa}\sqrt{R_2(\varphi_2)}.$$

(3.117)

Importantly, the displacements and rotation factors are the same for the second edge of a shell, when $\varphi_2 = \pi/2$, as then $\cot\varphi_2 = 0$. In the case of the cylindrical shell, the components of compatibility equations are as follows:

$$\delta_Y{}^{(1)} = 2\frac{1}{E_2 t}\varkappa R_0{}^{3/2}, \qquad \delta_Z{}^{(1)} = 2\frac{1}{E_2 t}\varkappa^2 R_0,$$

$$\vartheta_1{}^{(Y1)} = \frac{1}{2D_1\varkappa^2}R_0, \qquad \vartheta_1{}^{(Z1)} = \frac{1}{D_1\varkappa}\sqrt{R_0},$$

$$\delta_2{}^{(Y2)} = -2\frac{1}{E_2 t}\varkappa R_0{}^{\frac{3}{2}}, \qquad \delta_2{}^{(Z2)} = -2\frac{1}{E_2 t}\varkappa^2 R_0,$$

$$\vartheta_2{}^{(Y2)} = \frac{1}{2D_1\varkappa^2}R_0, \qquad \vartheta_2{}^{(Z2)} = \frac{1}{D_1\varkappa}\sqrt{R_0}.$$

(3.118)

The solution of Eq. (3.106) can be considered elementary after introducing static equilibrium in the juncture, i.e.:

$$Y_1 = Y_2, \qquad Z_1 = -Z_2.$$

(3.119)

The study of stress and deformations in the form of displacements and rotations can be further conducted considering the superposition of the MT and EET using the EETG or EETS approach. The superposition of deformations can be easily achieved using both theories; therefore is not further discussed. It is necessary to recall the plane stress state to resolve the principal stresses:

$$\sigma_1 = \frac{1}{h}\left(N_1{}^{(m)} + N_{11}{}^{(b)} + N_{12}{}^{(b)}\right) + 12\frac{z}{h^3}\left(M_{11}{}^{(b)} + M_{12}{}^{(b)}\right),$$

$$\sigma_2 = \frac{1}{h}\left(N_2{}^{(m)} + N_{21}{}^{(b)} + N_{22}{}^{(b)}\right) + 12\frac{z}{h^3}\left(M_{21}{}^{(b)} + M_{22}{}^{(b)}\right),$$

(3.120)

where z is a coordinate across the thickness of a shell (Fig. 2.3), therefore

$$-\frac{t}{2} \le z \le \frac{t}{2}.$$

(3.121)

The coordinate $z = t/2$ corresponds to the internal surface of the pressure vessel. Normal forces and moments in Eq. (3.120) have been complemented with additional superscripts. The symbol m refers to membrane solution while b corresponds to bending with the use of the EET.

To evaluate the load-carrying capacity of structures made of ductile metals, one may define equivalent von Mises stress, which for the analysed problem is as follows

$$\sigma_r = \sqrt{\sigma_1{}^2 - \sigma_1\sigma_2 + \sigma_2{}^2}. \tag{3.122}$$

3.4. Analytical solution

3.4.1. Geometrical and mechanical properties of shells

To perform an exemplary analysis, it is mandatory to assume values of parameters referring to geometry as well as the mechanical properties of the material. Those are selected to maintain comparability to a typical liquid petroleum gas pressure vessel. The parameters corresponding to the shape are following:

$$R_0 = 1000 \text{ mm}, \qquad L = 1000 \text{ mm}, \qquad \beta = 0.5,$$

the value of the introduced relative depth β is standard for ellipsoidal dished ends. The technical standards allow the manufacturing of ellipsoidal geometries as equivalent torispherical, i.e. of the same relative depth as ellipsoidal. For this reason, its value is applied for both shapes to maintain comparability.

A standard thickness of such a shell structure is within 7 mm to 10 mm. In the analytical solution, the range of thickness is expanded to four distinct values

$$t = 1, 5, 15, 30 \text{ mm}.$$

The considered mechanical properties of the material are consistent with typical structural steel:

$$E_1 = 2 \times 10^5 \text{ MPa}, \qquad \nu_1 = 0.3,$$

while isotropic and orthotropic material properties are considered

$$\alpha = 1, 1.2.$$

The pressure vessels are loaded with uniform internal pressure, which causes the equivalent von Mises stress of 100 MPa in a cylindrical shell, regardless of its thickness and radius:

$$p = \frac{200\sqrt{3}}{3} \frac{t}{R_0}.$$

3.4.2. Cylindrical pressure vessel with ellipsoidal dished ends

The geometry and interaction forces in the pressure vessel with the ellipsoidal dished ends are presented in Fig. 3.6.
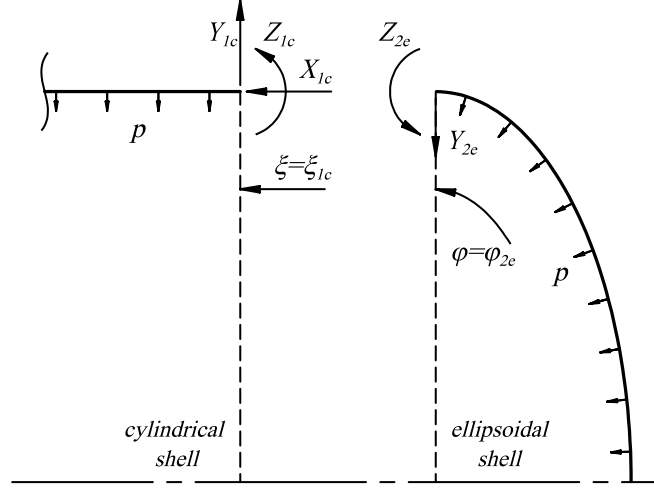

Fig. 3.6. Pressure vessel with ellipsoidal dished ends

The compatibility equations in Eq. (3.106) are rewritten to match the symbols of the analysed shells, i.e. e – ellipsoidal and c – cylindrical:

$$\delta_{Xc}{}^{(1)}X_{1c} + \delta_{Yc}{}^{(1)}Y_{1c} + \delta_{Zc}{}^{(1)}Z_{1c} + \delta_{pc}{}^{(1)}p = \delta_{Xe}{}^{(2)}X_{1e} + \delta_{Ye}{}^{(2)}Y_{2e} + \delta_{Ze}{}^{(2)}Z_{2e} + \delta_{pe}{}^{(2)}p,$$

$$\text{(3.123)}$$

$$\vartheta_{Xc}{}^{(1)}X_{1c} + \vartheta_{Yc}{}^{(1)}Y_{1c} + \vartheta_{Zc}{}^{(1)}Z_{1c} + \vartheta_{pc}{}^{(1)}p = \vartheta_{Xe}{}^{(2)}X_{1e} + \vartheta_{Ye}{}^{(2)}Y_2 + \vartheta_{Ze}{}^{(2)}Z_2 + \vartheta_{pe}{}^{(2)}p.$$

Within the analysis framework, the application of EET using both of the previously discussed solutions of governing differential equations Eq. (3.52) is considered. The exemplary derivation is conducted for $t = 15$ mm and isotropic material ($\alpha = 1$), while the final results are provided for $t = 1, 5, 15, 30$ mm.

The second edge of the ellipsoidal dished end corresponds to $\varphi_2 = \pi/2$, therefore the components of compatibility equations are the same in both EETS and EETG (Eqs. (3.116), (3.117)):

$$\delta_{Ye}{}^{(2)} = -6.997 \times 10^{-3}\frac{\text{mm}^2}{\text{N}}, \qquad \delta_{Ze}{}^{(2)} = -7.343 \times 10^{-5}\frac{\text{mm}}{\text{N}},$$

$$\delta_{pe}{}^{(2)} = 3.833 \times 10^{-1}\frac{\text{mm}^3}{\text{N}},$$

$$\text{(3.124)}$$

$$\vartheta_{Ye}{}^{(2)} = 7.343 \times 10^{-5}\frac{\text{mm}}{\text{N}}, \qquad \vartheta_{Ze}{}^{(2)} = 1.541 \times 10^{-6}\frac{1}{\text{N}},$$

$$\vartheta_{pe}{}^{(2)} = 0\frac{\text{mm}^2}{\text{N}}.$$

The ellipsoidal dished end is a closed-apex shell i.e. $\varphi_1 = 0$. The factors referring to the first edge in Eqs. (3.116), (3.117) are omitted. In the case of the cylindrical geometry, only the first edge is taken into consideration, where its corresponding values are:

$$\delta_{Xc}^{(1)} = 1 \times 10^{-4} \frac{mm^2}{N}, \qquad \delta_{Yc}^{(1)} = 6.997 \times 10^{-3} \frac{mm^2}{N}$$

$$\delta_{Zc}^{(1)} = 7.343 \times 10^{-5} \frac{mm}{N}, \qquad \delta_{pc}^{(1)} = -3.333 \times 10^{-1} \frac{mm^3}{N},$$

$$\vartheta_{Xc}^{(1)} = 0 \frac{mm}{N}, \qquad \vartheta_{Yc}^{(1)} = 7.343 \times 10^{-5} \frac{mm}{N}, \qquad (3.125)$$

$$\vartheta_{Zc}^{(1)} = 1.541 \times 10^{-6} \frac{1}{N}, \qquad \vartheta_{pc}^{(1)} = 0 \frac{mm^2}{N}.$$

The normal force acting upon the first edge of the ellipsoidal dished end is non-existent, thus

$$X_{1e} = 0. \qquad (3.126)$$

Consequently the coefficients $\delta_{Xe}^{(2)}$, $\vartheta_{Xe}^{(2)}$ are then omitted. The normal force acting on the cylindrical shell is defined as follows:

$$X_{1c} = -pR_0, \tilde{P}_{0c} \qquad (3.127)$$

where $\tilde{P}_{0c}$ is resolved according to Eq. (3.45). Following Eq. (3.119) yields:

$$Y_{1c} = Y_{2e}, \qquad Z_{1c} = -Z_{2e}. \qquad (3.128)$$

The solutions to the compatibility equations (Eq. (3.123)) are provided in Table 3.1.

Table 3.1. The interaction loads in the pressure vessel with ellipsoidal dished ends

t [mm]	1	5	15	30
Y_{c1} [N/mm]	1.420	1.588×10^1	8.252×10^1	2.334×10^2
Y_{e2} [N/mm]	1.420	1.588×10^1	8.252×10^1	2.334×10^2
Z_{c1} [N]	0	0	0	0
Z_{e2} [N]	0	0	0	0

3.4.3. Cylindrical pressure vessel with torispherical dished ends

In the analysis of the pressure vessel with torispherical dished ends, it is mandatory to consider two junctions, namely spherical to toroidal and toroidal to cylindrical. The loads resulting from their interactions are presented in Fig. 3.7.
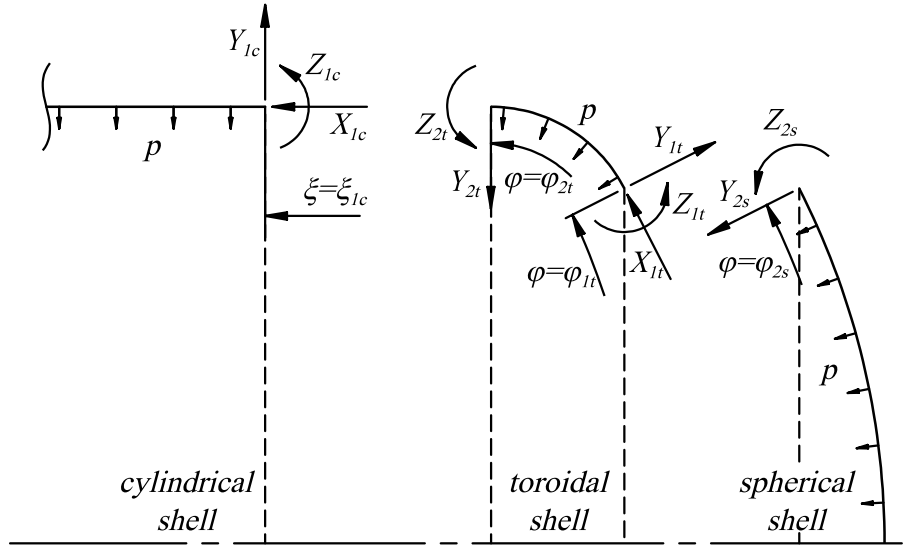

Fig. 3.7. Pressure vessel with torispherical dished ends

In the derivation of the constants in the EET, it is assumed that the moments and transverse forces applied at the first edge ($\varphi = \varphi_1$) cause no effects on the second edge ($\varphi = \varphi_2$) and vice versa. For that reason, the compatibility equations are separate at both edges. Such an approach is correct only for the cases when the length of a shell meridian is significant while thickness remains small. Those conditions assure that the corresponding functions $\bar{\vartheta}$ and U diminish to near-zero values before reaching the opposite edge. Realizing the meridian of the toroidal shell is relatively short, one may predict that the assumption can be violated with the increasing thickness of the pressure vessel.

Using Eq. (3.106), the compatibility equations are rewritten to the following form:

$$\delta_{Xt}^{(1)}X_{1t} + \delta_{Yt}^{(1)}Y_{1t} + \delta_{Zt}^{(1)}Z_{1t} + \delta_{pt}^{(1)}p = \delta_{Xs}^{(2)}X_{1s} + \delta_{Ys}^{(2)}Y_{2s} + \delta_{Zs}^{(2)}Z_{2s} + \delta_{ps}^{(2)}p,$$

$$\tag{3.129}$$

$$\vartheta_{Xt}^{(1)}X_{1t} + \vartheta_{Yt}^{(1)}Y_{1t} + \vartheta_{Zt}^{(1)}Z_{1t} + \vartheta_{pt}^{(1)}p = \vartheta_{Xs}^{(2)}X_{1s} + \vartheta_{Ys}^{(2)}Y_{2t} + \vartheta_{Zs}^{(2)}Z_{2t} + \vartheta_{ps}^{(2)}p,$$

$$\delta_{Xc}^{(1)}X_{1c} + \delta_{Yc}^{(1)}Y_{1c} + \delta_{Zc}^{(1)}Z_{1c} + \delta_{pc}^{(1)}p = \delta_{Xt}^{(2)}X_{1t} + \delta_{Yt}^{(2)}Y_{2t} + \delta_{Zt}^{(2)}Z_{2t} + \delta_{pt}^{(2)}p,$$

$$\tag{3.130}$$

$$\vartheta_{Xc}^{(1)}X_{1c} + \vartheta_{Yc}^{(1)}Y_{1c} + \vartheta_{Zc}^{(1)}Z_{1c} + \vartheta_{pc}^{(1)}p = \vartheta_{Xt}^{(2)}X_{1t} + \vartheta_{Yt}^{(2)}Y_{2t} + \vartheta_{Zt}^{(2)}Z_{2t} + \vartheta_{pt}^{(2)}p.$$

The coefficients for the spherical shell according to EETS (Eq. (3.116)) are:

$$\delta_{Ys}{}^{(2)} = -7.303 \times 10^{-3} \frac{mm^2}{N}, \qquad \delta_{Zs}{}^{(2)} = -5.732 \times 10^{-5} \frac{mm}{N},$$

$$\vartheta_{Ys}{}^{(2)} = 1.263 \times 10^{-4} \frac{mm}{N}, \qquad \vartheta_{Zs}{}^{(2)} = 1.980 \times 10^{-6} \frac{1}{N},$$

(3.131)

while in the case of EETG (Eq. (3.117)), the components are different:

$$\delta_{Ys}{}^{(2)} = -7.616 \times 10^{-3} \frac{mm^2}{N}, \qquad \delta_{Zs}{}^{(2)} = -5.972 \times 10^{-5} \frac{mm}{N},$$

$$\vartheta_{Ys}{}^{(2)} = 1.135 \times 10^{-4} \frac{mm}{N}, \qquad \vartheta_{Zs}{}^{(2)} = 2.063 \times 10^{-6} \frac{1}{N}.$$

(3.132)

The factors resulting from the MT (Eq. (3.107)) are:

$$\delta_{ps}{}^{(2)} = 1.700 \times 10^{-1} \frac{mm^3}{N}, \qquad \vartheta_{ps}{}^{(2)} = 0 \frac{mm^2}{N}.$$

(3.133)

For the toroidal shell, following the EETS approach, i.e. using Eq. (3.116), yields:

$$\delta_{Yt}{}^{(1)} = 7.942 \times 10^{-3} \frac{mm^2}{N}, \qquad \delta_{Zt}{}^{(1)} = 6.233 \times 10^{-5} \frac{mm}{N},$$

$$\vartheta_{Yt}{}^{(1)} = 1.373 \times 10^{-4} \frac{mm}{N}, \qquad \vartheta_{Zt}{}^{(1)} = 2.153 \times 10^{-6} \frac{1}{N},$$

(3.134)

while referring to expressions in Eq. (3.117) results in:

$$\delta_{Yt}{}^{(1)} = 7.616 \times 10^{-3} \frac{mm^2}{N}, \quad \delta_{Zt}{}^{(1)} = 5.972 \times 10^{-5} \frac{mm}{N},$$

$$\vartheta_{Yt}{}^{(1)} = 1.315 \times 10^{-4} \frac{mm}{N}, \qquad \vartheta_{Zt}{}^{(1)} = 2.063 \times 10^{-6} \frac{1}{N}.$$

(3.135)

The considered coefficients on the second edge of the toroidal shell are the same in both EET formulations as $\varphi_2 = \pi/2$:

$$\delta_{Yt}{}^{(2)} = -6.997 \times 10^{-3} \frac{mm^2}{N}, \qquad \delta_{Zt}{}^{(2)} = -7.343 \times 10^{-5} \frac{mm}{N},$$

$$\vartheta_{Yt}{}^{(2)} = 7.343 \times 10^{-5} \frac{mm}{N}, \qquad \vartheta_{Zt}{}^{(2)} = 1.541 \times 10^{-6} \frac{1}{N}.$$

(3.136)

Finally, the application of MT (Eqs. (3.107), (3.109), (3.110)) enables us to find the factors in the first:

$$\delta_{Xt}{}^{(1)} = 1.501 \times 10^{-3} \frac{mm^2}{N}, \qquad \delta_{pt}{}^{(1)} = -4.856 \times 10^{-1} \frac{mm^3}{N},$$

$$\vartheta_{Xt}{}^{(1)} = 3.181 \times 10^{-5} \frac{mm}{N}, \quad \vartheta_{pt}{}^{(1)} = -9.931 \times 10^{-3} \frac{mm^2}{N},$$

(3.137)

and the second edge:

$$\delta_{Xt}{}^{(2)} = 4.878 \times 10^{-4}\frac{\text{mm}^2}{\text{N}}, \qquad \delta_{pt}{}^{(2)} = -1.514 \times 10^{-1}\frac{\text{mm}^3}{\text{N}},$$

$$\vartheta_{Xt}{}^{(2)} = 0\frac{\text{mm}}{\text{N}}, \quad \vartheta_{pt}{}^{(2)} = 0\frac{\text{mm}^2}{\text{N}},$$

(3.138)

of the toroidal shell. The coefficients for the cylindrical shell remain the same as in the analysis of the pressure vessel with the ellipsoidal dished end (Eq. (3.125)). Considering the remaining unknown forces, the first edge of the spherical segment is a closed-apex shell, therefore

$$X_{1s} = 0,$$

(3.139)

which implies the neglection of the coefficients $\delta_{Xs}{}^{(2)}$, $\vartheta_{Xs}{}^{(2)}$. The normal force at the first edge of the toroidal shell is defined according to the membrane theory

$$X_{1t} = pR_0\tilde{P}_{0t},$$

(3.140)

while $\tilde{P}_{0t}$ is obtained according to Eq. (3.26). Similarly to the previous analysis, the normal force acting upon the cylindrical shell X_{1c} is resolved as in Eq. (3.127):

$$Y_{1c} = Y_{2t}, \qquad Z_{1c} = -Z_{2t}.$$

(3.141)

Setting the relations from Eq. (3.119):

$$Y_{1t} = Y_{2s}, \qquad Z_{1t} = -Z_{2s}, \qquad Y_{1c} = Y_{2t}, \qquad Z_{1c} = -Z_{2t},$$

(3.142)

to the compatibility equations (Eqs. (3.129), (3.130)) result in two systems of two equations with two unknowns in each of them. The solution to those is given in Table 3.2 for EETS and Table 3.3 for EETG.

Table 3.2. The interaction loads in the pressure vessel with torispherical dished ends – EETS solution

t [mm]	1	5	15	30
Y_{t1} [N/mm]	-2.011	-2.235×10^1	-1.144×10^2	-3.164×10^2
Y_{s2} [N/mm]	-2.011	-2.235×10^1	-1.144×10^2	-3.164×10^2
Z_{t1} [N]	-8.580	-4.795×10^2	-7.470×10^3	-4.222×10^4
Z_{s2} [N]	8.580	4.795×10^2	7.470×10^3	4.222×10^4
Y_{c1} [N/mm]	1.038	1.161×10^1	6.031×10^1	1.706×10^2
Y_{t2} [N/mm]	1.038	1.161×10^1	6.031×10^1	1.706×10^2
Z_{c1} [N]	0	0	0	0
Z_{t2} [N]	0	0	0	0

Table 3.3. The interaction loads in the pressure vessel with torispherical dished ends – EETG solution

t [mm]	1	5	15	30
Y_{t1} [N/mm]	-2.014	-2.251×10^1	-1.170×10^2	-3.309×10^2
Y_{s2} [N/mm]	-2.014	-2.251×10^1	-1.170×10^2	-3.309×10^2
Z_{t1} [N]	-8.939	-4.997×10^2	-7.790×10^3	-4.407×10^4
Z_{s2} [N]	8.939	4.997×10^2	7.790×10^3	4.407×10^4
Y_{c1} [N/mm]	1.038	1.161×10^1	6.031×10^1	1.706×10^2
Y_{t2} [N/mm]	1.038	1.161×10^1	6.031×10^1	1.706×10^2
Z_{c1} [N]	0	0	0	0
Z_{t2} [N]	0	0	0	0

The results provided in Table 3.2 and Table 3.3 imply that the differences between solutions in junction loads are moderate. It must be further determined whether such discrepancy can be impactful in solving the problems of deformations and stress distribution in the analysed shell structures.

3.5. Results comparison with FEM

It is complicated to evaluate the accuracy of any calculation method without a direct comparison with another. The solution with the use of the MT and EET is approximate, and it is expected that accuracy can diminish with the increase in thickness of a shell. In the presented work, the outcome of the analytical solution is compared with results from the finite element method (FEM) analysis. The details of the latter are described in [37] (A1).

Importantly, the coordinates ω_1 and ω_2 (Eq. (3.73)) in the EETS formulation are elliptic integrals, thus cannot be expressed by elementary functions. To address this issue, one can refer to the Taylor series expansion of the function ρ (Eq. (3.67)) at $\varphi = \varphi_1$ and $\varphi = \varphi_2$ for ω_1 and ω_2 correspondingly or integrate ρ numerically. The latter approach is adopted within this work. The correlation between analytical and numerical solutions is studied by comparing vertical displacements and equivalent stress. Two material models are considered, i.e. isotropic ($\alpha = 1$) and ortotropic, where $\alpha = 1.2$. Such difference between mechanical properties in two perpendicular directions can be viewed as exaggerated for structural steel. Realizing that the

orthotropy coefficient close to unity could bring no significant change in deformations and stress, thus elevated value is applied.

The results are summarized in Table 3.4 and Table 3.5 for the pressure vessel with ellipsoidal dished end considering isotropic material, while the maximum values from those are juxtaposed in Table 3.8. Similarly, the vertical displacements and stress distributions for the pressure vessel with torispherical dished ends are given in Table 3.6 and Table 3.7 and are further compared in Table 3.9.

According to Table 3.4, the EETS and EETG solutions are nearly identical to FEM results for relatively thin shells with ellipsoidal dished ends. As expected, when the thickness is increased, the differences become apparent. Those are substantially smaller for the EETS than EETG as the maximum relative difference reaches 9.393 % in the first, while it is 21.43 % for the latter (Table 3.8). Following the stress distributions presented in Table 3.5, one can observe that the analytical solution is in complete agreement with the numerical study for the shells characterised by the relatively low thickness. For thicker shells, visible discrepancies are observed as then the numerical results show distinct values of the stress in the inner, middle and outer shell surfaces beyond the juncture.

There are two reasons explaining such a phenomenon. The first refers to the normal to middle surface stress, which is omitted in the shell theory; however, such a stress component is expected to be marginal. The other cause of the stress variation is that the applied pressure causes the bending phenomenon by itself, which is neglected in the EET. Notably, such observation refers only to the shells with variable radii of curvature. Inspecting the stress in the area close to the junction of the shells, one can conclude that the difference between stress in the inner and outer surface in analytical and FEM solutions are close to the same differences beyond the junction. This implies that the observed differences are partially caused by the omitted effect of surface load on bending effects in the analytical solution. If the discrepancies would be caused only by the neglection of normal to surface stress components in shell theory, then the through-thickness stress variation would be the same in the dished end and cylindrical shell. According to the results in Table 3.5, the stress variation across thickness is considerably more remarkable in the ellipsoidal dished end beyond the edge disturbance.

Although the summarized results in Table 3.8 suggest that the EETG solution is closer to FEM in terms of stresses, further analysis can discredit this observation.

Taking a closer look at the plots for $t = 15, 30$ mm in Table 3.5 concludes the stress in the middle surface is more consistent for EETS than EETG. Additionally, the bending effect in the latter diminishes at a higher pace, which is somewhat incompatible with numerical solutions. Lastly, it is necessary to explain why the analytical solutions indicate different stress in the middle surface, putting aside the abovementioned discrepancies between EETS and EETG. Theoretically, any simplifications in analytical bending moments functions should not contribute to the stress distribution in the middle surface. For that reason, those differences can be either the effect of some inaccuracies in the formulation of normal forces in the MT or the omission of shear forces in the stress calculation, which could become apparent for thicker shells.

In the pressure vessel with torispherical dished ends, the discrepancies between analytical and numerical results become considerable even for relatively thin shells. The vertical displacements shown in Table 3.6 are in near ideal agreement for $t = 1$ mm, however any further increase shows a visible deviation, especially in the neighbourhood of the junction of the toroidal and spherical shell. For the thickness $t = 30$ mm, a severe inconsistancy is observed, to the point where the displacements are incompatible in the connected edges of the toroidal and cylindrical shell. It shows that the loads at the first edge of the toroidal shell have an immense impact on the displacements on the second edge, violating the prescribed condition of deformations continuity. The meridian length of the toroidal shell is relatively small compared to other shells, and as the thickness is increased, the disturbances caused by edge loads are carried over greater arc length and do not vanish before reaching the opposite edge. One could rewrite the equations of compatibility (Eq.(3.129), (3.130)) to include the effect of carrying the deformations to another edge, but it can be considered a partial and debatable solution. Foremost, in the derivation of constants of the edge effect theory (Eq. (3.94)), it is assumed that the edges do not interfere with each other, which contributes to the convenient description of the theory and its application. Enforcing the compatibility of deformations without rewriting the constants and then inevitably all the deformations components would lead to incompatibility of internal forces. Additionally, the components of rotations and displacements referring to the opposite edge would have a cumbersome form as then $\omega_1(\varphi_2)$, $\bar{\omega}_1(\varphi_2) \neq 0$ and $\omega_2(\varphi_1)$, $\bar{\omega}_2(\varphi_1) \neq 0$.

Table 3.4. Vertical displacements comparison for the pressure vessel

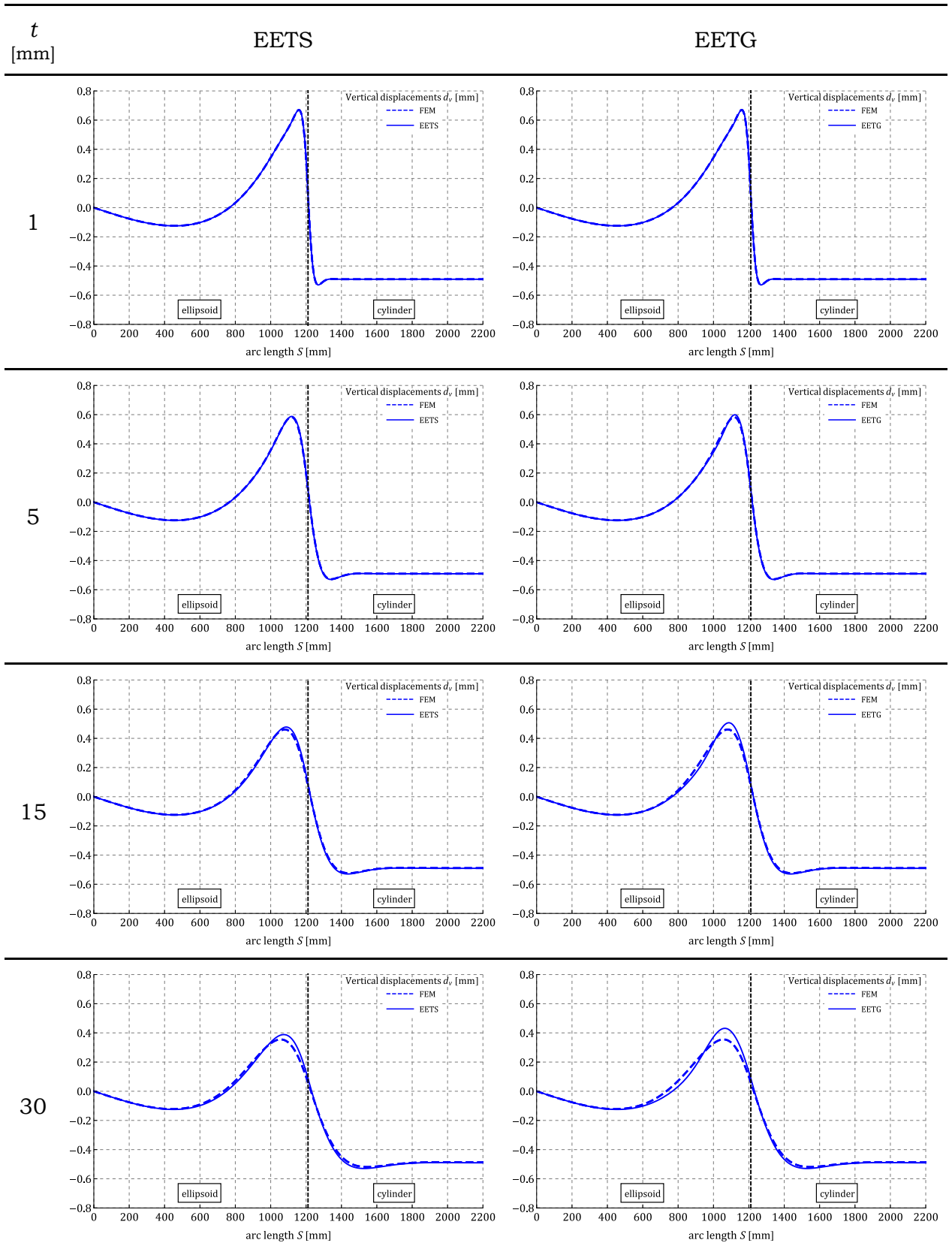*with ellipsoidal dished ends – isotropic material*

t [mm]	EETS	EETG
1		
5		
15		
30		

Table 3.5. Equivalent stress comparison for the pressure vessel with ellipsoidal dished ends – isotropic material

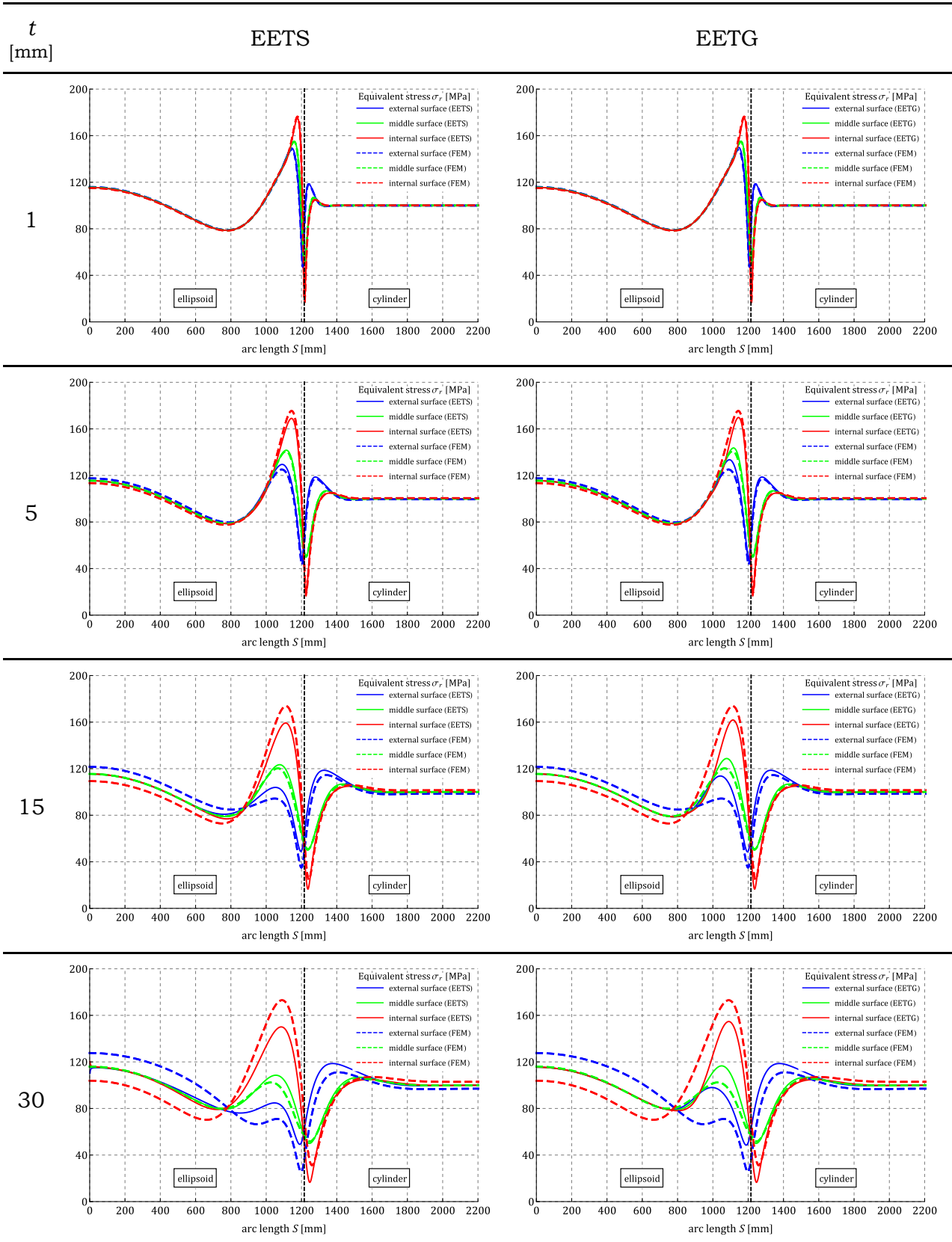| t [mm]	EETS	EETG
1		
5		
15		
30		

Table 3.6. Vertical displacements comparison for the pressure vessel

with torispherical dished ends – isotropic material

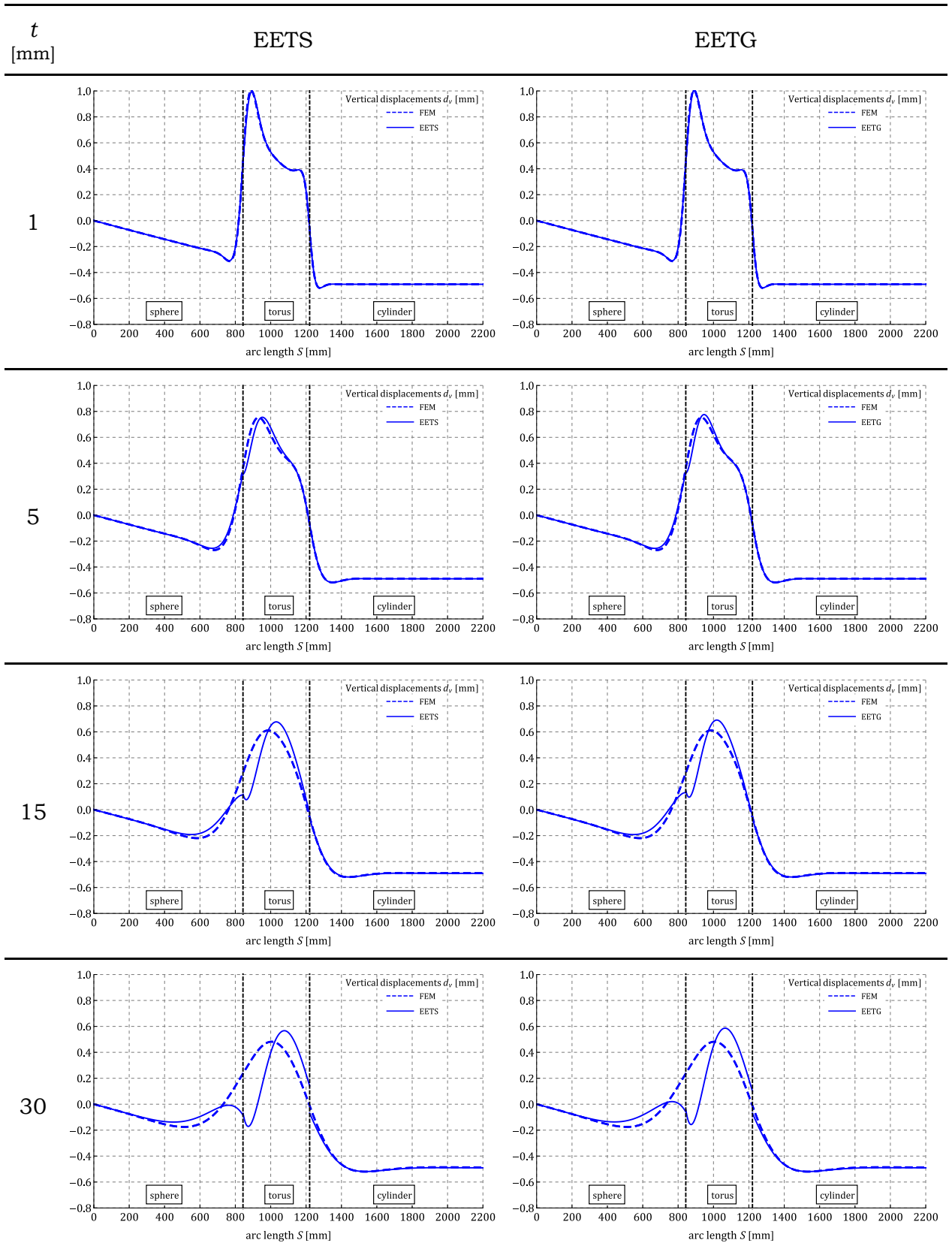| t [mm]	EETS	EETG
1		
5		
15		
30		

Table 3.7. Equivalent stress comparison for the pressure vessel

with torispherical dished ends – isotropic material

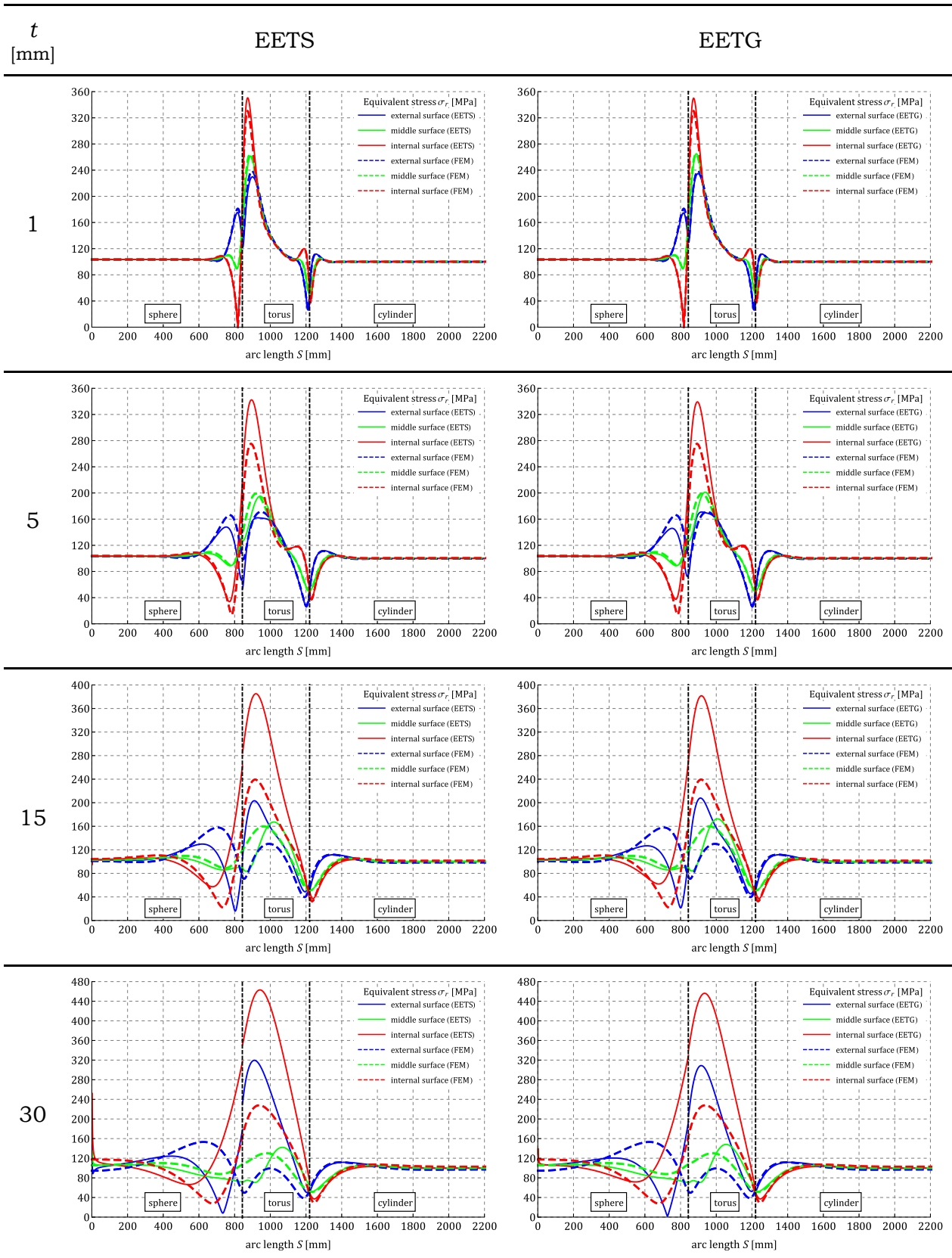| t [mm]	EETS	EETG
1		
5		
15		
30		

Table 3.8. The summary of results for a pressure vessel with ellipsoidal dished end – isotropic material

	t [mm]	Analytical solution		FEM	Relative difference [%]	
		EETS	EETG		EETS	EETG
$\sigma_{r\,max}$ [MPa]	1	174.9	175.0	176.3	0.7796	0.7251
	5	169.0	169.8	175.4	3.658	3.216
	15	159.2	161.8	173.8	8.374	6.895
	30	150.0	154.6	173.0	13.25	10.58
$d_{v\,max}$ [mm]	1	0.6701	0.6715	0.6693	0.1157	0.3306
	5	0.5876	0.5990	0.5830	0.7866	2.743
	15	0.4773	0.5068	0.4609	3.578	9.959
	30	0.3883	0.4311	0.3550	9.393	21.43

Table 3.9. The summary of results for a pressure vessel with torispherical dished end – isotropic material

	t [mm]	Analytical solution		FEM	Relative difference [%]	
		EETS	EETG		EETS	EETG
$\sigma_{r\,max}$ [MPa]	1	350.5	350.5	330.3	6.109	6.109
	5	342.3	339.2	275.1	24.40	23.28
	15	385.0	381.5	239.2	60.98	59.52
	30	463.0	456.1	227.9	103.1	100.1
$d_{v\,max}$ [mm]	1	0.9946	1.007	1.003	0.8672	0.412
	5	0.7547	0.7756	0.7529	0.2354	3.010
	15	0.677	0.691	0.6114	10.73	13.02
	30	0.5668	0.5865	0.4819	17.59	21.68

Analogous deviations are present in the stress distributions shown in Table 3.7. The substantial issues with the solution start for $t = 15$ mm and those include immense differences in stress values and their incompatibility. The latter can be explained just as in the case of displacements; however, the cause of excessive stress in the toroidal shell has a diverse nature. During the analysis of the results, attention has been brought to the values of the edge loads solved with the use of compatibility equations. Those have been compared referring to FEM and Ritz method (RM)[37](A1),

which showed severe discrepancies in the analytical solution. The compatibility equations have been carefully verified, including comparing the corresponding components in all three methods. It showed that the factors calculated with the use of MT differ the most. For that reason, the MT solution for the separate toroidal shell is further considered and compared to other methods. The results of such analysis are presented in Table 3.10 for $p = 1$ MPa and Table 3.11 for $X_{1t} = 1$ N/mm for the thickness $t = 1, 15$ mm. Those show that while displacements for $t = 1$ mm are very close in all methods, the similarity between values vanishes for $t = 15$ mm. For the rotations comparison, numerical FEM result is shown only on the first edge. The juxtaposed data show substantial differences even for the thinner shell, while relative difference reaches roughly 400% for the thicker structure. As expected, both of the compared quantities are in linear relation to thickness in the MT. The numerical solutions do not share such characteristics. It implies that the application of MT in the case of the open-apex shell induces significant errors in the solution because bending occurs even in the case of reasonably thin shells. Such an observation is based on the fact that the numerical results do not change proportionally with the thickness increase.

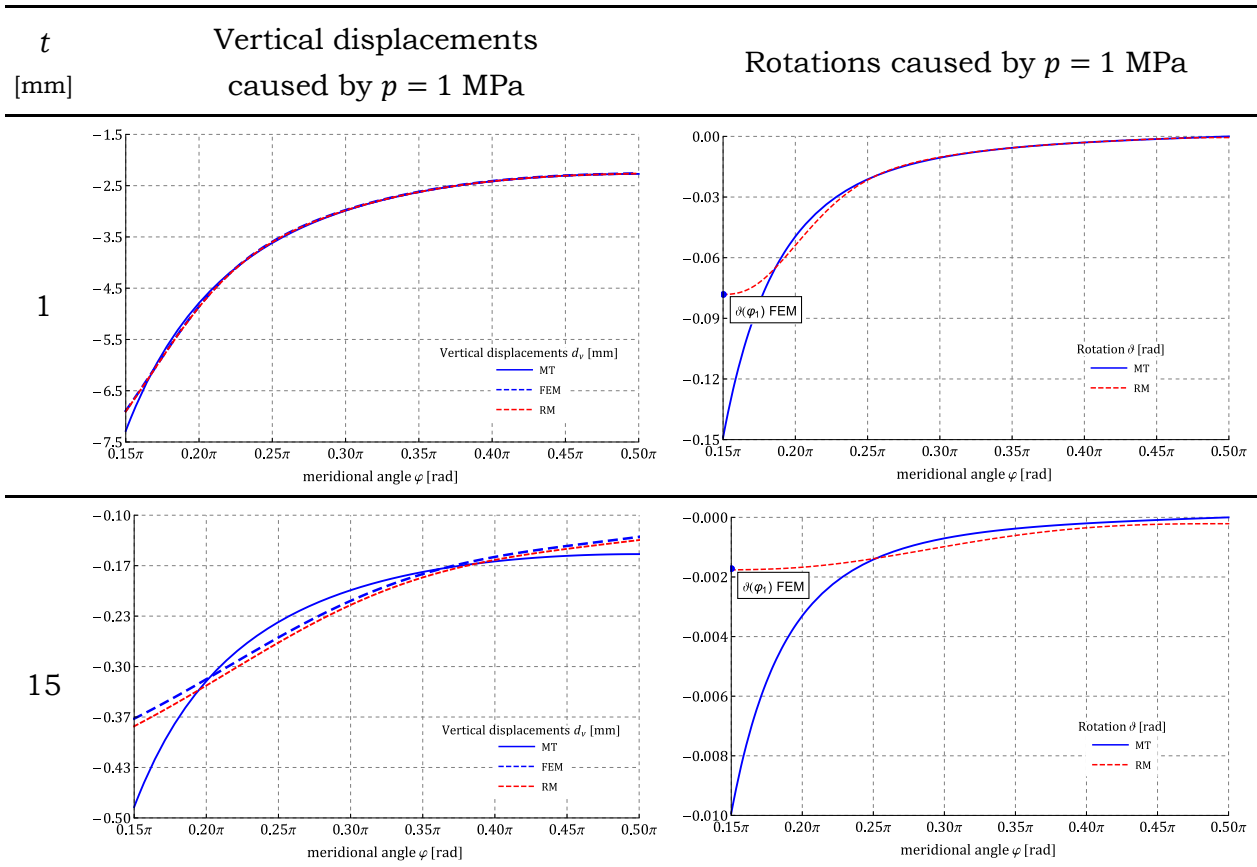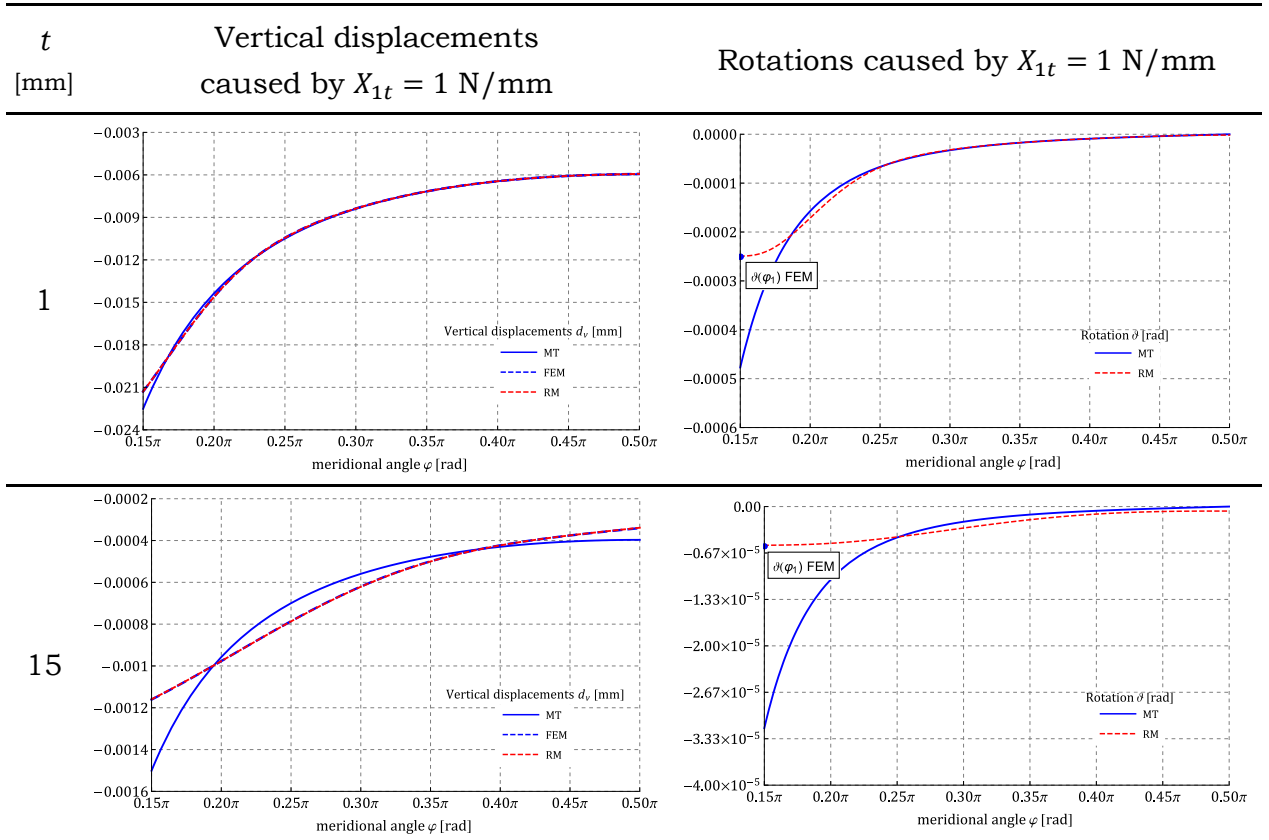*Table 3.10. The membrane state solution analysis for toroidal shell subject to a uniform pressure*

Table 3.11. The membrane state solution for toroidal shell subject to normal edge force

t [mm]	Vertical displacements caused by $X_{1t} = 1$ N/mm	Rotations caused by $X_{1t} = 1$ N/mm
1		
15		

To verify whether a structure is thin-walled, one can refer to the relation between thickness to minimum radii of curvature (Eq. (2.1)), which value is suggested to be below 0.05. For the analysed toroidal shell $R_{1t} \approx 342$ mm, therefore $t/R_{min} \approx 0.003$ and $t/R_{min} \approx 0.043$ for thinner and thicker shells correspondingly. It proves that the toroidal shell is considered thin-walled, and therefore the application of the MT is justified.

In the effect of a vast overestimation in the MT solution, the incompatibility of displacements and rotations becomes magnified. To resolve this, the edge loads in the compatibility equations must be excessive to compensate for enormous differences in deformations between the second edge of the spherical shell and the first edge of the toroidal shell. Although the continuity of those is achieved, the edge loads cause an immense bending phenomenon, leading to unrealistic stresses values. For the same reason, the distortions are visible in the comparison of vertical displacement in Table 3.6. Such an observation implies that the application of the EET for complex shell structures may be unsatisfactory, as the accuracy of the MT significantly contributes to the bending phenomenon due to the necessity of compatibility equations formulation.

The results shown in Table 3.12 and Table 3.13 consider the pressure vessel with ellipsoidal dished ends with the introduced orthothropy of $\alpha = 1.2$. Similarly, Table 3.14 and Table 3.15 refer to torispherical shape. As expected, the compared vertical displacements and stresses are in good agreement with the numerical method for the thinner shells. The results share the same issues for the thicker shells as for the isotropic material. In the case of equivalent von Mises stress comparison, an additional discrepancy is observed. Following the numerical method, a disturbance of stress is visible in the area of the dished end apex, i.e. $S = 0$ mm, which is compatible with the Ritz method solution [37] (A1). This feature does not appear in the analytical study

Taking into consideration thinner shells, the stress in this area is described only by the MT and depends entirely on normal membrane forces from Eq. (3.18). These are described only by the principal radii of curvature, and the material properties do not contribute to forces N_1, N_2. Realizing the differences of stress in the inner, middle and outer surface, such feature can be caused only by the bending phenomenon. The EET includes only the edge loads as the source of bending; therefore, the distortion seen in the numerical analysis cannot be reproduced by employing the analytical solution.

The content provided in Table 3.16 and Table 3.17 summarizes the maximum vertical displacements and stresses from analytical analysis and compares them to the numerical FEM values. The difference between them is moderately elevated, referring to the isotropic material. In the case of the ellipsoidal geometry, stress compliance for t/R_0 ratio in the range 0.1% ($t = 1$ mm) to 3% ($t = 30$ mm) is within 0.7251% to 13.25% relative difference. For the torispherical geometry, the same values range from 6.103% to 103.1%.

Discussion over the achieved results indicates severe problems with the analytical description of stress and deformations. The selection of one of two compared EET formulations shows the limited impact, as MT mainly introduces the observed inaccuracies. This is especially apparent for torispherical shell, where any thickness increase beyond 1 mm ($t/R_0 = 0.1\%$) leads to a technically unacceptable solution. Realizing the conditions of the MT applicability from section 3.1.1, one can conclude that these require additional, more strict guidelines.

Table 3.12. Vertical displacements comparison for the pressure vessel
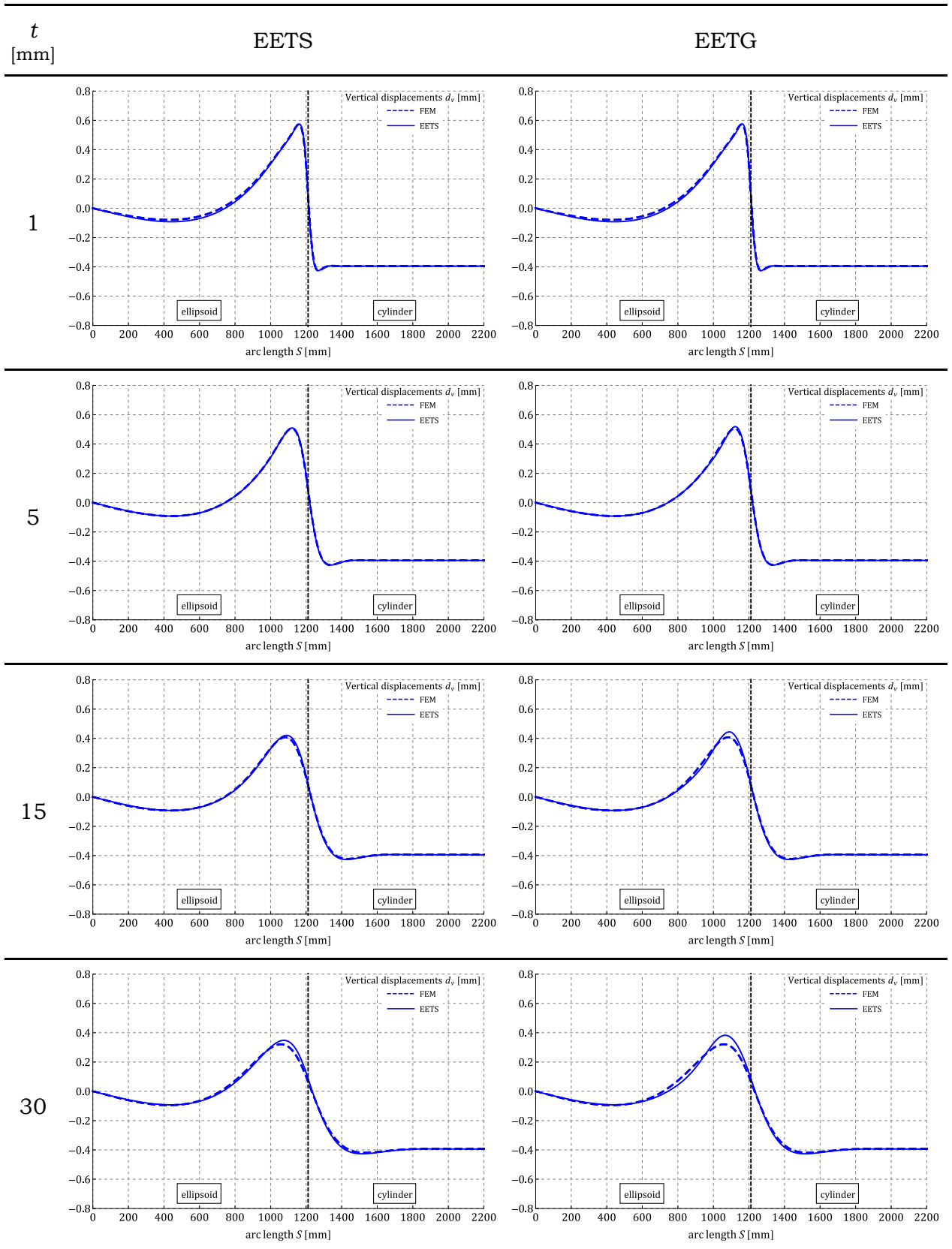*with ellipsoidal dished ends – orthotropic material*

t [mm]	EETS	EETG
1		
5		
15		
30		

Table 3.13. Equivalent stress comparison for the pressure vessel
with ellipsoidal dished ends – orthotropic material

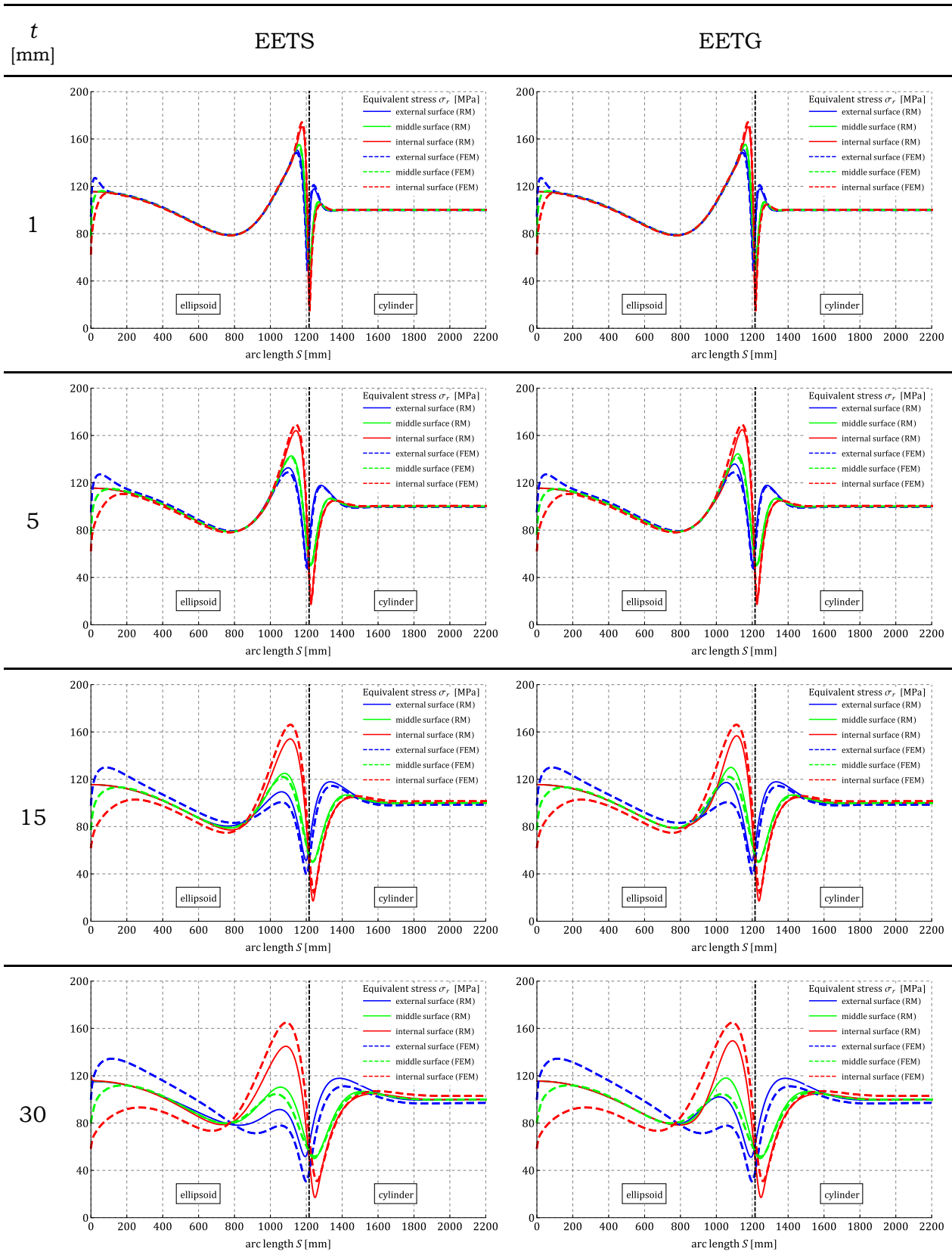*Table 3.14. Vertical displacements comparison for the pressure vessel*
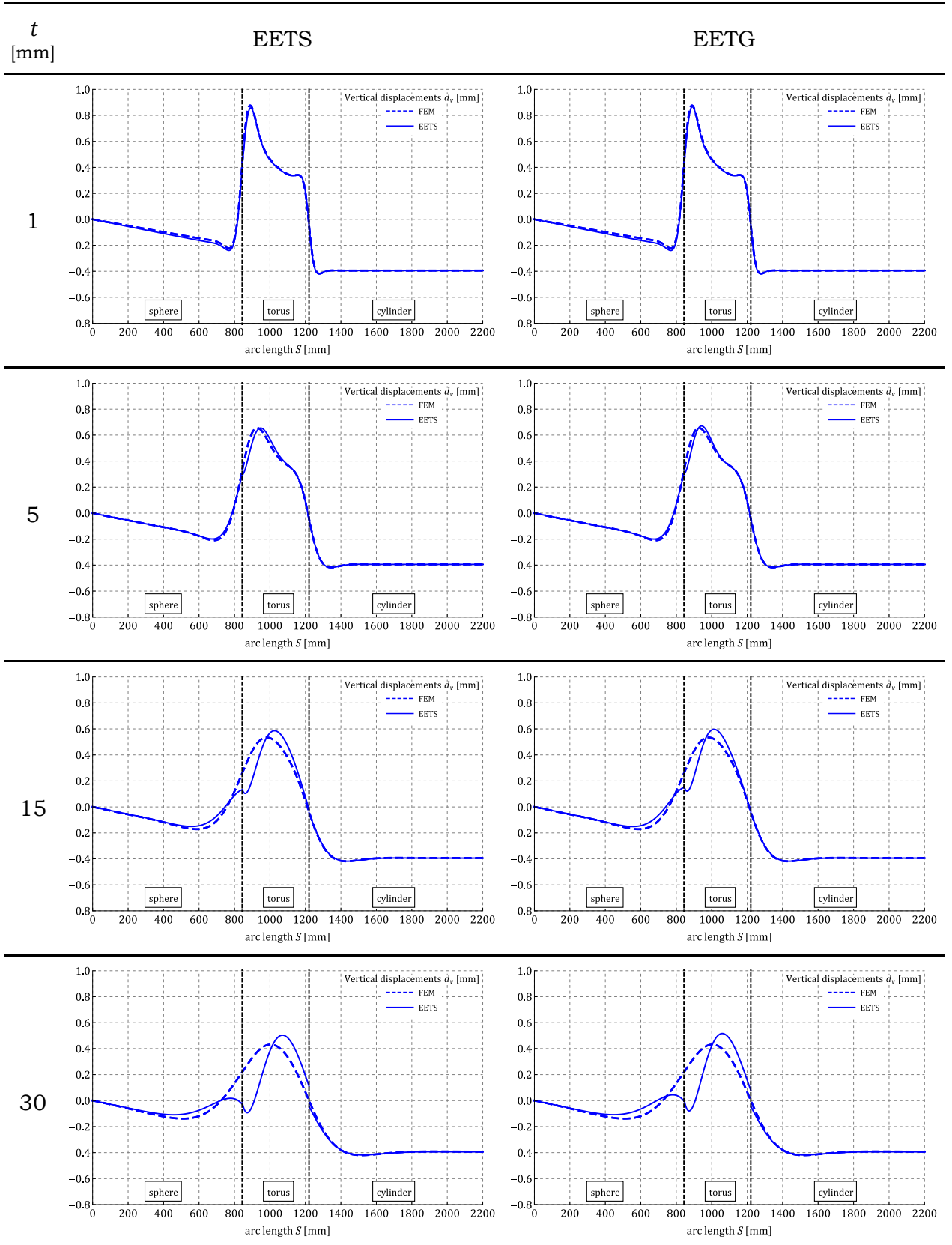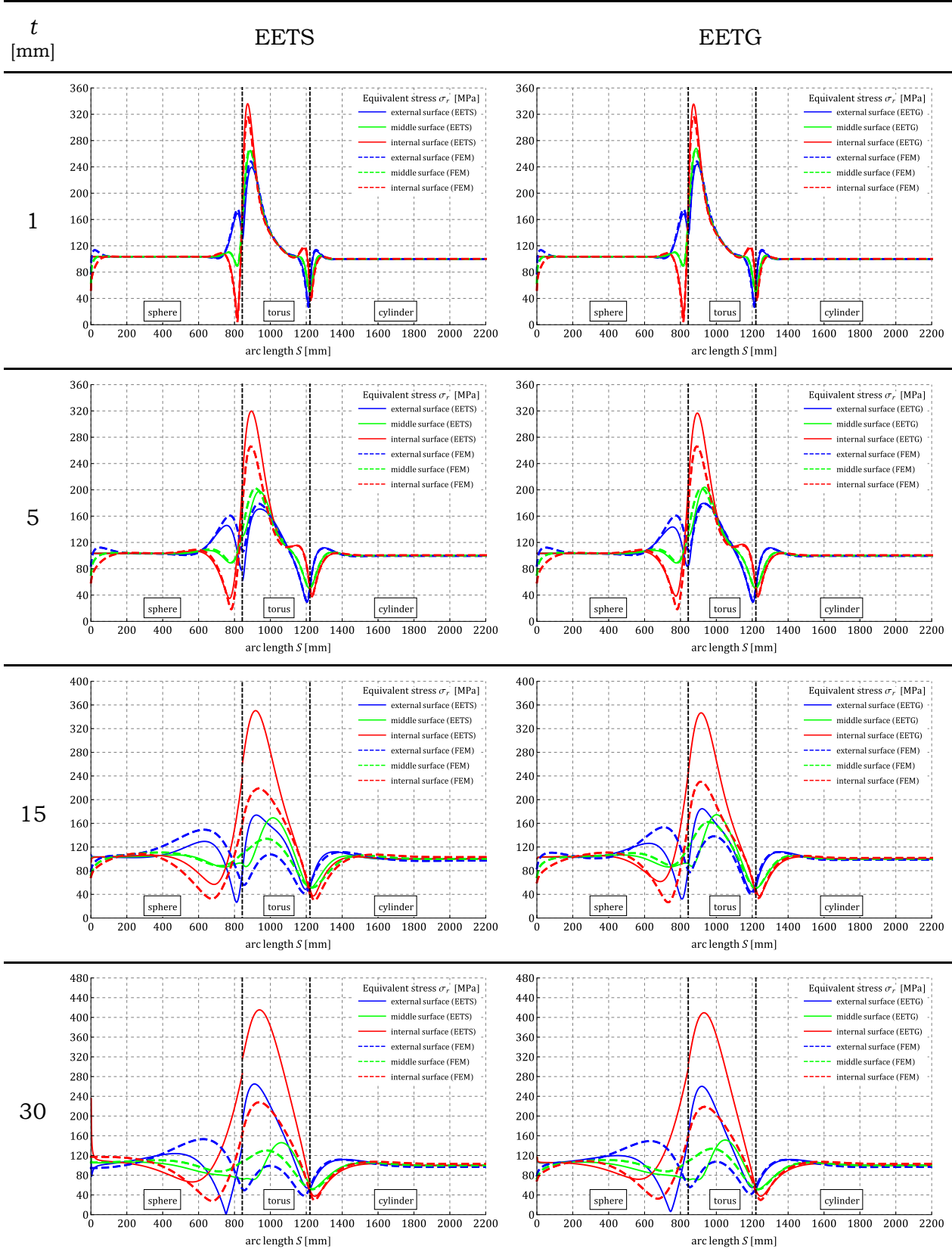
with torispherical dished ends – orthotropic material

t [mm]	EETS	EETG
1		
5		
15		
30		

Table 3.15. Equivalent stress comparison for the pressure vessel
with torispherical dished ends – orthotropic material

t [mm]	EETS	EETG
1		
5		
15		
30		

56

Table 3.16. The summary of results for a pressure vessel

with ellipsoidal dished end – orthotropic material

	t [mm]	Analytical solution		FEM	Relative difference [%]	
		EETS	EETG		EETS	EETG
$\sigma_{r\,max}$ [MPa]	1	170.2	170.3	174.1	2.218	2.162
	5	164.0	164.8	169.1	2.980	2.503
	15	154.1	156.7	166.1	7.249	5.672
	30	144.9	149.5	164.9	12.17	9.367
$d_{v\,max}$ [mm]	1	0.5748	0.5759	0.5727	0.3677	0.554
	5	0.5097	0.5185	0.5061	0.7121	2.443
	15	0.4208	0.4441	0.4077	3.216	8.927
	30	0.3479	0.3825	0.3212	8.307	19.09

Table 3.17. The summary of results for a pressure vessel

with torispherical dished end – orthotropic material

	t [mm]	Analytical solution		FEM	Relative difference [%]	
		EETS	EETG		EETS	EETG
$\sigma_{r\,max}$ [MPa]	1	335.9	335.4	316.4	6.162	5.992
	5	319.7	316.6	266.0	20.18	19.03
	15	350.3	346.6	230.1	52.21	50.59
	30	415.2	409.3	219.0	89.58	86.90
$d_{v\,max}$ [mm]	1	0.8575	0.8676	0.8765	2.166	1.01
	5	0.6541	0.6706	0.6549	0.1269	2.397
	15	0.5860	0.5966	0.5343	9.675	11.66
	30	0.5033	0.5162	0.4314	16.67	19.65

4. Ritz method application

As shown in the previous chapter, the superposition of MT and EET is far from satisfying for the analysed problems. Despite the numerous theories found in various valuable monographs and papers, the possibility of precise analytical solutions to static problems of shells, including bending effects, remains poor. It implies that the only available calculation method for obtaining a supposedly accurate solution in terms of stress and deformations is the FEM. The accuracy of the FEM results can be analysed only by comparing the results to the experimental data. Notably, such a numerical approach allows obtaining the solution in the discrete form, at each of the FE model nodes, often limiting the analysis of the internal forces and moments, especially for doubly-curved shell structures. In a further study, the Ritz method (RM) is used to investigate the stress and deformation in the standard pressure vessels with ellipsoidal and equivalent torispherical dished ends. The material model is consistent with the one introduced in chapter 3, describing the analytical solution. This study has been previously published [37] (A1), and the reprint of the paper can be found in Appendix A1.

The description of the RM and its basic assumptions is provided in the literature [1], [2]. It belongs to the group of so-called variational methods and is based on the principle of stationary potential energy. The total potential energy of a system is expressed as strain energy and potential energy of external loads. Those are described using displacement functions that constitute linear combinations of some other functions. Ultimately the variational problem is transformed into the differential formulation. Although the application of the RM can theoretically result in an analytical solution, it applies only to elementary, straightforward structural problems. For more advanced investigations, the formulation remains analytical; however, at some point, it is usually necessary to refer to numerical methods as the mathematics becomes cumbersome. The utilization of the RM in the presented study is considered a semi-analytical approach.

The strain energy and the potential energy of external forces are derived for an arbitrary shell structure using the linear theory of shells. The study considers three different displacement functions, i.e. polynomials, trigonometric series and modified trigonometric series. The latter is formulated to resemble the characteristics of displacements functions obtained using EET. The results are compared to the finite element method study outcome using ANSYS 19 software.

The convergence of the results is obtained for a wide range of shell thicknesses. Additionally, the research results refer to the design method of ellipsoidal and supposedly equivalent torispherical dished ends described in the technical standards [10]-[12], indicating significant ambiguities.

5. Diminishing of the edge effect

Following the analytical (MT and EET) and semi-analytical (RM) investigation, one can conclude that the equivalent von Mises stress distribution in the standard dished ends of cylindrical pressure vessels is disadvantageous. Notably, ellipsoidal dished ends are characterised by substantially smaller peak stress than comparable torispherical dished ends described in [10]-[12]. Despite that, the maximum stress in the ellipsoidal shell significantly exceeds the stress in the cylindrical segment, making the standard geometry an unsatisfactory solution. It has been shown in the previous studies of this work that such a negative feature is related to the loads in the junctions of the analysed complex shell structures. Investigation of the compatibility equations can lead to an observation that the calculated transverse forces and moments are zero when the deformations from the membrane state are equal at the edges of shells. It shows that developing a specific geometry of the dished end that satisfies such a deformation condition can theoretically eliminate the edge effect. Realizing the simplified nature of the MT, instead of eliminating the edge effect, it can rather lead to the diminishing of the bending phenomenon in the junction. The described topic has been already presented in the form of the paper [62], which reprint is provided in Appendix A2.

It is assumed within the paper that the desired shape of the dished head must meet two particular conditions. The maximum stress in a cylindrical pressure vessel shall not be higher than in a cylindrical shell in the membrane stress state. The above condition implies eliminating the edge effect in the junction area. The second condition is to achieve a membrane stress state in the whole structure, maintaining the lowest value of the relative depth of the dished end. Its reasoning lies strictly within practical importance, i.e. applications and manufacturing process. The subject of the study in the paper includes the following three analytical, nonstandard Cassini and Booth ovaloidal, as well as clothoidal dished ends. The meridional curves are explicitly formulated to enable modifying the relative depth of dished ends.

In the research, two geometrical conditions are introduced to the geometry of the dished ends. The first of them is referred to as the necessary condition of the edge effect elimination, which imposes equal meridional curvatures in the junction. The latter considers equal derivatives of the curvature. The stress concentration factor is analysed according to the relative depth of the selected curves. The problem is investigated analytically with the MT and verified using the FEM. According to the results, the stress disturbance in the junction area is substantially reduced. The peak stress is shifted beyond the junction, which ultimately does not bring a desired improvement in the stress distribution.

6. Shape optimization of dished ends

The standard geometries of dished ends of cylindrical pressure vessels were developed at the beginning of the last century. Among them, there are ellipsoidal and torispherical geometries (Fig. 3.3) characterized by disadvantageous stress distribution ([12], [37] (A1)), which is the primary determinant when designing shell structures. The research [62] (A2), briefly described in the previous chapter, brought insight into the problem of stress distribution. Despite that, it is necessary to refer to optimization to improve the stress distribution in dished ends of the cylindrical pressure vessels.

It has been concluded that the shape optimization of dished ends is the most suitable among a few possible methods for altering the stress distribution. It is assumed their depth is equivalent to the standard ones to maintain comparability and manufacturability. The formulation of the problem and its outcome is described within the paper [81], provided in Appendix A3.

Referring to the Bézier curve (BC), a unique geometry of arbitrary order is developed to describe the parametric shape of the dished end. The parametric curve always fits the initially defined feasibility region and satisfies all geometrical constraints, including non-negative curvature. The order of the curve must be at least three due to the constraints; however, it can be increased indefinitely. This property is critical for optimization as it enables arbitrarily assuming the number of independent parameters controlling the shape. The increase of the curve order raises the number of its degrees of freedom which potentially enables obtaining a better solution due to optimization. Notably, the geometry is proportional to the cylinder radius (Fig. 3.2); therefore, the optimized shape can be adapted to cylindrical pressure vessels with any diameter. The mentioned properties show that the curve is excellent for optimization

The procedure is performed using two methods. Initially, equivalent stress is solved analytically according to the MT, while the sequential quadratic programming (SQP) algorithm seeks the maximum stress along the meridian of the dished end and attempts to minimize it. Further, numerical FEM calculations are conducted to validate the outcome of the analysis. Realizing the simplified character of the MT and the impact of the bending phenomena in shell structures, the procedure is further changed. The stress distribution is resolved using FEM in ANSYS software, where its peak value constitutes the fitness function value. Due to its discontinuous character, the optimization is performed using a genetic algorithm (GA) in MATLAB software. A significant improvement in the maximum stress over the standard dished ends is achieved.

7. Experimental studies and numerical verification

7.1. Static tensile tests

The experimental verification of the results obtained in the optimization requires determining an appropriate manufacturing method. Industrial pressure vessels are usually made of structural steel by metal forming. The use of such manufacturing methods for individual vessel models is economically unjustified. The presented research refers to additive manufacturing methods (AMM), often referred to as 3D printing, to address this issue. Due to their significant, recent development, they allow the manufacture of structures of almost any shape while maintaining acceptable mechanical properties, strength and production costs.

There are many AMM methods, but not all of them are potentially valid for manufacturing pressure vessels. The models suitable for this study must be characterised by high geometric accuracy and tightness, allowing their pressurization. It is also essential that the vessels analysed in the optimization study in chapter 6 are considered thin-walled. When selecting the appropriate AAM, the smallest and largest dimensions of the model must be taken into account. Manufacturing exceptionally thin structures can lead to significant geometrical inaccuracies or unsatisfactory strength, as in this case, the load-carrying capacity is not necessarily proportional to the wall thickness. It creates the necessity of relatively large vessel models, so the wall thickness is within an acceptable range for a given manufacturing device - a 3D printer.

Based on the analysis of available AMMs that meet the above requirements and their availability, it is decided to consider two methods, i.e. Selective Laser Sintering (SLS) and Multi Jet Fusion (MJF). The more suitable method is selected by carrying out a static tensile test on standard, type 1A specimens according to ISO527 [82] (Fig. 7.1). It should be emphasised that this comparison depends not only on the AMM but also on the equipment used to manufacture them. The samples produced by the SLS method are obtained on an EOS P 396 device, while for the MJF, it is an HP Jet Fusion 3D 4200, both from polyamide PA12 material.
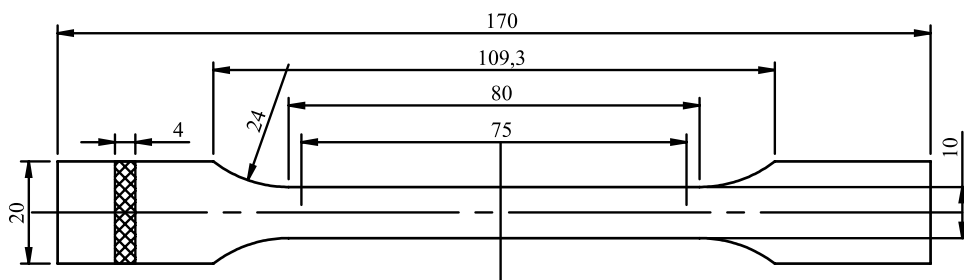

Fig. 7.1. The standard 1A specimen for static tensile test according to ISO527

Considering the potential orthotropic properties of models printed with both AMMs, specimens manufactured in two directions are analysed, as shown in Fig. 7.2. In the first case, the axis of the specimen lies in the plane of successive print layers, while in the second case, the axis is perpendicular to them. For clarity, these directions are referred to as longitudinal and transverse, respectively, which describe the alignment of the print layers concerning the specimen axis.
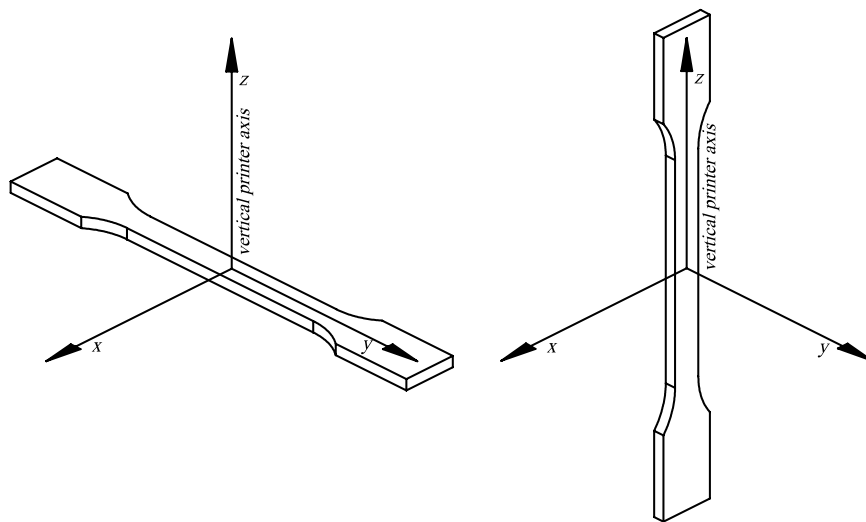

Fig. 7.2. Alignment of the specimens in the printing chamber

The introduced directions are coherent with the principal curvature directions of the cylindrical shell of the vessel, whose axis is considered parallel to the vertical axis of a 3D printer. Samples manufactured in the longitudinal and transverse directions in both AMMs are shown in Fig. 7.3.
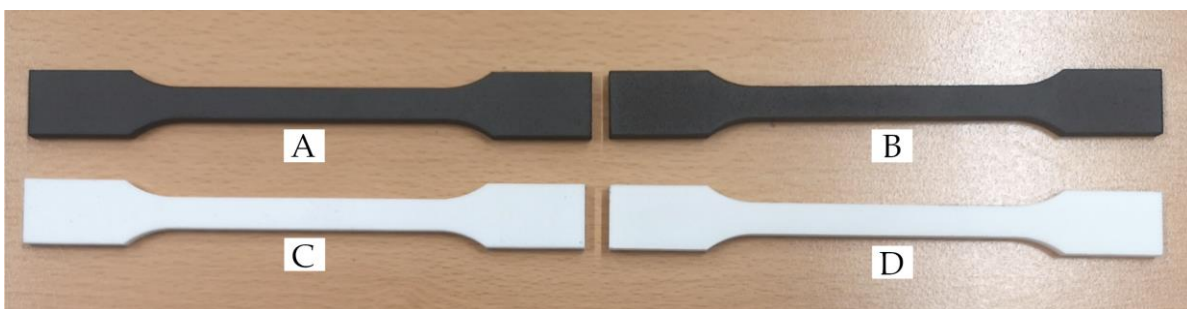
Fig. 7.3. The specimens manufactured in MJF (black) and SLS (white) technology in A, C - longitudinal direction, B, D - transverse direction

The static tensile test is carried out on a Zwick Z100 universal testing machine (Fig. 7.4) with a 50 N to 100 kN measurement range. The resolution of the force sensor is 1 N. The elongation during the test is evaluated using an extensometer with a resolution of 0.6 µm. The gauge length equals 75 mm, and the strain rate is 1 mm/min. Those values are based on the ISO527 standard. All of the measured quantities are sampled at 50 Hz. Specimens are clamped with flat, self-tightening grips during the experiment. The applied pre-test force is 50 N.

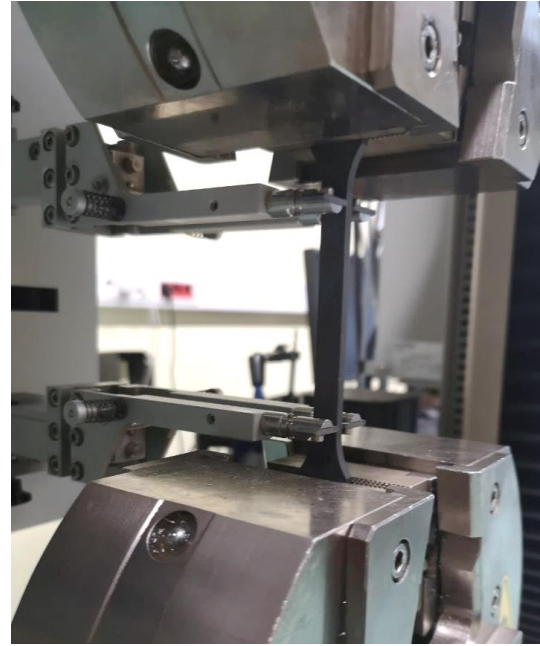*Fig. 7.4. Zwick Z100 universal testing machine*   *Fig. 7.5. The MJF specimen during the test*

In the first phase of the study, the specimens are tested to rupture. The registered stress-elongation relations are shown in Figs. 7.6, 7.7 for the MJF and Figs. 7.8, 7.9 for SLS technology. The applied test designation symbols are as follows: M - MJF, S - SLS, L - longitudinal direction, T - transverse direction, where the last digit indicates the specimen number.
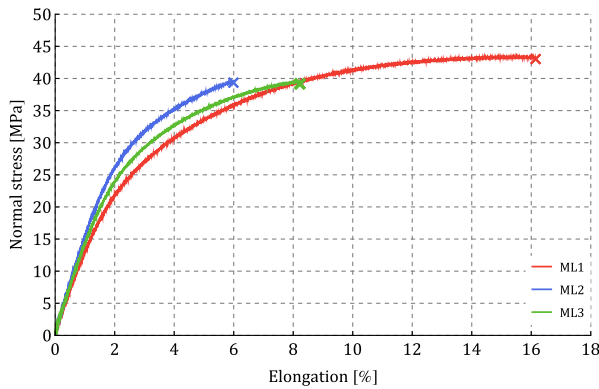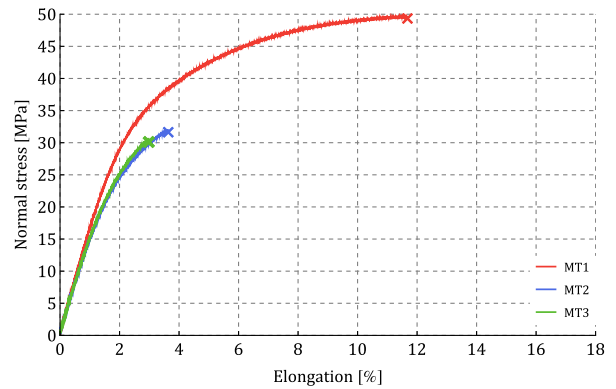

Fig. 7.6. The results for longitudinal MJF specimens   *Fig. 7.7. The results for transverse MJF specimens*
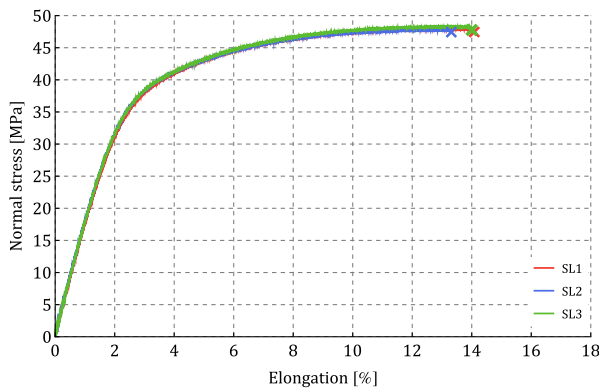
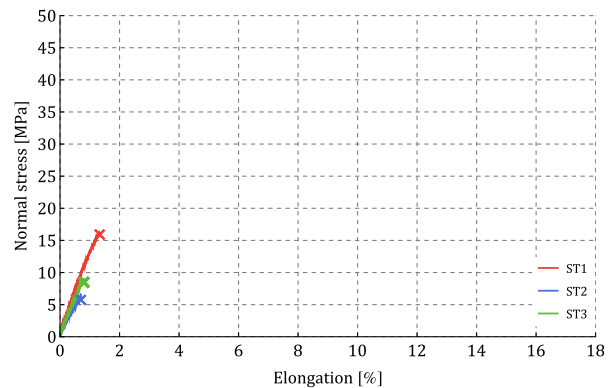*Fig. 7.8. The results for longitudinal SLS specimens*   *Fig. 7.9. The results for transverse SLS specimens*

The measurements conclude that the MJF specimens are characterised by noticeable discrepancies in ultimate strength and varying stress-elongation curves, even for specimens with the same layer orientation. The most satisfactory results are obtained for the SLS method with longitudinal printing, where all of the three curves are almost identical, indicating the repeatability of the material properties. Unfortunately, tests of SLS samples in the transverse direction show unacceptably low tensile strength, with failure occurring at stresses substantially smaller than for the longitudinal direction.

The values of Young's modulus E, offset yield strength $R_{e0,2}$ and ultimate strength R_m are determined in each of the tests. The former is determined by linear regression in the stress range of 2 to 15 MPa. A summary of these results and the initial dimensions of the samples are presented in Table 7.1. For two SLS specimens manufactured in the transverse direction, a rupture occurred at stresses lower than 15 MPa; hence, finding Young's modulus is futile. A similar problem is noted when determining offset yield strength for all the specimens in this group, as the failure occurred for strains below 0.2%.

Before the test, the dimensions characterising the cross-section are measured with a micrometer. The thicknesses a and widths b summarised in Table 7.1 are compared to the standardised dimensions shown in Fig. 7.1 by the relative differences δ_a and δ_b. The most considerable discrepanacy in thickness is obtained for the specimens with the most favourable strength parameters, i.e. for SLS manufactured in the longitudinal direction. For the SL1 sample, the calculated deviation $\delta_a = 6.90\%$ indicates significant difficulties in maintaining the assumed geometrical dimensions. The compared specimen widths b are on average larger for the SLS method. The average dimensional differences for MJF specimens are 0.61% for thickness a, and 0.96% for width b. Those values for SLS are 3.25% and 2.04%, respectively.

Based on the performed analyses, it is concluded that the MJF method has a significantly higher minimum ultimate strength and dimensional stability. The SLS technology is less suitable for the studied application. This observation only refers to the aforementioned 3D printers and specific manufacturing process parameters. Considering the differences in the stress-elongation curves for MJF technology, it should be assumed that strength tests of MJF products can be conducted for moderate stress values. Although it is difficult to specify the allowable stress value unambiguously, the mechanical behaviour below 10 MPa seems satisfactory. A possible explanation for their divergent characteristics is the positioning of the samples in the chamber of the printing device.

The determination of Young's moduli from three moderately different values (Table 7.1) can be perceived as inaccurate. Additional static tensile tests are carried out to achieve a more compelling outcome. Those are limited to MJF technology.

Table 7.1 Static tensile tests and measurements summary

Specimen name	E [GPa]	$R_{e0,2}$ [MPa]	R_m [MPa]	a [mm]	b [mm]	δ_a [%]	δ_b [%]
ML1	1.30	18.70	43.37	4.06	9.82	1.55	1.77
ML2	1.56	22.91	39.60	4.00	9.76	0.05	2.43
ML3	1.43	20.76	39.57	3.98	9.93	0.60	0.70
MT1	1.68	26.00	49.65	4.01	9.97	0.25	0.27
MT2	1.50	20.98	31.87	3.96	9.95	1.08	0.47
MT3	1.52	21.56	30.55	4.00	9.99	0.10	0.13
SL1	1.75	29.59	47.94	4.28	9.80	6.90	2.03
SL2	1.82	28.85	47.79	4.14	9.80	3.37	2.00
SL3	1.80	29.59	48.31	4.16	9.75	3.98	2.53
SP1	1,33	N/A	16.28	3.92	9.75	2.08	2.53
SP2	N/A	N/A	6.24	3.94	9.84	1.55	1.63
SP3	N/A	N/A	8.94	3.94	9.85	1.63	1.53

The manufacturing of the other specimens involves locating them as close as possible to the centre of the chamber of the HP Jet Fusion 3D 4200 machine. Due to previous research, it seems unreasonable to carry out the test up to rupture. It is decided to run five load-unload cycles from 1 MPa to 16 MPa to obtain a more accurate value of Young's moduli. Each time the desired value is reached, the testing machine holds the force for 120 seconds so that the creep effect is investigated. Exemplary results are shown in Figs. 7.10, 7.11 for a specimen manufactured in the longitudinal and transverse directions.
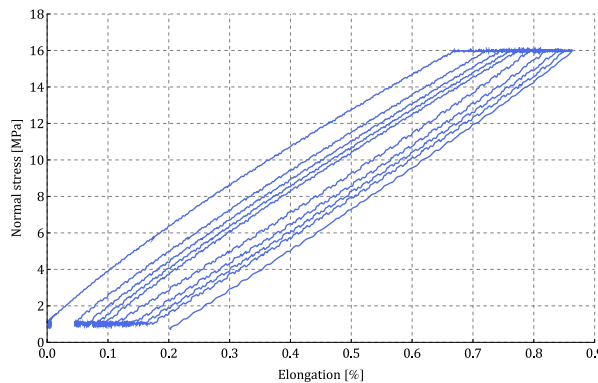

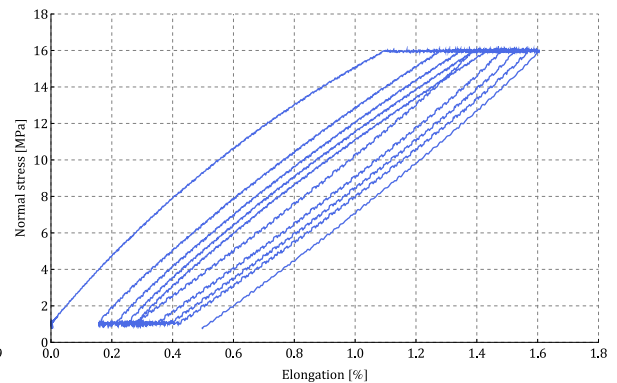*Fig. 7.10. Tensile load-unload cycles for longitudinal MJF specimen*

Fig. 7.11. Tensile load-unload cycles for transverse MJF specimen

A mechanical hysteresis can be observed with the simultaneous creep phenomenon in the studied material. After reaching the maximum load for the first time, the deformation increases at constant stress. A partial decrease in the strain is noted due to unloading and maintaining constant stress of 1 MPa. Subsequent loading cycles result in less and less creep, both in terms of strain increase and decrease at constant load. Samples printed in the longitudinal direction are characterised by significantly less intensive creep than those in which successive layers are arranged transversely. It explains why the recorded load-unload curves in Fig. 7.10 show a relationship, which is closer to linear.

Notably, the separate loading and unloading curves follow a similar pattern for each cycle. For all of them, Young's modulus is determined by linear regression in the range from 2 MPa to 10 MPa. A summary of the results is presented in Table 7.2, where the given designations are: L - longitudinal, T - transverse, and the number following them refers to the specimen number.

Table 7.2. The summary of load-unload tensile tests for MJF specimens

Test name	Young modulus in consecutive load cycles [GPa]					Mean value [GPa]
	$E^{(1)}$	$E^{(2)}$	$E^{(3)}$	$E^{(4)}$	$E^{(5)}$	
L1	1.78	1.71	1.71	1.71	1.71	
L2	1.76	1.74	1.73	1.73	1.72	$E_2 = 1.71$
L3	1.78	1.71	1.71	1.71	1.71	
T1	1.19	1.07	1.05	1.05	1.03	
T2	1.19	1.16	1.14	1.13	1.13	$E_1 = 1.13$
T3	1.25	1.24	1.23	1.22	1.22	

The static tensile tests indicate the equalization of Young's moduli in each successive loading cycle. The calculated mean values show that Young's modulus for the longitudinal direction of the printed model is $E_2 = 1.71$ GPa, while for the transverse direction, it is $E_1 = 1.13$ GPa. The designations of those quantities refer to the principal directions of the cylindrical shell, where its axis is aligned with the vertical printer axis (Fig. 7.2). The differences in Young's moduli indicate definite orthotropic properties of the material. Due to the observed unfavourable creep phenomenon, it seems advantageous to carry out further strain gauge measurements at a much higher strain rate than assumed in the static tensile test according to ISO527 guidelines.

7.2. Strain gauge measurements

7.2.1. Test bench and apparatus

A laboratory test bench is developed to verify the dished end optimization results. In combination with the appropriate shape of the pressure vessel model, it allows its pressurization. A schematic diagram of the test bench is shown in Fig. 7.12. The designed model of a pressure vessel consists of a dished end, cylindrical shell, and a flange. The flange is clamped between two standardised flange connectors fixed by four M16 bolts. The applied tightening torque is 20 Nm. The EPDM rubber gaskets are fitted between the flange connectors and the vessel flange to maintain the tightness of the system and evenly distribute the clamping force. Three threaded holes are drilled in the blind, bottom flange connector. Those allow connecting a pressure sensor, manometer and expansion tank with the inside of the pressure vessel. The expansion tank is further connected with the air compressor.
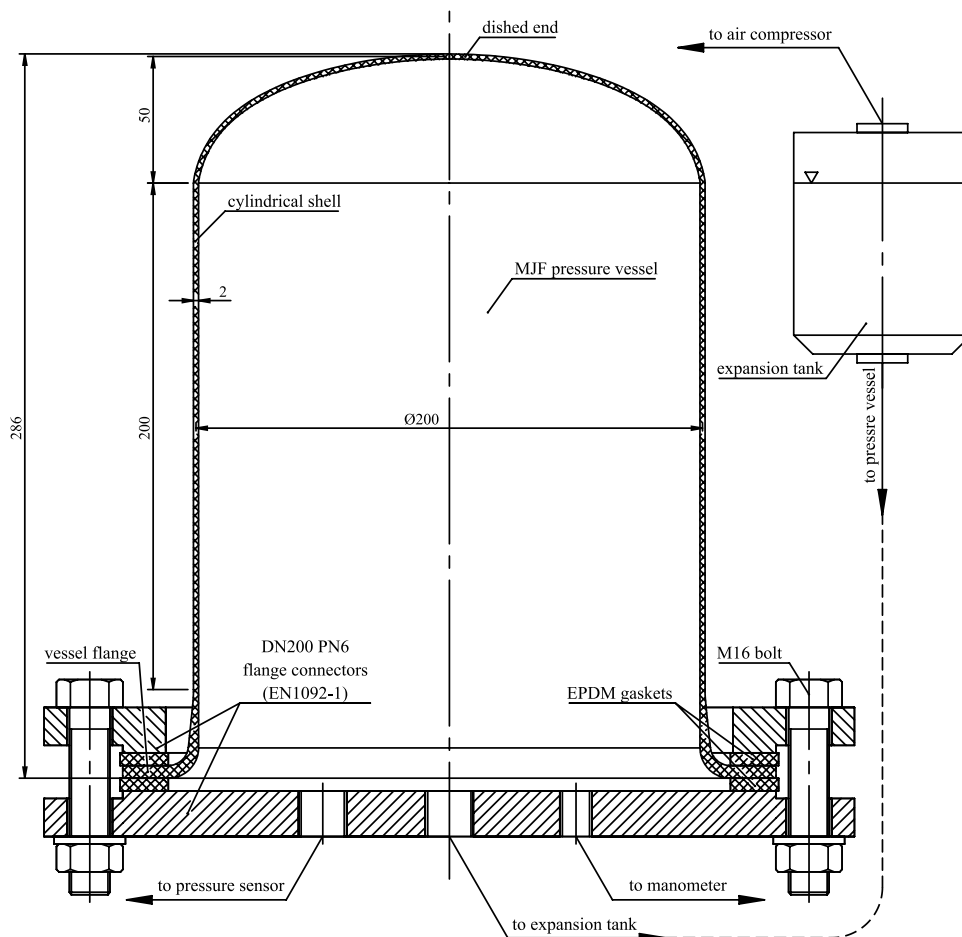

Fig. 7.12. Structure of the test bench

During the test, the inside of the vessel is filled with water, as compressing the air would increase its temperature. It could lead to thermal deformation, which would be difficult to compensate for in the measurements. Additionally, it increases the

thermal capacity of the system and protects against a possible explosion. After placing the test bench upside down, the system is filled with water. In this position, the air is easily removed from the inside of the vessel and the hoses connected to the apparatus. It should be noted that the hydrostatic pressure created by the presence of water does not affect the measurement, assuming that all of the sensors are zeroed right before the measurement is conducted. Such an approach implies that the measured strains are related only to the change in pressure inside the vessel applied by the air compressor.

The nominal diameter of pressure vessels tested in the developed test bench is 200 mm; hence according to the optimization study in chapter 6, the dished end height is 50 mm. These dimensions refer to the middle surface of the shell. The length of the cylindrical shell is designed to eliminate the possible impact of the deformations in the vessel flange area on the measured strains. The thickness of the models involved in this study is 2 mm for the cylindrical shell and the dished end. The vessel flange is 5 mm thick. The total height of the structure is 286 mm.

Data acquisition is carried out using two HBM QuantumX MX840 amplifiers (Fig. 7.13), connected to a computer with CATMAN EASY software installed. The sampling rate is set to 10 Hz. The total number of available measurement channels is 16. Pressure measurement is performed using an HBM P8AP strain gauge pressure sensor (Fig. 7.14) with a rated range of up to 10 bar. A manual reducing valve in the air compressor controls the applied pressure. The remaining 15 channels are operated by strain gauges bonded to the pressure vessel surface.


Fig. 7.13. Two HBM QuantumX MX840 amplifiers used for data acquisition

The first type of sensor used for strain analysis is the HBM KY41-4/120 chain strain gauge (Fig. 7.15). It has ten active sensors that alternately measure in two perpendicular directions and one optional compensating strain gauge. The distances

between the active sensors are 4 mm, thus allowing measurements over a length of 36 mm. The second strain gauge type is the HBM XY11-3/120 0°/90° T rosette. Both of the strain sensors are characterized by a nominal resistance of 120 Ω. The strain gauges are bonded to the pressure vessels using cyanoacrylate adhesive, for which no undesirable interaction with MJF PA12 models has been demonstrated.

Fig. 7.14. Pressure sensor HBM P8AP
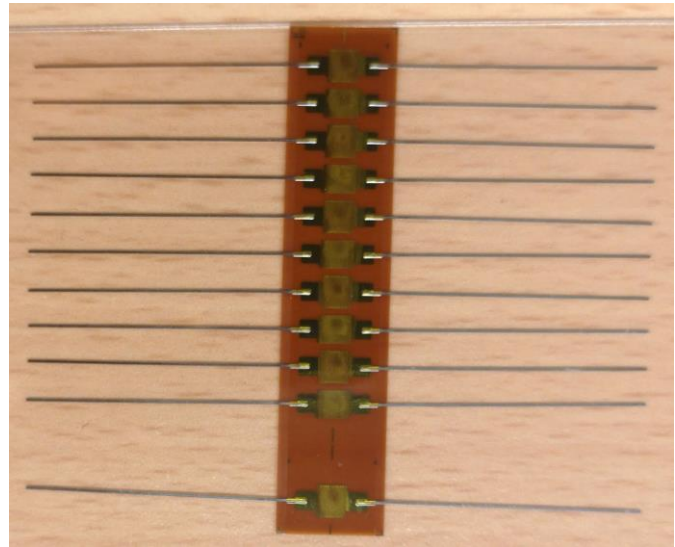
Fig. 7.15. Chain strain gauge HBM KY41-4/120

7.2.2. Determination of PA12 mechanical properties

The first MJF pressure vessel included in the study has a torispherical dished end and geometrical dimensions as shown in Fig. 7.12. This test aims primarily to determine the mechanical properties of the material by strain gauge measurements, taking into account the actual strain rates, which are difficult to determine for static tensile testing. It is also important to note that the mechanical properties may be slightly different for various geometrical dimensions of models manufactured with MJF technology. The second goal of this study is to verify the correct operation of the designed test bench and the system tightness, checking the dimensional accuracy of the obtained MJF model and indicating any possible problems with the test procedure.

The pressure vessel manufactured using MJF technology is shown in Fig. 7.16. The thickness measurements are conducted with an ultrasonic thickness sensor indicating a range of 1.9 to 2.3 mm. Additional measurements of the cylindrical shell are conducted using a dial thickness gauge, which confirmed the prior thickness measurements.

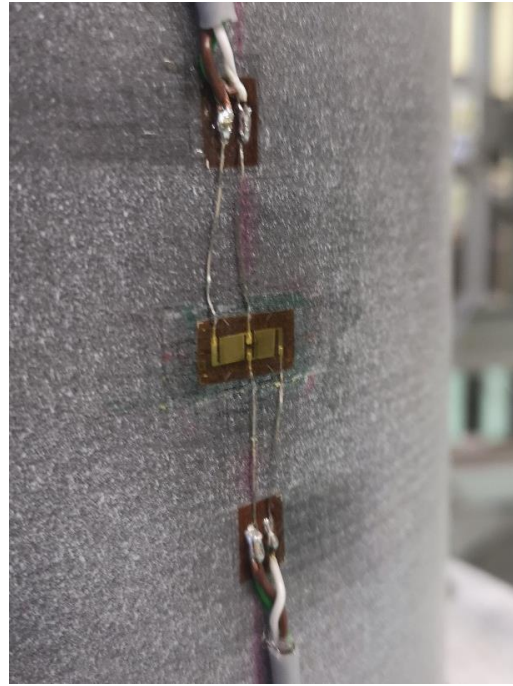*Fig. 7.16. Test bench setup for the pressure vessel with torispherical dished ends*

Fig. 7.17. HBM XY11-3/120 0°/90° T rosette bonded with the cylinder

Although the other strain gauges can be observed in Fig. 7.16, the analysis is limited to the T rosette (Fig. 7.17). It is bonded on the cylindrical shell, for which the relation between the pressure and principal strains is known from the membrane theory (MT). Such a description can be used to some extent to evaluate the material properties.

During the test, the pressure vessel is subjected to five load-unload cycles from $p = 0$ MPa to $0.7 > p > 0.6$ MPa. After each unloading cycle, the pressure is kept at zero for at least 30 s, allowing the creep deformations to return to a value close to zero. The pressure change during the test is shown in Fig. 7.18.
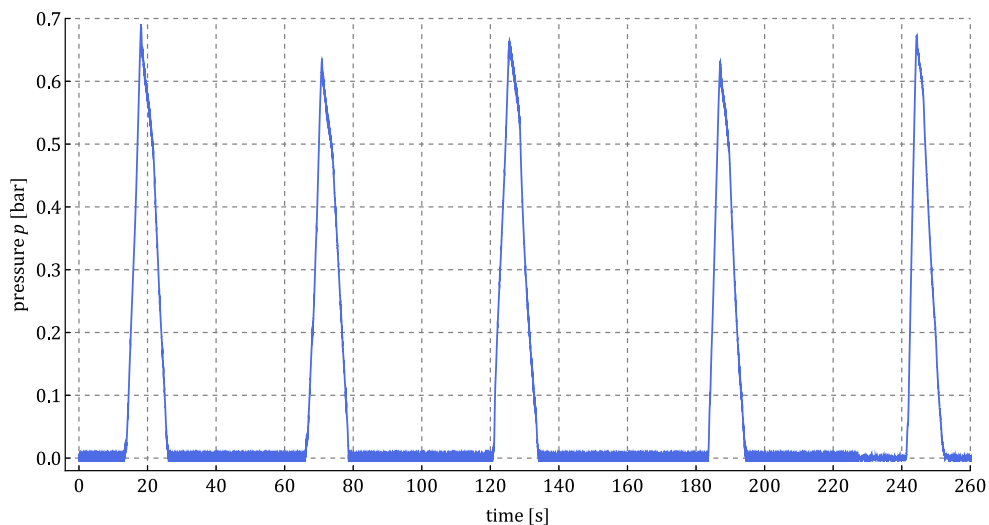

Fig. 7.18 The change in pressure during the five load-unload cycles

The registered stress-strain relation is presented in Fig. 7.19 for meridional and in Fig. 7.20 for circumferential direction. A significant nonlinearity is present in the case of ε_1, while the separate load and unload cycles for ε_2 can be considered nearly perfectly linear. Comparing the measured values, one can notice that the strain along the axis of the cylindrical shell ε_1 has negligible values compared to the circumferential direction.
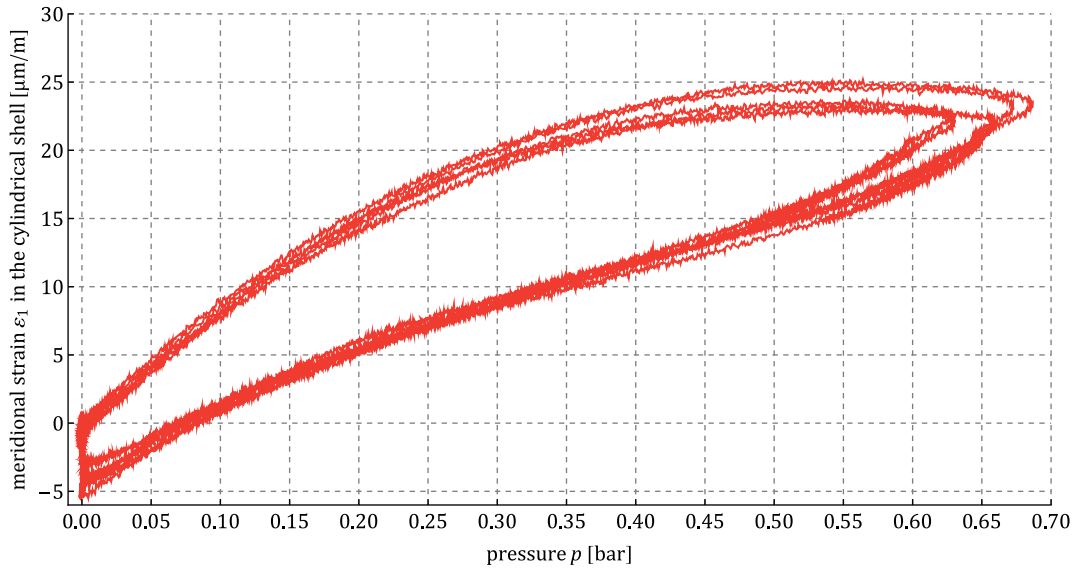
Fig. 7.19. Meridional strain measured by T rosette
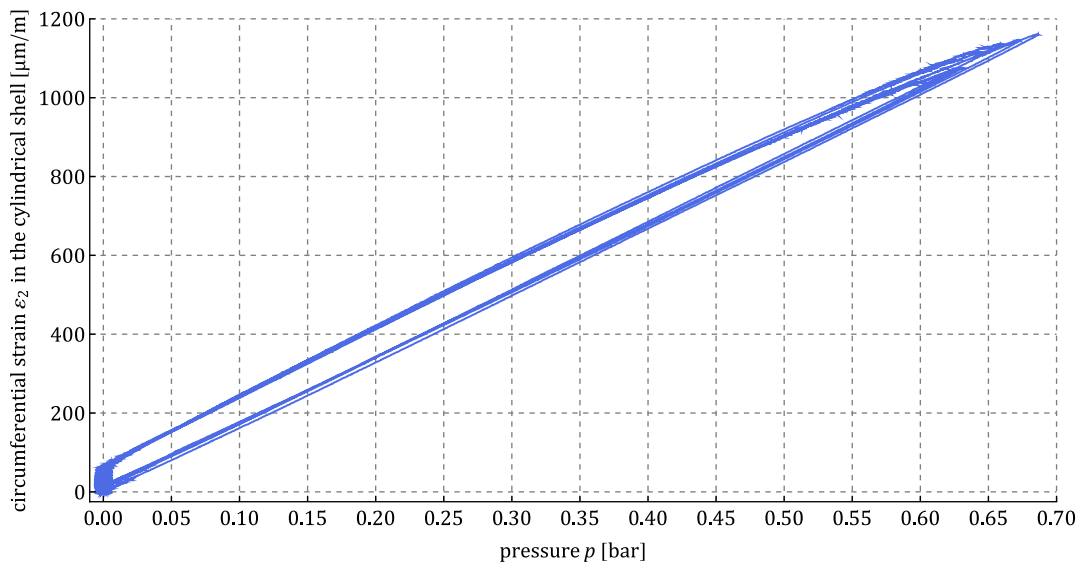
Fig. 7.20. Circumferential strain measured by T rosette

In the further analysis, the strain-pressure relationships are considered only for load cycles omitting unload phases, and it is assumed that at the start of each cycle, the strains and pressure are zero. The processed in such a manner results are juxtaposed in Fig. 7.21, where the linear regressions are fitted into the obtained data.
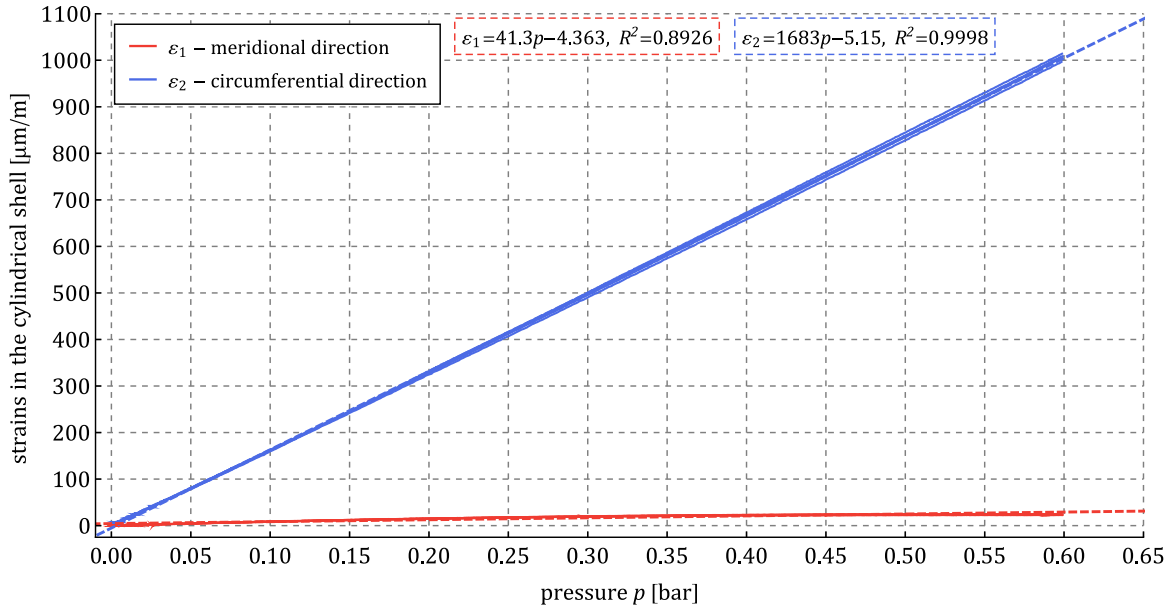
Fig. 7.21. The measurements of strains in the cylindrical shell - linear regressions for load cycles

In order to determine the mechanical properties of the material, one can refer to the analytical expressions for strains in the cylindrical shell (Eqs. (3.3), (3.46)). After converting the units and considering that the pressure p in the experiment is negative referring to the theory, the following relations are obtained:

$$\varepsilon_1 = \frac{pR_0}{E_1 t}\left(\nu_1 - \frac{1}{2}\right)10^5 \left[\frac{\mu m}{m}\right], \qquad \varepsilon_2 = \frac{pR_0}{E_2 t}\left(\frac{1}{2}\nu_2 - 1\right)10^5 \left[\frac{\mu m}{m}\right], \qquad (7.1)$$

where: p [bar] – applied pressure, R_0 [mm] – radius of the middle surface of cylindrical shell, t [mm] – thickness, E_1, E_2 [MPa] – Young's moduli towards principal curvature directions, ν_1, ν_2 – Poisson's ratios towards principal curvature directions. Considering the alignment of the pressure vessel in the printer chamber, the terms transverse and longitudinal refer to meridional and circumferential directions respectively. This observation is valid only for the cylindrical shell. Given the form of the first expression in Eq. (7.1) and assuming that Young's modulus in the meridional direction E_1 is finite, the following relation must hold

$$\varepsilon_1 \approx 0 \implies \nu_1 \approx 0.5. \qquad (7.2)$$

It explains the recorded ε_1 strain characteristics (Fig. 7.19), where its nonlinearity can be mainly attributed to the stiffness of the adhesive and the creep of the material in the circumferential direction. Due to the need for further numerical FEM calculations, the value of Poisson's ratio in the meridional direction is assumed as

$$\nu_1 = 0.49. \qquad (7.3)$$

Other material constants can be estimated by referring to the orthotropy coefficient (Eq. (3.11)). On the basis of a static tensile test, it was found that Young's modulus

in the longitudinal (circumferential) direction is certainly not less than in the transverse (meridional) direction

$$E_2 \geq E_1. \tag{7.4}$$

The Poisson's ratio in the circumferential direction must satisfy the relation

$$0.5 \geq v_2 \geq v_1. \tag{7.5}$$

It can therefore be assumed that the material presents almost isotropic properties:

$$v_2 = 0.49, \qquad \alpha = 1. \tag{7.6}$$

Transforming the relation for circumferential strain in terms of Young's modulus, the following expression is obtained

$$E_2 = \frac{pR_0}{\varepsilon_2(p)t}\left(\frac{1}{2}v_2 - 1\right)\frac{1}{10^5} \text{ [MPa].} \tag{7.7}$$

The thickness of the cylindrical shell at the location of the T rosette is measured using a dial gauge, which yields $t = 2.09$ mm. Using the other known parameters:

$$p = 0.6 \text{ bar}, \qquad R_0 = 100 \text{ mm}, \tag{7.8}$$

the following values of Young's moduli are resolved:

$$E_2 = E_1 = 2157 \text{ MPa.} \tag{7.9}$$

Note that the determined Young's moduli (Eq. (7.9)) are significantly different than those resulting from the static tensile test (Table 7.2). It is most likely connected with the much higher strain rate in the strain gauge test. A noteworthy discrepancy is also noticed between the orthotropy coefficient (Eq. (3.11)) in both tests. The reason for this may be the more intense creep phenomenon observed in the static tensile test. With a significant increase in strain rate, the creep phenomenon has little effect on the analysed strains; hence the material could become nearly isotropic.

7.2.3. Analysis of the optimized pressure vessel

Even though the dished end shape optimization was carried out as part of the research described in chapter 6 of the dissertation, their direct experimental verification is not justified. This is due to the different mechanical properties of the material considered in the optimization problem. The determined stress distributions for these shapes deteriorate when considering significantly different material properties of the models manufactured in the MJF technology. For this reason, the optimization of the dished end is carried out again, considering the material properties determined in the strain measurements (Eqs. (7.3), (7.6), (7.9)) and the t/R_0 ratio in accordance with the dimensions in Fig. 7.12. The procedure is performed

using the same methodology and parameters as in chapter 6, its description is therefore omitted. The resulting stress distribution is shown in Fig. 7.22.
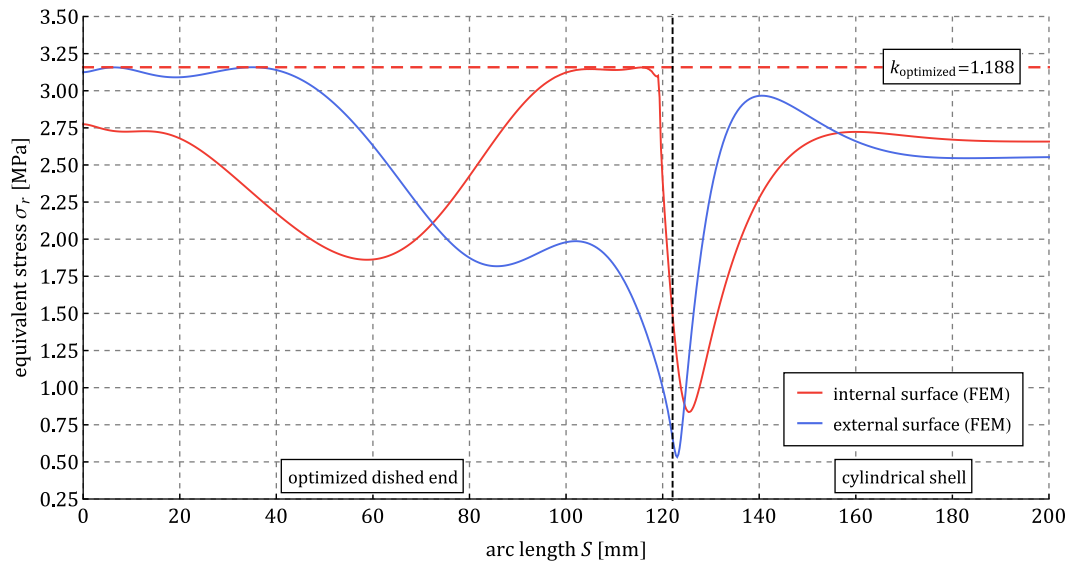

Fig. 7.22. The equivalent von Mises stress distribution in the optimized dished end with PA12 (MJF) material properties

The final pressure vessel model with optimized dished end manufactured in MJF technology is shown in Fig. 7.23. The layer thickness on the HP Jet Fusion 3D 4200 printer is set to a minimum value of 0.08 mm. The pressure vessel is located in the centre of the printer chamber. The model is positioned with the dished end facing upwards, while the axis of the cylindrical shell coincides with the vertical axis of the 3D printer. The total printing time is approximately 9 hours. The cooling time of the vessel is prolonged to 16 hours to minimize the possible thermal deformation.

Fig. 7.23. The model of pressure vessel with optimized dished end manufactured in MJF technology

After the printing process, the model is vibration-abrasive machined to achieve a smooth surface that allows better contact between the strain gauges and the surface. Prior to the experimental study, the pressure vessel is measured using a Hexagon Smartscan HE-R8 optical scanner. Measurements are taken for the entire geometry on both the external and internal surfaces. The recreated geometry is shown in Fig. 7.24 as an STL file. The number of points collected on the model surface is 631528, which is increased to 1126556 by regularization using SPACECLAIM software in ANSYS 2020 R2 system.
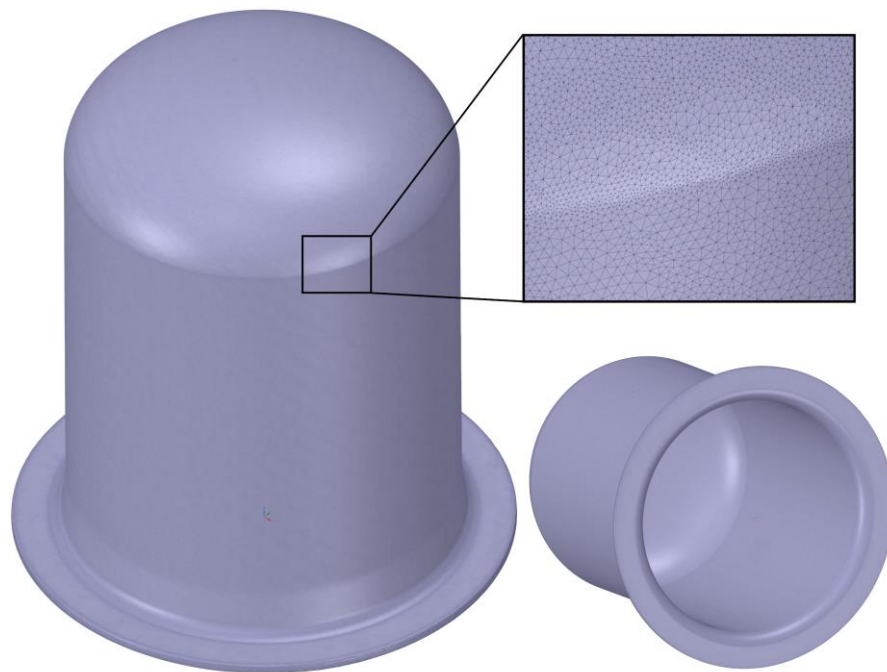
Fig. 7.24. The STL geometry of the scanned pressure vessel

In the next step, the STL file is converted into continuous geometry in the form of a CAD model. The geometry is split into parts, overlaid with surfaces and then stitched together to form a solid model. The geometric deviations between the optimized and scanned geometry are evaluated in SPACECLAIM (Fig. 7.25). For this purpose, their geometrical centres and principal axes of inertia are matched. Only the dished end and the cylindrical shell are considered, as the flange is not the subject of strain gauge measurements. The dimensional tolerance is set to ± 0.1 mm. Values below the lower tolerance limit are highlighted in blue, while red refers to values above 0.1 mm. The total deviation range is between -0.32 mm and 0.43 mm.

Based on the previous study, it has been recognised that ultrasonic thickness measurements can negatively affect plastics. Covering a relatively large surface with a coupling agent may, to some extent, change its mechanical properties. Thickness

measurements are only taken at a few selected locations and confirmed with a dial thickness gauge. Such verification is possible only for the cylindrical surface. The resulting CAD file is then subjected to thickness analysis in SOLIDWORKS 2021 software, as the software used previously does not have this functionality. The result of the thickness distribution analysis is shown in Fig. 7.26. The predominant surface of the model has a thickness between 1.9 and 2.06 mm, which is confirmed by the ultrasonic sensor and dial gauge. It constitutes an improved result compared to the previous model (Fig. 7.16), where thickness is in the range of 1.9 to 2.3 mm. The advancement is most likely due to the reduced layer thickness in the MJF manufacturing process.
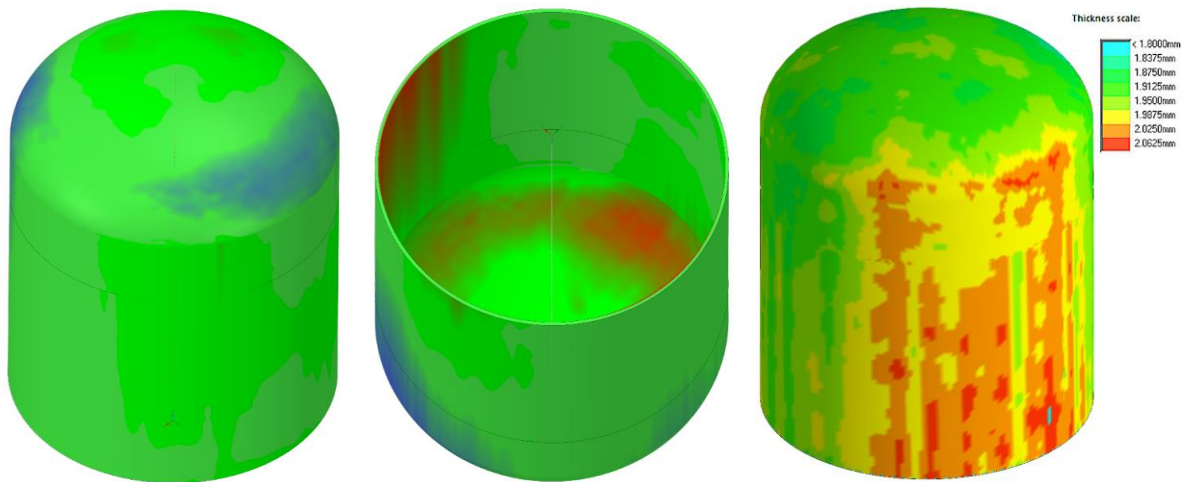

Fig. 7.25. The geometrical deviations between the optimized and scanned geometry   *Fig. 7.26. Thickness distribution in the scanned geometry*

The stress distribution obtained from the optimization (Fig. 7.22) is characterised by equal values of maximum equivalent stresses in the external and internal surfaces. It should be mentioned that strain gauge measurements inside the pressure vessel are technically possible on the designed test bench (Fig. 7.12), although difficult to perform in practice. The problems are related to the probable contact of strain gauges and connection cables with water, although it is possible to protect them with suitable covering agents. Another problem is the considerable difficulty of bonding a relatively long chain strain gauge on the curved dished end surface inside the model so that the sensor axis coincides with the meridional direction. In addition, such a test would require the development of a reliable method for routing the connection cables outside the vessel and maintaining the tightness of the system under pressure. It is decided to limit the experimental study to the external surface due to the abovementioned problems.

The test employed two KY41-4/120 chain strain gauges and an XY11-3/120 T rosette on the cylindrical shell (Fig. 7.27). To ensure that the strain gauges are aligned along the shell meridian, the model is placed on the levelled test bench, and the meridian shape is mapped using a self-levelling cross-line laser. The chain strain gauges labelled CSG1 and CSG2 (Fig. 7.27) correspond to the two stress extrema on the optimized stress distribution (Fig. 7.22). The T rosette labelled TR is used to compare the measurements with the previous test (Fig. 7.21).
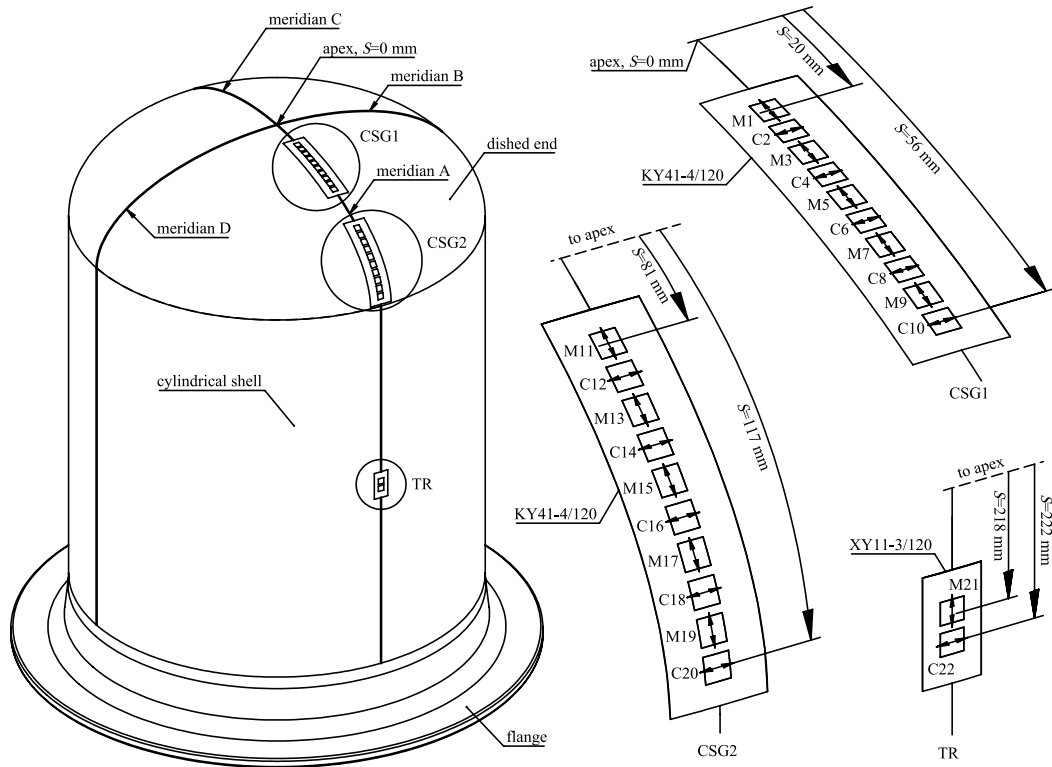

Fig. 7.27. Position of the strain gauges in the experimental study

Each measurement point (Fig. 7.27) is denoted with a symbol M (meridional) or C (circumferential), related to the direction of strain measurement, and a number counted from the dished end apex. The test bench prepared for the experiment is shown in Fig. 7.28. The soldering terminals are moved as far away as possible from the strain gauges to prevent potential local stiffening of the structure. The number of bonded sensors exceeds the number of available channels; therefore, the test is performed in two steps. Initially, measuring points M11 to C22 are considered, i.e. CSG1 is inactive. After the test, the connection cables are resoldered to include points M1 to C10 and M11, C12, M15, M19 and C20 (Fig. 7.29). Strain measurements at points belonging to CSG2 are conducted to ensure that the results obtained at these points are the same as in the first step of the test.

Fig. 7.28. Test bench setup for a pressure vessel with optimized dished end
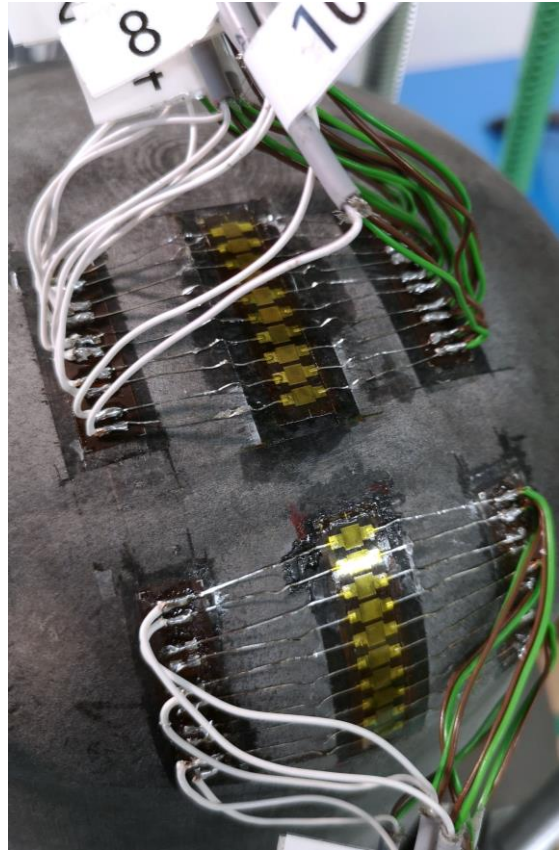

Fig. 7.29. KY41-4/120 chain strain gauges bonded with the dished end

Analogously to the previous study (Fig. 7.18), strain recordings are made for five load-unload cycles up to the pressure just above $p = 0.6$ bar. Between each cycle, no pressure is applied for at least 30 s.
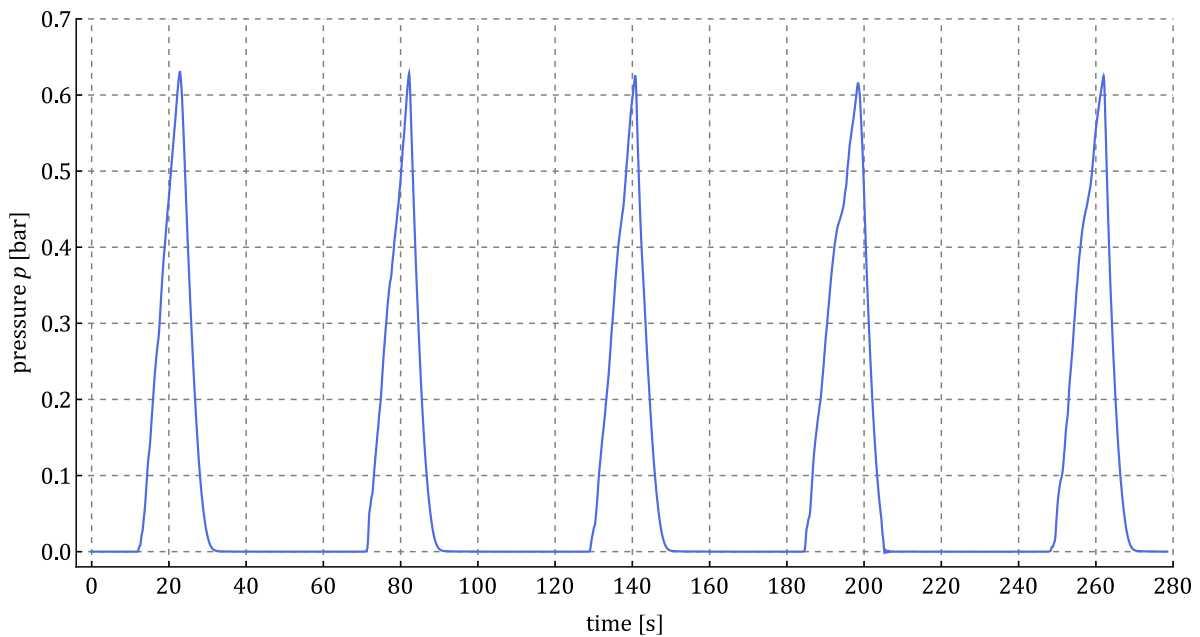

Fig. 7.30. The change of pressure during the cyclic load-unload test

The obtained results are presented in Figs. 7.31-7.40. The strains in Figs. 7.31, 7.33, 7.35, 7.37 and 7.39 are the unprocessed data recorded directly during the test. They show moderate material hysteresis related to material creep. More useful results are shown in Figs. 7.32, 7.34, 7.36, 7.38 and 7.40, where the consideration is limited to load cycles in the pressure range of about 0 to 0.6 bar. The pressure and strains are assumed to be zero at the beginning of each cycle. For each measuring point, i.e. M1-C22, linear regression is determined, taking all five load cycles into account. Dashed lines indicate these, and the corresponding equations are given in boxes provided in the figures. The values of coefficients of determination R^2 indicate almost perfectly linear relations.
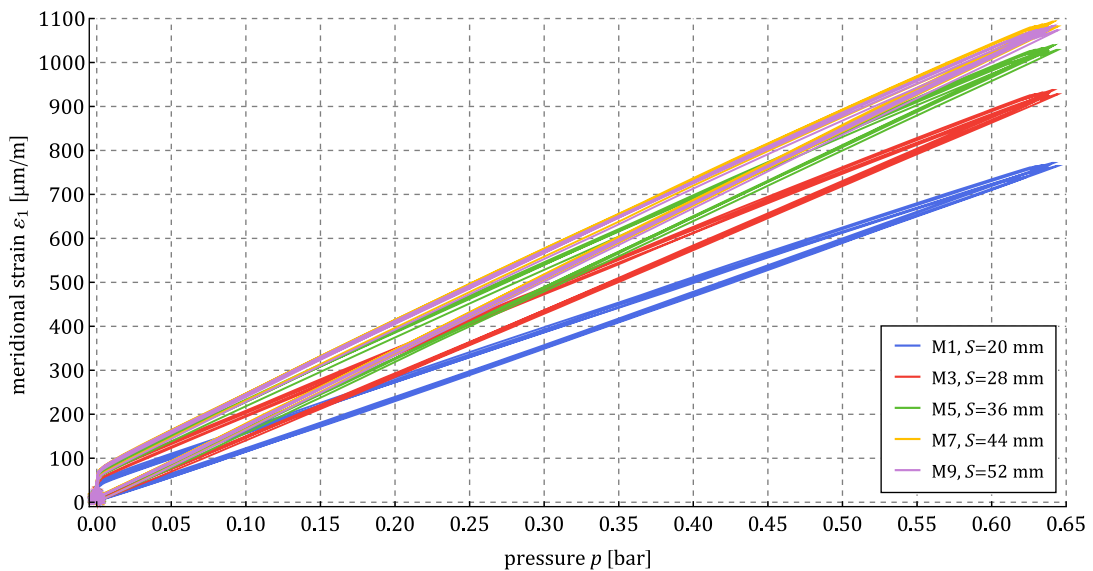

Fig. 7.31. The meridional strain from CSG1, load-unload cycles
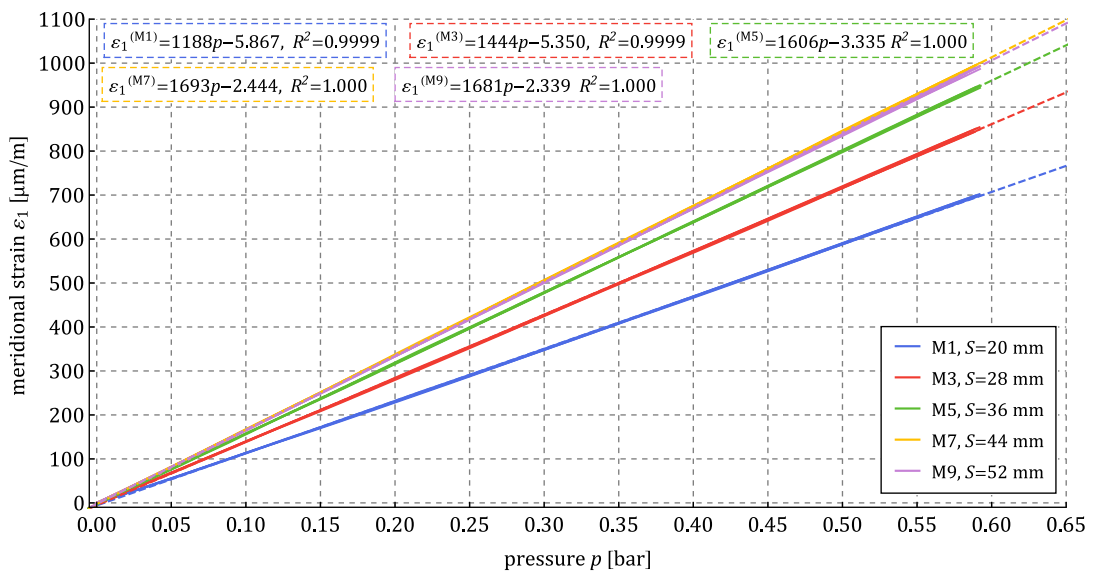
Fig. 7.32. The meridional strain from CSG1, load cycles with linear regressions

Fig. 7.33. The circumferential strain from CSG1, load-unload cycles
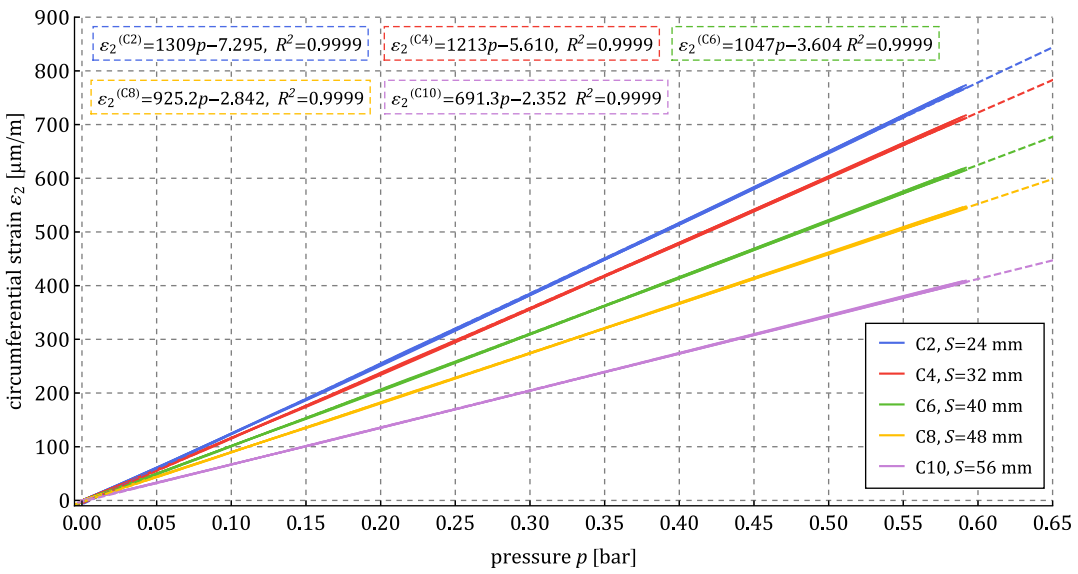
Fig. 7.34. The circumferential strain from CSG1, load cycles with linear regressions

In Fig. 7.34:

$\varepsilon_2^{(C2)}=1309p-7.295,\ R^2=0.9999$

$\varepsilon_2^{(C4)}=1213p-5.610,\ R^2=0.9999$

$\varepsilon_2^{(C6)}=1047p-3.604\ R^2=0.9999$

$\varepsilon_2^{(C8)}=925.2p-2.842,\ R^2=0.9999$

$\varepsilon_2^{(C10)}=691.3p-2.352\ R^2=0.9999$

Fig. 7.35. The meridional strain from CSG2, load-unload cycles

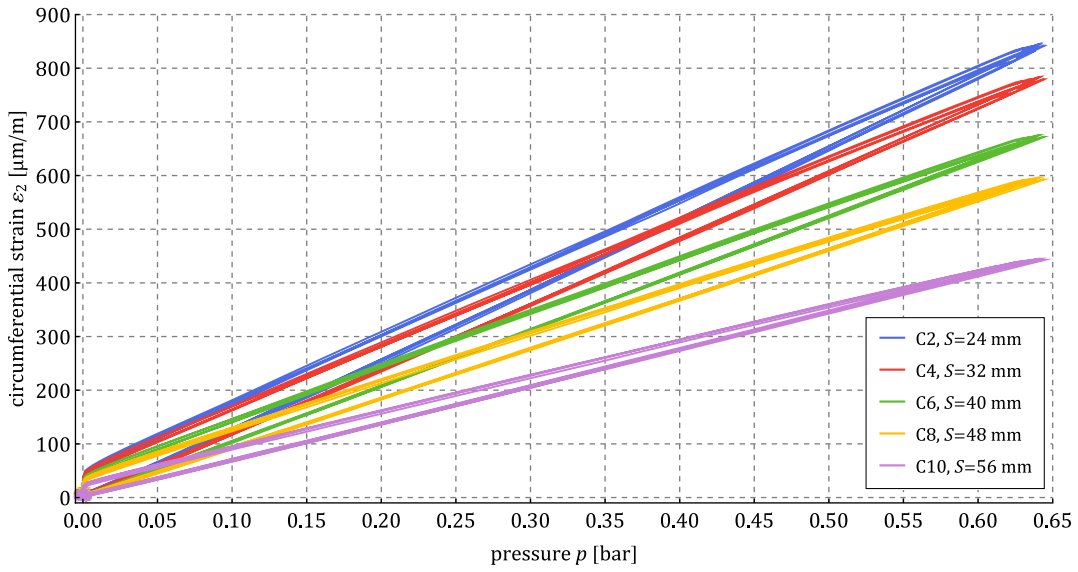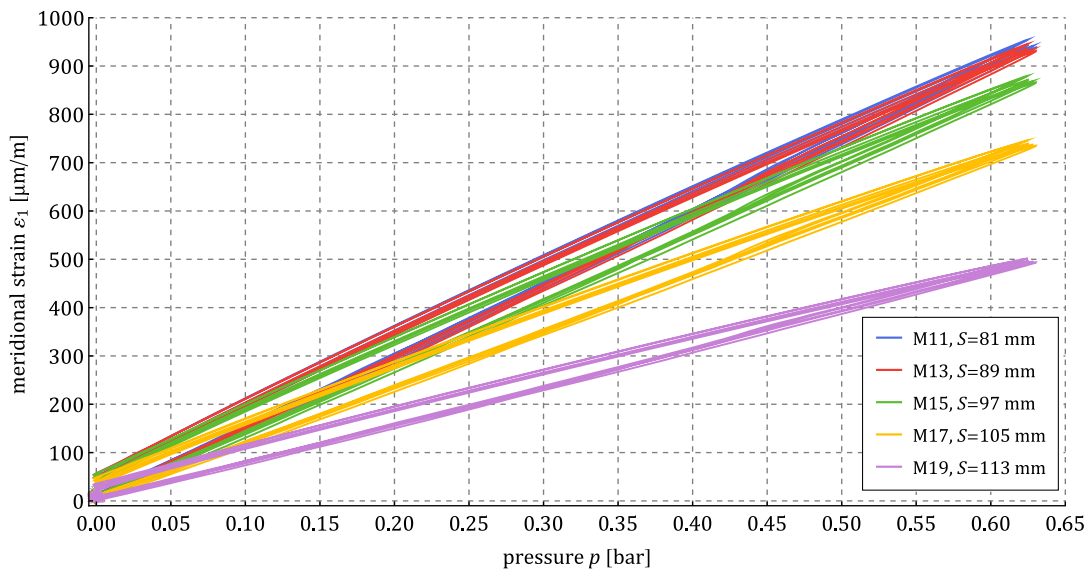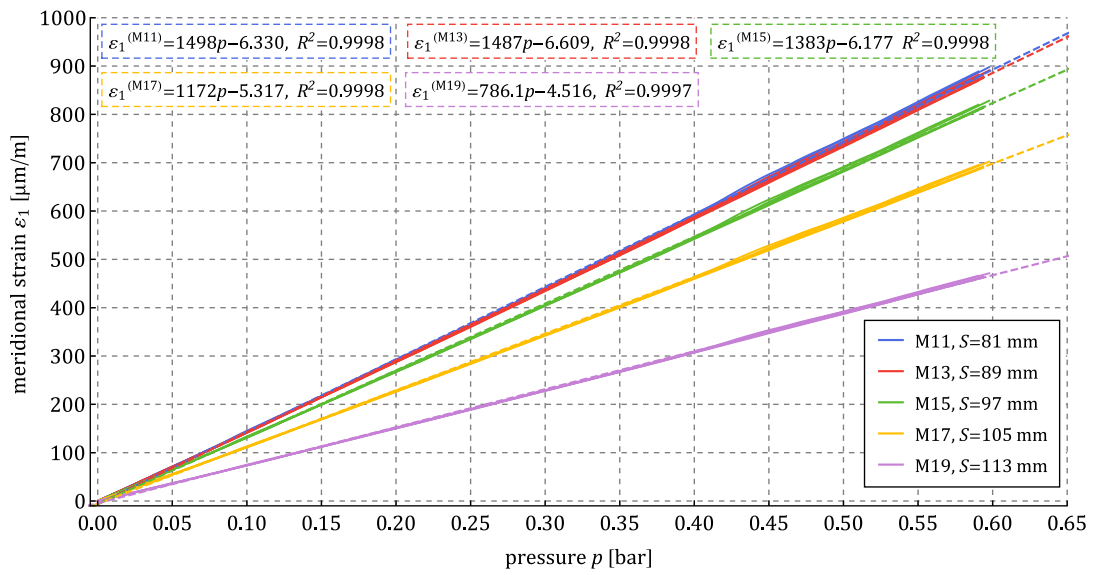Fig. 7.36. The meridional strain from CSG2, load cycles with linear regressions

$\varepsilon_1^{(M11)}=1498p-6.330, \ R^2=0.9998$

$\varepsilon_1^{(M13)}=1487p-6.609, \ R^2=0.9998$

$\varepsilon_1^{(M15)}=1383p-6.177 \ R^2=0.9998$

$\varepsilon_1^{(M17)}=1172p-5.317, \ R^2=0.9998$

$\varepsilon_1^{(M19)}=786.1p-4.516, \ R^2=0.9997$

M11, S=81 mm
M13, S=89 mm
M15, S=97 mm
M17, S=105 mm
M19, S=113 mm
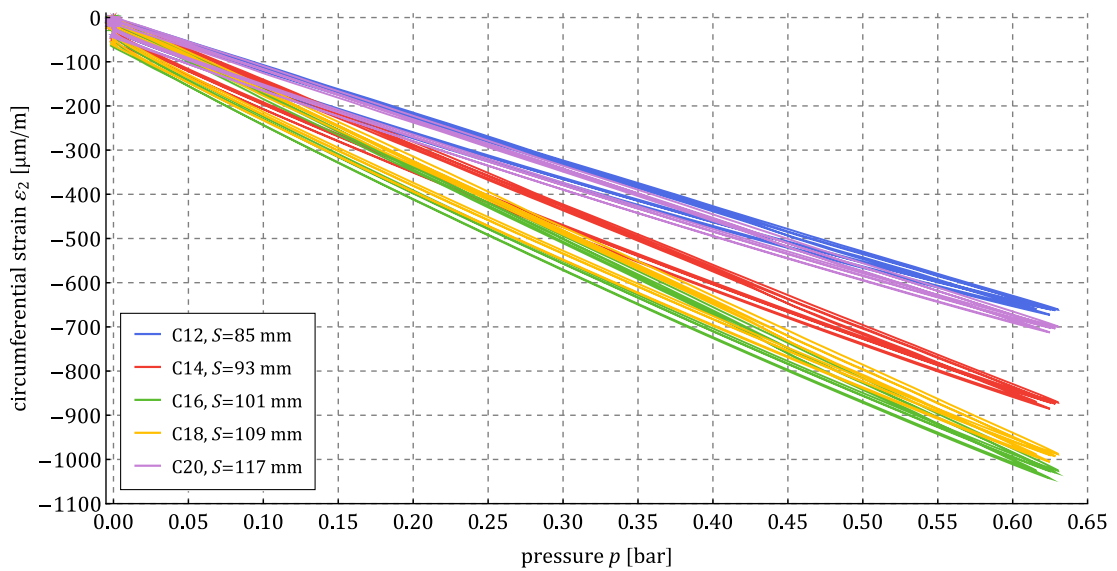
Fig. 7.37. The circumferential strain from CSG1, load-unload cycles

C12, S=85 mm
C14, S=93 mm
C16, S=101 mm
C18, S=109 mm
C20, S=117 mm
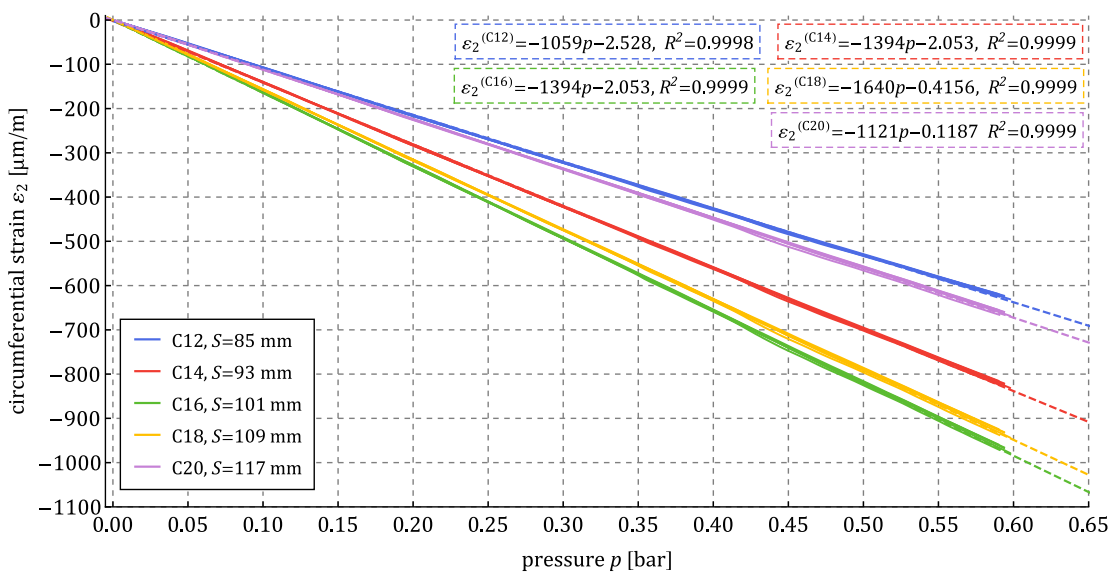
Fig. 7.38. The circumferential strain from CSG2, load cycles with linear regressions

$\varepsilon_2^{(C12)}=-1059p-2.528, \ R^2=0.9998$

$\varepsilon_2^{(C14)}=-1394p-2.053, \ R^2=0.9999$

$\varepsilon_2^{(C16)}=-1394p-2.053, \ R^2=0.9999$

$\varepsilon_2^{(C18)}=-1640p-0.4156, \ R^2=0.9999$

$\varepsilon_2^{(C20)}=-1121p-0.1187 \ R^2=0.9999$

C12, S=85 mm
C14, S=93 mm
C16, S=101 mm
C18, S=109 mm
C20, S=117 mm

The relations presented in Figs. 7.39 and 7.40 refer to measurements on a cylindrical shell. Comparing them with the results for the pressure vessel with a torispherical dished end (Fig. 7.21), one can see almost the same circumferential deformations. However, a significant difference is seen for deformations in the meridional direction. Their increased value may be caused by a slight deviation of the strain gauge axis from the meridional direction.
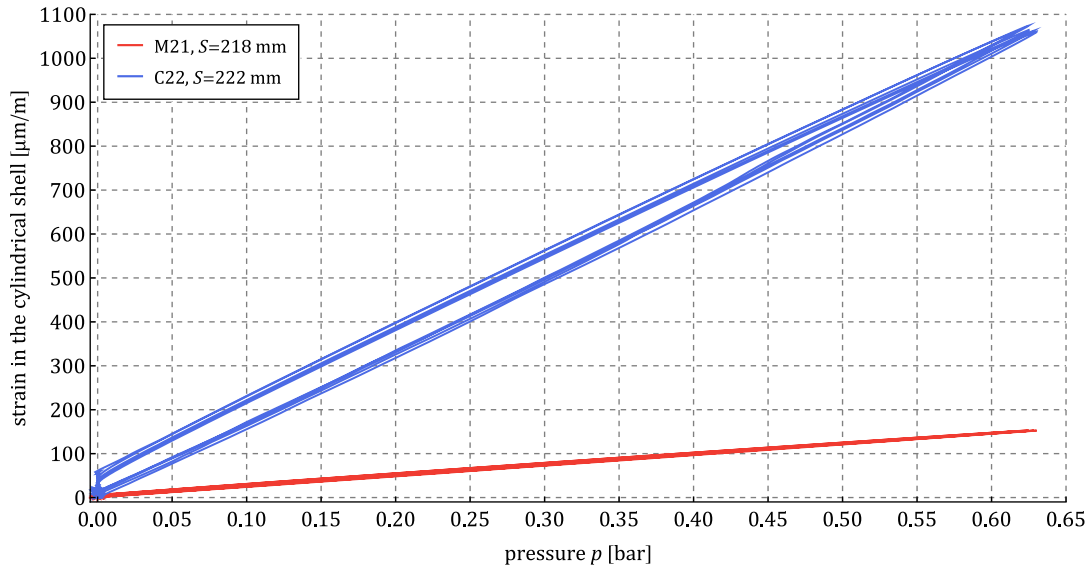
Fig. 7.39. The strain in cylindrical shell from TR, load-unload cycles

Fig. 7.40. The strain in cylindrical shell from TR, load cycles with linear regressions

The conducted measurements enable interpolating the meridional and circumferential deformations over the chain strain gauges length. Tables 7.3-7.6 summarize the strains determined from linear regressions for pressure $p = 0.6$ bar and the distance from the apex of the dished end to each measurement point.

Table 7.3. The meridional calculated from linear regressions for p=0.6 bar - CSG1

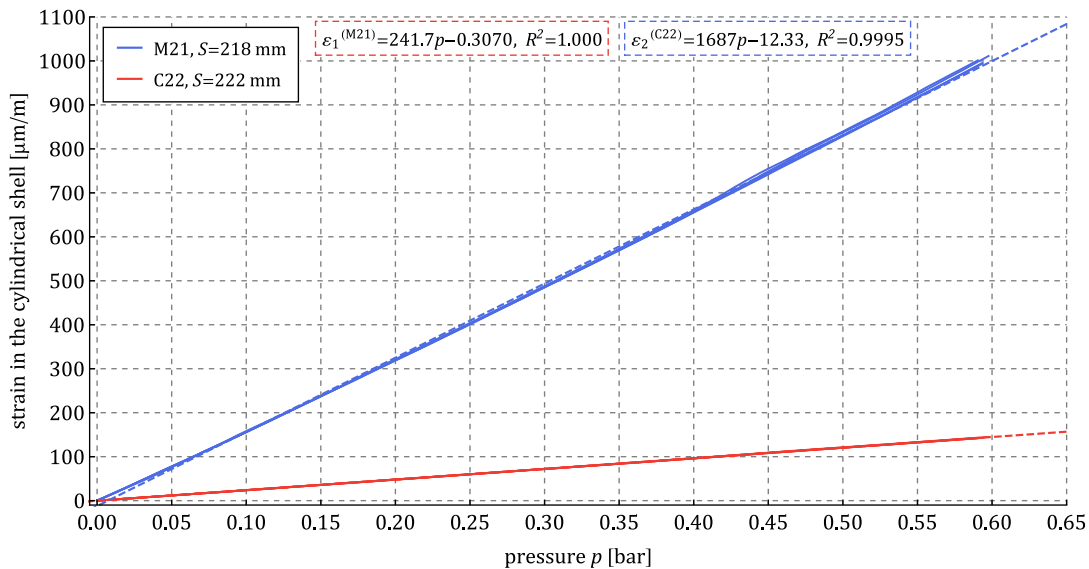| Measurement point	M1	M3	M5	M7	M9
S [mm]	20	28	36	44	52
$\varepsilon_1(0.6)$ [µm/m]	707.03	861.24	960.32	1013.3	1006.3

Table 7.4. The circumferential calculated from linear regressions for p=0.6 bar - CSG1

Measurement point	C2	C4	C6	C8	C10
S [mm]	24	32	40	48	56
$\varepsilon_2(0.6)$ [µm/m]	778.30	722.27	624.80	552.29	412.45

Table 7.5. The meridional strains calculated from linear regressions for p=0.6 bar – CSG2

Measurement point	M11	M13	M15	M17	M19
S [mm]	81	89	97	105	113
$\varepsilon_1(0.6)$ [µm/m]	892.53	885.64	823.38	698.14	467.14

Table 7.6. The circumferential strains calculated from linear regressions for p=0.6 bar – CSG2

Measurement point	C12	C14	C16	C18	C20
S [mm]	85	93	101	109	117
$\varepsilon_2(0.6)$ [µm/m]	−637.67	−838.36	−984.43	−948.57	−672.54

Interpolation is achieved using fourth-order polynomials (Eqs. (7.10)-(7.13)). The interpolation functions are applicable only within the distance from the first to the last considered strain gauge. The described further equations refer to meridian A (Fig. 7.27):

$$\varepsilon_1^{(CSG1)} = -2.3227 \times 10^{-4}s^4 + 3.2667 \times 10^{-2}s^3 - 2.0673s^2 + 74.74s - 184.9 \left[\frac{\mu m}{m}\right],$$

$$S \epsilon < 20 \,; 52 >,$$

(7.10)

$$\varepsilon_2^{(CSG1)} = -1.6145 \times 10^{-3}s^4 + 0.25411s^3 - 14.696s^2 + 358.88s - 2347.3 \left[\frac{\mu m}{m}\right],$$

$$S \epsilon < 24 \,; 56 >,$$

(7.11)

$$\varepsilon_1^{(CSG2)} = -3.5800 \times 10^{-4}s^4 + 0.13070s^3 - 18.293s^2 + 1155.2s - 26712 \left[\frac{\mu m}{m}\right],$$

$$S \epsilon < 81 \,; 113 >,$$

(7.12)

$$\varepsilon_2^{(CSG2)} = -7.0306 \times 10^{-4}s^4 + 0.31424s^3 - 50.716s^2 + 3516.7s - 89411 \left[\frac{\mu m}{m}\right],$$

$$S \epsilon < 85 \,; 117 >.$$

(7.13)

The expression of strains by the continuous functions allows the principal stresses to be determined from the plane stress state:

$$\sigma_1{}^{(CSG1)} = \frac{E_1}{1 - \nu_1\nu_2}\left(\varepsilon_1{}^{(CSG1)} + \nu_2\varepsilon_2{}^{(CSG1)}\right)10^{-6} \text{ [MPa]}, \qquad S \epsilon < 24\,; 52 >, \qquad (7.14)$$

$$\sigma_2{}^{(CSG1)} = \frac{E_1}{1 - \nu_1\nu_2}\left(\varepsilon_2{}^{(CSG1)} + \nu_1\varepsilon_1{}^{(CSG1)}\right)10^{-6} \text{ [MPa]}, \qquad S \epsilon < 24\,; 52 >, \qquad (7.15)$$

$$\sigma_1{}^{(CSG2)} = \frac{E_1}{1 - \nu_1\nu_2}\left(\varepsilon_1{}^{(CSG2)} + \nu_2\varepsilon_2{}^{(CSG2)}\right) 10^{-6} \text{ [MPa]}, \qquad S \epsilon < 85\,; 113 >, \qquad (7.16)$$

$$\sigma_2{}^{(CSG2)} = \frac{E_1}{1 - \nu_1\nu_2}\left(\varepsilon_2{}^{(CSG2)} + \nu_1\varepsilon_1{}^{(CSG2)}\right) 10^{-6} \text{ [MPa]}, \qquad S \epsilon < 85\,; 113 >. \qquad (7.17)$$

Finally, the equivalent von Mises subjected previously to the dished end optimization can be determined from the following relations:

$$\sigma_r{}^{(CSG1)} = \sqrt{\sigma_1{}^{(CSG1)^2} - \sigma_1{}^{(CSG1)}\sigma_2{}^{(CSG1)} + \sigma_2{}^{(CSG1)^2}} \text{ [MPa]}, \qquad S \epsilon < 24\,; 52 >, \qquad (7.18)$$

$$\sigma_r{}^{(CSG2)} = \sqrt{\sigma_1{}^{(CSG2)^2} - \sigma_1{}^{(CSG2)}\sigma_2{}^{(CSG2)} + \sigma_2{}^{(CSG2)^2}} \text{ [MPa]}, \qquad S \epsilon < 85\,; 113 >. \qquad (7.19)$$

It is strongly emphasised that the von Mises hypothesis is not suitable for considering the failure criteria for plastics, which is not in the scope of the experimental study.

7.3. Numerical study

The experimental tests outcome can be directly compared with the distribution (Fig. 7.22) after calculating the equivalent stress from Eqs. (7.18) and (7.19). However, such a comparison would not consider the impact of geometric imperfections. To address this issue, the optimized (Fig. 7.41) and scanned geometry (Fig. 7.42) are numerically investigated, taking into account the three-dimensional geometric models and the other conditions corresponding to the experiment. The geometries presented in Figs. 7.41 and 7.42 include the simplified flange connectors and the gaskets.

The numerical studies are carried out in ANSYS 2020 R2 software. They assume materially linear and geometrically nonlinear calculations. The latter occurs due to the large deformations that can exhibit in the FE model. The flange connectors are assumed to be made of structural steel with Young's modulus of 200 GPa and a Poisson's ratio of 0.3. The gaskets are characterized by Young's modulus of 6 MPa and Poisson's ratio $\nu = 0.47$. The material properties of the pressure vessel are as determined in the strain gauge measurements (Eqs. (7.3), (7.6) and (7.9))

Fig. 7.41. The geometric model of the optimized pressure vessel

Fig. 7.42. The geometric model of the scanned pressure vessel

The studied geometries are divided into second-order solid elements with twenty nodes and sixty degrees of freedom, designated as SOLID186 in the ANSYS system. To obtain a uniform, high-quality mesh, the geometries are split into parts, and their topology is shared.
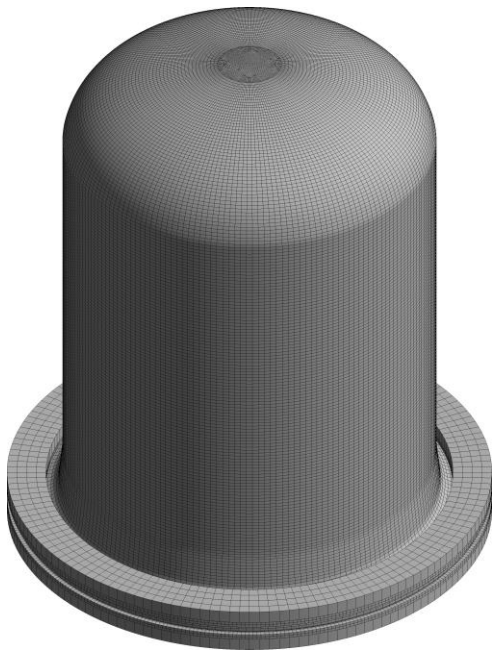
Fig. 7.43. The FE model of the optimized pressure vessel
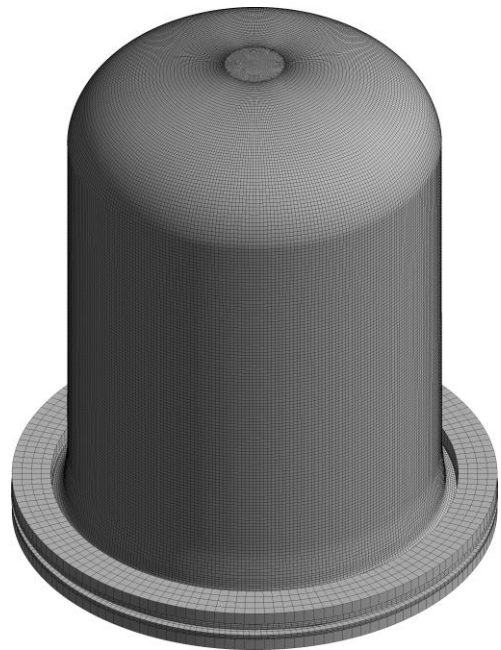
Fig. 7.44. The FE model of the scanned pressure vessel

The FE models for both pressure vessels are shown in Fig. 7.43 and Fig. 7.44. There are three finite elements across the thickness at any point of the dished end and cylindrical shell, as shown in Fig. 7.45 and Fig. 7.46. The FEM shape

optimization study in chapter 6 considered four elements across the thickness in the axisymmetric study. Such a division in the case of three-dimensional analysis becomes difficult to solve, given the nonlinear nature of the study. The total number of mesh nodes is 659512 for the optimized geometry (Fig. 7.43) and 981007 for the scanned shape (Fig. 7.44). The lower number of nodes for the FE model with the ideal geometry is considered due to the regular shapes that do not require that accurate discretization.
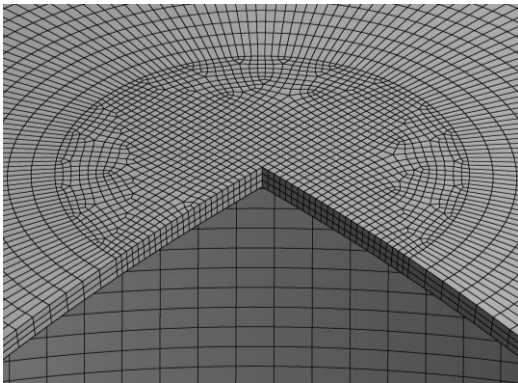

Fig. 7.45. The FE model of the optimized pressure
vessel in the area of the dished end apex
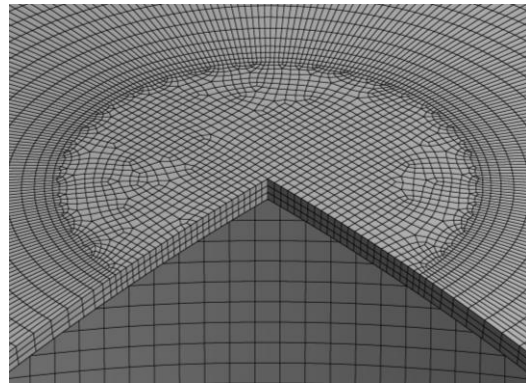
Fig. 7.46. The FE model of the scanned pressure
vessel in the area of the dished end apex

A plot of the mesh quality in terms of the orthogonal quality parameter for the scanned geometry is shown in Fig. (Fig. 7.47). According to ANSYS documentation, the quality of elements with a coefficient of $0.2 - 0.69$ is considered good, $0.7 - 0.95$ is very good, and $0.95 - 1.00$ refers to excellent quality. Almost 76% of the total number of 194012 elements are classified as excellent, with almost all the remaining elements being considered of very good quality.

Fig. 7.47. The orthogonal quality of the FE model of imperfect geometry

The first step of the numerical study is to consider only the clamping of the pressure vessels with the flange connectors. Initially, the vessel flange is not in contact with the gaskets; a minimal clearance is provided. The translations at the vessel flange are limited by introducing elastic support of near-zero stiffness. It

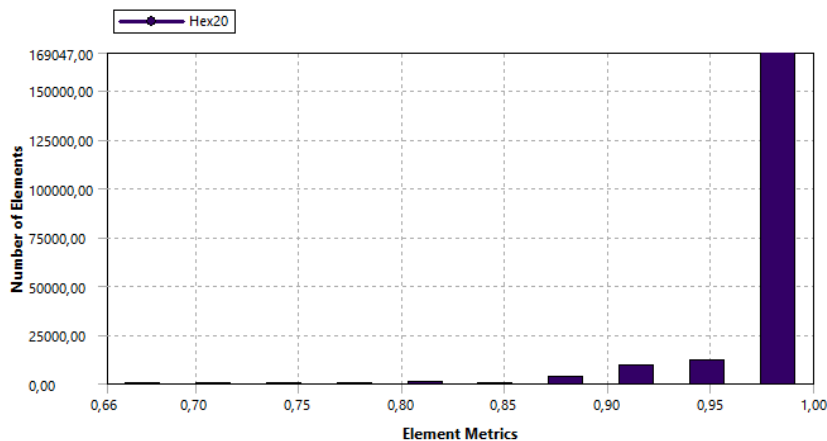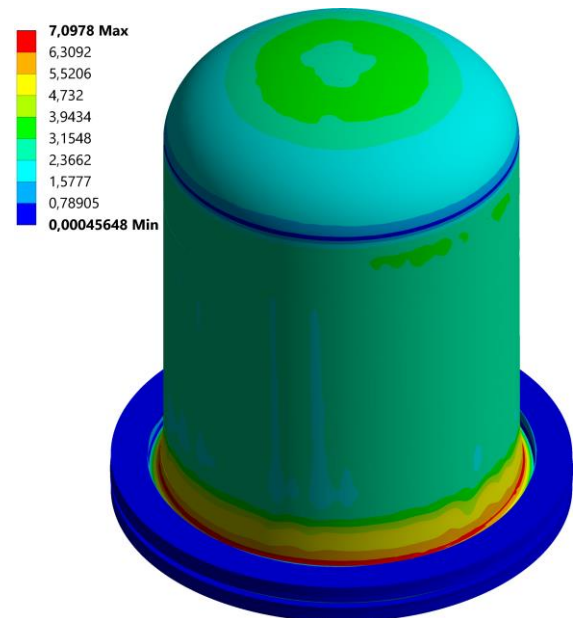prevents rigid body motion but allows the model to be freely displaced during clamping between gaskets. All of the degrees of freedom are restrained for the bottom flange connector. A translation is applied to the upper flange, which causes a clamping force of approximately 26 kN, and the remaining degrees of freedom are restrained. It corresponds to a 20 Nm tightening torque of four M16 bolts, assuming the friction coefficient between the bolt and nut threads of 0.15. Those conditions are coherent with the experimental study. The friction coefficient equal to 0.5 between the vessel flange and the rubber gaskets is assumed. The bonded contact between flange connectors and gaskets is applied. The purpose of the calculations is solely to obtain a deformed FE model to be further studied in the pressurization analysis. Importantly for the optimized geometry (Fig. 7.41), this does not lead to any significant deformation as the flange is perfectly flat, so no bending occurs.
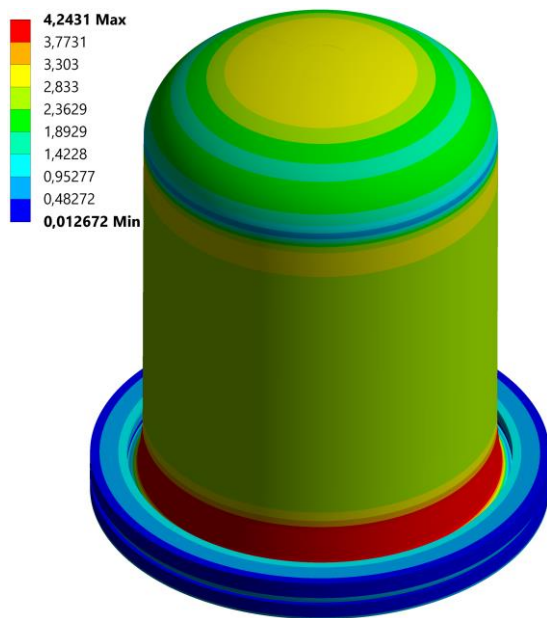
Fig. 7.48. The equivalent von Mises stress distribution in the optimized geometry	*Fig. 7.49. The equivalent von Mises stress distribution in the scanned geometry*

The same conditions as in the first study are considered in a subsequent numerical analysis, except the elastic support. A vertical displacement of 0.05 mm is applied to the upper flange connector, which prevents the rigid body motion of the vessel. The internal surface of the model is loaded with a pressure of 0.6 bar. The resulting distributions of equivalent von Mises stress are shown in Fig. 7.48 and Fig. 7.49 taking into account all bodies of the numerical model. As expected, their distribution is axisymmetric for the geometrically perfect model (Fig. 7.48). For this reason, its analysis might seem futile, but it allows for direct reference to the scanned geometry and provides insight into the numerical accuracy of the axisymmetrical analysis from the optimization study (Fig. 7.22).

In the case of the other model, it is noteworthy that the stress values are significantly higher in the area of transition of the flange to the cylindrical shell. The reason for this is a moderately deformed flange on the scanned model, which leads to an increase in the intensity of the bending phenomenon. Considering the goal of the study, this is not a significant issue. In the case of the scanned geometry, the stress distribution is not axisymmetric, although noticeable regularity resembling such a state is obtained. It is convenient to investigate the equivalent stress only in the cylindrical shell and dished end. Such results are presented in Fig. 7.50 and Fig. 7.51. The maximum stress values on the legends are adjusted to the highest stresses in the dished ends. The areas where the resulting stress is higher correspond to the grey colour. Those are related only to the flange-cylinder transition.
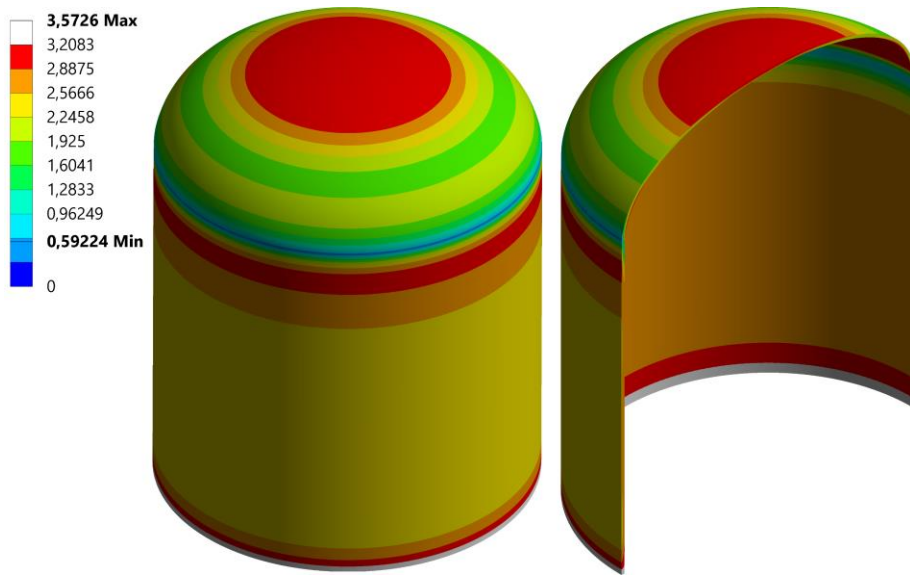

Fig. 7.50. The equivalent stress in the cylindrical shell and dished end - geometrically perfect model
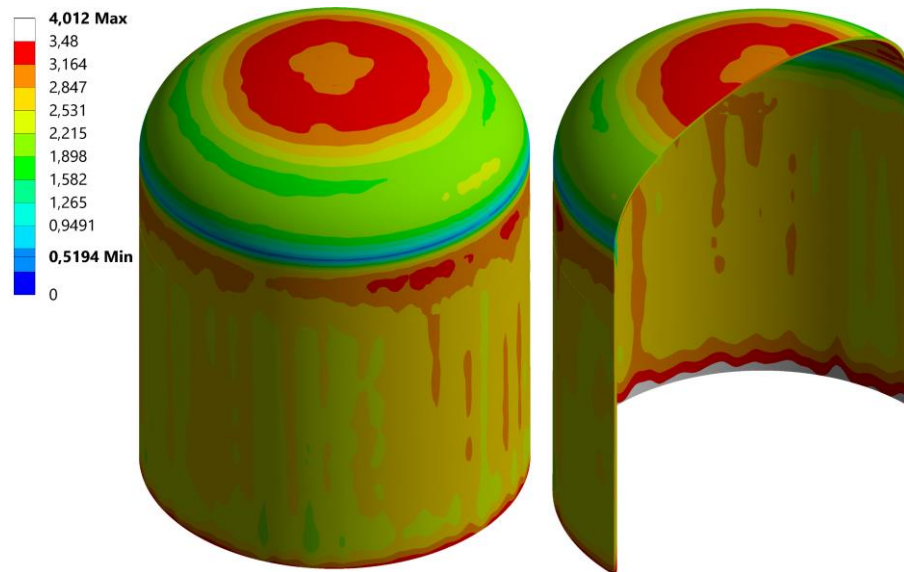

Fig. 7.51. The equivalent stress in the cylindrical shell and dished end - geometrically imperfect model

On the basis of the numerical FEM calculations, it is concluded that the maximum values of the equivalent stresses in the dished ends vary moderately. Reading the values $\sigma_{r\,max}$ = 3.208 MPa (Fig. 7.50) and $\sigma_{r\,max}$ = 3.480 MPa (Fig. 7.51), it can be evaluated that the relative difference is 8.469%. With a high degree of certainty, it can be deduced that the stress increase is mainly due to the smaller thickness of the dished end in the scanned model. At the point where the maximum stresses occur in the imperfect dished end, the thickness is about 1.9 mm (Fig. 7.26), so the relative thickness difference is close to 5%. Because of the local character of variations in thickness, it would not be correct to recalculate the stresses for the case where the thickness would hypothetically be 2 mm as in the optimization.

7.4. Comparison of experimental and numerical studies

The numerically and experimentally obtained results require a more in-depth comparison due to their varied form. The data included in Fig. 7.52 summarises meridional strain for the optimized and scanned geometries obtained using FEM as well as experimentally determined values. The strain of the imperfect shape is studied for four meridians, i.e. A, B, C, D (Fig. 7.27). It is important to note that the functions in Eqs. (7.10)-(7.19) correspond to the meridian A. A moderate difference in deformations can be seen for the optimized and scanned geometries, especially in the range from S = 50 mm to S = 70 mm.
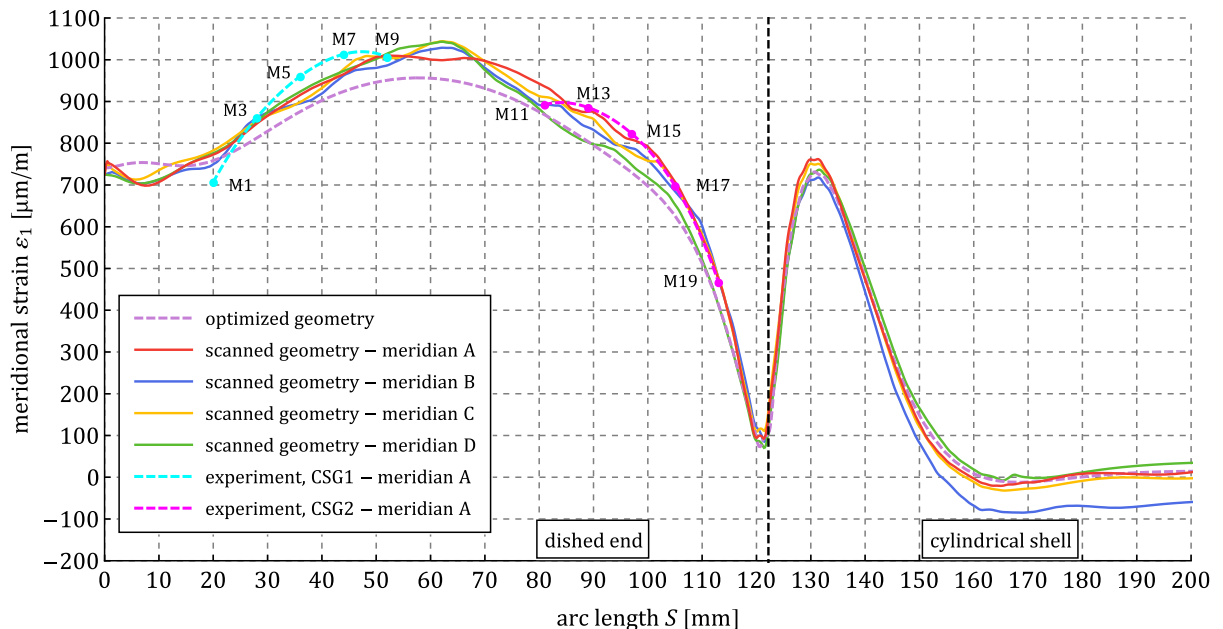

Fig. 7.52. The comparison of meridional strains

Comparing the results of the FEM calculations for the imperfect geometry, the most considerable differences are seen for the cylindrical shell. They are expected due

to the occurrence of thickness variations for this geometry (Fig. 7.26). In the case of the dished end, they are in good agreement. Relating them to the experiment, it may be concluded that they share similar characteristics and values. The measurement points where these deformations are most divergent are M1 for CSG1 and M11 for CSG2.

The circumferential strains are juxtaposed in Fig. 7.53. The observed differences between the results of the FEM study for the scanned geometry can be seen in the cylindrical shell and the area of minimum strain, i.e. close to $S = 100$ mm. Nevertheless, it can be considered that the distributions of the analysed values are more convergent than for the meridional direction. The obtained deformations are almost identical within the CSG2 range, while minor inconsistencies are visible for points C2 and C10 in CSG1.
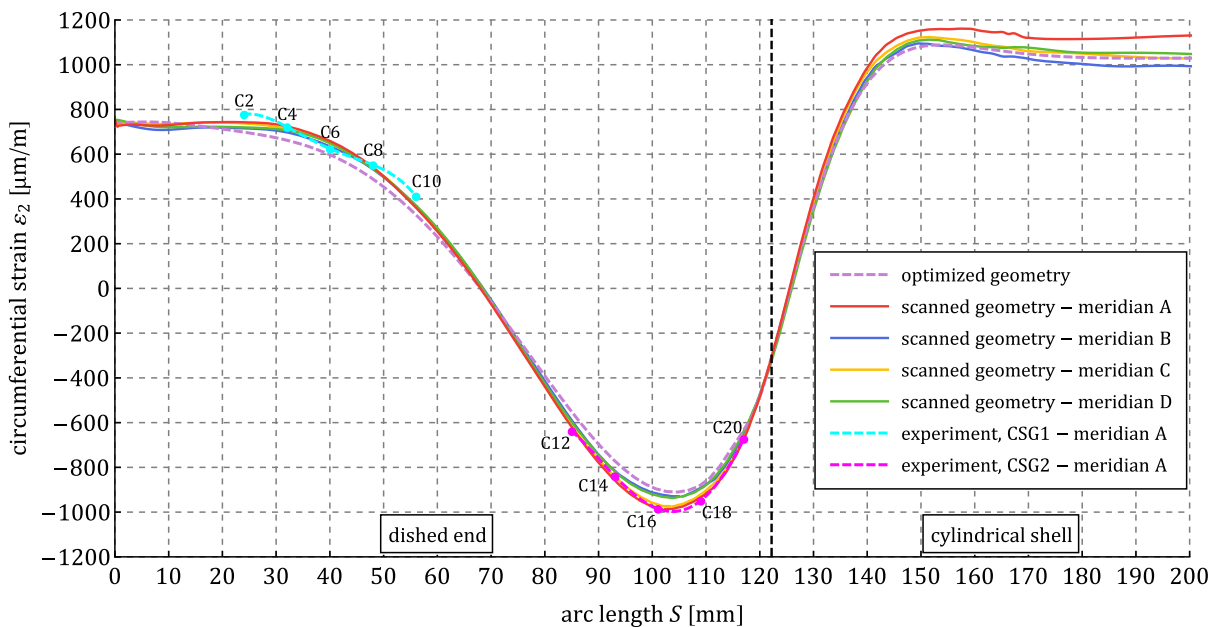
Fig. 7.53. The comparison of circumferential strains

Given the dissertation topic, a comparison of the stress distributions obtained for all of the studied cases in this chapter should be considered the most critical analysis. The values for the experiment are obtained using Eqs. (7.18) and (7.19). For interpretation clarity, the stress distributions are limited to meridian A in the case of imperfect geometry. The obtained stress distribution differs slightly for the optimized geometry compared to the axisymmetric analysis (Fig. 7.22). The value of the stress concentration (Eq. (3.22)) factor increased from $k_{optimized} = 1.188$ to $k_{optimized} = 1.204$. Due to its small change, this can be considered as an acceptable numerical error. The reason for this issue is the modestly lower quality of the mesh than in the simplified analysis, where four instead of three elements across the thickness are

present. Additionally, the elements are less regular, as can be observed in Fig. 7.45. The stress character for the scanned geometry is similar to that obtained in the optimized model. An increased value of the stress in the inner and outer surfaces can be perceived as considerably regular. Such a phenomenon is expected due to the smaller thickness of the imperfect structure. The determined value of maximum stress corresponds to the stress concentration factor $k_{scanned} = 1.284$, which corresponds to relative increase of 6.645% concerning the optimization result. The equivalent stress referring to the experimental study (Eqs. (7.18), (7.19)) is almost identical for the CSG2 sensor and moderately different for the CSG1 compared to the FEM study results of imperfect geometry. As expected, the maximum value of the investigated stress occurs within CSG1, and its value corresponds to the $k_{experiment} = 1.304$ stress concentration factor. The relative increase of the stress concentration factor is then 1.558% and 8.306% referring to the scanned and optimized geometry, respectively.
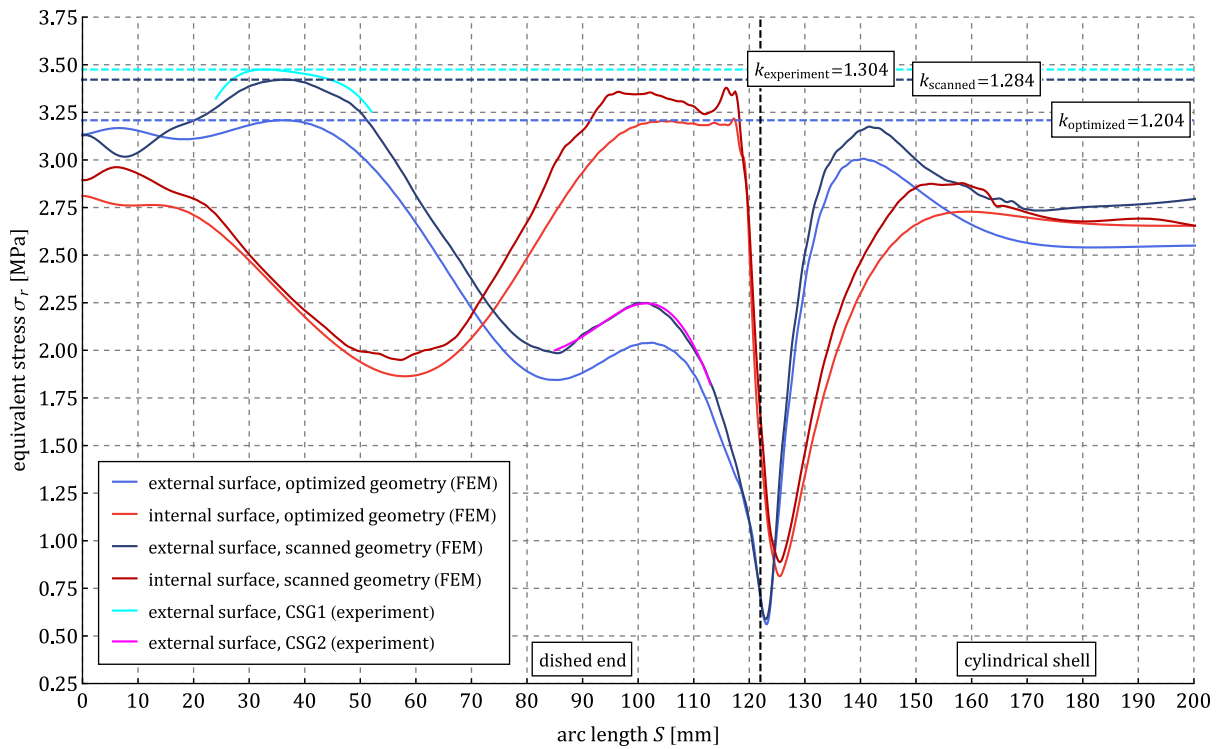
Fig. 7.54. The comparison of equivalent stress distributions

Summarising the achieved results, one can conclude that the experimental study confirms the results obtained numerically using FEM. This is particularly evident in the study of geometry, which is obtained from optical measurements. Differences between the optimal stress distribution and those resulting from the experimental study are noticeable. This phenomenon is expected due to imperfections in the form of shape differences and smaller, variable thickness in the manufactured

pressure vessel. The selected AMM leads to satisfactory dimensional and geometrical tolerances in contrast to other technologies from this group. However, it should be noted that conventional manufacturing methods can lead to much higher geometrical precision when producing full-scale cylindrical pressure vessels. The experimental study confirms the stress distribution in an imperfect model; therefore, it can be concluded that errors in shape and thickness distribution mainly contribute to the discrepancies in results. Reducing the magnitude of those imperfections can lead to near-optimal stress distribution.

When evaluating the quality of the presented experimental investigation, it is necessary to consider the number of factors that could negatively affect its outcome. Among many, the most relevant can be considered the mechanical characteristics of the plastic, the well established but still developed manufacturing method, the known errors occurring in the strain gauge measurements and the difficulty in bonding them to the curvilinear surface while maintaining correct orientation. Having those in mind, the difference in the stress concentration factor of 8.306% between the geometrically ideal and the actual pressure vessel in the experimental study can be considered satisfactory. The conducted numerical and experimental studies confirmed the favourable stress distribution obtained in the shape optimization study, showing potential in their application in the industry.

8. Conclusions

In this work, analytical, semi-analytical, numerical and experimental investigations have been carried out within the shell structures framework. Complex forms of these structures have been taken into account, referring to cylindrical pressure vessels.

Analytical studies were carried out according to the theories available in the literature, i.e. membrane theory and the edge effect theory. A description of the geometries of standard dished ends was presented. The formulae allowing to describe displacements and stresses by means of the membrane theory were derived for them. Analysis of the problem using the edge effect theory referred to its two known formulations. Isotropic and orthotropic material properties were taken into account. Superposition of solutions resulting from both theories has been carried out for a pressure vessel with the ellipsoidal and torispherical dished end. The obtained results were compared with numerical calculations using the finite element method. In the case of the ellipsoidal geometry, stress compliance for t/R_0 in the range 0.1% to 3% was within 0.7251% to 13.25% relative difference. For the torispherical geometry, the same values range from 6.103% to 103.1%, indicating a significant inaccuracy of the analytical solution with increasing shell thickness. The reason for this is shown to be due to the occurrence of normal force at the edge of the toroidal shell, considered within the framework of the membrane theory, which leads to acceptable results only for minimal thickness.

Deficiencies in the selected analytical solutions constituted a motivation to use other methods to achieve more satisfactory results. The next stage of the study concerned semi-analytical analysis using the Ritz method. The elastic strain energy was formulated on the basis of linear shell theory with Kirchoff-Love assumptions. The work of external forces involved all possible loads, i.e. pressure, normal forces, transverse forces and moments at the edge of the shells. Compatibility equations for displacements and rotations were defined, allowing the interaction of the shells to be taken into account. The displacement functions were in the form of polynomials, trigonometric series and functions resembling the solutions of governing differential equations of the edge effect theory. The influence of the order of these functions on the solution was analysed and compared to the results of finite element calculations. It was shown that satisfactory results could be obtained with a sufficiently high order of displacement functions, while their form has a limited influence on the solutions. For both dished ends with a t/R_0 ratio between 0.5% and 3%, the relative differences in maximum stresses were from 0.02064% to 1.310%, regardless of the value of the

orthotropy coefficient. This represents a tremendous improvement over the analytical solution. The outcome of the study shows the potential in applying the Ritz method to the static problems, not only considering the pressure vessels but also for the design of a broad spectrum of shell structures. Such observations prove the validity of the first hypothesis posed in the dissertation.

In the conducted analytical and semi-analytical investigations of cylindrical pressure vessels, attention was drawn to the unfavourable stress distribution. Their maximum values in standard ellipsoidal and torispherical dished ends significantly exceed the stress in the cylindrical shell, making them unsatisfactory solutions. An explanation for such a phenomenon are the loads acting upon the edges of the shells, leading to an intense bending effect. This remark has led to research aimed to develop dished end shapes in which the edge effect is negligible. For this purpose, expressions describing the shapes of the shells were derived in the form of analytical curves, i.e., Cassini and Booth's oval and generalized clothoid. These were characterised by continuous curvatures and their derivatives in the juncture with the cylindrical shell. The effect of dished ends relative depth on the distribution of equivalent stresses was also analysed. The research had the intended effect, although it indicated that the location of maximum stresses was shifted away from the area where the segments of the structures were joined.

Conclusions from previous studies have shown the enormous influence of the dished end shape on the stress distribution. In order to further improve it, the problem of shape optimization was addressed. A unique shape based on the Bézier curve of arbitrary order was developed, satisfying numerous constraints, including a non-negative meridional radius of curvature. Regardless of the parameters describing its shape, the geometry maintains manufacturability and the relative depth as the standard dished ends.

Initially, the optimization assumed an analytical evaluation of the fitness function using membrane theory and employing a sequential quadratic programming algorithm. Different curve orders were considered to evaluate sufficient numbers of the independent variables describing the dished end geometry. The membrane theory optimization enabled the reduction of the stress concentration factor to $k = 1.141$. The corresponding value for the standard geometries is $k = 1.712$ to $k = 1.746$ for ellipsoidal shape and $k = 2.356$ to $k = 2.738$ for equivalent torispherical, depending on the thickness. The verification of the developed geometry was performed using the finite element method, which led to an increase in k parameter to 1.350, 1.378, 1.415,

depending on thickness to cylinder radius ratio t/R_0. Such an issue is the effect of the bending phenomenon neglection in the membrane theory,

As the next step, the optimization was conducted using a more complex approach. The commercial software MATLAB and ANSYS were coupled to perform the procedure by evaluating the fitness function in the latter. A genetic algorithm has been used to optimize the stress concentration factor. Despite the substantial computational time needed to process the calculations, the results can be considered compelling. The analysed parameter was reduced to 1.199, 1.184 and 1.206 for the t/R_0 ratio 0.5, 1.0, 1.5% respectively. Summarizing the findings of the optimization study, the stress in the standard dished ends is 71.2% to 173.8% higher than in the cylindrical shell beyond any disturbance. The developed shapes are characterised merely by 18.4% to 20.6% greater equivalent von Mises stress. The proposed geometries constitute a significant improvement over the shapes described by the current technical standards while maintaining their manufacturability and general dimensions.

It was decided to carry out experimental studies to verify the optimization results. This started with searching for an appropriate method to manufacture the pressure vessels models. The production of those using conventional methods is economically unjustified; hence additive manufacturing methods were employed. Two possible technologies that could potentially be used were considered, namely Selective Laser Sintering and Multi Jet Fusion. The more suitable method was selected based on a static tensile test on specimens manufactured from PA12 in two orientations. Multi Jet Fusion was found to have a higher minimum ultimate strength and more satisfactory dimensional stability. In order to determine the mechanical properties, a vessel with a torispherical dished end was manufactured and studied using strain gauge measurements on a developed test bench. The material properties were determined for an appropriate strain rate using analytical formulae describing deformations in the cylindrical shell.

The shape of the dished end was re-optimised, taking into account the mechanical properties of the printed PA12 model. The pressure vessel with the optimized shape was manufactured using the Multi Jet Fusion method and then measured using an optical scanner. The actual, imperfect geometry of the structure was compared with the ideal, optimized geometry. The model of the printed pressure vessel was reconstructed as a CAD file and numerically studied using the finite element method to investigate the influence of geometric imperfections on the optimal

stress distribution. The actual model was then subjected to strain gauge measurements on the test bench. Those were taken at twenty-two points, allowing for the determination of equivalent stresses in the area where the extrema were expected.

Finally, the numerical calculations using the finite element method for the optimized and scanned geometry were compared with the experimental results. The experimental and numerical results for the scanned geometry were shown to be in good agreement. The relative difference in the stress concentration factor k was 1.558%. Both of these results differ slightly from the result for the optimized geometry, compared to which the experimental study indicates a relative difference of 8.306%. This is mainly due to the reduced thickness of the actual model at the measurement locations, caused by inevitable geometric imperfections introduced in the manufacturing process. It should be noted that conventional manufacturing methods can lead to much higher geometrical precision when producing full-scale cylindrical pressure vessels. According to the second dissertation hypothesis, shape optimization had the intended effect.

Given that the results obtained for a plastic pressure vessel obtained by 3D printing are satisfactory, it is expected that the actual stress distribution can be even closer to the optimal for industrial pressure vessels. It shows that developed dished end shapes have significant potential for their application. The proposed improvements enable to increase their load-carrying capacity or reduce their weight, which is essential in any industry involving the transport or storage of liquids and gases.

References

[1] Z. E. Mazurkiewicz, R. T. Nagórski, Powłoki obrotowe sprężyste, Państwowe Wydawnictwo Naukowe, Warsaw 1987.

[2] E. Ventsel, T. Krauthammer, Thin plates and shells. Theory, Analysis, and Applications, Marcel Dekker, Inc., New York, Basel, 2001.

[3] A. L. Gol'Denveizer, Theory of elastic thin shells, Pergamon Press, New York 1961.

[4] C.R. Calladine, Theory of shell structures, Cambridge University Press, Cambridge 1983

[5] A. Zingoni, Shell Structures in Civil and Mechanical Engineering, ICE Publishing, 2017.

[6] K. Magnucki, Wytrzymałość i optymalizacja zbiorników cienkościennych, Wydawnictwo Naukowe PWN, Warszawa, Poznań 1998

[7] J. Spence, A. S. Tooth, Pressure vessel design. Concepts and principles, E&FN SPON, London, Glasgow, New York, Melbourne, Madras, 1994

[8] K. Magnucki, J. Lewiński, R. Cichy, Strength and Buckling Problems of Dished Heads of Pressure Vessels – Contemporary Look, Journal of Pressure Vessel Technology 140(4) (2018) 041201

[9] J. Ziółko, Zbiorniki metalowe na ciecze i gazy, Arkady, Warszawa 1970

[10] EN 13445-3:2002 Unfired pressure vessels – Part 3: Design, European Committee for Standardization.

[11] ASME Boiler and Pressure Vessel Code, Section VIII, Division 1, 2015, American Society of Mechanical Engineers, New York, NY.

[12] ASME Boiler and Pressure Vessel Code, Section VIII, Division 2, 2015, American Society of Mechanical Engineers, New York, NY.

[13] T. G. Seipp, N. Barkley, C. Wright, Ellipsoidal Head Rules: A Comparison Between ASME Section VIII, Divisions 1 and 2, Proceedings of the ASME 2017 Pressure Vessels and Piping Conference, PVP 2017-65858

[14] Reissner H., Spannungen in Kugelschalen, Fetschrift Müller-Breslau, 1912, 181-193

[15] Meissner E., Das Elastizitatsproblem für dünne Schalen von Ringflächen-Kugel, und Kegelform, Physik Zeit. 14 (1913): 343–349.

[16] Blumenthal, O., Über die asymptotische Integration von Differentialgleichungen mit Anwendung auf die Berechnung von Spannungen in Kugelschalen. Zeitschrift für Mathematik und Physik, vol. 63, pp. 342 – 362, 1913.

[17] Geckeler J. W., Über die Festigkeit achsensymmetrischer Schalen. Forschungsarbeiten auf dem Gebiete des Ingenieurwesens, No. 276. Berlin: VDI-Verlag, 1926.

[18] Steuermann E., Die Grundgedanken der neuzeitlichen Theorie der Kuppeln, Bauingenieur, 1933

[19] Steuermann E., Berechnung der Kuppeln Als Bogen auf elastischer Unterlage, Bauingenieur, 1933

[20] W. Pietraszkiewicz, V. Konopińska, Junctions in shell structures: A review, Thin-Walled Struc., 95 (2015) 310-334.

[21] V. Vullo, Circular cylinders and pressure vessels. Stress analysis and design, Springer, Rome, 2014

[22] A. Zingoni, Liquid-containment shells of revolution: A review of recent studies on strength, stability and dynamics, Thin-Walled Structures 87 (2015) 102-114.

[23] A. Zingoni, Stresses and deformations in egg-shaped sludge digesters: discontinuity effects, Thin-Walled Structures 23 (2001) 1373-1382.

[24] A. Zingoni, Parametric stress distribution in shell-of-revolution sludge digesters of parabolic ogival form, Thin-Walled Structures 40 (2002) 691-702.

[25] A. Zingoni, Discontinuity effect at cone-cone axisymmetric shell junctions, Thin-Walled Structures 40 (2002) 877-891.

[26] A. Zingoni, N. Enoma, N. Govender, Equatorial bending of an elliptic toroidal shell, Thin-Walled Structures 96 (2015) 286-294

[27] A. Zingoni, B. Mokhothu, N. Enoma, A theoretical formulation for the stress analysis of multi-segmented spherical shells for high-volume liquid containment, Engineering Structures, 87 (2015) 21–31.

[28] A. Zingoni, Simplification of the derivation of influence coefficients for symmetric frusta of shells of revolution, Thin-Walled Structures, 47 (2009) 912–918.

[29] Y. Kumar, The Rayleigh-Ritz method for linear dynamic, static and buckling behaviour of beams, shells and plates: A literature review, Journal of Vibration and Control 24 (2018) 1205-1227.

[30] D. Shahgholian-Ghahfarokhi, M. Safarpour, A. Rahimi, Torsional buckling analyses of functionally graded porous nanocomposite cylindrical shells reinforced with graphene platelets (GPLs), Mechanics Based Design of Structures and Machines 49(1) (2021) 81-102

[31] B. Qin, R. Zhong, T. Wang, Q. Wang, Y. Xu, Z. Hu, A unified Fourier series solution for vibration analysis of FG-CNTRC cylindrical, conical shells and

annular plates with arbitrary boundary conditions, Composite Structures 235 (2020) 111549.

[32] A. V. Lopatin, E. V. Morozov, Axisymmetric vibrations of the composite orthotropic cylindrical shell with rigid weightless end disks, Thin-Walled Structures 135 (2019) 463-471.

[33] Z. Qin, X. Pang, B. Safaei, F. Chu, Free vibration analysis of rotating functionally graded CNT reinforced composite cylindrical shells with arbitrary boundary conditions, Composite Structures 220 (2019) 847-860

[34] F. Pang, H. Li, X. Wang, X. Miao, S. Li, A semi analytical method for the free vibration of doubly-curved shells of revolution, Computers and Mathematics with Applications, 75 (2018) 3249-3268

[35] I. Senajovic, I. Áatipovic, N. Alujevic, D. Cakmak, N. Vladimir, A Finite Strip for the Vibration Analysis of Rotating Toroidal Shell under Internal Pressure, Journal of Vibration and Acoustics, Transactions of the ASME 141(2) (2019) 021013

[36] K. Choe, K. Kim, Q. Wang, Dynamic analysis of composite laminated doubly-curved revolution shell based on higher order shear deformation theory, Composite Structures 225 (2019) 111155

[37] (A1) K. Sowiński, The Ritz method application for stress and deformation analyses of standard orthotropic pressure vessels, Thin-Walled Structures 162 (2021) 107585

[38] M. J. Kochenderfer, A. Wheeler, Algorithms for optimization, MIT Press, Cambridge, Massachusetts, 2019

[39] M. Ostwald, Podstawy optymalizacji konstrukcji w projektowaniu systemowym, Wydawnictwo Politechniki Poznańskiej, Poznań 2016

[40] J. Nocedal, S. J. Wright, Numerical Optimization, Second Edition, Springer Series in Operations Research, Springer Verlag, 2006

[41] Z. Ugray, L. Lasdon, J. Plummer, J. Kelly, R. Martí, Scatter Search and Local NLP Solvers: A Multistart Framework for Global Optimization, INFORMS Journal on Computing 19(3) (2007) 313-484

[42] J. Arabas, Wykłady z algorytmów ewolucyjnych, Wydawnictwa Naukowo-Techniczne, Warszawa

[43] B. Bochenek, J. Krużelecki, Optymalizacja stateczności konstrukcji. Współczesne problemy, Politechnika Krakowska, Kraków 2007

[44] K. Magnucki, O. Marian, Stateczność i optymalizacja konstrukcji trójwarstwowych, Wydawnictwo i Zakład Poligrafii Instytutu Technologii eksploatacji, Poznań-Zielona Góra 2001

[45] R. Moradi, K. M. Groth, Hydrogen storage and delivery: Review of the state of the art technologies and risk and reliability analysis, International Journal of Hydrogen Energy 44(23) (2019) 12254-12269

[46] N. Ortega, S. Robles, Form finding of revolution shells by analyzing mechanical behaviour by means of the finite element method, J Strain Anal Eng Des., 40(8) (2005) 775–784.

[47] N. V. Banichuk, Optimization of axisymmetric membrane shells, Journal of Applied Mathematics and Mechanics 71 (2007) 527-535

[48] J. Błachut, K. Magnucki, Strength, stability, and optimization of pressure vessels: Review of selected problems, Appl. Mech. Rev. Trans. ASME, 61 (6) (2008) (Ar 060801).

[49] B. Bochenek, A new concept of optimization for postbuckling behaviour, Engineering Optimization 33(4) 2001, 503-522

[50] P. Jasion, Buckling and post-buckling analysis of shells of revolution with positive and negative Gaussian curvature, Wydawnictwo Politechniki Poznańskiej, Poznań 2015

[51] P. Jasion, Stability analysis of shells of revolution under pressure conditions. Thin-Walled Structures 47(3) (2009) 311-317.

[52] P. Jasion, K. Magnucki, Elastic buckling of Cassini ovaloidal shells under external pressure – Theoretical study, Archives of Mechanics 67(2) (2015) 179-192.

[53] P. Jasion, K. Magnucki. Theoretical investigation of the strength and stability of special pseudospherical shells under external pressure, Thin-Walled Structures 93 (2015) 88-93.

[54] P. Jasion, K. Magnucki, Elastic buckling of clothoidal-spherical shells under external pressure - Theoretical study, Thin-Walled Structures 86, (2015) 18-23.

[55] P. Jasion, K. Magnucki, Elastic buckling of barrelled shell under external pressure, Thin-Walled Structures 45(4) (2007) 393-399.

[56] K. Sowiński, P. Jasion, Closed shell of revolution with meridian based on Booth lemniscate loaded with external pressure, Thin-Walled Structures 144 (2019) 106284.

[57] K. Sowiński, Buckling of shells with special shapes with corrugated middle surfaces – FEM study, Engineering Structures 179 (2019) 310-320.

[58] P. Paczos, J. Zielnica, Stability of orthotropic elastic-plastic open conical shells, Thin-Walled Structures 46(5) 2008 530-540

[59] J. Zhang, M. Wang, W. Wang, W. Tang, Y. Zhu, Investigation on egg-shaped pressure hulls, Marine Structures 52 (2017) 50-66.

[60] J. Zhang, W. M. Wang, W. C. Cui, W. X. Tang, F. Wang, Y. Chen, Buckling of longan-shaped shells under external pressure, Marine Structures 60 (2018) 218-225.

[61] J. Zhang, W. Wang, F. Wang, W. Tang, W. Cui, W. Wang, Elastic buckling of externally pressurized Cassini oval shells with various shape indices. Thin-Walled Structures 122 (2018) 83-89.

[62] (A2) K. Sowiński, K. Magnucki, Shaping of dished heads of the cylindrical pressure vessel for diminishing of the edge effect, Thin-Walled Structures 131 (2018) 746-754.

[63] J. Lewiński, Optymalne kształtowanie wypukłych den naczyń ciśnieniowych, Wydawnictwo Politechniki Poznańskiej, Poznań 2012

[64] K. Magnucki, W. Szyc, J. Lewiński, Minimization of stress concentration factor in cylindrical pressure vessels with ellipsoidal heads, International Journal of Pressure Vessels and Piping 79 (2002) 841-846

[65] J. Lewiński, K. Magnucki, Shaping of a middle surface of a dished head of a circular cylindrical pressure vessel, Journal of theoretical and applied mechanics 48(2) (2010) 297-307

[66] J. Krużelecki, R. Proszowski, Shape optimization of thin-walled pressure vessel end closures, Structural and Multidisciplinary Optimization 46 (2012) 739-754

[67] Y. Kisioglu, J.R. Brevick, G.L. Kinzel, Minimum material design for propane cylinder end closures, Journal Pressure Vessel Technology 130, (2008) 015001.

[68] K. Magnucki, P. Jasion, M. Rodak, Strength and buckling of an untypical dished head of a cylindrical pressure vessel, International Journal of Pressure Vessels and Piping 161 (2018) 17-21

[69] R.C. Carbonari, P.A. Muñoz-Rojas, E.Q. Andrade, G.H. Paulino, K. Nishimoto a nd E.C.N. Silva, Design of pressure vessels using shape optimization: An integrated approach, International Journal of Pressure Vessels and Piping, 88 (2011), 198-212

[70] J. Błachut, L. S. Ramachandra, Optimization of internally pressurized torispheres subject to shakedown via Gas, Engineering Optimization 29 1997 1-4

[71] Z. Wang, A. Sobey, A comparative review between Genetic Algorithm use in composite optimisation and state-of-the-art in evolutionary computation, Composite Structures 223 (2020) 111739

[72] B. Firlik, T. Staśkiewicz, W. Jaśkowski, L. Wittenbeck, Optimisation of a tram wheel profile using a biologically inspired algorithm, Wear 430-431 (2019) 12-24

[73] M. Yang, B. Han, P. Su, Q. Zhang, Q. Zhang, Z. Zhao, C. Ni, T. J. Lu, Crashworthiness of hierarchial truncated conical shells with corrugated cores, International Journal of Mechanical Sciences 193 (2020) 106171

[74] D. Kumar, L. H. Poh, S. T. Quek, Isogeometric shape optimization of missing rib auxetics with prescribed negative Poisson's ratio over large strains using genetic algorithm, International Journal of Mechanical Sciences 193 (2021) 106169

[75] K. Liang, Z. Li, Postbuckling analysis and optimization of composite laminated panels using a novel perturbation-based approximation FE method, Thin-Walled Structures 160 (2021) 107398

[76] M. Imran, D. Shi, L. Tong, H. M. Waqas, Design optimization of composite submerged cylindrical pressure hull using genetic algorithm and finite element analysis, Ocean Engineering 190 (2019) 106443

[77] A. Eshani, H. Dalir, Multi-Objective optimization of composite angle grid plates for maximum buckling load and minimum weight using genetic algorithms and neural networks, Composite Structures 229 (2019) 111450

[78] S. Zhu, M. Ohsaki, X. Guo, Q. Zeng, Shape optimization for non-linear buckling load of aluminium alloy reticulated shells with gausset joints, Thin-Walled Structures 154 (2020) 106830

[79] Y. Dias, M. Mahendran, Shape optimisation of cold-formed steel framed wall studs with sheathing restraints, Thin-Walled Structures 158 (2021) 107135

[80] H. Karimi, I. M. Kani, Finding the worst imperfection pattern in shallow lattice domes using genetic algorithms, Journal of Building Engineering 23 (2019) 107-113,

[81] (A3) K. Sowiński, Stress distribution optimization in dished ends of cylindrical pressure vessels, Thin-Walled Structures 171 (2022) 108808

[82] ISO527, Plastics – Determination of tensile properties, 2019, International Organization for Standardization

[83] I. Gibson, D. Rosen, B. Stucker, Additive Manufacturing Technologies, 3D printing, Rapid Prototyping, and Direct Digital Manufacturing, Springer New York Heidelberg Dordrecht London, 2015

[84] K. Hoffman, An introduction to measurements using strain gages, Hottinger Baldwin Messtechnik GbmH, Darmstadt 1989

[85] P. Paczos, Experimental investigation of C-beam with non-standard flanges, Journal of Constructional Steel Research 93 (2014) 77-87

[86] P. Paczos, P. Wasilewicz, E. Magnucka-Blandzi, Experimental and numerical investigations of five-layered trapezoidal beams, Composite Structures 145 (2016) 129-141

[87] P. Paczos, P. Wasilewicz, Experimental investigations of buckling of lipped, cold-formed thin-walled beams with I-section, Thin-Walled Structures 47 (2009) 1354-1362

[88] P. Jasion, A. Pawlak, P. Paczos, Buckling and post-buckling behaviour of selected cold-formed C-beams with atypical flanges, Engineering Structures 244 (2021) 112693

[89] J. Zhang, F. Wang, F. Wang, X. Zhao, W. Tang, F. Chen, Buckling properties of bulged barrels under external pressure, Thin-Walled Structures 168 (2021) 108226

[90] J. Zhang, P. Cheng, F. Wang, W. Tang, X. Zhao, Hydroforming and buckling of an egg-shaped shell based on a petal-shaped preform, Ocean Engineering 250 (2022) 111057

[91] J. Zhang, C. Di, F. Wang, W. Tang, Buckling of segmented toroids under external pressure, Ocean Engineering 239 (2021) 109921

[92] J. Zhang, J. Tan, W. Tang, F. Wang, X. Zhao, Collapse performance of externally pressurized resin egg-shaped shell with corrosion thinning, International Journal of Pressure Vessels and Piping 177 (2019) 103993

[93] W. Tang, S. Zhang, J. Zhang, Z. Tang, Experimental study on the failure modes of circumferentially corrugated cylinders under external hydrostatic pressure, Thin-Walled Structures 156 (2020) 106988

[94] E. Labans, C. Bisagni, Buckling of 3D-printed cylindrical shells with corrugated surface, AIAA Scitech forum, 1 PartF, 2020

[95] S. Sharifi, S. Gohari, M. Sharifiteshnizi, Z. Vrcelj, Numerical and experimental study on mechanical strength of internally pressurized laminated woven composite shells incorporated with surface-bonded sensors, Composites Part B 94 (2016) 224-237

The publications reprints

Appendix A1. The Ritz method application for stress and deformation analyses of standard orthotropic pressure vessels

Full length article

The Ritz method application for stress and deformation analyses of standard orthotropic pressure vessels

Krzysztof Sowiński

Faculty of Mechanical Engineering, Institute of Applied Mechanics, Poznan University of Technology, ul. Jana Pawła II 24, 60-965 Poznan, Poland

ARTICLE INFO

ABSTRACT

Currently, the design of pressure vessels is based mainly on the simplified calculations described in the technical standards. Despite the numerous theories found in various valuable monographs and papers, the possibility of precise analytical solutions of static problems of shells including bending effects remains poor. The only alternative to such calculations is the finite element method. The presented paper focuses on the application of the Ritz method for the stress and deformation analyses of standard pressure vessels assuming orthotropic model of the material. The strain energy and the potential energy of external forces are derived for an arbitrary shell structure. Three different displacement functions are considered within the study. The results are compared to the solutions obtained with a use of the finite element method. The convergence of the results is obtained for wide range of the shell thickness. Additionally, the outcome of the study is referred to the design method of ellipsoidal and supposedly equivalent torispherical dished ends described in the technical standards, indicating significant ambiguities.

1. Introduction

Pressure vessels constitute a group of thin-walled structures composed of shells of revolution, widely used in numerous branches of the industry to storage and transport of gases and liquids. Most of the pressure vessels consist of cylindrical shell and two convex dished ends. There are three main shapes of the dished ends used to manufacture the pressure vessels, namely torispherical, ellipsoidal and hemispherical. Due to the required operational safety, their design is based on calculations provided in the coherent European and American standards. The formulae describing recommended thickness of the shell is based on the membrane theory — a significantly simplified shell theory, complemented by coefficients from experimental analyses. Although such calculations methods are not necessarily precise, they allow to design the structures that meet the required operational safety. Importantly the design approach described within the standards may result in obtaining the structures, which load-carrying capacity significantly exceeds the mandatory level. The overestimated thickness of the shell structures leads to an increased mass and cost of the manufacturing process. To obtain more satisfactory solutions, different approach for calculating the stress and deformation should be used.

One may distinguish two theories describing stress and deformation in the shell structures i.e. the membrane theory and the moment theory. The latter allows to study the bending effects caused by changes of principal radii of curvature of a structure. The exact solution of the governing differential equations of moment theory is currently not

possible to obtain for shells with variable radii of curvature. The theory of the edge effect constitutes a simplification of the moment theory, in which the bending effects result from the loads at the edges of a shell structure, assuming the applied pressure causes only membrane forces. The solutions based on the edge effect theory is correct merely for the shells of constant radii of curvature. An example of a shell structures for which the edge effect theory is valid are the pressure vessels with hemispherical dished ends. In case of the other dished ends such assumptions lead to the imprecise solution, where stress values can be overestimated or underestimated, depending on the shape of the dished end.

Currently the only available calculation method allowing for obtaining supposedly accurate solution in terms of stress and deformation is the finite element method. The accuracy of the finite element method results can be analysed only by comparing the results to the experimental data. Importantly finite element method allows to obtain the solution in the discrete form at each of the FE model nodes, often limiting the analysis of the internal forces and moments, especially for doubly-curved shell structures. In the presented paper the Ritz method is used to study the stress and deformation in the standard pressure vessels, where orthotropic material model is taken into consideration. The results are compared to the finite element method study outcome using ANSYS 19 software.

Mazurkiewicz and Nagórski [1] among others described profoundly the basis of the theory of elastic thin-walled isotropic and orthotropic
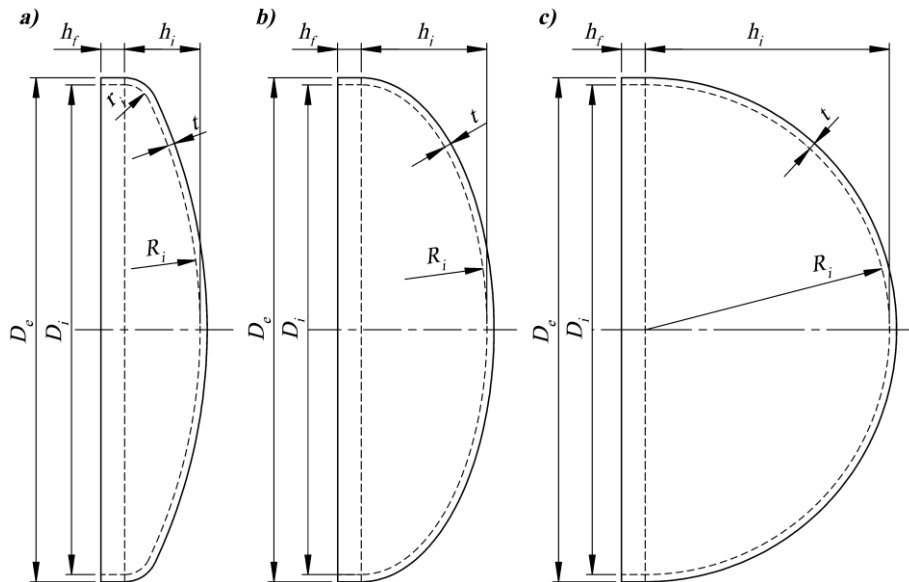

Fig. 1. Dished ends according to EN 13445; (a) - torispherical, (b) - ellipsoidal, (c) - hemispherical.
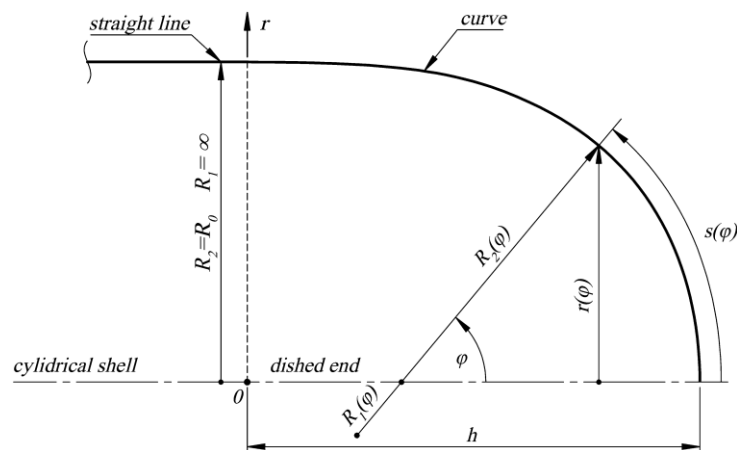

Fig. 2. General geometry of the cylindrical pressure vessel.

shell structures including static, dynamic and buckling problems. Ventsel and Krauthammer [2] formulated the theories of plates and shells concerning static and buckling problems with some examples of their application. Zingoni [3] explained the theories of membrane and bending phenomena of shell structures and applied them to multiple practical engineering cases.

The design of pressure vessels is performed strictly within standards [4–6], allowing to ensure safe operation of the structures. There are many papers dealing with the problems of cylindrical pressure vessels. Błachut and Magnucki [7] presented a review work of selected problems concerning strength, buckling and optimization of cylindrical pressure vessels. Magnucki et al. [8] performed an analysis of stress concentration factor minimization in cylindrical pressure vessels with ellipsoidal heads. Kisigolu et al. [9] studied design of propane cylinder end closures considering geometry, material thickness, strength and buckling.

Magnucki et al. [10] performed a comprehensive review of dished ends of the cylindrical pressure vessels. Magnucki and Lewiński [11] focused on finding a shape of the dished end with favourable stress

distribution. Sowiński and Magnucki [12] defined and studied non-standard dished heads of internally pressurized cylindrical pressure vessels with a view to diminish the edge effect. Zingoni et al. [13] analysed the problem of discontinuous multi-segmented spherical shells for high volume liquid containment. Zingoni [14] performed a research considering simplification of the derivation of influence coefficients in symmetric frusta by decomposing a system of arbitrary shell-edge actions into symmetric and anti-symmetric components.

The shape optimization of dished ends is of special significance in the field of pressure vessels analyses. Lewiński and Magnucki [15] proposed an approach for shaping the dished heads with a use of trigonometric series. Magnucki et al. [16] optimized the shape of dished head based on a curve composed of a circular arc and a fifth degree polynomial. Karużelecki and Proszowski [17] used a convex parametric Bézier polynomial as the geometry of dished end and optimized its shape.

The cylindrical pressure vessels are thin-walled structures, therefore structural stability has a great meaning in their analysis. The description of stability of cylindrical shells is presented in [1–3]. Jasion
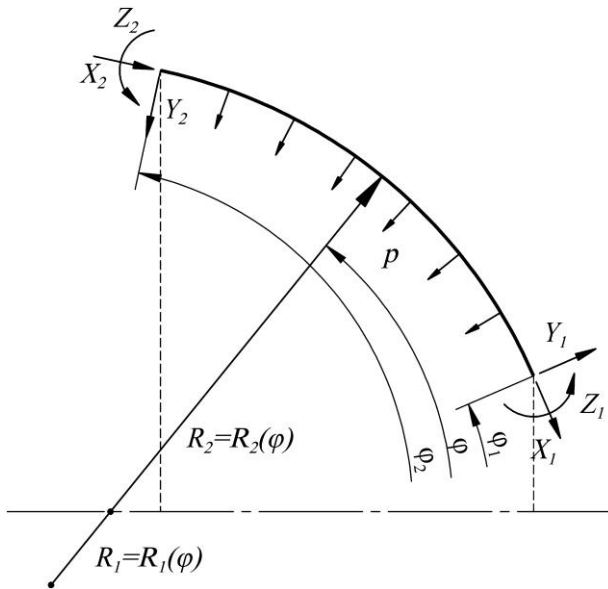
Fig. 3. Geometry description and loads of an arbitrary shell structure.

and Magnucki [18–22] studied multiple untypical shapes of pressure vessels including Cassini ovaloids, pseudospheres, clothoidal-spherical, barrelled shells and ellipsoidal heads with a central nozzle. Sowiński and Jasion [23] considered the pressure vessel with meridian based on Booth lemniscate of variable shape. Sowiński [24] researched the linear and nonlinear stability problems of corrugated cylindrical shells. Zhang et al. [25–27] analysed stability of pressure vessels based shapes found in the nature and Cassini ovals.

The importance of the Ritz method in the field of structural analysis is indisputable. Kumar [28] presented a wide review of the Ritz method to analyse vibration, static and buckling characteristics of beams, shells and plates. In the case of shell structures the Ritz method is rarely used to analyse stress and deformation. Shahgholian-Ghahfarokhi et al. [29] investigated torsional buckling analysis of functionally graded graphene-platelets reinforced composite porous cylindrical shells with a use of Ritz method. Qin et al. [30] presented a unified Fourier series solution to solve the vibration problem of functionally graded carbon nanotube-reinforcement composite cylindrical shells, conical shells and annular plates. Lopatin and Morozov [31] considered a problem of axisymmetric vibrations of composite orthotropic cylindrical shell with rigid weightless disks attacked to its ends. Qin et al. [32] provided a general approach for the free vibration analysis of rotating functionally graded carbon nanotube reinforced composite cylindrical shells. Pang et al. [33] used a semi analytical method to investigate the free vibration of doubly-curved shells of revolution with arbitrary boundary conditions. Senjanovic et al. [34] developed a finite strip method for vibration analysis of rotating toroidal shells subjected to internal pressure. Choe et al. [35] established an analysis model for dynamic analysis of composite laminated doubly-curved revolution shell on the higher order shear deformation theory.

The Ritz method has not been applied to the practical cases of the pressure vessels. The analytical solution for such problems can be imprecise, therefore the use of Ritz method may allow to obtain satisfactory results in the analyses of stress and deformations in the standard pressure vessels. Additionally, the semi-analytical formulation of the problem can include orthotropic properties of the material.

2. Geometry of standard dished ends

The standard dished ends according to EN 13445 [4] are ellipsoidal, torispherical and hemispherical (Fig. 1). The latter type is not considered within the paper as the accurate solution for those can be obtained in analytical approach with the use of the edge effect theory.

The shape of torispherical ends is based on two radii i.e. r_i – inside radius of curvature of a knuckle and R_i – inside spherical radius of the central part of the torispherical end. According to EN 13445 [4], ellipsoidal end shall be designed as nominally equivalent torispherical ends with

$$r_i = D_i \left(\frac{0.5}{K} - 0.08 \right), \tag{1}$$

and

$$R_i = D_i \left(0.44K + 0.02 \right), \tag{2}$$

where

$$K = \frac{D_i}{2h_i}, \tag{3}$$

D_i — internal diameter of the cylindrical shell, h_i — internal height of the head. According to the standard the parameter K is within the range

$$1.7 < K < 2.2. \tag{4}$$

The identical formulae for shaping the ellipsoidal end is presented in ASME Section VIII, Division 1, 2 [5,6]. Despite the fact, that obtained geometry of the equivalent ellipsoidal and torispherical shells can be considered visually similar, the stress distribution in the elastic range differs significantly for those. Such problem was recently studied and discussed by Seipp et al. [36], indicating the equivalency between torispherical and ellipsoidal ends is not supported by the finite element method analyses and the membrane theory. In this paper ellipsoidal dished end is assumed to be the one described by the true elliptical shape.

Within the framework of this study, the dished ends are defined with a reference to the geometry of their middle surfaces, which is preferable to perform further mathematical description. The general geometry of the cylindrical pressure vessel is presented in Fig. 2.

The relative depth of a dished end is defined as

$$\beta = \frac{h}{R_0}. \tag{5}$$

The parameter β is similar to the inverse of K (Eq. (3)). In the paper the case of $\beta = 0.5$ is analysed, as it is the most common value for the pressure vessels. The principal radii of curvature R_1, R_2 are related with parallel radius r in the following manner:

$$R_1 = \frac{dr}{d\varphi} \frac{1}{\cos\varphi}, \qquad R_2 = r \frac{1}{\sin\varphi}. \tag{6}$$

To perform the necessary calculations using the Ritz method, four separate shells have to be considered i.e. toroidal, spherical, ellipsoidal and cylindrical. The torispherical dished end consists of the toroidal and spherical shell. The principal radii of curvature of latter is following

$$R_{1s} = R_{2s} = R_0 \left[\frac{1}{1 - \cos\varphi_{s2}} \left(\beta - \frac{R_{1t}}{R_0 \cos\varphi_{s2}} \right) \right]. \tag{7}$$

The principal radii of curvature for the toroidal segment are described by the following formulae:

$$R_{1t} = R_0 \frac{\beta \cot\left(\frac{\varphi_{s2}}{2} \right) - 1}{\cot\left(\frac{\varphi_{s2}}{2} \right) - 1},$$

$$R_{2t} = R_0 \left\{ \frac{\beta \cot\left(\frac{\varphi_{s2}}{2} \right) - 1}{\cot\left(\frac{\varphi_{s2}}{2} \right) - 1} + \frac{1}{\sin\varphi} \left[1 - \frac{\beta \cot\left(\frac{\varphi_{s2}}{2} \right) - 1}{\cot\left(\frac{\varphi_{s2}}{2} \right) - 1} \right] \right\}. \tag{8}$$
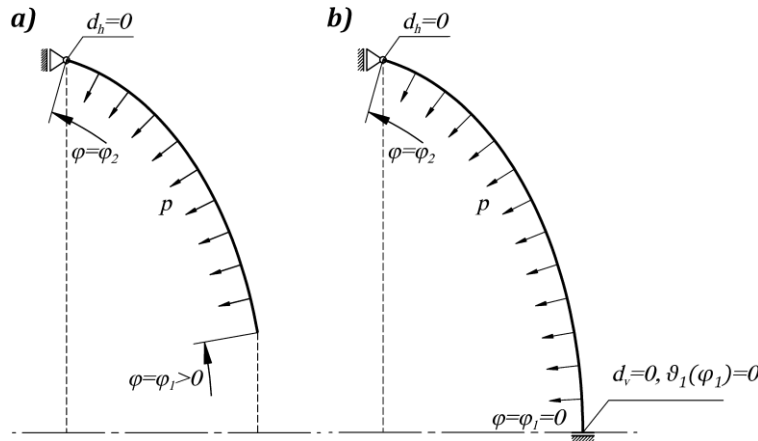
Fig. 4. Boundary conditions for (a) open apex shell, (b) closed apex shell.

In the case of ellipsoidal dished end the principal radii of curvature depend on the angle φ:

$$R_{1e} = R_0 \frac{\beta^2}{\sin^3 \varphi} (1 + \beta^2 \cot^2 \varphi)^{-\frac{3}{2}}, \quad R_{2e} = R_0 \frac{1}{\sin \varphi} (1 + \beta^2 \cot^2 \varphi)^{-\frac{1}{2}}. \quad (9)$$

Finally, the geometry of the cylindrical shell is described as follows:

$$R_{1c} \to \infty, \qquad R_{2c} = R_0. \quad (10)$$

Each of the shells is described by individual range of a parameter along which its geometry is defined. For the doubly curved shells, the parameter is meridional angle φ shown in Fig. 2. For the torispherical, spherical and ellipsoidal shell the parameter changes in the following ranges:

$$\varphi_{t1} \le \varphi \le \varphi_{t2}, \quad \varphi_{s1} \le \varphi \le \varphi_{s2}, \quad \varphi_{e1} \le \varphi \le \varphi_{e2}, \quad (11)$$

where:

$$\varphi_{s1} = \varphi_{e1} = 0, \qquad \varphi_{s2} = \varphi_{t2} = \varphi_{e2} = \frac{\pi}{2}. \quad (12)$$

The parameter $\varphi_{t1} = \varphi_{s2}$ has to be determined. Following the description in the standard [4] it is possible to estimate that

$$\varphi_{t1} = \varphi_{s2} \approx \frac{3}{20} \pi. \quad (13)$$

The geometry of the cylindrical shell is defined with a use of coordinate ξ, assuming:

$$\xi = \frac{x}{L}, \qquad 0 \le x \le L. \quad (14)$$

where L — length of the cylindrical shell. The coordinate ξ is within the following bounds

$$\xi_{c1} \le \xi \le \xi_{c2}. \quad (15)$$

3. General theory of shells

3.1. Axisymmetric orthotropic shells

The shell theory adopted in the paper is Kirchhoff–Love linear shell theory [1]. To apply the Ritz method, it is necessary to describe the theory with a use of displacements functions. Strains in the middle surface are defined as follows:

$$\varepsilon_1 = \frac{1}{R_1} \left(\frac{du}{d\varphi} - w \right), \qquad \varepsilon_2 = \frac{1}{R_2} (u \cot \varphi - w), \quad (16)$$

where: u, w — tangent and normal displacements. Vertical and horizontal displacements:

$$d_v = u \cos \varphi - w \sin \varphi, \qquad d_h = u \sin \varphi + w \cos \varphi. \quad (17)$$

The rotation of a line tangent to meridian

$$\vartheta_1 = \frac{1}{R_1} \left(\frac{dw}{d\varphi} + u \right). \quad (18)$$

The change in the curvatures

$$\chi_1 = -\frac{1}{R_1} \frac{d}{d\varphi} \left[\frac{1}{R_1} \left(u + \frac{dw}{d\varphi} \right) \right], \qquad \chi_2 = \frac{1}{R_1 R_2} \left(u - \frac{dw}{d\varphi} \right). \quad (19)$$

To analyse the stress beyond middle surface, one must define strains across the thickness t of a shell:

$$\varepsilon_{1z} = \frac{1}{1 - \frac{z}{R_1}} (\varepsilon_1 + z\chi_1), \qquad \varepsilon_{2z} = \frac{1}{1 - \frac{z}{R_2}} (\varepsilon_2 + z\chi_2), \quad (20)$$

where $-t/2 \le z \le t/2$. The internal forces in the form of forces and moments are following:

$$N_1 = C_1 (\varepsilon_1 + \nu_2 \varepsilon_2), \qquad N_2 = C_2 (\varepsilon_2 + \nu_1 \varepsilon_1), \quad (21)$$

$$M_1 = D_1 (\chi_1 + \nu_2 \chi_2), \qquad M_2 = D_2 (\chi_2 + \nu_1 \chi_1), \quad (22)$$

where:

$$C_1 = \frac{E_1 t}{1 - \nu_1 \nu_2}, \qquad C_2 = \frac{E_2 t}{1 - \nu_1 \nu_2}, \quad (23)$$

$$D_1 = \frac{E_1 t^3}{12(1 - \nu_1 \nu_2)}, \qquad D_2 = \frac{E_2 t^3}{12(1 - \nu_1 \nu_2)}, \quad (24)$$

in which: E_1, E_2 — Young's modulus, ν_1, ν_2 — Poisson's ratio. The principal stresses are defined as follows:

$$\sigma_1 = \frac{C_1}{t} (\varepsilon_1 + \nu_2 \varepsilon_2), \qquad \sigma_2 = \frac{C_2}{t} (\varepsilon_2 + \nu_1 \varepsilon_1). \quad (25)$$

Stress across the thickness of a shell:

$$\sigma_{1z} = \frac{C_1}{t} (\varepsilon_{1z} + \nu_2 \varepsilon_{2z}), \qquad \sigma_{2z} = \frac{C_2}{t} (\varepsilon_{2z} + \nu_1 \varepsilon_{1z}). \quad (26)$$

Strain energy is formulated in the following manner

$$U_\varepsilon = \pi \int_{\varphi_1}^{\varphi_2} (N_1 \varepsilon_1 + N_2 \varepsilon_2 + M_1 \chi_1 + M_2 \chi_2) r \frac{dr}{d\varphi} \frac{1}{\cos \varphi} d\varphi, \quad (27)$$

where: φ_1, φ_2 are the coordinates describing boundaries of a shell (Fig. 3).

3.2. Orthotropic cylindrical shells

In the case of cylindrical shells, most of the formulae from the previous section can be significantly simplified. Strains definition can be rewritten to the form:

$$\varepsilon_1 = \frac{1}{L} \frac{du}{d\xi}, \qquad \varepsilon_2 = -\frac{1}{R_0} w, \quad (28)$$

Importantly, the vertical and horizontal displacements are coherent with normal and tangent directions correspondingly. The changes in curvature are following:

$$\chi_1 = \frac{1}{L^2}\frac{d^2 w}{d\xi^2}, \qquad \chi_2 = 0, \tag{29}$$

therefore the strains across the thickness:

$$\varepsilon_{1z} = \varepsilon_1 + z\chi_1, \qquad \varepsilon_{2z} = \frac{1}{1-\frac{z}{R_0}}\varepsilon_2. \tag{30}$$

The internal forces and stresses are described as in the case of general axisymmetric shell theory. Strain energy of the cylindrical shell is formulated analogously to the doubly curved shells

$$U_\varepsilon = \pi L \int_{\xi_{c1}}^{\xi_{c2}} \left(N_1\varepsilon_1 + N_2\varepsilon_2 + M_1\chi_1 + M_2\chi_2\right) r\,d\xi. \tag{31}$$

4. The Ritz method application

4.1. Theoretical description

The Ritz method is described widely in the literature [1,2]. The method is based on minimization of the total potential energy of a system Π expressed as strain energy U_ε and potential energy of external forces W_p

$$\Pi = U_\varepsilon - W_p. \tag{32}$$

An arbitrary shell structure of revolution is determined by the meridional angle in the range $\varphi_1 \leq \varphi \leq \varphi_2$ (Fig. 3).

The structure is loaded on its edges with normal forces X_1, X_2, transverse loads Y_1, Y_2 and moments Z_1, Z_2, while uniform pressure p acts on the middle surface of the shell. To apply the Ritz method for such a problem, it is necessary to describe the strain energy and potential energy of the external forces as functions of unknown displacements functions. The latter is expressed as

$$W_p = 2\pi \left[\sum_{i=1}^{2} X_i r\left(\varphi_i\right) u(\varphi_i) + \sum_{i=1}^{2} Y_i r\left(\varphi_i\right) w(\varphi_i)\right.$$
$$\left. + \sum_{i=1}^{2} Z_i r\left(\varphi_i\right)\vartheta_1(\varphi_i) - p\int_{\varphi_1}^{\varphi_2} wr\frac{dr}{d\varphi}\frac{1}{\cos\varphi}d\varphi\right]. \tag{33}$$

In the paper the potential energy is derived using the function of parallel radius r instead principal radii of curvature R_1, R_2, which can be simply calculated from the second expression of Eq. (6). The components of strain energy expression (Eq. (27)) for an orthotropic shell are derived using Eqs. (6), (16), (19), (21), (22):

$$N_1\varepsilon_1 = C_1\left[-2\cos\varphi\, rw\frac{du}{d\varphi}\left(\frac{dr}{d\varphi}\right)^{-1} + \cos\varphi\, r\left(\frac{du}{d\varphi}\right)^2\left(\frac{dr}{d\varphi}\right)^{-1}\right.$$
$$+ \cos\varphi\, rw^2\left(\varphi\right)\left(\frac{dr}{d\varphi}\right)^{-1} + v_2(\cos\varphi\, u\frac{du}{d\varphi}$$
$$\left. - \sin\varphi\, w\frac{du}{d\varphi} - \cos\varphi\, uw + \sin\varphi\, w^2)\right]$$

$$N_2\varepsilon_2 = C_2\left\{\cos\varphi\, u^2 r^{-1}\frac{dr}{d\varphi} - 2\sin\varphi\, uwr^{-1}\frac{dr}{d\varphi} + \sin\varphi\,\tan\varphi w^2 r^{-1}\frac{dr}{d\varphi}\right.$$
$$\left. + v_1\left[\cos\varphi\, u\frac{du}{d\varphi} - \sin\varphi\, w\frac{du}{d\varphi} - \cos\varphi\, uw + \sin\varphi\, w^2\right]\right\}$$

$$M_1\chi_1 = D_1\left\{\cos\varphi\, r\sin^2\varphi u^2\left(\frac{dr}{d\varphi}\right)^{-3}\right.$$
$$-2\cos^2\varphi\sin\varphi\, ru\frac{du}{d\varphi}\left(\frac{dr}{d\varphi}\right)^{-3} + \cos^3\varphi r\left(\frac{du}{d\varphi}\right)^2\left(\frac{dr}{d\varphi}\right)^{-3}$$
$$+2\cos\varphi\,\sin^2\varphi ru\frac{dw}{d\varphi}\left(\frac{dr}{d\varphi}\right)^{-3} - 2\cos^2\varphi\sin\varphi\, r\frac{du}{d\varphi}\frac{dw}{d\varphi}\left(\frac{dr}{d\varphi}\right)^{-3}$$
$$+\cos\varphi\,\sin^2\varphi r\left(\frac{dw}{d\varphi}\right)^2\left(\frac{dr}{d\varphi}\right)^{-3}$$
$$+2\cos^2\varphi\sin\varphi\, ru^2\frac{d^2 r}{d\varphi^2}\left(\frac{dr}{d\varphi}\right)^{-4} - 2\cos^3\varphi ru\frac{du}{d\varphi}\frac{d^2 r}{d\varphi^2}\left(\frac{dr}{d\varphi}\right)^{-4}$$
$$+4\cos^2\varphi\sin\varphi\, ru\frac{dw}{d\varphi}\frac{d^2 r}{d\varphi^2}\left(\frac{dr}{d\varphi}\right)^{-4}$$
$$-2\cos^3\varphi r\frac{du}{d\varphi}\frac{dw}{d\varphi}\frac{d^2 r}{d\varphi^2}\left(\frac{dr}{d\varphi}\right)^{-4} + 2\cos^2\varphi\sin\varphi\, r\left(\frac{dw}{d\varphi}\right)^2\frac{d^2 r}{d\varphi^2}\left(\frac{dr}{d\varphi}\right)^{-4}$$
$$+\cos^3\varphi ru^2\left(\frac{d^2 r}{d\varphi^2}\right)^2\left(\frac{dr}{d\varphi}\right)^{-5}$$
$$+2\cos^3\varphi ru\frac{dw}{d\varphi}\left(\frac{d^2 r}{d\varphi^2}\right)^2\left(\frac{dr}{d\varphi}\right)^{-5} + \cos^3\varphi r\left(\frac{dw}{d\varphi}\right)^2\left(\frac{d^2 r}{d\varphi^2}\right)^2\left(\frac{dr}{d\varphi}\right)^{-5}$$
$$-2\cos^2\varphi\sin\varphi\, ru\frac{d^2 w}{d\varphi^2}\left(\frac{dr}{d\varphi}\right)^{-3}$$
$$+2\cos^3\varphi r\frac{du}{d\varphi}\frac{d^2 w}{d\varphi^2}\left(\frac{dr}{d\varphi}\right)^{-3} - 2\cos^2\varphi r\sin\varphi\frac{dw}{d\varphi}\frac{d^2 w}{d\varphi^2}\left(\frac{dr}{d\varphi}\right)^{-3}$$
$$-2\cos^3\varphi ru\frac{d^2 r}{d\varphi^2}\frac{d^2 w}{d\varphi^2}\left(\frac{dr}{d\varphi}\right)^{-4} - 2\cos^3\varphi r\frac{dw}{d\varphi}\frac{d^2 r}{d\varphi^2}\frac{d^2 w}{d\varphi^2}\left(\frac{dr}{d\varphi}\right)^{-4}$$
$$+\cos^3\varphi r\left(\frac{d^2 w}{d\varphi^2}\right)^2\left(\frac{dr}{d\varphi}\right)^{-3}$$
$$+v_2\left[-\cos^2\varphi\sin\varphi\, u^2\left(\frac{dr}{d\varphi}\right)^{-2} + \cos^3\varphi u\frac{du}{d\varphi}\left(\frac{dr}{d\varphi}\right)^{-2}\right.$$
$$-2\cos^2\varphi\sin\varphi\, u\frac{dw}{d\varphi}\left(\frac{dr}{d\varphi}\right)^{-2} + \cos^3\varphi\frac{du}{d\varphi}\frac{dw}{d\varphi}\left(\frac{dr}{d\varphi}\right)^{-2}$$
$$-\cos^2\varphi\sin\varphi\left(\frac{dw}{d\varphi}\right)^2\left(\frac{dr}{d\varphi}\right)^2 - \cos^3\varphi u^2\frac{d^2 r}{d\varphi^2}\left(\frac{dr}{d\varphi}\right)^{-3}$$
$$-2\cos^3\varphi u\frac{dw}{d\varphi}\frac{d^2 r}{d\varphi^2}\left(\frac{dr}{d\varphi}\right)^{-3}$$
$$-\cos^3\varphi\left(\frac{dw}{d\varphi}\right)^2\frac{d^2 r}{d\varphi^2}\left(\frac{dr}{d\varphi}\right)^{-3} + \cos^3\varphi u\frac{d^2 w}{d\varphi^2}\left(\frac{dr}{d\varphi}\right)^{-2}$$
$$\left.\left. +\cos^3\varphi\frac{dw}{d\varphi}\frac{d^2 w}{d\varphi^2}\left(\frac{dr}{d\varphi}\right)^{-2}\right]\right\}$$

$$\tag{34}$$

$$M_2\chi_2 = D_2\left\{\cos^3\varphi u^2 r^{-1}\left(\frac{dr}{d\varphi}\right)^{-1} + 2\cos^3\varphi u\frac{dw}{d\varphi}r^{-1}\left(\frac{dr}{d\varphi}\right)^{-1}\right.$$
$$+\cos^3\varphi\left(\frac{dw}{d\varphi}\right)^2 r^{-1}\left(\frac{dr}{d\varphi}\right)^{-1}$$
$$+v_1\left[-\cos^2\varphi\sin\varphi\, u^2\left(\frac{dr}{d\varphi}\right)^{-2} + \cos^3\varphi u\frac{du}{d\varphi}\left(\frac{dr}{d\varphi}\right)^{-2}\right.$$
$$-2\cos^2\varphi\sin\varphi\, u\frac{dw}{d\varphi}\left(\frac{dr}{d\varphi}\right)^{-2}$$
$$+\cos^3\varphi\frac{dw}{d\varphi}\frac{du}{d\varphi}\left(\frac{dr}{d\varphi}\right)^{-2} - \cos^2\varphi\sin\varphi\left(\frac{dw}{d\varphi}\right)^2\left(\frac{dr}{d\varphi}\right)^{-2}$$
$$-\cos^3\varphi u^2\frac{d^2 r}{d\varphi^2}\left(\frac{dr}{d\varphi}\right)^{-3}$$
$$-2\cos^3\varphi u\frac{dw}{d\varphi}\frac{d^2 r}{d\varphi^2}\left(\frac{dr}{d\varphi}\right)^{-3} - \cos^3\varphi\left(\frac{dw}{d\varphi}\right)^2\frac{d^2 r}{d\varphi^2}\left(\frac{dr}{d\varphi}\right)^{-3}$$
$$+\cos^3\varphi u\frac{d^2 w}{d\varphi^2}\left(\frac{dr}{d\varphi}\right)^{-2}$$
$$\left.\left. +\cos^3\varphi\frac{dw}{d\varphi}\frac{d^2 w}{d\varphi^2}\left(\frac{dr}{d\varphi}\right)^{-2}\right]\right\}$$

The analogous expressions are obtained for the cylindrical shell. Those can be further substituted into Eq. (31):

$$N_1 \varepsilon_1 = C_1 \left[\frac{R_o}{L} \left(\frac{du}{d\xi} \right)^2 + v_2 w \frac{du}{d\xi} \right], \quad N_2 \varepsilon_2 = C_2 \left[\frac{L}{R_o} w^2 + v_1 w \frac{du}{d\xi} \right],$$

$$M_1 \chi_1 = D_1 \frac{R_o}{L^3} \left(\frac{d^2 w}{d\xi^2} \right)^2, \qquad M_2 \chi_2 = 0.$$

(35)

Within the study three different displacement functions are considered, namely polynomial, trigonometric series and modified trigonometric series. Each function is represented by unknown parameters a_i or b_i. Polynomials are defined in Eq. (36):

$$u = \sum_{i=0}^{n_1} a_i \varphi^i, \qquad w = \sum_{i=0}^{n_1} b_i \varphi^i.$$

(36)

The trigonometric series are based on both sine and cosine functions in the following order:

$$u = a_0 + \sum_{i=1}^{n_2} \left[a_{2i-1} \sin \left(i \frac{\varphi - \varphi_1}{\varphi_2 - \varphi_1} \frac{\pi}{2} \right) + a_{2i} \cos \left(i \frac{\varphi - \varphi_1}{\varphi_2 - \varphi_1} \frac{\pi}{2} \right) \right],$$

$$w = b_0 + \sum_{i=1}^{n_2} \left[b_{2i-1} \sin \left(i \frac{\varphi - \varphi_1}{\varphi_2 - \varphi_1} \frac{\pi}{2} \right) + b_{2i} \cos \left(i \frac{\varphi - \varphi_1}{\varphi_2 - \varphi_1} \frac{\pi}{2} \right) \right].$$

(37)

The modified trigonometric series are formulated with a reference to the analytical solution of differential equations of the edge effect theory [1,2] and suited for the Ritz method application:

$$u = a_0 + \frac{\varphi_2 - \varphi}{\varphi_2 - \varphi_1} \sum_{i=1}^{n_3} e^{-\frac{1}{i} \frac{S}{t^2} (\varphi - \varphi_1)}$$

$$\times \left[a_{2i-1} \sin \left(\frac{1}{i} \frac{S}{t^3} \frac{\varphi - \varphi_1}{\varphi_2 - \varphi_1} \right) + a_{2i} \cos \left(\frac{1}{i} \frac{S}{t^3} \frac{\varphi - \varphi_1}{\varphi_2 - \varphi_1} \right) \right]$$

$$+ \frac{\varphi - \varphi_1}{\varphi_2 - \varphi_1} \sum_{i=1}^{n_4} e^{-\frac{1}{i} \frac{S}{t^2} (\varphi_2 - \varphi)}$$

$$\times \left[a_{2n_1+2i-1} \sin \left(\frac{1}{i} \frac{S}{t^3} \frac{\varphi_2 - \varphi}{\varphi_2 - \varphi_1} \right) + a_{2n_1+2i} \cos \left(\frac{1}{i} \frac{S}{t^3} \frac{\varphi_2 - \varphi}{\varphi_2 - \varphi_1} \right) \right],$$

$$w = b_0 + \frac{\varphi_2 - \varphi}{\varphi_2 - \varphi_1} \sum_{i=1}^{n_3} e^{-\frac{1}{i} \frac{S}{t^2} (\varphi - \varphi_1)}$$

$$\times \left[b_{2i-1} \sin \left(\frac{1}{i} \frac{S}{t^3} \frac{\varphi - \varphi_1}{\varphi_2 - \varphi_1} \right) + b_{2i} \cos \left(\frac{1}{i} \frac{S}{t^3} \frac{\varphi - \varphi_1}{\varphi_2 - \varphi_1} \right) \right]$$

$$+ \frac{\varphi - \varphi_1}{\varphi_2 - \varphi_1} \sum_{i=1}^{n_4} e^{-\frac{1}{i} \frac{S}{t^2} (\varphi_2 - \varphi)}$$

$$\times \left[b_{2n_1+2i-1} \sin \left(\frac{1}{i} \frac{S}{t^3} \frac{\varphi_2 - \varphi}{\varphi_2 - \varphi_1} \right) + b_{2n_1+2i} \cos \left(\frac{1}{i} \frac{S}{t^3} \frac{\varphi_2 - \varphi}{\varphi_2 - \varphi_1} \right) \right],$$

(38)

where S is the meridian length of a shell

$$S = \int_{\varphi_1}^{\varphi_2} R_1 d\varphi = \int_{\varphi_1}^{\varphi_2} \frac{dr}{d\varphi} \frac{1}{\cos \varphi} d\varphi.$$

(39)

It is important to note that the displacement functions described by Eq. (38) are not suitable for the shells with variable radii of curvature. The modified trigonometric series is designed to describe normal displacements characterized by the disturbances in the area of the shell edges that diminish relatively quickly along the shell meridian. Aside from those disturbances, the displacements remain constant which is true for the shells with constant radii of curvature.

The boundary conditions applied on the displacement functions vary, depending on whether the closed apex or open apex shell is considered (Fig. 4).

In the case of closed apex i.e. $\varphi_1 = 0$ following boundary conditions are assumed:

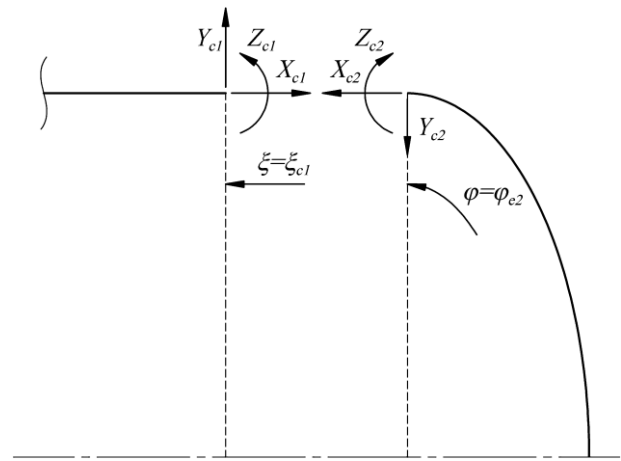$$d_v (\varphi_1) = 0, d_h (\varphi_2) = 0, \vartheta_1 (\varphi_1) = 0.$$

(40)

Fig. 5. Edge loads for the pressure vessel with ellipsoidal ends.

Table 1
Number of the unknown parameters in the displacement functions and number of the independent variables.

	P	TS	MTS
n_p	$2(n_1 + 1)$	$2(2n_2 + 1)$	$2(2n_3 + 2n_4 + 1)$
n (closed apex)	$2n_1 - 1$	$4n_2 - 1$	$4(n_3 + n_4) - 1$
n (open apex)	$2n_1 + 1$	$4n_2 + 1$	$4(n_3 + n_4) + 1$
n (cylindrical shell)	$2n_1$	$4n_2$	$4(n_3 + n_4)$

Considering an open apex shell i.e. $\varphi_1 > 0$ the boundary condition is imposed only on the horizontal displacements

$$d_h (\varphi_2) = 0.$$

(41)

For the symmetrical half of the cylindrical pressure vessel the boundary conditions are following:

$$d_h (\xi_{c2}) = 0, \qquad \vartheta_1 (\xi_{c2}) = 0.$$

(42)

The boundary conditions provided in Eqs. (40)–(42) consider separated shell structures. To achieve structural compatibility in the junctions of deformed pressure vessel additional boundary conditions have to be applied. The compatibility equations i.e. boundary conditions for the junction of the ellipsoidal and cylindrical shell (Fig. 5) have the form:

$$d_v (\varphi_{e2}) = d_v (\xi_{c2}), \qquad \vartheta_1 (\varphi_{e2}) = \vartheta_1 (\xi_{c2}).$$

(43)

For the pressure vessel with torispherical dished ends (Fig. 6) three shells constituting two junctions have to be considered, therefore:

$$d_v (\varphi_{s2}) = d_v (\varphi_{t1}), \qquad \vartheta_1 (\varphi_{s2}) = \vartheta_1 (\varphi_{t1}),$$
$$d_v (\varphi_{t2}) = d_v (\xi_{c2}), \qquad \vartheta_1 (\varphi_{t2}) = \vartheta_1 (\xi_{c2}).$$

(44)

After applying the boundary conditions described in Eqs. (40)–(42) to the displacement functions it is possible to formulate the total potential energy as a function of the remaining a_i and b_i parameters. Importantly, one must consider the number of parameters a_i and b_i in the displacement functions hereinafter denoted n_p, as well as number of independent variables n in the total potential energy expression. Those are presented in Table 1, where: P — polynomials, TS — trigonometric series, MTS — modified trigonometric series.

The independent variables are defined in a form of the vector c (Eq. (45)). The form of c varies depending on the applied boundary conditions

$$c = \{ a_0, a_1, \dots, b_0, b_1, \dots \}^T.$$

(45)

After integrating the functions in Eq. (34) or Eq. (35) to obtain total potential energy it is further differentiated with respect to each of the
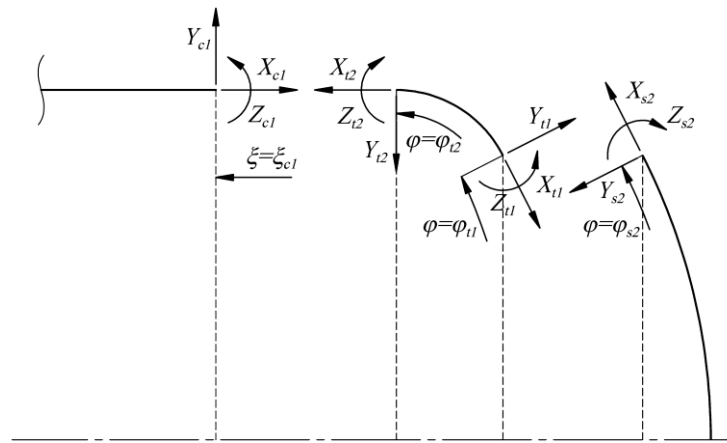
Fig. 6. Edge loads for the pressure vessel with torispherical ends.

Table 2
Solution for the ellipsoidal shell resulting from the unit edge loads.

	$c_e^{(X2)}$	$c_e^{(Y2)}$	$c_e^{(Z2)}$	$c_e^{(p)}$
a_2	0	-1.213×10^{-3}	-6.858×10^{-6}	7.908×10^{-2}
a_3	0	-3.116×10^{-4}	-4.574×10^{-5}	-1.179
a_4	0	4.922×10^{-3}	1.113×10^{-4}	1.029
a_5	0	-4.803×10^{-3}	-6.992×10^{-5}	-3.883×10^{-1}
a_6	0	1.164×10^{-3}	1.181×10^{-5}	5.632×10^{-2}
b_0	0	1.646×10^{-3}	5.884×10^{-6}	1.105
b_2	0	-1.412×10^{-2}	-2.235×10^{-4}	-5.898
b_3	0	4.761×10^{-2}	6.224×10^{-4}	9.064
b_4	0	-5.281×10^{-2}	-5.289×10^{-4}	-6.280
b_5	0	2.155×10^{-2}	1.605×10^{-4}	2.151
b_6	0	-2.860×10^{-3}	-1.704×10^{-5}	-2.954×10^{-1}

Table 3
Solution for the cylindrical shell resulting from the unit edge loads.

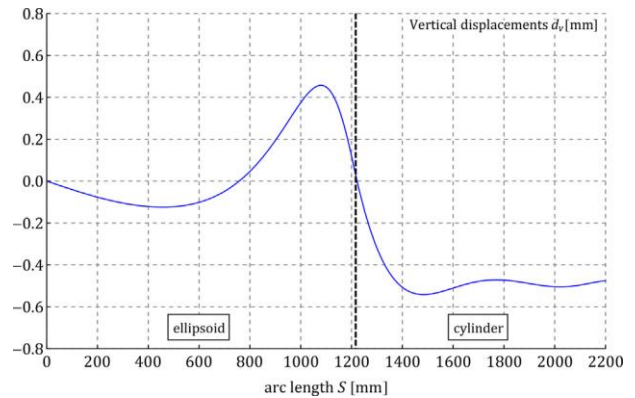|	$c_c^{(X1)}$	$c_c^{(Y1)}$	$c_c^{(Z1)}$	$c_c^{(p)}$
a_1	3.333×10^{-4}	-2.013×10^{-3}	1.960×10^{-5}	1.000×10^{-1}
a_2	0	1.159×10^{-2}	-1.825×10^{-4}	0
a_3	0	-2.944×10^{-2}	6.312×10^{-4}	0
a_4	0	3.711×10^{-2}	-1.028×10^{-3}	0
a_5	0	-2.273×10^{-2}	7.971×10^{-4}	0
a_6	0	5.375×10^{-3}	-2.373×10^{-4}	0
b_0	1.00×10^{-4}	-6.599×10^{-3}	7.264×10^{-5}	3.333×10^{-1}
b_2	0	-2.481×10^{-1}	9.386×10^{-3}	0
b_3	0	3.096×10^{-1}	-2.600×10^{-2}	0
b_4	0	-3.147×10^{-2}	3.634×10^{-2}	0
b_5	0	-1.981×10^{-1}	-2.503×10^{-2}	0
b_6	0	1.019×10^{-1}	6.762×10^{-3}	0

Fig. 7. Vertical displacements for the pressure vessel with ellipsoidal end for t = 15 mm.

Fig. 8. Meridional stress for the pressure vessel with ellipsoidal end for t = 15 mm.

independent variables in the vector c to find the minimum of it

$$\frac{d\Pi}{dc_i} = \frac{d}{d c_i}(U_\varepsilon - W_p) = 0, \qquad (46)$$

where c_i are the components of the vector c (Eq. (45)) for $i = 1, 2, \ldots, n$. The problem is then rewritten to the system of equations considering all of the derivatives in Eq. (47)

$$U c - W f = 0, \qquad (47)$$

where: U — strain energy matrix, W — energy of external forces matrix , f — force vector

$$f = \left\{ X_1, Y_1, Z_1, X_2, Y_2, Z_2, p \right\}^T . \qquad (48)$$

The solution of the problem is obtained in the following form

$$c = U^{-1} W f . \qquad (49)$$
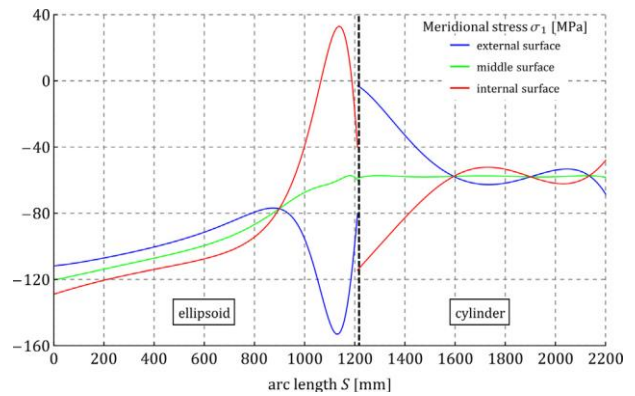
The above approach for obtaining displacement functions assumes that the edge loads contained in f (Eq. (48)) are known. The aim of this study is to take into consideration complex shell structures, i.e.: the structures that consist of more than one shell described by continuous principal radii of curvature. To analyse the interaction between connected shells it is necessary to formulate the compatibility equations based on Eqs. (43), (44). The edge loads for the pressure vessel with ellipsoidal dished ends are presented in Fig. 5.
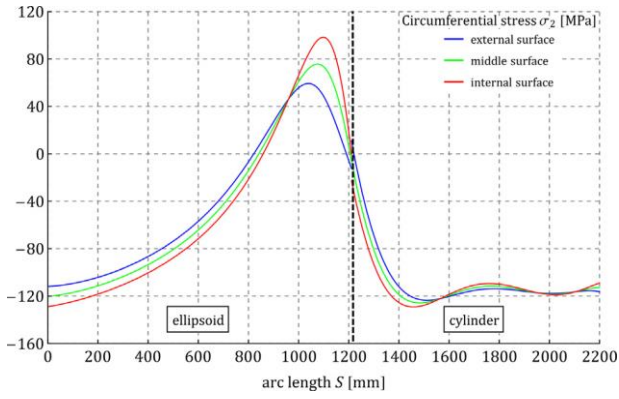
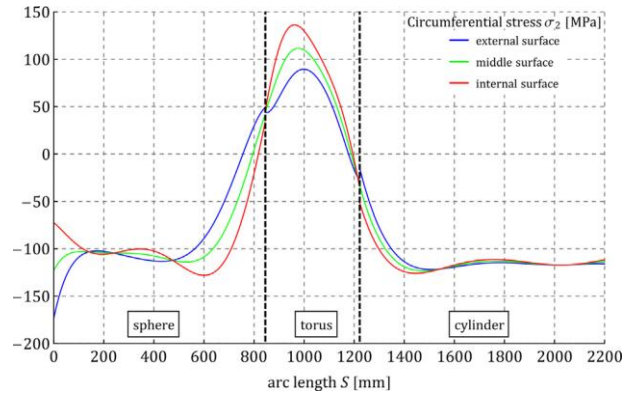**Fig. 9.** Circumferential stress for the pressure vessel with ellipsoidal end for t = 15 mm.
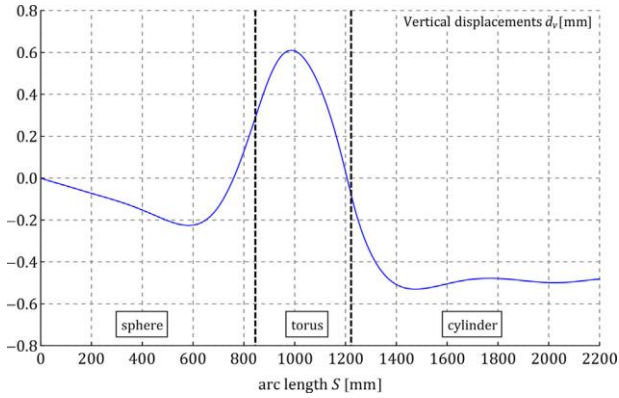

Fig. 10. The vertical displacements for the pressure vessel with torispherical ends for t = 15 mm.

Fig. 11. The meridional stress for the pressure vessel with torispherical ends for t = 15 mm.
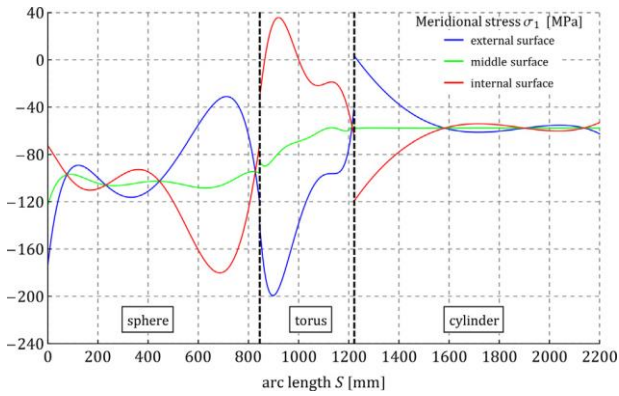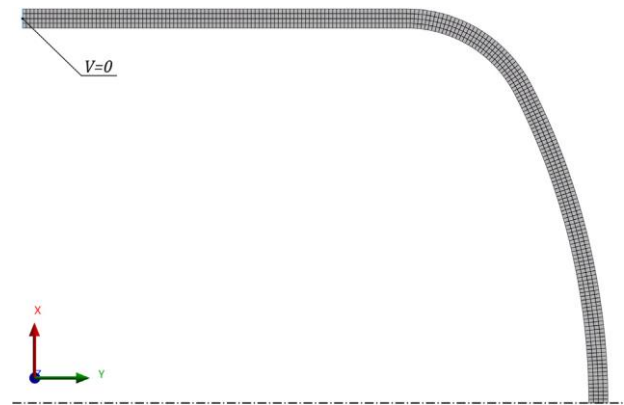

Fig. 12. The circumferential stress for the pressure vessel with torispherical ends for t = 15 mm.

Fig. 13. Exemplary FE model of the pressure vessel with torispherical dished ends.

Table 4
Solution for the ellipsoidal shell.

	c_e
a_2	2.493×10^{-1}
a_3	-1.989
a_4	1.280
a_5	-2.038×10^{-1}
a_6	-1.316×10^{-2}
b_0	1.764
b_2	-8.827
b_3	1.109×10^{1}
b_4	-5.858
b_5	1.708
b_6	-2.463×10^{-1}

The compatibility equations are following:

$$\delta_{c1}^{(X1)} X_{c1} + \delta_{c1}^{(Y1)} Y_{c1} + \delta_{c1}^{(Z1)} Z_{c1} + \delta_{c1}^{(p)} p = \delta_{e2}^{(X2)} X_{e2}$$
$$+ \delta_{e2}^{(Y2)} Y_{e2} + \delta_{e2}^{(Z2)} Z_{e2} + \delta_{e2}^{(p)} p,$$
$$\vartheta_{c1}^{(X1)} X_{c1} + \vartheta_{c1}^{(Y1)} Y_{c1} + \vartheta_{c1}^{(Z1)} Z_{c1} + \vartheta_{c1}^{(p)} p = \vartheta_{e2}^{(X2)} X_{e2} + \vartheta_{e2}^{(Y2)} Y_{e2}$$
$$+ \vartheta_{e2}^{(Z2)} Z_{e2} + \vartheta_{e2}^{(p)} p.$$

$$(50)$$

The above formulae defines that in the deformed structure, displacements as well as rotations on the shells edges must be equal. Coefficients δ and ϑ refer to the vertical displacement (Eq. (17)) and rotations (Eq. (18)) at the shell edge, caused by one of the unit loads X, Y, Z. The edge loads are normal X and transverse Y, while Z is the moment (Fig. 5). Each of the components in the compatibility equations is related to a certain shell structure, where: e — ellipsoidal shell, c — cylindrical shell. For example $\delta_{e2}^{(X2)}$ is a vertical displacement component on the second edge ($\varphi = \varphi_2 = \varphi_{e2}$) of the ellipsoidal shell caused by the normal force $X_2 = 1$.

Obtaining each of the displacement δ and rotation ϑ components requires solving Eq. (49) for a specific edge load contained in the vector f (Eq. (48)). In the case of $\delta_{e2}^{(X2)}$ and $\vartheta_{e2}^{(X2)}$ the only non-zero

Table 5
Solution for the cylindrical shell.

	c_c
a_1	-2.844×10^{-1}
a_2	9.338×10^{-1}
a_3	-2.277
a_4	2.74
a_5	-1.584
a_6	3.471×10^{-1}
b_0	-5.845×10^{-2}
b_2	-1.691×10^{1}
b_3	1.306×10^{1}
b_4	1.762×10^{1}
b_5	-3.179×10^{1}
b_6	1.291×10^{1}

Table 6
Solution for the spherical shell load with the unit edge loads.

	$c_s^{(X2)}$	$c_s^{(Y2)}$	$c_s^{(Z2)}$	$c_s^{(p)}$
a_1	-5.592×10^{-3}	2.849×10^{-3}	1.094×10^{-4}	4.675
a_2	-2.195×10^{-2}	1.119×10^{-2}	1.860×10^{-4}	1.966×10^{1}
a_3	2.030×10^{-1}	-1.034×10^{-1}	-1.140×10^{-3}	-1.818×10^{2}
a_4	-8.037×10^{-1}	4.095×10^{-1}	7.443×10^{-4}	7.199×10^{2}
a_5	1.342	-6.837×10^{-1}	9.364×10^{-3}	-1.202×10^{3}
a_6	-7.202×10^{-1}	3.669×10^{-1}	-1.589×10^{-2}	6.450×10^{2}
b_0	-6.141×10^{-3}	-3.129×10^{-3}	-1.128×10^{-4}	5.541
b_2	-1.817×10^{-1}	9.260×10^{-2}	3.329×10^{-3}	1.629×10^{2}
b_3	2.614	-1.332	-4.555×10^{-2}	-2.342×10^{3}
b_4	-1.380×10^{1}	7.031	2.133×10^{-1}	1.236×10^{4}
b_5	3.010×10^{1}	-1.534×10^{1}	-3.758×10^{-1}	-2.696×10^{4}
b_6	-2.236×10^{1}	1.139×10^{1}	1.919×10^{-1}	2.003×10^{4}

component is $X_2 = 1$

$$f^{(X2)} = \{0,0,0,1,0,0,0\}^T . \tag{51}$$

The unknown parameters in the displacement functions are obtained with a use of Eq. (49), which example is as follows

$$c_e^{(X2)} = U_e^{-1} W_e f^{(X2)}. \tag{52}$$

Vertical displacements and rotations are further considered as functions of the parameters c and the meridional angle φ:

$$d_v = d_v(c, \varphi), \qquad \vartheta_1 = \vartheta_1(c, \varphi). \tag{53}$$

The coefficients in the compatibility equations are calculated for the selected edge of the shell, for example:

$$\delta_{e2}^{(X2)} = d_v\left(c_e^{(X2)}, \varphi_{e2}\right), \qquad \vartheta_{e2}^{(X2)} = \vartheta_1\left(c_e^{(X2)}, \varphi_{e2}\right). \tag{54}$$

The expressions in Eq. (50) contain six unknown edge loads: X_{1c}, Y_{1c}, Z_{1c}, X_{2e}, Y_{2e}, Z_{2e}. The number of unknowns can be reduced assuming:

$$X_{c1} = -X_{e2}, \quad Y_{c1} = -Y_{e2}, \quad Z_{c1} = -Z_{e2}. \tag{55}$$

To further reduce the number of the unknown forces to two, the edge loads X, Y are expressed with their horizontal H and vertical V load components:

$$\begin{aligned} X_{c1} = -H_{c1}, \qquad Y_{c1} = V_{c1}, \\ X_{e2} = -V_{e2}\cos\varphi_{e2} - H_{e2}\sin\varphi_{e2}, \qquad Y_{e2} = V_{e2}\sin\varphi_{e2} - H_{e2}\cos\varphi_{e2}. \end{aligned} \tag{56}$$

Similarly to Eq. (55), following condition occurs:

$$H_{c1} = -H_{e2}, \qquad V_{c1} = -V_{e2}. \tag{57}$$

Horizontal force H_{e2} is known from the equilibrium equation

$$H_{e2} = -\frac{1}{2} r_e\left(\varphi_{e2}\right) p. \tag{58}$$

Substituting Eq. (57) to Eq. (56) using Eqs. (55), (58) allows to express the compatibility equations (Eq. (50)) with one of the vertical forces V and edge moments Z, therefore it is possible to calculate the edge

loads X_{1c}, Y_{1c}, Z_{1c}, X_{2e}, Y_{2e}, Z_{2e}. The unknown parameters c in the displacement functions can be then obtained for both of the shells:

$$f_c = \{X_{c1}, Y_{c1}, Z_{c1}, 0, 0, 0, p\}^T , \tag{59}$$

$$c_c = U_c^{-1} W_c f_c, \tag{60}$$

$$f_e = \{0, 0, 0, X_{e2}, Y_{e2}, Z_{e2}, p\}^T , \tag{61}$$

$$c_e = U_e^{-1} W_e f_e. \tag{62}$$

Torispherical dished end, unlike ellipsoidal, is characterized by the discontinuous radii of curvature along its meridian. Such fact implies that spherical and toroidal shells have to be considered separately. The edge loads for the pressure vessel with torispherical ends are presented in Fig. 6.

The compatibility equations must include both junctions simultaneously, namely spherical to toroidal and toroidal to cylindrical. Such approach implies the both edges of the toroidal shell are interacting with each other i.e. loads at the first edge cause displacement and rotation on the second edge and vice versa. Therefore, in the following equations, displacements and rotations on both of the edges of the toroidal shell contain all of the forces, namely X_{1t}, Y_{1t}, Z_{1t}, X_{2t}, Y_{2t}, Z_{2t}:

$$\begin{aligned} \delta_{c1}^{(X1)} X_{c1} &+ \delta_{c1}^{(Y1)} Y_{c1} + \delta_{c1}^{(Z1)} Z_{c1} + \delta_{c1}^{(p)} p \\ = \delta_{t2}^{(X2)} X_{t2} &+ \delta_{t2}^{(Y2)} Y_{t2} + \delta_{t2}^{(Z2)} Z_{t2} + \delta_{t2}^{(p)} p + \delta_{t2}^{(X1)} X_{t1} \\ &+ \delta_{t2}^{(Y1)} Y_{t1} + \delta_{t2}^{(Z1)} Z_{t1}, \\ \delta_{t1}^{(X1)} X_{t1} &+ \delta_{t1}^{(Y1)} Y_{t1} + \delta_{t1}^{(Z1)} Z_{t1} + \delta_{t1}^{(p)} p + \delta_{t1}^{(X2)} X_{t2} \\ &+ \delta_{t1}^{(Y2)} Y_{t2} + \delta_{t1}^{(Z2)} Z_{t2} \\ = \delta_{s2}^{(X2)} X_{s2} &+ \delta_{2s}^{(Y2)} Y_{s2} + \delta_{s2}^{(Z2)} Z_{2s} + \delta_{s2}^{(p)} p, \\ \vartheta_{c1}^{(X1)} X_{c1} &+ \vartheta_{c1}^{(Y1)} Y_{c1} + \vartheta_{c1}^{(Z1)} Z_{c1} + \vartheta_{c1}^{(p)} p \\ = \vartheta_{t2}^{(X2)} X_{t2} &+ \vartheta_{t2}^{(Y2)} Y_{t2} + \vartheta_{t2}^{(Z2)} Z_{t2} + \vartheta_{t2}^{(p)} p + \vartheta_{t2}^{(X1)} X_{t1} \\ &+ \vartheta_{t2}^{(Y1)} Y_{t1} + \vartheta_{t2}^{(Z1)} Z_{t1}, \\ \vartheta_{t1}^{(X1)} X_{t1} &+ \vartheta_{t1}^{(Y1)} Y_{t1} + \vartheta_{t1}^{(Z1)} Z_{t1} + \vartheta_{t1}^{(p)} p + \vartheta_{t1}^{(X2)} X_{t2} \\ &+ \vartheta_{t1}^{(Y2)} Y_{t2} + \vartheta_{t1}^{(Z2)} Z_{t2} \\ = \vartheta_{s2}^{(X2)} X_{s2} &+ \vartheta_{s2}^{(Y2)} Y_{s2} + \vartheta_{s2}^{(Z2)} Z_{s2} + \vartheta_{s2}^{(p)} p. \end{aligned} \tag{63}$$

Displacements and rotations components δ, ϑ caused by the unit forces are obtained in the same manner as in case of the pressure vessel with ellipsoidal ends (Eq. (52)). The conditions of the edge loads equality are assumed:

$$\begin{aligned} X_{t1} = -X_{s2}, \ Y_{t1} = -Y_{s2}, \ Z_{t1} = -Z_{s2}, \ X_{c1} = -X_{t2}, \ Y_{c1} = -Y_{t2}, \\ Z_{c1} = -Z_{t2}. \end{aligned} \tag{64}$$

The edge loads are expressed by their horizontal and vertical components H and V:

$$\begin{aligned} X_{c1} = -H_{c1}, \qquad Y_{c1} = V_{c1}, \\ X_{t2} = -V_{t2}\cos\varphi_{t2} - H_{t2}\sin\varphi_{t2}, \qquad Y_{t2} = V_{t2}\sin\varphi_{t2} - H_{t2}\cos\varphi_{t2}, \\ X_{t1} = -V_{t1}\cos\varphi_{t1} - H_{t1}\sin\varphi_{t1}, \qquad Y_{t1} = V_{t1}\sin\varphi_{t1} - H_{t1}\cos\varphi_{t1}, \\ X_{s2} = -V_{s2}\cos\varphi_{s2} - H_{s2}\sin\varphi_{s2}, \qquad Y_{s2} = V_{s2}\sin\varphi_{s2} - H_{s2}\cos\varphi_{s2}. \end{aligned} \tag{65}$$

The horizontal and vertical load components must be equal at each juncture:

$$H_{c1} = -H_{t2}, \quad V_{c1} = -V_{t2}, \quad H_{t1} = -H_{s2}, \quad V_{t1} = -V_{s2}. \tag{66}$$

Forces H_{t2} and H_{s2} are known from the equilibrium conditions:

$$H_{t2} = -\frac{1}{2} r_t\left(\varphi_{t2}\right) p, \qquad H_{s2} = -\frac{1}{2} r_s\left(\varphi_{s2}\right) p. \tag{67}$$

Substituting Eqs. (64)–(67) to the compatibility equations (Eq. (63)) one obtains a system of four equations with two unknown vertical forces V and two unknown moments Z. The system can be easily

Table 7
Solution for the toroidal shell resulting from the unit edge loads.

	$c_t^{(X1)}$	$c_t^{(Y1)}$	$c_t^{(Z1)}$	$c_t^{(X2)}$	$c_t^{(Y2)}$	$c_t^{(Z2)}$	$c_t^{(p)}$
a_1	1.217×10^{-3}	-2.046×10^{-2}	7.682×10^{-4}	0	-1.230×10^{-2}	-1.300×10^{-4}	3.787×10^{-1}
a_2	1.684×10^{-3}	-2.108×10^{-2}	-1.124×10^{-3}	0	3.999×10^{-2}	3.038×10^{-4}	5.344×10^{-1}
a_3	-3.617×10^{-3}	8.067×10^{-2}	7.055×10^{-4}	0	-6.210×10^{-2}	-3.858×10^{-4}	-1.137
a_4	2.646×10^{-3}	-7.682×10^{-2}	-1.354×10^{-4}	0	5.289×10^{-2}	2.633×10^{-4}	8.283×10^{-1}
a_5	-8.682×10^{-4}	3.183×10^{-2}	-4.089×10^{-5}	0	-2.279×10^{-2}	-7.319×10^{-5}	-2.708×10^{-1}
a_6	1.061×10^{-4}	-5.008×10^{-3}	1.553×10^{-5}	0	3.703×10^{-3}	1.671×10^{-6}	3.295×10^{-2}
b_0	1.257×10^{-3}	-3.556×10^{-3}	5.508×10^{-4}	0	5.362×10^{-3}	5.330×10^{-5}	4.299×10^{-1}
b_1	4.259×10^{-4}	-1.433×10^{-1}	-9.688×10^{-4}	0	-3.986×10^{-2}	-6.252×10^{-4}	1.148×10^{-1}
b_2	-1.447×10^{-3}	5.075×10^{-1}	-1.115×10^{-3}	0	1.405×10^{-1}	2.193×10^{-3}	-4.121×10^{-1}
b_3	-2.888×10^{-3}	-6.847×10^{-1}	3.877×10^{-3}	0	-2.478×10^{-1}	-3.658×10^{-3}	-9.686×10^{-1}
b_4	5.911×10^{-3}	4.568×10^{-1}	-3.592×10^{-3}	0	-1.168×10^{-1}	3.250×10^{-3}	1.902
b_5	-3.410×10^{-3}	-1.521×10^{-1}	1.457×10^{-3}	0	-1.168×10^{-1}	-1.434×10^{-3}	-1.087
b_6	6.526×10^{-4}	2.025×10^{-2}	-2.242×10^{-4}	0	2.237×10^{-2}	2.362×10^{-4}	2.073×10^{-1}

Table 8
Solution for the spherical shell.

	c_s
a_2	4.831
a_3	-4.560×10^1
a_4	1.875×10^2
a_5	-3.317×10^2
a_6	1.971×10^2
b_0	1.3154
b_2	3.714×10^1
b_3	-5.342×10^2
b_4	2.867×10^3
b_5	-6.413×10^3
b_6	4.917×10^3
b_5	2.602×10^1
b_6	-4.061

Table 9
Solution for the toroidal shell.

	c_t
a_1	2.955
a_2	-3.560
a_3	2.118×10^{-2}
a_4	1.893
a_5	-1.073
a_6	1.984×10^{-1}
b_0	4.337×10^{-2}
b_1	1.360×10^1
b_2	-5.622×10^1
b_3	8.710×10^1
b_4	-6.701×10^1
b_6	2.982

solved, which enables to define the edge loads: X_{1c}, Y_{1c}, Z_{1c}, X_{1t}, Y_{1t}, Z_{1t}, X_{2t}, Y_{2t}, Z_{2t}, X_{2s}, Y_{2s}, Z_{2s}. Using Eq. (49) the unknown parameters in the displacement functions are calculated:

$$f_c = \left\{ X_{c1}, Y_{c1}, Z_{c1}, 0, 0, 0, p \right\}^T, \tag{68}$$

$$c_c = U_c{}^{-1} W_c f_c, \tag{69}$$

$$f_t = \left\{ X_{t1}, Y_{t1}, Z_{t1}, X_{t2}, Y_{t2}, p \right\}^T, \tag{70}$$

$$c_t = U_t{}^{-1} W_t f_t, \tag{71}$$

$$f_s = \left\{ 0, 0, 0, X_{s2}, Y_{s2}, Z_{s2}, p \right\}^T, \tag{72}$$

$$c_s = U_s{}^{-1} W_s f_s. \tag{73}$$

4.2. Geometric parameters and mechanical properties of the studied shells

To perform further calculations, it is necessary to assume numerical values of geometric parameters of the studied pressure vessels as well as mechanical properties of the material. Following values of the geometric parameters are considered:

$$R_0 = 1000 \text{ mm}, \qquad L = 1000 \text{ mm}, \qquad \beta = 0.5.$$

The value of R_0 corresponds to the typical liquid petroleum gas pressure vessel. The thickness of such shell structures is usually within the range of 7 mm to 10 mm, however to generalize the problem, the following values are assumed

$$t = 5, 15, 30 \text{ mm}.$$

Following the authors of [1], the orthotropy coefficient is introduced

$$\alpha = \frac{E_2}{E_1} = \frac{\nu_2}{\nu_1}.$$

Mechanical properties of the material are related to the standard structural steel:

$$E_1 = 2 \times 10^5 \text{ MPa}, \qquad \nu_1 = 0.3.$$

The applied pressure is proportional to the thickness of the shells. Its magnitude causes equivalent von Mises stress of 100 MPa in the cylindrical shell in the membrane state

$$p = \frac{200\sqrt{3}}{3} \frac{t}{R_0}.$$

4.3. Solution for the pressure vessel with ellipsoidal dished ends

In the further presentation both displacement functions are considered in a form of six degree polynomial (Eq. (36)), therefore $n_1 = 6$. According to Table 1 the number of unknown parameters in displacement functions is $n = 11$. The exemplary analysis is performed for the thickness $t = 15$ mm and isotropic material i.e. $\alpha = 1$. For the ellipsoidal shell the boundary conditions (Eq. (40)) lead to the following expressions:

$$a_0 = 0, \quad a_1 = -\pi \left(\frac{1}{2} a_2 + \frac{1}{4} \pi a_3 + \frac{1}{8} \pi^2 a_4 + \frac{1}{16} \pi^3 a_5 + \frac{1}{32} \pi^4 a_6 \right), \quad b_1 = 0.$$

The obtained, normalized strain matrix has the form which is given as Eq. (74) in Box I.

The first three columns of the energy of external forces matrix are equal to zero (Eq. (75)) due to form of the force vector f_e (Eq. (61)), where $X_{e1} = Y_{e1} = Z_{e1} = 0$. The fourth column equals to zero as the horizontal displacements are restrained at the second edge $\varphi = \varphi_{e2} = \pi/2$, therefore the presence of the normal load X_{e2} has no effect on the

U_e

$$
=
\begin{bmatrix}
0.05902 & 0.1554 & 0.3141 & 0.5747 & 1 & -0.03586 & -0.08420 & -0.1184 & -0.1666 & -0.2356 & -0.3355 \\
0.05346 & 0.1461 & 0.3033 & 0.5659 & 1 & -0.02999 & -0.07605 & -0.1097 & -0.1573 & -0.2259 & -0.3257 \\
0.04968 & 0.1394 & 0.2951 & 0.5591 & 1 & -0.02628 & -0.07061 & -0.1038 & -0.1512 & -0.2198 & -0.3200 \\
0.04692 & 0.1343 & 0.2887 & 0.5535 & 1 & -0.02373 & -0.06671 & -0.09962 & -0.1468 & -0.2156 & -0.3166 \\
0.04483 & 0.1303 & 0.2835 & 0.5490 & 1 & -0.02188 & -0.06377 & -0.09642 & -0.1436 & -0.2126 & -0.3143 \\
-0.07346 & -0.1786 & -0.3404 & -0.5954 & -1 & 0.1692 & 0.2147 & 0.2701 & 0.3531 & 0.4742 & 0.6498 \\
-0.05919 & -0.1554 & -0.3139 & -0.5743 & -1 & 0.07367 & 0.1213 & 0.1630 & 0.2237 & 0.3118 & 0.4401 \\
-0.05505 & -0.1483 & -0.3053 & -0.5672 & -1 & 0.06130 & 0.1078 & 0.1481 & 0.2067 & 0.2923 & 0.4178 \\
-0.05201 & -0.1428 & -0.2985 & -0.5615 & -1 & 0.05382 & 0.09935 & 0.1388 & 0.1966 & 0.2817 & 0.4074 \\
-0.04968 & -0.1385 & -0.2931 & -0.5568 & -1 & 0.04881 & 0.09353 & 0.1326 & 0.1902 & 0.2758 & 0.4033 \\
-0.04785 & -0.1350 & -0.2886 & -0.5529 & -1 & 0.04524 & 0.08929 & 0.1282 & 0.1861 & 0.2728 & 0.4033
\end{bmatrix}
\tag{74}
$$

Box I.

solution.

$$
W_e =
\begin{bmatrix}
0 & 0 & 0 & 0 & 0 & 0 & 0 \\
0 & 0 & 0 & 0 & 0 & 0 & 0 \\
0 & 0 & 0 & 0 & 0 & 0 & 0 \\
0 & 0 & 0 & 0 & 0 & 0 & 0 \\
0 & 0 & 0 & 0 & 0 & 0 & 0 \\
0 & 0 & 0 & 0 & -1.290 \times 10^{-5} & 0 & 8.899 \times 10^{-3} \\
0 & 0 & 0 & 0 & -1.092 \times 10^{-5} & -5.561 \times 10^{-8} & 1.873 \times 10^{-3} \\
0 & 0 & 0 & 0 & -1.134 \times 10^{-5} & -8.666 \times 10^{-8} & 1.339 \times 10^{-3} \\
0 & 0 & 0 & 0 & -1.197 \times 10^{-5} & -1.219 \times 10^{-7} & 1.072 \times 10^{-3} \\
0 & 0 & 0 & 0 & -1.269 \times 10^{-5} & -1.616 \times 10^{-7} & 9.158 \times 10^{-4} \\
0 & 0 & 0 & 0 & -1.349 \times 10^{-5} & -2.061 \times 10^{-7} & 8.153 \times 10^{-4}
\end{bmatrix}.
\tag{75}
$$

Using the matrices given in Eqs. (74), (75) the unknown parameters in the displacements functions c can be calculated at the selected edge for the specific loads in the vector f. The solution based on Eq. (51) for the separate unit edge loads $X_{e2}, Y_{e2}, Z_{e2}, p$ acting on the ellipsoidal shell is provided in Table 2.

Using the parameters in Table 2, the displacement and rotation components of compatibility equations (Eq. (50)) are obtained according to Eq. (54) for the second edge:

$$
\delta_{e2}^{(X2)} = 0 \, \frac{\text{mm}^2}{\text{N}}, \quad \delta_{e2}^{(Y2)} = 7.027 \times 10^{-3} \, \frac{\text{mm}^2}{\text{N}},
$$
$$
\delta_{e2}^{(Z2)} = 7.464 \times 10^{-5} \, \frac{\text{mm}}{\text{N}}, \quad \delta_{e2}^{(p)} = 4.207 \times 10^{-1} \, \frac{\text{mm}^3}{\text{N}},
$$
$$
\vartheta_{e2}^{(X2)} = 0 \, \frac{\text{mm}}{\text{N}}, \quad \vartheta_{e2}^{(Y2)} = -7.464 \times 10^{-5} \, \frac{\text{mm}}{\text{N}},
\tag{76}
$$
$$
\vartheta_{e2}^{(Z2)} = -1.550 \times 10^{-6} \, \frac{1}{\text{N}}, \quad \vartheta_{e2}^{(p)} = -1.101 \times 10^{-3} \, \frac{\text{mm}^2}{\text{N}}.
$$

To obtain the edge loads at the junction of the ellipsoidal and cylindrical shell the analogous calculations have to be performed for the cylindrical shell. The boundary conditions (Eq. (42)) are expressed as:

$$
a_o = -\left(a_1 + a_2 + a_3 + a_4 + a_5 + a_6 \right),
$$
$$
b_1 = -(2b_2 + 3b_3 + 4b_4 + 5b_5 + 6b_6).
\tag{77}
$$

The normalized strain matrix for the analysed shell is presented as Eq. (78) given in Box II. The energy of external forces matrix for the cylindrical segment W_c is obtained

$$
W_c =
\begin{bmatrix}
3.033 \times 10^{-4} & 0 & 0 & 0 & 0 & 0 & 0 \\
1.769 \times 10^{-4} & 0 & 0 & 0 & 0 & 0 & 0 \\
1.348 \times 10^{-4} & 0 & 0 & 0 & 0 & 0 & 0 \\
1.137 \times 10^{-4} & 0 & 0 & 0 & 0 & 0 & 0 \\
1.011 \times 10^{-4} & 0 & 0 & 0 & 0 & 0 & 0 \\
9.269 \times 10^{-5} & 0 & 0 & 0 & 0 & 0 & 0 \\
0 & -1.062 \times 10^{-4} & 0 & 0 & 0 & 0 & 1.062 \times 10^{-1} \\
0 & 0 & 2.569 \times 10^{-7} & 0 & 0 & 0 & -8.564 \times 10^{-2} \\
0 & 0 & 2.011 \times 10^{-7} & 0 & 0 & 0 & -8.378 \times 10^{-2} \\
0 & 0 & 1.841 \times 10^{-7} & 0 & 0 & 0 & -8.283 \times 10^{-2} \\
0 & 0 & 1.763 \times 10^{-7} & 0 & 0 & 0 & -8.227 \times 10^{-2} \\
0 & 0 & 1.720 \times 10^{-7} & 0 & 0 & 0 & -8.192 \times 10^{-2}
\end{bmatrix}.
\tag{79}
$$

The calculated parameters in the vector c for the cylindrical shell are given in Table 3.

Further, the displacements and rotations components are calculated according to Eq. (54) at the first edge ($\xi = \xi_{c1}$) of the cylindrical shell:

$$
\delta_{c1}^{(X1)} = -1.000 \times 10^{-4} \, \frac{\text{mm}^2}{\text{N}}, \quad \delta_{c1}^{(Y1)} = 6.599 \times 10^{-3} \, \frac{\text{mm}^2}{\text{N}},
$$
$$
\delta_{c1}^{(Z1)} = -7.264 \times 10^{-5} \, \frac{\text{mm}}{\text{N}}, \quad \delta_{c1}^{(p)} = -3.333 \times 10^{-1} \, \frac{\text{mm}^3}{\text{N}},
$$
$$
\vartheta_{c1}^{(X1)} = 0 \, \frac{\text{mm}}{\text{N}}, \quad \vartheta_{c1}^{(Y1)} = 7.264 \times 10^{-5} \, \frac{\text{mm}}{\text{N}},
\tag{80}
$$
$$
\vartheta_{c1}^{(Z1)} = -1.524 \times 10^{-6} \, \frac{1}{\text{N}}, \quad \vartheta_{c1}^{(p)} = 0 \, \frac{\text{mm}^2}{\text{N}}.
$$

$$U_c$$

$$=
\begin{bmatrix}
1 & 1 & 1 & 1 & 1 & 1 & -0.3 & 0.2 & 0.375 & 0.5400 & 0.7 & 0.8571 \\
0.5833 & 0.7778 & 0.875 & 0.9333 & 0.9722 & 1 & -0.175 & 0.1458 & 0.28 & 0.4083 & 0.5333 & 0.6563 \\
0.4444 & 0.6667 & 0.8 & 0.8889 & 0.9524 & 1 & -0.1333 & 0.1200 & 0.2333 & 0.3429 & 0.45 & 0.5556 \\
0.3750 & 0.6 & 0.75 & 0.8571 & 0.9375 & 1 & -0.1125 & 0.105 & 0.2057 & 0.3037 & 0.4 & 0.4950 \\
0.3333 & 0.5556 & 0.7143 & 0.8333 & 0.9259 & 1 & -0.1 & 0.09524 & 0.1875 & 0.2778 & 0.3667 & 0.4545 \\
0.3056 & 0.5238 & 0.6875 & 0.8148 & 0.9167 & 1 & -0.09167 & 0.08839 & 0.1746 & 0.2593 & 0.3429 & 0.4256 \\
-0.105 & -0.100 & -0.105 & -0.105 & -0.105 & -0.105 & 0.35 & -0.2333 & -0.4375 & -0.6300 & -0.8167 & -1 \\
0.08470 & 0.1059 & 0.1143 & 0.1186 & 0.1210 & 0.1225 & -0.2823 & 0.2259 & 0.4306 & 0.6252 & 0.8143 & 1 \\
0.08286 & 0.1061 & 0.116 & 0.1212 & 0.1243 & 0.1263 & -0.2762 & 0.2247 & 0.4294 & 0.6243 & 0.8138 & 1 \\
0.08192 & 0.1062 & 0.117 & 0.1229 & 0.1264 & 0.1287 & -0.2731 & 0.224 & 0.4286 & 0.6237 & 0.8135 & 1 \\
0.08137 & 0.1063 & 0.1177 & 0.124 & 0.1279 & 0.1304 & -0.2712 & 0.2235 & 0.4281 & 0.6234 & 0.8133 & 1 \\
0.08102 & 0.1063 & 0.1182 & 0.1248 & 0.1289 & 0.1317 & -0.2701 & 0.2232 & 0.4278 & 0.6231 & 0.8132 & 1
\end{bmatrix}
\tag{78}$$

Box II.

The edge loads resulting from the interaction of the ellipsoidal and cylindrical shell are obtained substituting Eqs. (76), (78), (79) into compatibility equations (Eq. (50)):

$$X_{c1} = -8.660 \times 10^2 \, \frac{\text{N}}{\text{mm}}, \quad Y_{c1} = 8.942 \times 10^1 \, \frac{\text{N}}{\text{mm}}, \quad Z_{c1} = 5.623 \times 10^2 \, \text{N},$$
$$X_{e2} = 8.660 \times 10^2 \, \frac{\text{N}}{\text{mm}}, \quad Y_{e2} = -8.942 \times 10^1 \, \frac{\text{N}}{\text{mm}}, \quad Z_{e2} = -5.623 \times 10^2 \, \text{N}.$$
$$\tag{81}$$

The final solution for the pressure vessel with ellipsoidal dished ends is achieved applying the edge loads (Eq. (81)) to Eqs. (59), (61) and then solving Eqs. (60), (62). The results are summarized in Tables 4, 5.

Table 10
Solution for the cylindrical shell.

	c_c
a_1	-2.426×10^{-1}
a_2	7.631×10^{-1}
a_3	-2.013
a_4	2.641
a_5	-1.692
a_6	4.218×10^{-1}
b_0	7.022×10^{-2}
b_2	-1.877×10^1
b_3	2.979×10^1
b_4	-1.803×10^1
b_5	-5.087×10^{-1}

The vertical displacements (Eq. (17)) based on the solution in Tables 4, 5 are presented in Fig. 7. Importantly, the results along the cylindrical shell are not constant beyond the junction of the shells. This phenomenon is not compatible with analytical solution based on the edge effect theory [1–3]. According to such formulation of the problem, the bending deformations caused by the edge loads diminish relatively promptly along the meridian of the shell. In the case of the cylindrical shell, lack of the edge loads implies the membrane state of the shell, as the applied pressure cause no bending effects. Such consequence does not apply to the shells with variable principal radii of curvature e.g. ellipsoidal, where the pressure itself cause bending of the shell. The fluctuation of vertical displacements for the cylindrical shell in Fig. 7 results from insufficient number of the independent variables in the displacement functions.

The meridional and circumferential stress components in the inner, middle and outer surface are given in Figs. 8 and 9 correspondingly.

The problem with the displacement functions is more significant for the principal stresses, especially for the meridional stress in cylindrical shell in Fig. 8. Despite the stress in the middle surface of both shells at the junction is comparable, the discontinuity of stress in the inner and outer surface is severe. The observed phenomenon implies that degree of polynomial should be higher or different displacement functions should be used.

4.4. Solution for the pressure vessel with torispherical dished ends

In the analysis of the pressure vessel with torispherical dished ends, the thickness as well as the displacement functions remain the same as in the previous section. The boundary conditions for the spherical shell are obtained according to Eq. (40):

$$a_0 = 0,$$
$$b_1 = -\tan\left(\varphi_{s2}\right)\left(a_0 + a_1\varphi_{s2} + a_2\varphi_{s2}^2 + a_3\varphi_{s2}^3 + a_4\varphi_{s2}^4 \right.$$
$$+ a_5\varphi_{s2}^5 + a_6\varphi_{s2}^6\left.\right) - b_2\varphi_{s2}^2$$
$$+ b_3\varphi_{s2}^3 + b_4\varphi_{s2}^4 + b_5\varphi_{s2}^5 + b_6\varphi_{s2}^6.$$

The strain energy matrix is formulated for the spherical segment of the pressure vessel as Eq. (82) given in Box III.

$$
U_s =
\begin{bmatrix}
1 & 0.4713 & 0.2221 & 0.1047 & 0.04933 & 0.02325 & 0.09191 & 0.05189 & 0.02714 & 0.01369 & 0.006769 \\
1 & 0.5316 & 0.2675 & 0.1314 & 0.0637 & 0.03064 & 0.07701 & 0.04489 & 0.02400 & 0.0123 & 0.00616 \\
1 & 0.5676 & 0.2977 & 0.1504 & 0.07445 & 0.03639 & 0.0671 & 0.03989 & 0.02165 & 0.01123 & 0.005675 \\
1 & 0.5915 & 0.3191 & 0.1646 & 0.0828 & 0.04098 & 0.06003 & 0.03615 & 0.01982 & 0.01037 & 0.005278 \\
1 & 0.6086 & 0.3352 & 0.1757 & 0.08947 & 0.04473 & 0.05474 & 0.03325 & 0.01837 & 0.009668 & 0.004947 \\
1 & 0.6213 & 0.3477 & 0.1845 & 0.09492 & 0.04785 & 0.05063 & 0.03092 & 0.01717 & 0.009084 & 0.004667 \\
1 & 0.3949 & 0.1622 & 0.06837 & 0.02938 & 0.01281 & 0.1211 & 0.06602 & 0.03361 & 0.01659 & 0.008062 \\
1 & 0.4077 & 0.1707 & 0.07292 & 0.0316 & 0.01385 & 0.1169 & 0.06431 & 0.03294 & 0.01634 & 0.007967 \\
1 & 0.4168 & 0.1772 & 0.07646 & 0.03338 & 0.01471 & 0.1138 & 0.06298 & 0.03241 & 0.01614 & 0.007892 \\
1 & 0.4236 & 0.1822 & 0.0793 & 0.03484 & 0.01543 & 0.1114 & 0.06193 & 0.03199 & 0.01597 & 0.007832 \\
1 & 0.4290 & 0.1862 & 0.08162 & 0.03605 & 0.01603 & 0.1095 & 0.06108 & 0.03164 & 0.01584 & 0.007784
\end{bmatrix}
\tag{82}
$$

Box III.

The energy of external loads matrix is expressed in the following manner

$$
W_s =
\begin{bmatrix}
0 & 0 & 0 & -2.748 \times 10^{-4} & 1.400 \times 10^{-4} & -1.534 \times 10^{-7} & -6.023 \times 10^{-2} \\
0 & 0 & 0 & -2.748 \times 10^{-4} & 1.400 \times 10^{-4} & -1.534 \times 10^{-7} & -6.022 \times 10^{-2} \\
0 & 0 & 0 & -2.748 \times 10^{-4} & 1.400 \times 10^{-4} & -1.534 \times 10^{-7} & -6.021 \times 10^{-2} \\
0 & 0 & 0 & -2.748 \times 10^{-4} & 1.400 \times 10^{-4} & -1.534 \times 10^{-7} & -6.021 \times 10^{-2} \\
0 & 0 & 0 & -2.748 \times 10^{-4} & 1.400 \times 10^{-4} & -1.534 \times 10^{-7} & -6.021 \times 10^{-2} \\
0 & 0 & 0 & -2.747 \times 10^{-4} & 1.400 \times 10^{-4} & -1.534 \times 10^{-7} & -6.020 \times 10^{-2} \\
0 & 0 & 0 & 0 & 0 & -3.339 \times 10^{-6} & -3.049 \times 10^{-1} \\
0 & 0 & 0 & 0 & 0 & -4.180 \times 10^{-6} & -3.051 \times 10^{-1} \\
0 & 0 & 0 & 0 & 0 & -5.022 \times 10^{-6} & -3.053 \times 10^{-1} \\
0 & 0 & 0 & 0 & 0 & -5.864 \times 10^{-6} & -3.054 \times 10^{-1} \\
0 & 0 & 0 & 0 & 0 & -6.707 \times 10^{-6} & -3.055 \times 10^{-1}
\end{bmatrix}.
\tag{83}
$$

The coefficients of the displacement functions caused by the unit edge loads are obtained according to Eq. (49). Their values are summarized in Table 6.

The coefficients of the compatibility equations (Eq. (63)) are calculated at the second edge $\varphi = \varphi_{s2} = 3\pi/20$ of the spherical shell:

$$
\delta_{s2}^{(X2)} = -2.919 \times 10^{-3} \, \frac{\text{mm}^2}{\text{N}}, \quad \delta_{s2}^{(Y2)} = 1.487 \times 10^{-3} \, \frac{\text{mm}^2}{\text{N}},
$$
$$
\delta_{s2}^{(Z2)} = 6.055 \times 10^{-5} \, \frac{\text{mm}}{\text{N}}, \quad \delta_{s2}^{(p)} = 2.444 \frac{\text{mm}^3}{\text{N}},
$$
$$
\vartheta_{s2}^{(X2)} = 5.395 \times 10^{-5} \, \frac{\text{mm}}{\text{N}}, \quad \vartheta_{s2}^{(Y2)} = -2.749 \times 10^{-5} \, \frac{\text{mm}}{\text{N}},
$$
$$
\vartheta_{s2}^{(Z2)} = -2.105 \times 10^{-6} \frac{1}{\text{N}}, \quad \vartheta_{s2}^{(p)} = -4.832 \times 10^{-2} \frac{\text{mm}^2}{\text{N}}.
\tag{84}
$$

The toroidal segment of the torispherical dished end is the shell with open apex, therefore the boundary condition described by Eq. (41) are used. Applying such restriction on the horizontal displacements yields

Table 11
Mesh convergence study results for the pressure vessel with torispherical dished ends and $t = 5$ mm.

	n_t	n_m				
		100	200	300	400	500
σ_{rmax} [MPa]	2	277.4	275.3	274.7	275.0	275.1
	4	278.8	276.3	275.5	275.2	275.3
	6	279.8	276.0	275.4	275.3	275.3
	8	277.7	275.7	275.3	275.3	275.3

Table 12
Mesh convergence study results for the pressure vessel with torispherical dished ends and $t = 30$ mm.

	n_t	n_m				
		100	200	300	400	500
σ_{rmax} [MPa]	2	227.4	227.4	227.1	227.0	227.0
	4	228.4	227.9	228.0	227.9	228.0
	6	228.6	228.1	228.2	228.1	228.2
	8	228.7	228.2	228.3	228.2	228.2

the result

$$
a_0 = -\pi \left(\frac{1}{2} a_1 + \frac{1}{4} \pi a_2 + \frac{1}{8} \pi^2 a_3 + \frac{1}{16} \pi^3 a_4 + \frac{1}{32} \pi^4 a_5 + \frac{1}{64} \pi^5 a_6 \right).
$$

The strain energy matrix is obtained for the toroidal shell as Eq. (85) given in Box IV.

In the external load energy matrix W_t, the fourth column equals zero, as the load X_{t2} causes no horizontal displacements due to the applied boundary condition (See Eq. (86) given in Box V).

The problem is further solved for the unit edge loads contained in the vector f_t (Eq. (70)). For each of the unit loads the unknown parameters in the displacement functions take different values which are given in Table 7.

The components of compatibility equations for the torispherical dished ends are determined according to Eq. (54)

U_t

$$= \begin{bmatrix} 0.0679 & 0.1424 & 0.244 & 0.3961 & 0.6315 & 1 & -0.07238 & -0.07691 & -0.0887 & -0.1088 & -0.1394 & -0.1845 & -0.2501 \\ 0.0519 & 0.1193 & 0.2187 & 0.3727 & 0.6155 & 1 & -0.05456 & -0.06361 & -0.0785 & -0.101 & -0.134 & -0.1819 & -0.2514 \\ 0.04271 & 0.105 & 0.202 & 0.3565 & 0.6038 & 1 & -0.04444 & -0.05556 & -0.07202 & -0.09594 & -0.1306 & -0.1807 & -0.2535 \\ 0.03704 & 0.09562 & 0.1904 & 0.3446 & 0.5949 & 1 & -0.03827 & -0.05035 & -0.06762 & -0.09243 & -0.1282 & -0.1801 & -0.2557 \\ 0.03331 & 0.08907 & 0.1819 & 0.3356 & 0.588 & 1 & -0.03425 & -0.04677 & -0.06447 & -0.08984 & -0.1265 & -0.1799 & -0.2578 \\ 0.03072 & 0.08427 & 0.1755 & 0.3285 & 0.5823 & 1 & -0.03149 & -0.04417 & -0.0621 & -0.08787 & -0.1252 & -0.1797 & -0.2597 \\ -0.07061 & -0.146 & -0.2476 & -0.3992 & -0.6336 & -1 & 0.08806 & 0.09262 & 0.106 & 0.1293 & 0.1652 & 0.2182 & 0.2955 \\ -0.05348 & -0.1214 & -0.2207 & -0.3744 & -0.6165 & -1 & 0.06602 & 0.07558 & 0.0922 & 0.1178 & 0.1556 & 0.2106 & 0.2906 \\ -0.04387 & -0.1065 & -0.2035 & -0.3576 & -0.6045 & -1 & 0.05376 & 0.06558 & 0.08379 & 0.1107 & 0.15 & 0.207 & 0.29 \\ -0.03802 & -0.09687 & -0.1916 & -0.3455 & -0.5955 & -1 & 0.04635 & 0.05921 & 0.07825 & 0.1061 & 0.1465 & 0.2054 & 0.2915 \\ -0.03419 & -0.09017 & -0.183 & -0.3364 & -0.5884 & -1 & 0.04154 & 0.05487 & 0.07438 & 0.1028 & 0.1443 & 0.2049 & 0.2941 \\ -0.03153 & -0.08529 & -0.1764 & -0.3292 & -0.5827 & -1 & 0.03823 & 0.05176 & 0.07153 & 0.1004 & 0.1428 & 0.2051 & 0.2973 \\ -0.02958 & -0.08158 & -0.1713 & -0.3234 & -0.5781 & -1 & 0.03583 & 0.04943 & 0.06936 & 0.09864 & 0.1418 & 0.2058 & 0.3011 \end{bmatrix} \tag{85}$$

Box IV.

$$W_t = \begin{bmatrix} 6.425 \times 10^{-6} & 0 & 1.878 \times 10^{-8} & 0 & 0 & 0 & 0 \\ 4.782 \times 10^{-6} & 0 & 1.398 \times 10^{-8} & 0 & 0 & 0 & 0 \\ 3.858 \times 10^{-6} & 0 & 1.128 \times 10^{-8} & 0 & 0 & 0 & 0 \\ 3.3 \times 10^{-6} & 0 & 9.648 \times 10^{-9} & 0 & 0 & 0 & 0 \\ 2.94 \times 10^{-6} & 0 & 8.596 \times 10^{-9} & 0 & 0 & 0 & 0 \\ 2.694 \times 10^{-6} & 0 & 7.877 \times 10^{-9} & 0 & 0 & 0 & 0 \\ 0 & -5.701 \times 10^{-6} & 0 & 0 & -7.01 \times 10^{-6} & 0 & 2.465 \times 10^{-3} \\ 0 & -1.915 \times 10^{-6} & -1.188 \times 10^{-8} & 0 & -7.848 \times 10^{-6} & -1.461 \times 10^{-8} & 1.827 \times 10^{-3} \\ 0 & -6.418 \times 10^{-7} & -7.964 \times 10^{-9} & 0 & -8.769 \times 10^{-6} & -3.264 \times 10^{-8} & 1.475 \times 10^{-3} \\ 0 & -2.138 \times 10^{-7} & -3.979 \times 10^{-9} & 0 & -9.735 \times 10^{-6} & -5.436 \times 10^{-8} & 1.264 \times 10^{-3} \\ 0 & -7.068 \times 10^{-8} & -1.754 \times 10^{-9} & 0 & -1.073 \times 10^{-5} & -7.988 \times 10^{-8} & 1.128 \times 10^{-3} \\ 0 & -2.321 \times 10^{-8} & -7.199 \times 10^{-10} & 0 & -1.174 \times 10^{-5} & -1.093 \times 10^{-7} & 1.035 \times 10^{-3} \\ 0 & -7.57 \times 10^{-9} & -2.818 \times 10^{-10} & 0 & -1.277 \times 10^{-5} & -1.426 \times 10^{-7} & 9.686 \times 10^{-4} \end{bmatrix}. \tag{86}$$

Box V.

$$\delta_{t1}^{(X1)} = -1.159 \times 10^{-3} \frac{\text{mm}^2}{\text{N}}, \quad \delta_{t2}^{(X1)} = -3.388 \times 10^{-4} \frac{\text{mm}^2}{\text{N}},$$
$$\delta_{t1}^{(X2)} = 0 \frac{\text{mm}^2}{\text{N}}, \quad \delta_{t2}^{(X2)} = 0 \frac{\text{mm}^2}{\text{N}},$$
$$\delta_{t1}^{(Y1)} = 5.848 \times 10^{-3} \frac{\text{mm}^2}{\text{N}}, \quad \delta_{t2}^{(Y1)} = -8.813 \times 10^{-4} \frac{\text{mm}^2}{\text{N}},$$
$$\delta_{t1}^{(Y2)} = -1.208 \times 10^{-4} \frac{\text{mm}^2}{\text{N}}, \quad \delta_{t2}^{(Y2)} = 7.017 \times 10^{-3} \frac{\text{mm}^2}{\text{N}},$$
$$\delta_{t1}^{(Z1)} = -5.335 \times 10^{-5} \frac{\text{mm}}{\text{N}}, \quad \delta_{t2}^{(Z1)} = -3.731 \times 10^{-6} \frac{\text{mm}}{\text{N}},$$
$$\delta_{t1}^{(Z2)} = 2.694 \times 10^{-6} \frac{\text{mm}}{\text{N}}, \quad \delta_{t2}^{(Z2)} = 7.412 \times 10^{-5} \frac{\text{mm}}{\text{N}},$$

$$\delta_{t1}^{(p)} = -3.789 \times 10^{-1} \frac{\text{mm}^3}{\text{N}}, \quad \delta_{t2}^{(p)} = -1.328 \times 10^{-1} \frac{\text{mm}^3}{\text{N}},$$
$$\vartheta_{t1}^{(X1)} = -5.562 \times 10^{-6} \frac{\text{mm}}{\text{N}}, \quad \vartheta_{t2}^{(X1)} = -6.496 \times 10^{-7} \frac{\text{mm}}{\text{N}},$$
$$\vartheta_{t1}^{(X2)} = 0 \frac{\text{mm}}{\text{N}}, \quad \vartheta_{t2}^{(X2)} = 0 \frac{\text{mm}}{\text{N}},$$
$$\vartheta_{t1}^{(Y1)} = 1.066 \times 10^{-4} \frac{\text{mm}}{\text{N}}, \quad \vartheta_{t2}^{(Y1)} = -6.101 \times 10^{-6} \frac{\text{mm}}{\text{N}},$$
$$\vartheta_{t1}^{(Y2)} = 4.587 \times 10^{-6} \frac{\text{mm}}{\text{N}}, \quad \vartheta_{t2}^{(Y2)} = -7.412 \times 10^{-5} \frac{\text{mm}}{\text{N}},$$
$$\vartheta_{t1}^{(Z1)} = -1.808 \times 10^{-6} \frac{1}{\text{N}}, \quad \vartheta_{t2}^{(Z1)} = 1.050 \times 10^{-7} \frac{1}{\text{N}},$$
$$\vartheta_{t1}^{(Z2)} = 1.291 \times 10^{-7} \frac{\text{mm}}{\text{N}}, \quad \vartheta_{t2}^{(Z2)} = -1.549 \times 10^{-6} \frac{\text{mm}}{\text{N}},$$
$$\vartheta_{t1}^{(p)} = -1.762 \times 10^{-3} \frac{\text{mm}^2}{\text{N}}, \quad \vartheta_{t2}^{(p)} = -2.132 \times 10^{-4} \frac{\text{mm}^2}{\text{N}}. \tag{87}$$

Substituting Eqs. (87), (84) and (80) to the compatibility equations (Eq. (63)) leads to the following edge loads resulting from the interaction between the shells:

$$X_{c1} = -8.660 \times 10^2 \frac{N}{mm}, \quad Y_{c1} = 5.883 \times 10^1 \frac{N}{mm}, \quad Z_{c1} = -4.453 \times 10^2 \, N,$$

$$X_{t2} = 8.660 \times 10^2 \frac{N}{mm}, \quad Y_{t2} = -5.883 \times 10^1 \frac{N}{mm}, \quad Z_{t2} = 4.453 \times 10^2 N,$$

$$X_{t1} = -1.365 \times 10^3 \frac{N}{mm}, \quad Y_{t1} = -9.504 \times 10^1 \frac{N}{mm}, \quad Z_{t1} = -1.756 \times 10^3 \, N,$$

$$X_{s2} = 1.365 \times 10^3 \frac{N}{mm}, \quad Y_{s2} = 9.504 \times 10^1 \frac{N}{mm}, \quad Z_{s2} = 1.756 \times 10^3 \, N.$$

$$(88)$$

The calculated edge loads allow to resolve the unknown parameters of the polynomials describing the displacements of the shells. Those are presented in Tables 8, 9, 10 for each of the shells.

The vertical displacements for the pressure vessel with torispherical dished ends based on solution given in Tables 8, 9, 10 is shown in Fig. 10. Similarly to the pressure vessel with ellipsoidal dished ends, the vertical displacements slightly fluctuate along the meridian of the cylindrical shell.

Such issue is more evident for the meridional and circumferential stress in the inner, middle and outer surface, presented in Figs. 11, 12. The stress distributions seem far from satisfactory. The disturbances in meridional stress at the edges of the shells are significant, especially in the inner and outer surface of the pressure vessel. Interestingly, principal stresses tend to be characterized by abnormal distribution for $S = \varphi = 0$. In the case of the circumferential stress the discontinuities at the junctions can be considered acceptable. The obtained results for the both pressure vessels suggest that the order of polynomials is insufficient. It is necessary to consider the displacement functions with higher number of the independent variables as well as different displacement functions in the further analysis.

5. Result comparison with FEM

The results presented in the previous section of the paper focused merely on one example of the pressure vessel with ellipsoidal and torispherical dished ends. The solutions were also described by one of the displacements functions, namely polynomials (Eq. (36)). According to the obtained displacements and principal stresses functions, it is important to note that the order of polynomials is insufficient to obtain satisfactory solution. Such observation results from the discontinuous functions at the edges of the analysed shells, non-constant displacements and stresses far from the loaded edge of the cylindrical segments.

The evaluation of accuracy of the solutions based on the Ritz method requires their comparison with the finite element method. In the paper the numerical FEM calculations are performed with a use of Ansys 19 software. The analysis type is static, linear, axisymmetric with

Table 13

Vertical displacements comparison for the displacement functions based on polynomials — isotropic material.

Table 14
Equivalent stress comparison for the displacement functions based on polynomials — isotropic material.

t [mm]	torispherical ends	ellipsoidal ends
5		
15		
30		
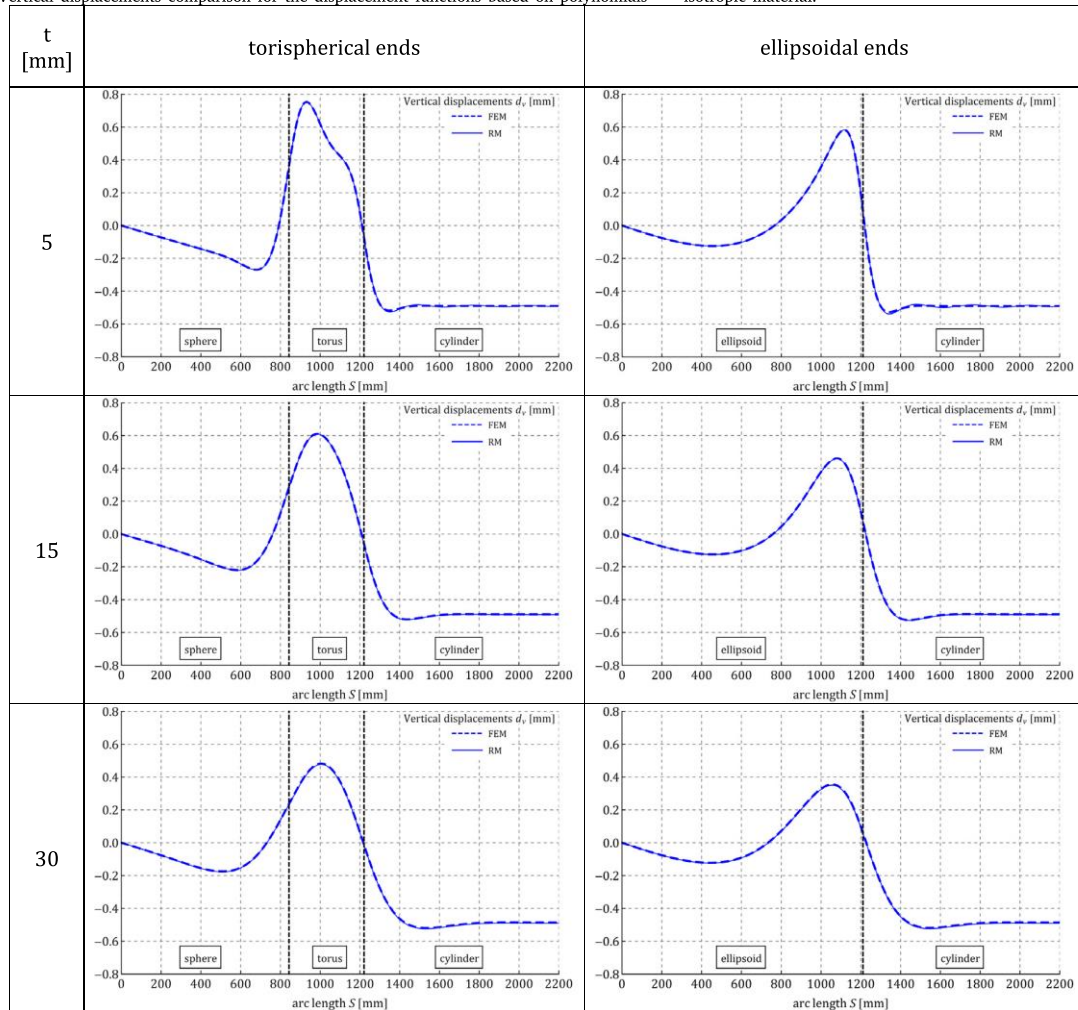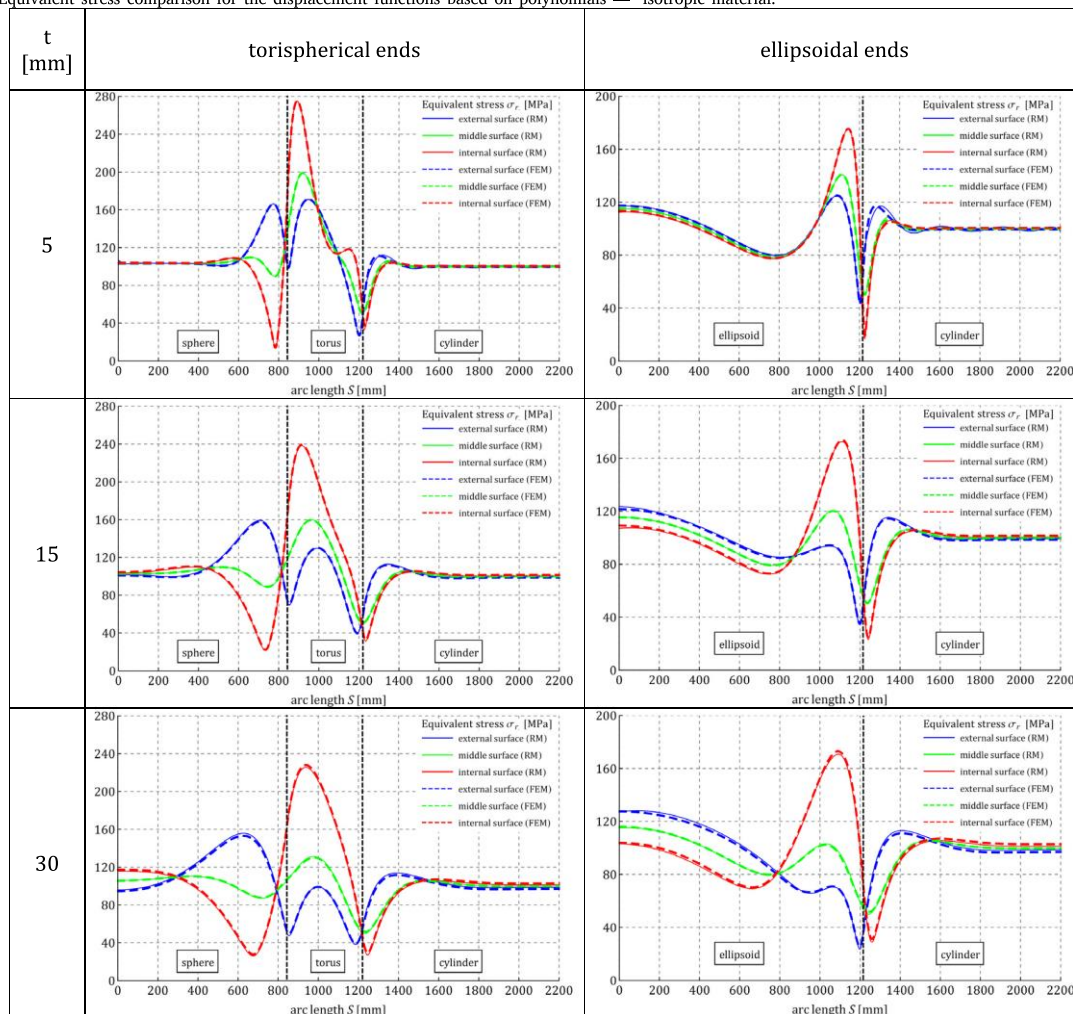
perfectly elastic material. The geometry is divided into quadrilateral, two dimensional, eight-node finite elements PLANE183 with three degrees of freedom at each node.

Performing mesh convergence study enabled to evaluate the sufficient density of finite element mesh. Two considered factors in the study are the number of elements across the thickness n_t and along the meridian n_m. Because the geometry has to be virtually split in the middle surface to read the analysed values, the parameter n_t has to be an even number. During the mesh convergence study the maximum stress and displacement as well as total strain energy value were investigated in the pressure vessels with ellipsoidal and torispherical dished ends. According to the obtained results the peak stress value σ_{rmax} for the latter is the most susceptible for the changes in the finite element mesh.

It is assumed that the mesh density is sufficient if the increase in the finite element number results in up to 0.1% relative difference in σ_{rmax}. According to the results presented in Tables 11, 12 in the case of the thickness $t = 5$ mm the finite element model requires relatively high value of n_m. For the thicker pressure vessel i.e. $t = 30$ mm more elements are required across the thickness n_t. By calculating the relative differences with respect to the changes in n_t and n_m, the assumed accuracy condition is fulfilled for $n_t = 4$ and $n_m = 400$ considering both thickness values.

An exemplary FE model is presented in Fig. 13, where the thickness of the model was increased to $t = 50$ mm and the number of elements along the meridian reduced to $n_m = 200$ for better readability. To reduce size of the problem, only symmetrical half of the axisymmetric model of the pressure vessel is considered. The normal displacements are restrained i.e. $v = 0$ at the edge highlighted in Fig. 13 to obtain the symmetry boundary condition. The pressure is applied to the inner edge of the FE model.

The comparison of results is performed for the pressure vessels with torispherical and ellipsoidal ends of the thickness $t = 5, 15, 30$ mm, where orthotropy coefficient $\alpha = 1, 1.2$. The analysed results are vertical displacements and equivalent stress. In the case of the Ritz method, the equivalent stress is based on the state of plane stress. The displacement functions are considered in a form of polynomials (Eq. (36)), trigonometric series (Eq. (37)) and polynomials complemented with modified trigonometric series (Eq. (38)). The latter is used to describe the normal displacements in the shells with constant radii of curvature, namely spherical and cylindrical, while the remaining displacements functions are polynomials. The number of unknown parameters (Table 1) for all types of the displacement functions corresponds to the two polynomials of order ten, representing normal and tangent displacements.

Table 15
Vertical displacements comparison for the displacement functions based on trigonometric series — isotropic material.
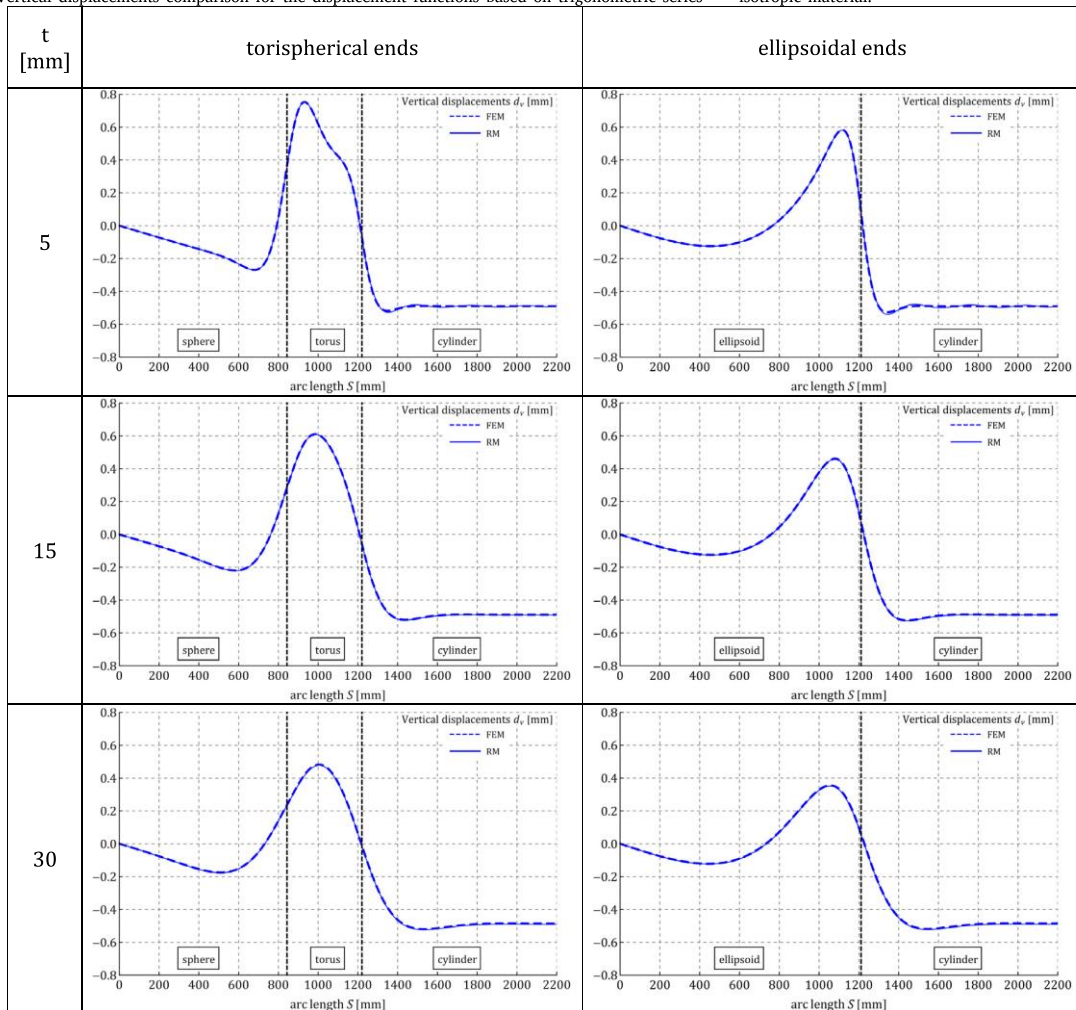
The vertical displacements obtained using the Ritz method and the finite element method are compared in Table 13 for the isotropic material ($\alpha = 1$). The solutions from the Ritz method nearly perfectly match FEM solutions. Insignificant differences can be observed for the pressure vessels of the thickness $t = 5$ mm. Relatively far from the loaded edge of cylindrical shells, where displacements shall be constant, the vertical displacements for the cylindrical shell fluctuate around the FEM solution. It indicates that the displacement functions have difficulties to preserve constant value when it occurs over the greater arc length and when the edge disturbances are abrupt. Such phenomenon was also observed in the previous section of the paper for the polynomials of order six (Figs. 8 and 9), however for the pressure vessels of the thickness $t = 15$ mm.

Equivalent stress distributions comparison presented in Table 14 demonstrates similar results in both of the methods. The peak stress value occurs always in the inner surface, therefore the other two curves can be easily referred to the middle and outer surface. For the thickness $t = 30$ mm a slight differences in the maximum stress values can be observed, the Ritz method tends to yield insignificantly lower value of the peak stress. Due to fluctuation of the vertical displacements in the cylindrical shell for $t = 5$ mm the stress share the same characteristics.

The vertical displacements for the displacement functions in the form of trigonometric series shown in Table 15 are nearly identical to those described by the polynomials. The change of the form of the displacement functions does not have an effect on the fluctuation of the solution for the cylindrical shell.

As expected, negligible differences are also observed in the stress distributions in Table 16. The displacement functions in the form of polynomials and trigonometric series are not suitable to describe constant values over the arc length S. Importantly the compatibility equations are not imposed on the meridional stress, therefore the continuity of equivalent stress is fulfilled solely on the basis of minimum potential energy principle. The agreement of the circumferential stress is achieved due to the equivalency of the vertical displacements.

The solutions shown in Tables 17, 18 refer to the displacement functions in a form of polynomials (Eq. (36)) and modified trigonometric series (Eq. (38)). The latter is used to describe normal displacements in the spherical and cylindrical shell. The character of modified trigonometric series allowed to obtain constant value of the vertical displacements beyond the loaded edges of the spherical and cylindrical shell. As a result the stress remains constant as well, which is coherent with the FEM solution. Similar character of the solution can be obtained from an analytical approach using theory of the edge effect, however its values would significantly vary from the presented results.

For more detailed comparison the maximum equivalent stress values σ_{rmax}, maximum vertical displacements d_{vmax} and strain energy U_ε are compared for Ritz method and FEM in Tables 19, 20 considering all of

Table 16
Equivalent stress comparison for the displacement functions based on trigonometric series — isotropic material.

t [mm]	torispherical ends	ellipsoidal ends
5		
15		
30		
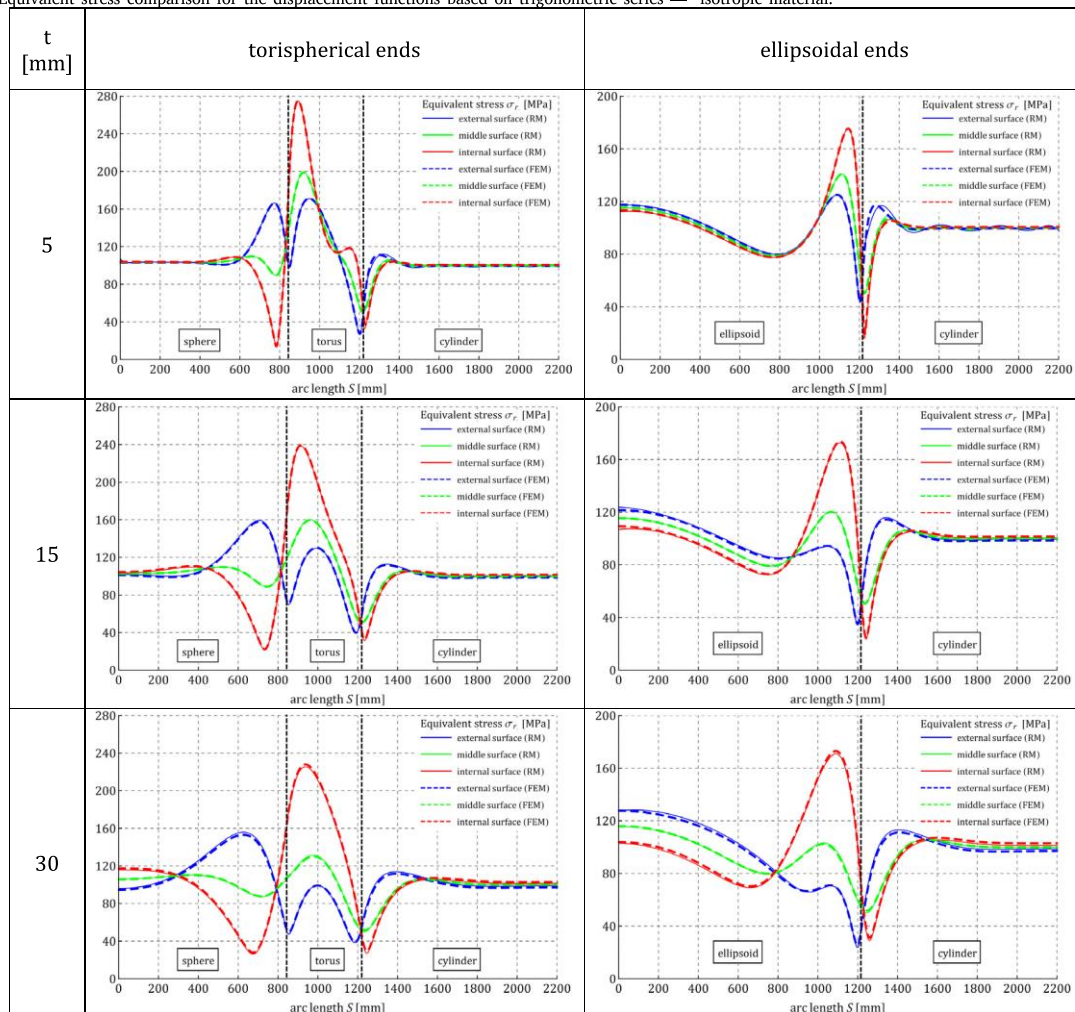
the displacement functions. The following abbreviations are used for the displacement functions: P — polynomials, TS — trigonometric series, PMTS — polynomials and modified trigonometric series. The calculation of the relative differences considers FEM result as reference value, which do not exceed 2% for all of the analysed cases. The type of displacements functions has insignificant effect on the results in Tables 19, 20, which indicates regularity of the calculations based on Ritz method.

The greatest discrepancies of the results are observed for the thickness $t = 30$ mm, and the least for $t = 5$ mm. It is necessary to consider the difference in the applied load in both of the methods. The Ritz method based on the general shell theory implies the load is applied to the middle surface of the shell. Finite element method solutions assume the pressure acts on the inner surface of the pressure vessel. The latter case represents a realistic condition, while general shell theory uses simplified approach which is valid for thin-walled structures. The area of the middle surface is greater than area of inner surface of the pressure vessel, therefore the magnitude of load is greater in case of the Ritz method. Such phenomenon leads to the increased values of strain energy for thicker shells. Interestingly, the maximum value of vertical displacements and equivalent stress are lower for the solutions based on the general shell theory.

The previously presented results assume isotropic properties of the material. The manufacturing process of the pressure vessels is based on plastic forming where material exhibits strain hardening. Degree of the strain hardening is different along meridional and circumferential direction. Moreover, the properties of the material are non-uniform along the principal directions. Such phenomenon is manifested by non-uniform thickness of the manufactured dished ends. The variable mechanical properties and thickness towards meridional direction is not considered within the paper. In the further analyses, the material model is perfectly elastic and orthotropic, where orthotropy coefficient $\alpha = 1.2$. Such value might be considered excessive for a structural steel, however the greater the value of the coefficient, the more significant discrepancies between the methods are expected. As the aim of this section is to evaluate the accuracy the Ritz method application, the assumed value is justified. The orthotropy coefficient $\alpha > 1$ indicates that the degree of the strain hardening is greater towards circumferential direction.

According to the analyses results considering the isotropic material, the change of displacement functions has rather insignificant effect on the solution. In case of the orthotropic material, only polynomial based displacement functions are studied. The displacements comparison between the both methods for the orthotropic material is presented

Table 17

Vertical displacements comparison for the displacement functions based on polynomials and modified trigonometric series — isotropic material.

t [mm]	torispherical ends	ellipsoidal ends
5		
15		
30		
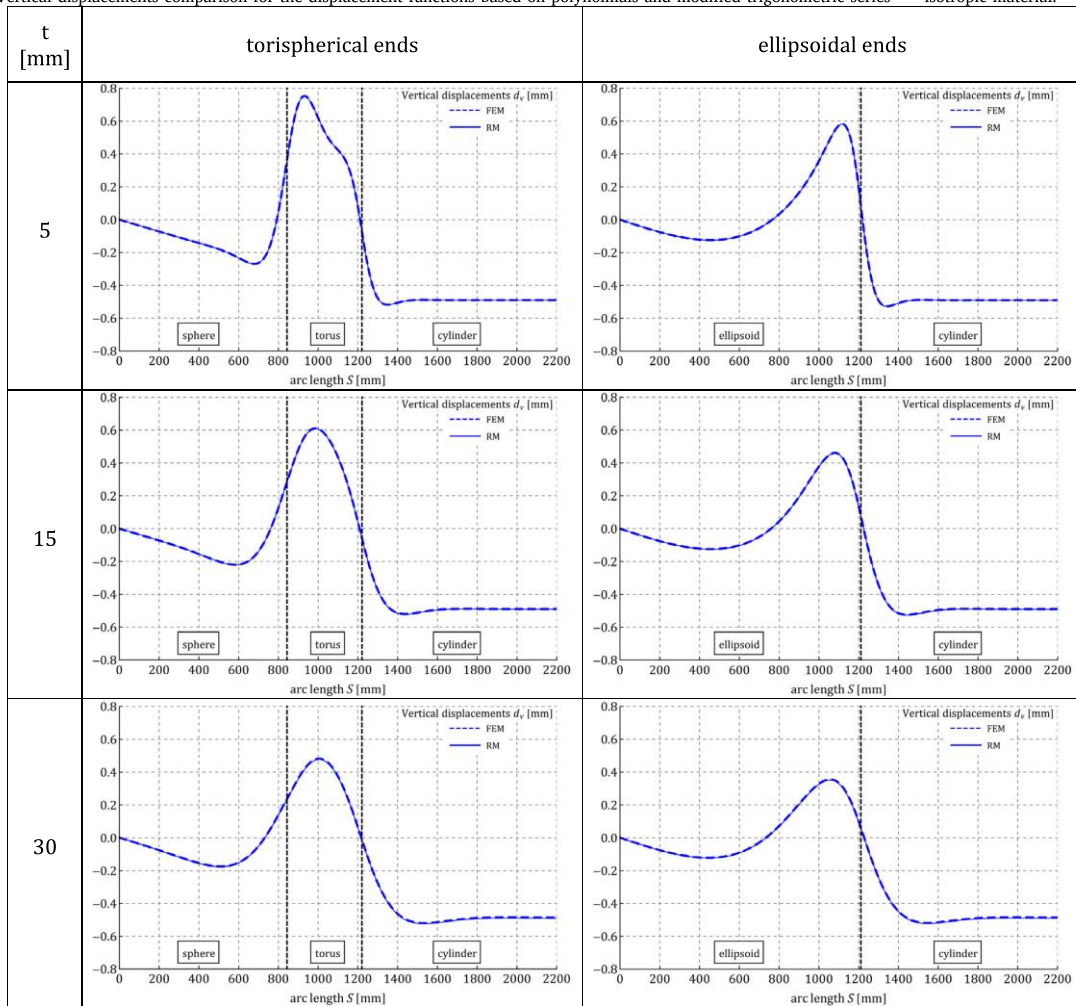
in Table 21. The applied change in the material properties did not influence the coherence of the results.

Unlike the vertical displacements, the distribution of equivalent stress exhibits a significant change in the area of $S = 0$ mm in both of the methods due to the change of material properties. The correlation of equivalent stress between the Ritz method and finite element method is shown in Table 22. In the result of abrupt change of the stress distribution in the mentioned area, Ritz method solutions differs moderately from finite element method. To address this issue more complex displacement functions can be used.

The maximum values of the vertical displacements, equivalent stress and total strain energy are juxtaposed in Table 23 for the torispherical end and in Table 24 for the ellipsoidal end. According to the obtained data, the increase in thickness leads to higher values of the relative differences. Such phenomenon is also observed in the case of the isotropic material and results from the differences in the location of the applied pressure.

6. Conclusions

The possibilities of solving the problems of stress and deformation in the pressure vessels is undoubtedly poor. Despite the analytical formulation of the selected shell problems is well defined in the literature,

the solution is not possible for most of the practical cases of shell structures. The design of pressure vessels is regulated by the procedures described in the technical standards. Such calculations are based on the membrane theory. The assumption of no bending phenomena in the membrane theory usually results in serious miscalculations of displacements and stresses. The edge effect theory is accurate only for the shells of constant radii of curvature near their edges, which was the basis of the derivation performed by Geckeler [1,2]. Additionally, the analyses of the shell structures with discontinuous radii of curvature based on the edge effect theory require the definition of the compatibility equations similar to those presented in the paper. In the process of calculation of the edge loads one must use the deformations based on the membrane theory in the compatibility equations, which introduces erratic values to the solution before its obtained. These deformations are accurate only for the shells with constant radii of curvature due to the nature of the membrane theory. Importantly, application of the edge effect theory for the shells with variable radii of curvature can result in technically correct solution, however it is difficult to evaluate the impact of such simplification. The application of the Ritz method enables to perform semi-analytical analyses of shell structures including the bending effects as the result of the applied pressure and interaction between shells in the juncture. Furthermore the form of the solution

Table 18
Equivalent stress comparison for the displacement functions based on polynomials and modified trigonometric series — isotropic material.
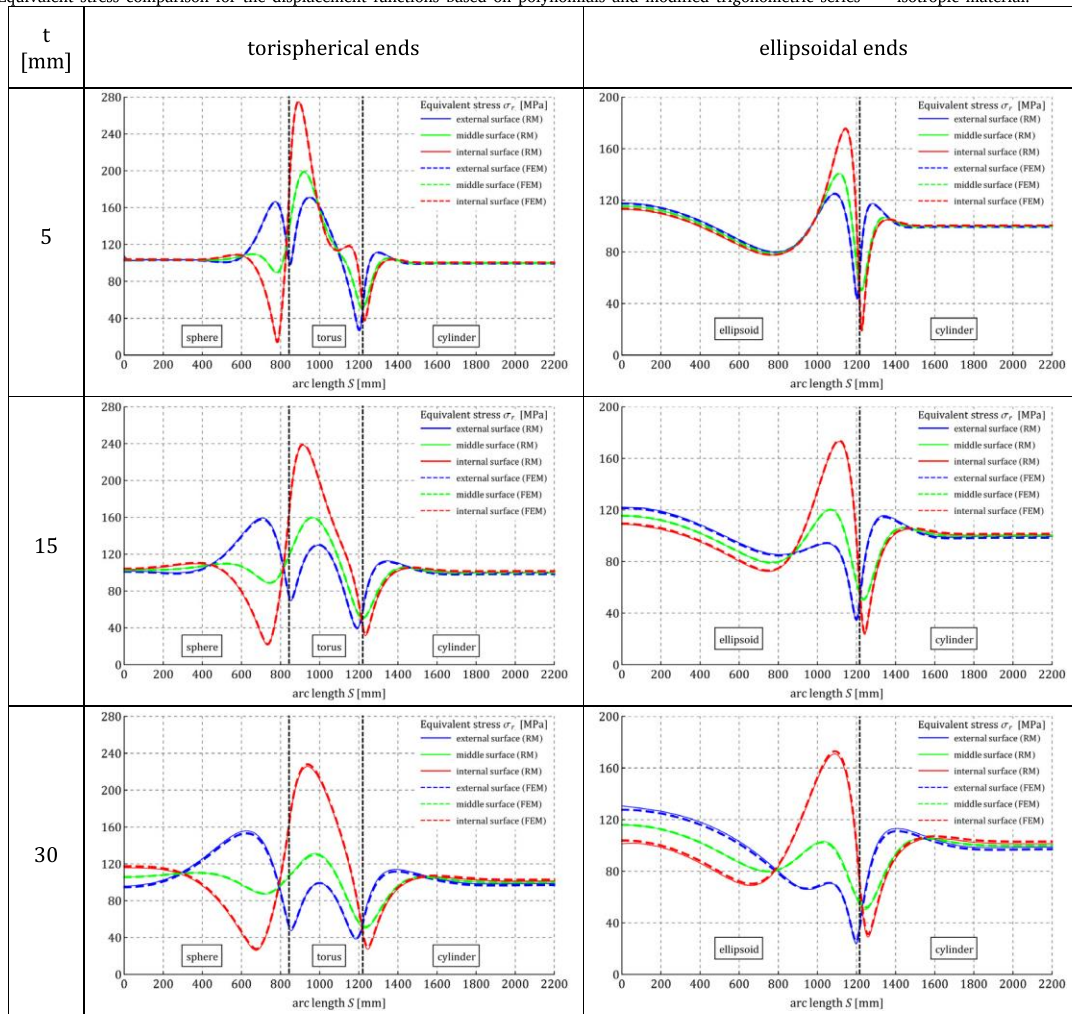
Table 19
Results comparison summary for the pressure vessel with torispherical dished ends — isotropic material.

	t [mm]	Ritz method functions			FEM	Relative difference [%]		
		P	TS	PMTS		P	TS	PMTS
σ_{rmax} [MPa]	5	274.9	274.8	274.9	275.2	0.1029	0.1412	0.1030
	15	238.2	238.2	238.2	239.2	0.4117	0.4098	0.4117
	30	225.6	225.6	225.6	227.9	1.036	1.036	1.036
d_{vmax} [mm]	5	0.7524	0.7524	0.7524	0.7529	0.07514	0.07526	0.07612
	15	0.6097	0.6097	0.6097	0.6114	0.2657	0.2660	0.2657
	30	0.4778	0.4778	0.4778	0.4820	0.8698	0.8698	0.8698
U_{ε} [kJ]	5	18.95	18.94	18.95	18.90	0.2213	0.2174	0.2311
	15	53.55	53.55	53.55	53.15	0.7576	0.7575	0.7576
	30	100.5	100.5	100.5	98.83	1.647	1.647	1.647

Table 20
Results comparison summary for the pressure vessel with ellipsoidal dished ends — isotropic material.

	t [mm]	Ritz method functions			FEM	Relative difference [%]		
		P	TS	PMTS		P	TS	PMTS
σ_{rmax} [MPa]	5	175.3	175.3	175.2	175.4	0.08000	0.08120	0.1337
	15	172.7	172.7	173.0	173.80	0.6372	0.6306	0.4811
	30	170.8	170.9	170.8	173.0	1.291	1.216	1.291
d_{vmax} [mm]	5	0.5821	0.5821	0.5825	0.5830	0.1502	0.1583	0.08763
	15	0.4591	0.4591	0.4591	0.4609	0.3806	0.3866	0.3937
	30	0.3509	0.3509	0.3509	0.3550	1.152	1.149	1.152
U_{ε} [kJ]	5	15.79	15.79	15.79	15.75	0.2522	0.2435	0.2740
	15	45.80	45.80	45.80	45.41	0.8657	0.8655	0.8658
	30	88.16	88.16	88.16	86.57	1.827	1.827	1.827

based on the Ritz method enables to define continuous functions of displacements, strains, stresses and internal forces.

Due to the formulation of the general shell theory of thin shells, it was initially expected that the precision of the analyses may be unsatisfactory for relatively thick shells, especially in the areas of the junctions where the bending effects arise. The trend of relative differences growth with the increasing thickness is evident throughout the comparison of the results between the two methods. It can be simply explained by the discrepancy in the method of external load application. The

Table 21
Vertical displacements comparison for the displacement functions based on polynomials orthotropic material.

t [mm]	torispherical ends	ellipsoidal ends
5		
15		
30		
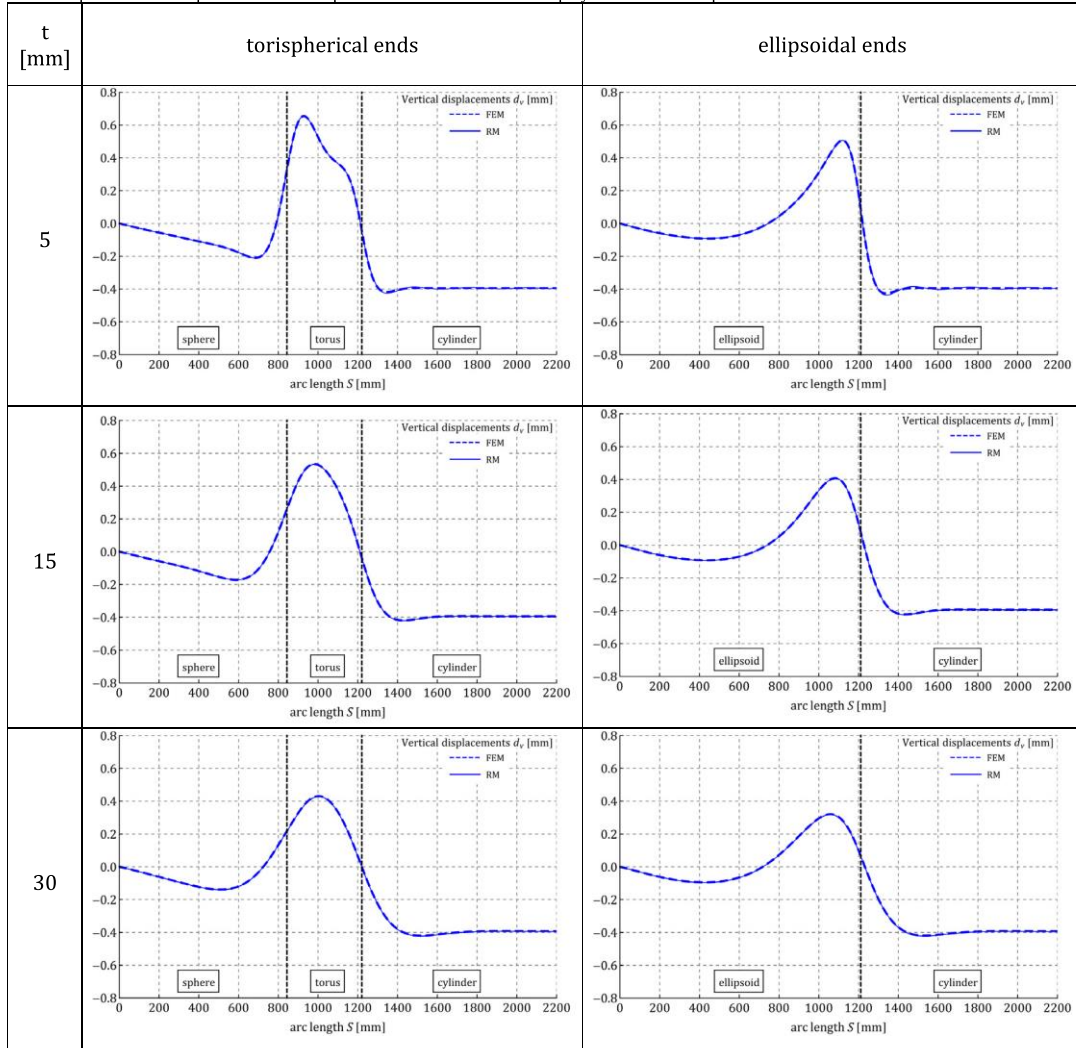
analyses based on the Ritz method assume that the load is acting on the middle surface of the shells. The finite element method allows to model more realistic case, where the load is applied to the internal surface of the pressure vessels. In the effect of this issue, the total external load magnitude is greater in the Ritz method analyses, which causes elevated values of the strain energy. Nonetheless, to evaluate the quality of the solutions based on the semi-analytical approach it is necessary to address the significance of such differences. Among the results given in Tables 19, 20, 23 and 24 the peak stress value is of the greatest importance in the design of the pressure vessels. The maximum relative difference of 1.31% for the peak equivalent stress is observed for the pressure vessel with ellipsoidal ends and the orthotropic material. Importantly, the change of the material properties from isotropic to orthotropic did not influence significantly the accuracy of the solutions. The minor inconsistency is seen for the equivalent stress (Table 22) at the apex of the dished ends where arc length $S = 0$, due to nonuniform material properties towards principal directions of the shells. Such issue can be easily addressed by applying more independent variables into the displacement functions.

The results of the study indicate that the form of the displacement functions does not have a great effect on the solution, however the number of independent variables must be relatively high to meet required precision of the displacement and stress distributions. Within the paper it is suggested that polynomials of order six are insufficient to successfully describe the displacements in the analysed pressure vessels. The increase of the polynomial order to ten enabled to achieve satisfactory results. The displacement functions in the form of polynomials and trigonometric series led to minor problems with the solution for the cylindrical and spherical shells for the thickness $t = 5$ mm. The problem was addressed by introducing the displacement function based on modified trigonometric series formulated in the similar manner to the analytical solution of differential equations of the edge effect theory. The function was used exclusively to describe the normal displacements in the shells of constant radii of curvature i.e. cylindrical and spherical.

According to the obtained results there are severe differences between stress and displacement distributions for the pressure vessels with ellipsoidal and equivalent torispherical ends. Such issue indicates that the design method provided in the standards is far from

Table 22

Vertical displacements comparison for the displacement functions based on polynomials and modified trigonometric series — orthotropic material.

t [mm]	torispherical ends	ellipsoidal ends
5		
15		
30		
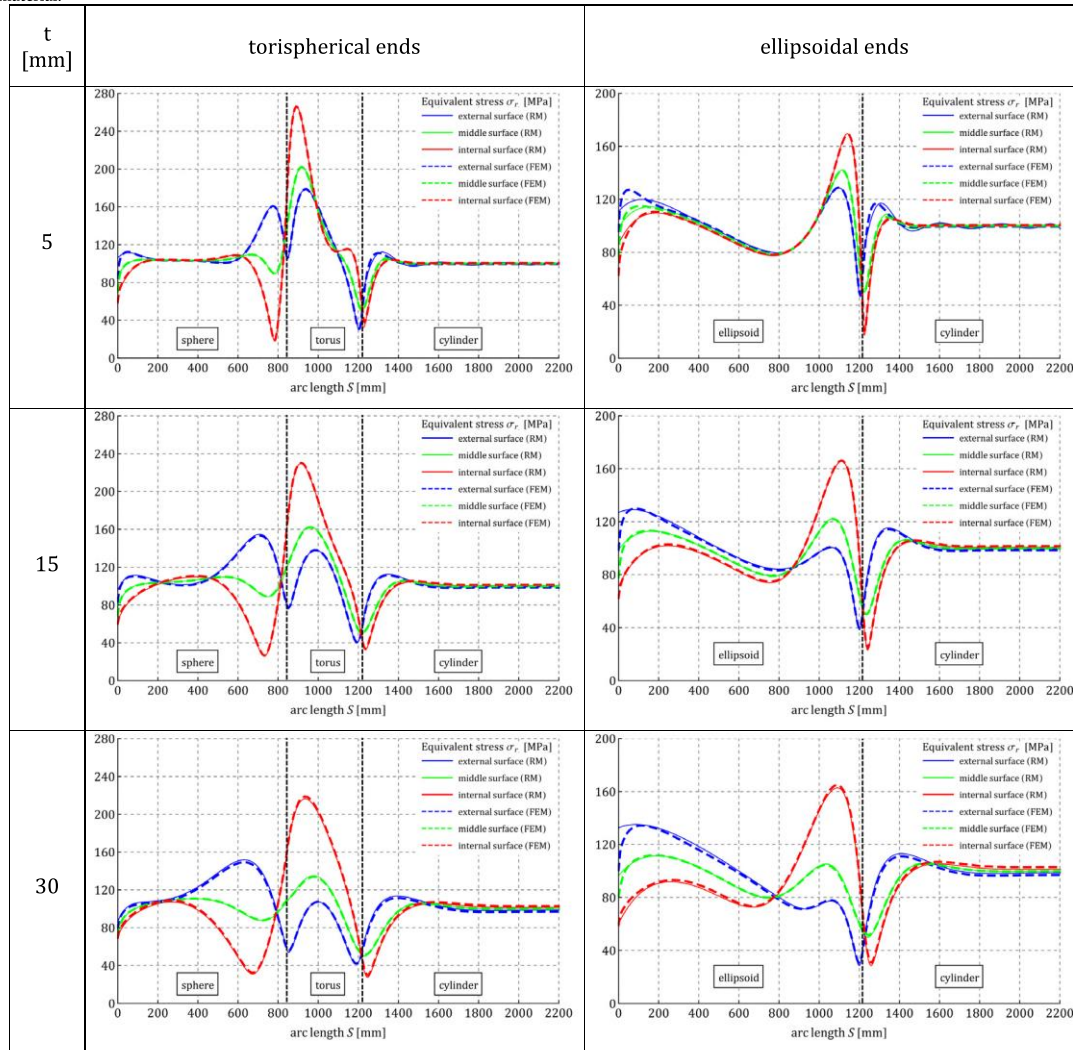
precise. Despite the relative peak stress difference between ellipsoidal and equivalent torispherical end ranges from 32% to 56% depending on thickness, the standards allow to design the latter as true ellipsoidal end. To further investigate this discrepancy, the analyses should consider the shape of the imperfect, manufactured dished ends. The performed analyses showed that the influence of the orthotropy on the stress distribution is crucial, therefore it should be taken into consideration during the design of pressure vessels. The values of the orthotropy coefficient lesser than unity i.e. when strain hardening is greater towards the meridional direction can lead to the problem where the peak stress moves to the vertex of the dished end. The presented results considered less negative case where the orthotropy coefficient is greater than unity. The real values of the orthotropy coefficient in the pressure vessels are difficult to predict due to the possible variances in the mechanical properties of different steels as well as the manufacturing processes.

Summarizing the findings of the performed analyses one may conclude that the accuracy of the achieved results is preserved for relatively thick shells considering their thickness to radii of curvature ratio, even in the areas of discontinuity. The outcome of the study shows the potential in the application of the Ritz method to the static problems

Table 23

Results comparison summary for the pressure vessel with torispherical dished ends — orthotropic material.

	t [mm]	Ritz method	FEM	Relative difference [%]
σ_{rmax} [MPa]	5	266.0	266.1	0.02064
	15	229.7	230.2	0.2098
	30	216.5	219.0	1.096
d_{vmax} [mm]	5	0.6546	0.6549	0.04571
	15	0.5333	0.5343	0.1799
	30	0.4289	0.4314	0.5885
U_{ε} [kJ]	5	16.40	16.36	0.1858
	15	46.502	46.203	0.64758
	30	87.690	86.463	1.4190

not only considering the pressure vessels, but for the design of wide spectrum of the shell structures.

CRediT authorship contribution statement

Krzysztof Sowiński: Conceptualization, Methodology, Validation, Formal analysis, Investigation, Writing - original data, Writing - review

Table 24
Results comparison summary for the pressure vessel with ellipsoidal dished ends — orthotropic material.

	t [mm]	Ritz method	FEM	Relative difference [%]
σ_{rmax} [MPa]	5	169.5	169.1	0.1931
	15	165.8	166.1	0.2163
	30	162.8	165.0	1.310
d_{vmax} [mm]	5	0.5061	0.5061	0.0007731
	15	0.4067	0.4228	0.2549
	30	0.3188	0.4193	0.7548
U_ε [kJ]	5	13.69	13.65	0.3154
	15	39.89	39.50	0.9985
	30	77.14	75.61	2.020

& editing, Visualisation, Supervision, Project administration, Funding acquisition.

Declaration of competing interest

The authors declare that they have no known competing financial interests or personal relationships that could have appeared to influence the work reported in this paper.

Acknowledgement

Funding

References

[1] Z.E. Mazurkiewicz, R.T. Nagórski, Powłoki Obrotowe Sprężyste, Państwowe Wydawnictwo Naukowe, Warsaw, 1987.

[2] E. Ventsel, T. Krauthammer, Thin plates and shells, in: Theory, Analysis, and Applications, Marcel Dekker, Inc., New York, Basel, 2001.

[3] A. Zingoni, Shell Structures in Civil and Mechanical Engineering, ICE Publishing, 2017.

[4] EN 13445-3:2002 Unfired pressure vessels – Part 3: Design, European Committee for Standardization.

[5] ASME, ASME Boiler and Pressure Vessel Code, Section VIII, Division 1, American Society of Mechanical Engineers, New York, NY, 2015.

[6] ASME, ASME Boiler and Pressure Vessel Code, Section VIII, Division 2, American Society of Mechanical Engineers, 2015.

[7] J. Błachut, K. Magnucki, Strength, stability, and optimization of pressure vessels: Review of selected problems, Appl. Mech. Rev. 61 (6) (2008) 060801.

[8] K. Magnucki, W. Szyc, J. Lewiński, Minimization of stress concentration factor in cylindrical pressure vessels with ellipsoidal heads, Int. J. Press. Vessels Pip. 79 (12) (2002) 841–846.

[9] Y. Kisioglu, J.R. Brevick, G.L. Kinzel, Minimum material design for propane cylinder end closures, J. Press. Vessel Technol. 130 (2008) 015001.

[10] K. Magnucki, J. Lewiński, R. Cichy, Strength and buckling problems of dished heads of pressure vessels—Contemporary look, J. Press. Vessel Technol. 140 (4) (2018) 041201.

[11] K. Magnucki, J. Lewiński, Fully stressed head of a pressure vessel, Thin-Walled Struct. 38 (2) (2000) 167–178.

[12] K. Sowiński, K. Magnucki, Shaping of dished heads of the cylindrical pressure vessel for diminishing of the edge effect, Thin-Walled Struct. 131 (2018) 746–754.

[13] A. Zingoni, B. Mokhothu, N. Enoma, A theoretical formulation for the stress analysis of multi-segmented spherical shells for high-volume liquid containment, Eng. Struct. 87 (2015) 21–31.

[14] A. Zingoni, Simplification of the derivation of influence coefficients for symmetric frusta of shells of revolution, Thin-Walled Struct. 47 (2009) 912–918.

[15] J. Lewiński, K. Magnucki, Shaping of a middle surface of a dished head of a circular cylindrical pressure vessel, Press. Vessels Pip. Conf. 48 (2) (2010) 297–307.

[16] K. Magnucki, P. Jasion, M. Rodak, Strength and buckling of an untypical dished head of a cylindrical pressure vessel, Int. J. Press. Vessels Pip. 161 (2018) 17–21.

[17] J. Krużelecki, R. Proszowski, Optimization of the geometry of thin-walled uniform-strength pressure vessel end closures, Eng. Optim. 47 (2015) 238–264.

[18] P. Jasion, K. Magnucki, Elastic buckling of Cassini ovaloidal shells under external pressure – Theoretical study, Arch. Mech. 67 (2) (2015) 179–192.

[19] P. Jasion, K. Magnucki, Theoretical investigation of the strength and stability of special pseudospherical shells under external pressure, Thin-Walled Struct. 93 (2015) 88–93.

[20] P. Jasion, K. Magnucki, Elastic buckling of clothoidal-spherical shells under external pressure - Theoretical study, Thin-Walled Struct. 86 (2015) 18–23.

[21] P. Jasion, K. Magnucki, Elastic buckling of barrelled shell under external pressure, Thin-Walled Struct. 45 (4) (2007) 393–399.

[22] P. Jasion, Stability analysis of shells of revolution under pressure conditions, Thin-Walled Struct. 47 (3) (2009) 311–317.

[23] K. Sowiński, P. Jasion, Closed shell of revolution with meridian based on Booth lemniscate loaded with external pressure, Thin-Walled Struct. 144 (2019) 106284.

[24] K. Sowiński, Buckling of shells with special shapes with corrugated middle surfaces – FEM study, Eng. Struct. 179 (2019) 310–320.

[25] J. Zhang, M. Wang, W. Wang, W. Tang, Y. Zhu, Investigation on egg-shaped pressure hulls, Mar. Struct. 52 (2017) 50–66.

[26] J. Zhang, W.M. Wang, W.C. Cui, W.X. Tang, F. Wang, Y. Chen, Buckling of longan-shaped shells under external pressure, Mar. Struct. 60 (2018) 218–225.

[27] J. Zhang, W. Wang, F. Wang, W. Tang, W. Cui, W. Wang, Elastic buckling of externally pressurized Cassini oval shells with various shape indices, Thin-Walled Struct. 122 (2018) 83–89.

[28] Y. Kumar, The Rayleigh-Ritz method for linear dynamic, static and buckling behaviour of beams, shells and plates: A literature review, J. Vib. Control 24 (2018) 1205–1227.

[29] D. Shahgholian-Ghahfarokhi, M. Safarpour, A. Rahimi, Torsional buckling analyses of functionally graded porous nanocomposite cylindrical shells reinforced with graphene platelets (GPLs), Mech. Based Des. Struct. Mach. 49 (1) (2021) 81–102.

[30] B. Qin, R. Zhong, T. Wang, Q. Wang, Y. Xu, Z. Hu, A unified Fourier series solution for vibration analysis of FG-CNTRC cylindrical, conical shells and annular plates with arbitrary boundary conditions, Compos. Struct. 235 (2020) 111549.

[31] A.V. Lopatin, E.V. Morozov, Axisymmetric vibrations of the composite orthotropic cylindrical shell with rigid weightless end disks, Thin-Walled Struct. 135 (2019) 463–471.

[32] Z. Qin, X. Pang, B. Safaei, F. Chu, Free vibration analysis of rotating functionally graded CNT reinforced composite cylindrical shells with arbitrary boundary conditions, Compos. Struct. 220 (2019) 847–860.

[33] F. Pang, H. Li, X. Wang, X. Miao, S. Li, A semi analytical method for the free vibration of doubly-curved shells of revolution, Comput. Math. Appl. 75 (2018) 3249–3268.

[34] I. Senjanovic, I. Áatipovic, N. Alujevic, D. Cakmak, N. Vladimir, A finite strip for the vibration analysis of rotating toroidal shell under internal pressure, J. Vib. Acoust. Trans. ASME 141 (2) (2019) 021013.

[35] K. Choe, K. Kim, Q. Wang, Dynamic analysis of composite laminated doubly-curved revolution shell based on higher order shear deformation theory, Compos. Struct. 225 (2019) 111155.

[36] T.G. Seipp, N. Barkley, C. Wright, Ellipsoidal head rules: A comparison between ASME section VIII, Divisions 1 and 2, in: Proceedings of the ASME 2017 Pressure Vessels and Piping Conference, PVP 2017-65858.

Appendix A2. Shaping of dished heads of the cylindrical pressure vessel for diminishing of the edge effect

Full length article

Shaping of dished heads of the cylindrical pressure vessel for diminishing of the edge effect

Krzysztof Sowiński[a,*], Krzysztof Magnucki[b]

[a] Institute of Applied Mechanics, Faculty of Mechanical Engineering and Management, Poznan University of Technology, ul. Jana Pawla II 24, 60-965 Poznan, Poland
[b] Institute of Rail Vehicles "TABOR", ul. Warszawska 181, 61-055 Poznan, Poland

ABSTRACT

The paper is devoted to diminishing of the edge effect in three nonstandard dished heads of a cylindrical pressure vessel subjected to internal uniform pressure. The problem of the edge effect diminishing in the joint of the dished head with the cylindrical shell is analytically and numerically studied. The meridians of the analysed dished heads as the shells of revolution are plane curves in the Cassini oval, Booth lemniscate and clothoid forms. Geometrical relationships of the middle surfaces of the dished heads are formulated. The stress state of these dished heads are analytically and numerically studied using finite element method in Ansys system. The results of the studies are compared and presented in Tables and Figures.

1. Introduction

Stationary or mobile pressure vessels usually consist of the cylinder and two dished heads. Such structures are loaded with internal, uniform pressure. Standard shapes of the dished head i.e.: hemispherical, torispherical and ellipsoidal are subjected to the stress concentration occurring in the area of joint of the cylinder and dished head. The minimization of the stress concentration is a significant problem, particularly in designing of pressure vessels. Stress concentration phenomenon, caused by the bending of the structure in the meridional plane is called the edge effect. Reason of such structural behaviour is sudden change in the meridional curvature in a dished head.

Ventsel and Krauthammer [1] among others, described, the basis of the theory of thin-walled shells, membrane and bending states with special attention paid to the edge effect. There are many papers devoted to the problem of the edge effect minimization. Magnucki and Lewiński [2] formulated and theoretically analysed the problem of bending and shear stresses in the joint of the pressure vessels by introducing some special function describing shape of the meridian. Zingoni [3] explained the theories of membrane and bending behaviour of elastic shells, and applied those theories to numerous practical engineering cases. Magnucki et al. [4] described the minimization of stress concentration factor in cylindrical pressure vessels with ellipsoidal heads. Ortega and Robles [5] investigated a methodology of finding optimal forms of shells of revolution, which enables obtaining approximately bending-free geometries. Banichuk [6] presented shape and thickness

optimization of the shell of revolution. Kisioglu et al. [7] considered strength and buckling of propane cylinder end-closures using experimental and numerical approaches. Błachut and Magnucki [8] presented a review work concerning optimization in terms of structural stability and strength of pressure vessels. Zingoni [9] presented simplification of determining influence coefficients in force method referring to various shells in non-membrane stress state. Lewiński and Magnucki [10] proposed cosinusoidal-spherical dished head shape of a cylindrical pressure vessel which highly reduced the edge effect. Kruzelecki and Proszowski [11] presented the shape optimization of dished head represented by convex Bézier polynomial. Zingoni investigated discontinuity effect in the shells junctions considering multi-segmented spherical shells [12], sludge digesters [13,14] and conical shells [15]. Pietraszkiewicz and Konopińska [16] delivered a wide review of multiple types of joints in shell structures in the aspects of stress distribution. Magnucki et al. [17] focused on elimination of the edge effect in pressure vessels. Authors proposed a meridian of dished head in form of a polynomial of the fifth degree and a circular arc. Such shape ensured significantly lower effect of the bending. Zingoni [18] reviewed recent research on the strength, stability and vibration behaviour of liquid-containment shell structures.

Due to thin-walled nature of pressure vessels, structural stability has great meaning in their analysis. Błachut [19] presented buckling of composite shallow spherical caps loaded with external pressure. Błachut [20] reviewed buckling behaviour of multiple shell structures including domed ends. Błachut [21] compared sensitivity of buckling

---

load to initial shape imperfection of externally pressurised steel domes. Jasion and Magnucki described the buckling problems of Cassini ovaloidal [22] and clothoidal-spherical [23] shells under external pressure. Błachut [24] investigated buckling, collapse and first ply failure of spheroidal shells under external pressure. Zhang et al. [25] analysed buckling and post-buckling behaviour of egg-shaped shells. Zhang et al. [26] examined the effect of shape on elastic buckling of Cassini oval shells under uniform external pressure.

It is assumed within paper, the desired shape of the dished head must meet two particular conditions. Maximum stress in a cylindrical pressure vessel shall not be higher than in a cylindrical shell in the membrane stress state. The above condition implies elimination of the edge effect in the area of joint. The second condition is to achieve membrane stress state in the whole structure, maintaining possibly lowest value of the relative depth of dished head. Reasoning behind it lies strictly within practical importance i.e. applications and manufacturing process.

The subject of the analytical and numerical studies of the paper includes the following three nonstandard Cassini ovaloidal, Booth ovaloidal and clothoidal dished heads. Exemplary shapes of these curves are shown in Fig. 1. Their mathematical description is presented later in the paper.

The meridional curves are formulated in such a manner that allows to modify relative depth of the dished head, therefore their curvatures and stress distribution change. Stress concentration factor is being analysed in a function of the relative depth for the selected curves. The problem is investigated analytically as well as with the use of FE method.

2. Analytical study

2.1. Membrane stress state

Meridional and circumferential force intensity: N_1, N_2 in the shell structure loaded with internal uniform pressure are following:

$$N_1 = \frac{1}{2} p R_2, \tag{1}$$

$$N_2 = \frac{1}{2} p R_2 \left(2 - \frac{R_2}{R_1} \right), \tag{2}$$

where: p – internal uniform pressure, R_1, R_2 - meridional and circumferential radius correspondingly

Stress resultants in the principal directions:

$$\sigma_1 = \frac{N_1}{t_s}, \quad \sigma_2 = \frac{N_2}{t_s}, \tag{3}$$

where t_s is the thickness of a shell.

Equivalent von Mises stress

$$\sigma_{eq} = \sqrt{\sigma_1{}^2 - \sigma_1 \sigma_2 + \sigma_2{}^2}. \tag{4}$$

Applying above for the cylindrical shell for which $R_1 \rightarrow \infty$, $R_2 = R_0$ one obtains

$$\sigma_{eq\,0} = \frac{\sqrt{3}}{2} \frac{p}{t_s} R_0, \tag{5}$$

where R_0 is radius of cylindrical shell.

To compare equivalent stress in both parts of a vessel, relative equivalent stress is introduced

$$\tilde{\sigma} = \frac{\sigma_{eq\,h}}{\sigma_{eq\,0}}, \tag{6}$$

where: $\sigma_{eq\,h}$ — equivalent von Mises stress in a dished head.

2.2. General geometry of dished head

Any dished head as a part of cylindrical pressure vessel is a surface of revolution with positive Gaussian curvature. Standard dished heads are ellipsoidal, torispherical and hemispherical. The geometrical relation for any surface of revolution is

$$\frac{d}{d\theta} (R_2 sin\theta) = R_1 cos\theta, \tag{7}$$

where angular coordinate $\theta_0 \leq \theta \leq \theta_1$.

Geometry of a cylindrical pressure vessel is presented in Fig. 2.

As it appears from Fig. 2 and Eq. (7) geometry of a dished head can be defined by the principal radii: R_1, R_2 in a function of the angular coordinate $0 \leq \theta \leq \pi/2$. Assuming that dished head is represented by a plane curve (meridian) $r(x)$ described in Cartesian coordinate system, meridional principal radius can be resolved from equation

$$R_1 = - \frac{\left[1 + \left(\frac{dr}{dx} \right)^2 \right]^{\frac{3}{2}}}{\frac{d^2 r}{dx^2}}. \tag{8}$$

$$R_2 = r \sqrt{1 + \left(\frac{dr}{dx} \right)^2}. \tag{9}$$

Circumferential radius is defined in following manner

Length of an arbitrary meridian in Cartesian coordinate system

$$s = \int_0^h \sqrt{1 + \left(\frac{dr}{dx} \right)^2} \, dx \tag{10}$$

To maintain consistency of the vessel geometry in the joint of the cylindrical shell and a dished head, following conditions must be fulfilled

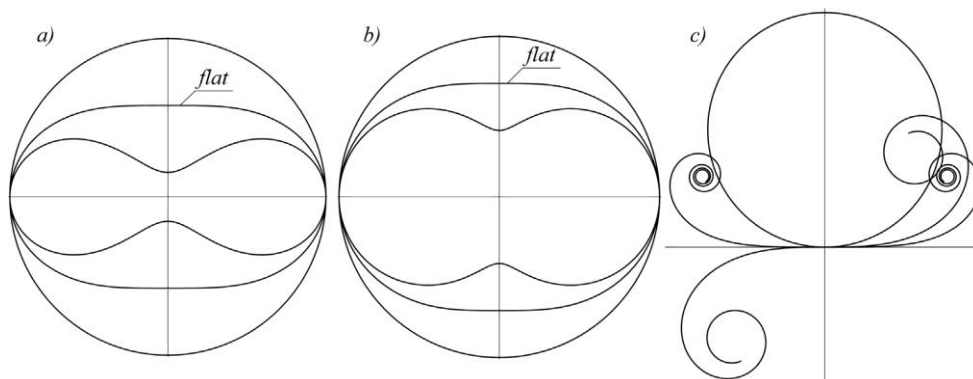$$\frac{dr}{dx} \Big|_0 = 0, \quad r(0) = R_0. \tag{11}$$

Fig. 1. Exemplary shapes of: a) Cassini ovals, b) Booth ovals, c) generalized clothoids.
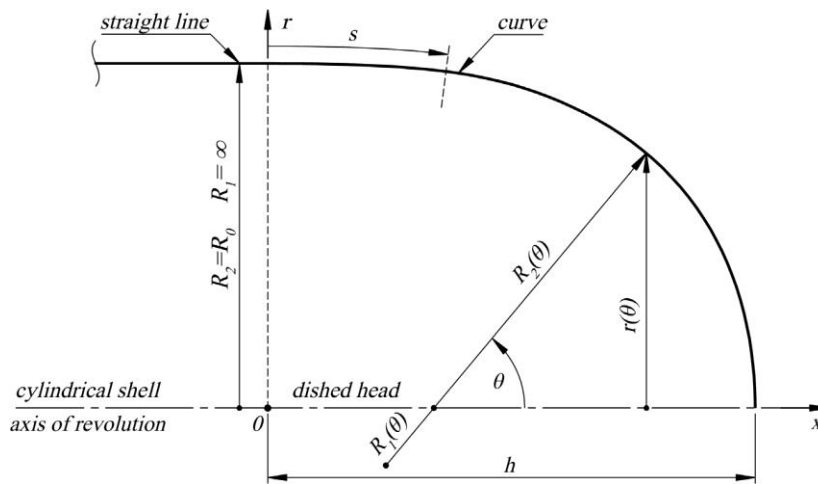
Fig. 2. Geometry of a cylindrical pressure vessel.

Standard dished heads are subjected to stress concentration due to discontinuity of their curvatures with the cylindrical shell. Necessary condition of the edge effect elimination is equality of the meridional radius in the joint

$$\lim_{x \to 0} R_1 = \infty. \tag{12}$$

It is more convenient to express necessary condition (Eq. (12)) in terms of the curvature

$$K_1 = \frac{1}{R_1}, \tag{13}$$

$$K_1(0) = 0. \tag{14}$$

Necessary condition is insufficient to eliminate the edge effect. To define sufficient condition one must consider the change in the meridional curvature of the dished head. Such condition is not defined yet, therefore the problem remains vital. However, to reduce intensity of the edge effect in the joint, condition of continuity of the meridional curvature is introduced

$$\frac{dK_1}{dx}\Big|_0 = 0. \tag{15}$$

Important geometrical parameter of the dished head is its relative depth β, defined as follows

$$\beta = \frac{h}{R_0}, \tag{16}$$

where: R_0 – radius of the cylindrical shell, h - depth of the head (Fig. 2).

Due to practical limitations related to manufacturing process of the dished heads it is essential to keep relatively low value of parameter β. For standardised ellipsoidal heads it is $\beta \approx 0.5$.

2.3. Cassini ovaloidal dished head

Cassini oval is a quadratic plane curve described as a set of points, such that the product of its distances from two fixed points is constant. Considering the desired shape of dished head, only flat (Fig. 1) oval is taken into account. Such choice ensures continuity of meridional radius in the joint of the pressure vessel (Eq. (15)). To change the relative depth of the head, standard geometry of Cassini oval is modified to following form

$$r_c(\xi) = R_0 \tilde{r}_c(\xi), \tag{17}$$

$$\tilde{r}_c(\xi) = \sqrt{-1 - 3\frac{\xi^2}{\beta^2} + 2\sqrt{1 + 3\frac{\xi^2}{\beta^2}}}, \tag{18}$$

where $\xi = x/R_0$ is a dimensionless coordinate $0 \le \xi \le \beta$.

Ovaloidal heads, based on Eq. (18) for various value of parameter β are shown in Fig. 3.

Meridional radius R_{1c} and dimensionless meridional radius $\tilde{R}_{1c}$ for Cassini oval are obtained

$$R_{1c} = R_0 \tilde{R}_{1c}, \tag{19}$$

$$\tilde{R}_{1c} = -\frac{1}{3}\beta^2 \frac{\left[1 + \frac{9}{\beta^4}\frac{(2 - A_1(\xi))^2}{A_1(\xi)^2 \tilde{r}_c(\xi)^2}\xi^2\right]^{\frac{3}{2}}}{\frac{2 - A_1(\xi)}{A_1(\xi)\tilde{r}_c(\xi)} - \frac{3}{\beta^2}\frac{(2 - A_1(\xi))^2 A_1(\xi) + 8\tilde{r}_c(\xi)^2}{A_1(\xi)^3 \tilde{r}_c(\xi)^3}\xi^2}, \tag{20}$$
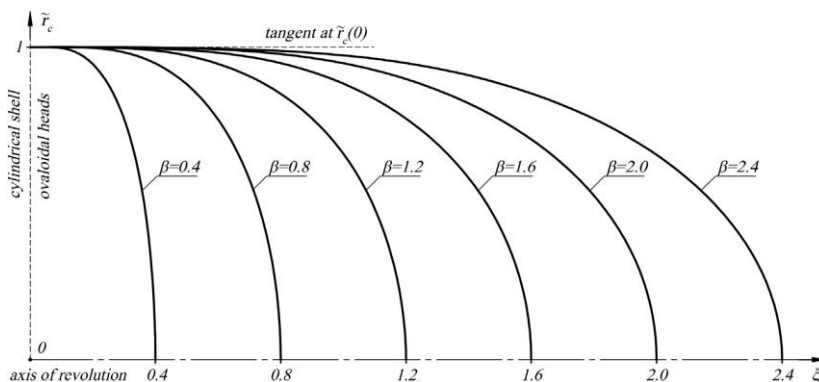
Fig. 3. Dished heads based on the flat Cassini oval with various relative depth β.

where

$$A_1\left(\xi\right) = 2\sqrt{1 + 3\frac{\xi^2}{\beta^2}}.$$
(21)

It follows from Eq. (20) that regardless of relative depth β, necessary condition (Eq. (12)) is fulfilled. Moreover condition described by Eq. (15) occurs

$$\frac{dK_{1c}}{dx}\big|_0 = 0.$$
(22)

Full description of Eq. (22) is not presented due to its cumbersome form. Referring to Eq. (9) circumferential radius of Cassini ovaloid is obtained

$$R_{2c} = R_0\widetilde{r}_c(\xi)\sqrt{1 + \frac{9}{\beta^4}\frac{(2 - A_1(\xi))^2}{A_1(\xi)^2 r_c(\xi)^2}\xi^2}.$$
(23)

Length of the meridian in form of modified Cassini oval is following

$$s_c = R_0\widetilde{s}_c,$$
(24)

dimensionless curve length

$$\widetilde{s}_c = \int_0^\beta \sqrt{1 + \frac{9}{\beta^4}\frac{(2 - A_1(\xi))^2}{A_1(\xi)^2 r_c(\xi)^2}\xi^2}\,d\xi.$$
(25)

Dimensionless meridional curvature $\widetilde{K}_{1c}$ in a function of dimensionless curve length $\widetilde{s}_c$ for Cassini ovaloids with different β parameter is presented in Fig. 4.

From Eqs. (1) and (2) meridional and circumferential force intensity are obtained. Applying those to Eqs. (3) and (4) equivalent von Mises stress distribution is evaluated. Fig. 5 presents relative equivalent stress for Cassini ovaloidal heads $\widetilde{\sigma}_c$ (Eq. (6))

2.4. Booth ovaloidal dished head

Booth lemniscate is a plane curve of order four. Assuming desired shape of a dished head only flat (Fig. 1) Booth lemniscate is considered. To change relative depth of a dished head, standard geometry of flat Booth lemniscate is modified to following form:

$$r_b(\xi) = R_0\widetilde{r}_b(\xi),$$
(26)

$$\widetilde{r}_b(\xi) = \frac{\sqrt{2}}{2}\sqrt{1 - \left(2\frac{\xi}{\beta}\right)^2 + \sqrt{1 + 2\left(2\frac{\xi}{\beta}\right)^2}}.$$
(27)

Dished head, based on the curve (Eq. (27)) for various parameter β are shown in Fig. 6.

Meridional radius R_{1b} and dimensionless meridional radius $\widetilde{R}_{1b}$ of Booth ovaloid are obtained
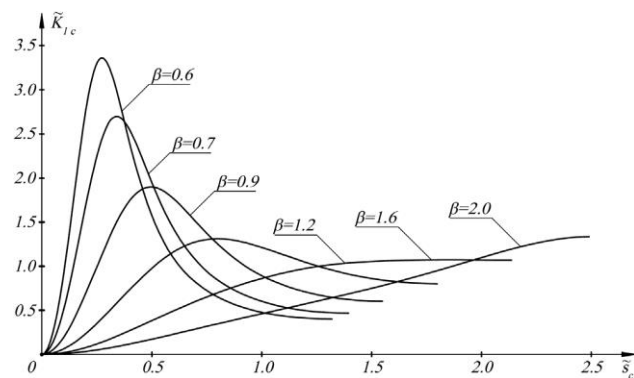
Fig. 4. Dimensionless meridional curvature for Cassini ovaloids with different relative depth β.
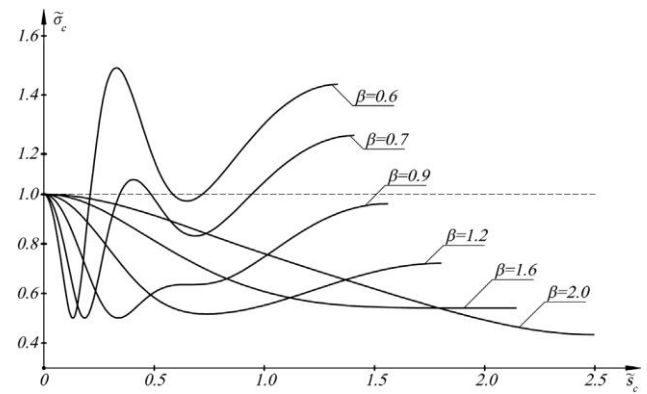
Fig. 5. Relative equivalent von Mises stress for Cassini ovaloids with diverse relative depth β.

$$R_{1b} = R_0\widetilde{R}_{1b},$$
(28)

$$\widetilde{R}_{1b} = -\frac{\sqrt{2}}{4}\beta^2\frac{\left[1 + \frac{8}{\beta^4}\frac{(1 - B_1(\xi))^2}{B_1(\xi)^2 B_2(\xi)^2}\xi^2\right]^{\frac{3}{2}}}{\frac{1 - B_1(\xi)}{B_1(\xi)B_2(\xi)} - \frac{4}{\beta^2}\frac{(B_1(\xi) - 1)^2 B_1(\xi) + 2B_2(\xi)^2}{B_1(\xi)^3 B_2(\xi)^3}\xi^2},$$
(29)

where:

$$B_1(\xi) = \sqrt{1 + 2\left(2\frac{\xi}{\beta}\right)^2},$$
(30)

$$B_2(\xi) = \sqrt{1 - \left(2\frac{\xi}{\beta}\right)^2 + B_1(\xi)}.$$
(31)

Analogously to Cassini ovaloid, Booth lemniscate, regardless of β parameter meets the condition (Eq. (12)). Additionally such curve meets the condition described by Eq. (15). Dimensionless meridional curvature for Booth ovaloids $\widetilde{K}_{1b}$ with different β parameter is presented in Fig. 7.

Circumferential radius is determined from Eq. (9)

$$R_{2b} = R_0\widetilde{r}_b(\xi)\sqrt{1 + \frac{8}{\beta^4}\frac{(1 - B_1(\xi))^2}{B_1(\xi)^2 B_2(\xi)^2}\xi^2}.$$
(32)

Length of the meridian in form of modified Cassini oval is following

$$s_b = R_0\widetilde{s}_b,$$
(33)

dimensionless curve length

$$\widetilde{s}_b = \int_0^\beta \sqrt{1 + \frac{8}{\beta^4}\frac{(1 - B_1(\xi))^2}{B_1(\xi)^2 B_2(\xi)^2}\xi^2}\,d\xi.$$
(34)

From Eqs. (1) and (2) meridional and circumferential force intensity is obtained. Applying those to Eqs. (3) and (4) equivalent von Mises stress distribution is evaluated. Fig. 8 presents relative equivalent von Mises stress for Booth lemniscate $\widetilde{\sigma}_b$ (Eq. (6)).

2.5. Clothoidal dished head

Clothoid is a curve the curvature of which changes linearly with its curve length. Complete description of its geometry can be found in [27]. To study the edge effect, geometry of a clothoid is modified by adding exponential coefficient k. The new curve is named generalized form of clothoid. Such modification allows to change relative depth of the dished head. Principal radius of the generalized form of clothoid is expressed in following manner
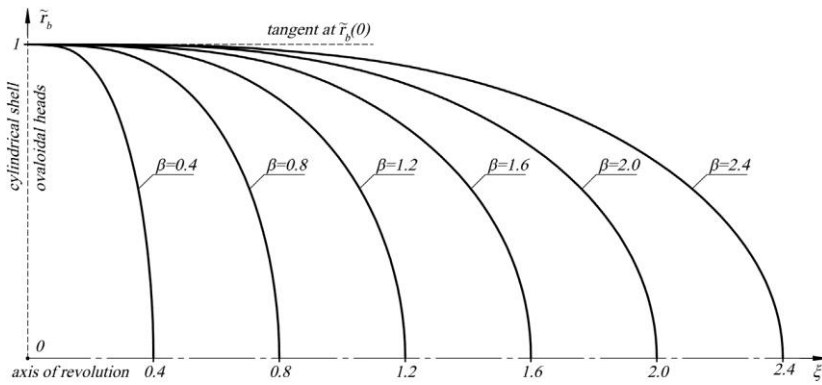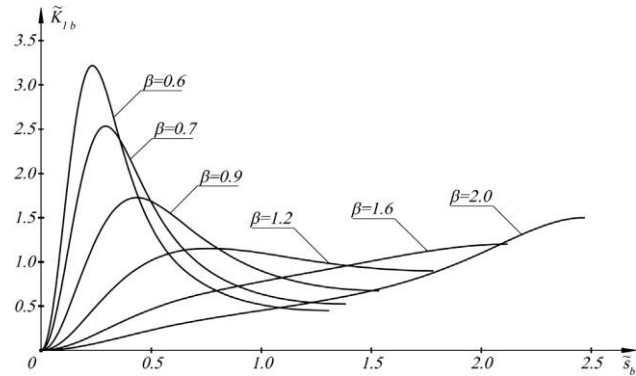
$$R_{1s} = a\left(\frac{a}{s}\right)^k,$$
(35)

Fig. 6. Dished heads based on the flat Booth lemniscate with various relative depth β.

Fig. 7. Dimensionless meridional curvature for Booth ovaloids with different relative depth β.
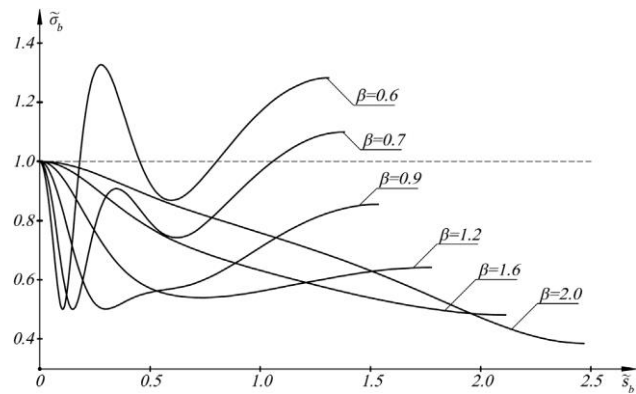

Fig. 8. Relative equivalent von Mises stress for Booth ovaloids with diverse relative depth β.

where: a – size coefficient, s – curve length.

Geometry of generalized form of clothoid is described by the parametric equations:

$$x = c_k a \widetilde{x}, \tag{36}$$

$$y = c_k a \widetilde{y}, \tag{37}$$

where coefficient c_k

$$c_k = \left(\frac{1+k}{2}\pi\right)^{\frac{1}{1+k}}. \tag{38}$$

Dimensionless coordinates $\widetilde{x}$ and $\widetilde{y}$ are following:

$$\widetilde{x} = \int_0^{t_1} \cos\left(\frac{\pi}{2}t^{1+k}\right)dt, \tag{39}$$

$$\widetilde{y} = \int_0^{t_1} \sin\left(\frac{\pi}{2}t^{1+k}\right)dt, \tag{40}$$

t – dimensionless parameter ($0 \leq t \leq t_1$). Assuming the shape of the dished head parameter t_1 must be in the range $0 \leq t_1 \leq 1$.

Size coefficient a can be evaluated assuming value of cylindrical shell radius R_0

$$a = \frac{R_0}{c_k \widetilde{y}(1)}. \tag{41}$$

To describe generalized clothoid in a similar manner to previous curves it requires modification of its coordinates. Considering above description of the geometry one may obtain coordinates in following form:

$$x_s = R_0 \widetilde{x}_s, \tag{42}$$

$$r_s = R_0 \widetilde{r}_s, \tag{43}$$

where dimensionless coordinates:

$$\widetilde{x}_s = \frac{\int_0^{t_1} \cos\left(\frac{\pi}{2}t^{1+k}\right)dt}{\int_0^1 \sin\left(\frac{\pi}{2}t^{1+k}\right)dt}, \tag{44}$$

$$\widetilde{r}_s = 1 - \frac{\int_0^{t_1} \sin\left(\frac{\pi}{2}t^{1+k}\right)dt}{\int_0^1 \sin\left(\frac{\pi}{2}t^{1+k}\right)dt}. \tag{45}$$

Determining geometry of generalized clothoid requires solving Eqs. (44) and (45) by numerical integration. To obtain exponential coefficient k for some specific values of parameter β one must take into account following relation

$$\beta = \frac{\int_0^1 \cos\left(\frac{\pi}{2}t^{1+k}\right)dt}{\int_0^1 \sin\left(\frac{\pi}{2}t^{1+k}\right)dt}. \tag{46}$$

Considering the form of Eq. (46), coefficient k cannot be resolved analytically, therefore numerical methods are required. Selected values of β and corresponding parameters k are shown in Table 1.

Geometry of dished heads described by generalized form of clothoid are presented in Fig. 9.

From Eq. (35) it stands that for $k = 1$ generalized clothoid represents a standard clothoid, and for $k = 0$ it is an circular arc. With the

Table 1
Relative depth β and corresponding exponential coefficient k.

Relative depth β	0.4	0.8	1.2	1.6	2.0	2.4
Exponential coefficient k	-0.676	-0.241	0.250	0.764	1.292	1.825
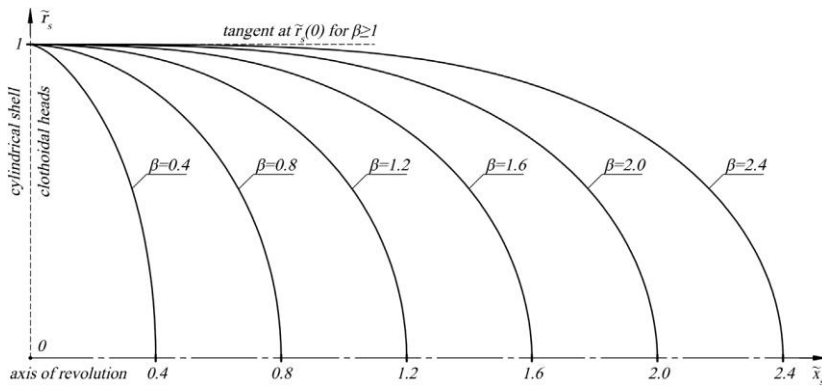
increase of exponential parameter k the relative depth β of the dished head increases. As it is shown in Fig. 9, for $k < 0$ ($\beta < 1$) there is no consistency of the geometry (Eq. (11)), therefore such cases are omitted, thus $k \geq 0$. Meridional and circumferential radii are expressed correspondingly:

$$R_{1s} = c_k a \widetilde{R}_{1s}, \tag{47}$$

$$R_{2s} = c_k a \widetilde{R}_{2s}, \tag{48}$$

where dimensionless radii $\widetilde{R}_1$, $\widetilde{R}_2$:

$$\widetilde{R}_{1s} = \frac{2}{(1+k)\pi t^k}, \tag{49}$$

$$\widetilde{R}_{2s} = \frac{\widetilde{r}_s}{\cos\left(\frac{\pi}{2}t_1^{1+k}\right)}. \tag{50}$$

For $k > 0$ radius of generalized clothoid in the joint is infinite $\widetilde{R}_{1s}(0) \rightarrow \infty$, while for $k = 0$, meridional radius remains constant $\widetilde{R}_{1s} = R_0$, which represents the hemispherical head. To analyse the geometry profoundly, curvature is derived

$$\frac{dK_{1s}}{dt} = \frac{1}{c_k a}\frac{d\widetilde{K}_{1s}}{dt}, \tag{51}$$

$$\frac{d\widetilde{K}_{1s}}{dt} = k\frac{(1+k)\pi t^{k-1}}{2}. \tag{52}$$

Unlike the previous two curves, derivative of curvature (Eq. (52)) in the joint ($t = 0$) varies depending on k parameter. Moreover it is described with a different parameter. Although it can be assumed that $t \rightarrow x$ for $t \approx 0$, therefore derivatives of curvature for all curves can be compared in the joint. It can be observed that for $k < 1$, Eq. (52) is infinity, while for $k > 1$ it remains zero. Additionally, when $k = 1$, limit of derivative of curvature remains constant and is equal to π. In this case, it describes standard clothoid for which curvature changes linearly along its length. Length s_s and dimensionless length $\widetilde{s}_s$ of generalized clothoid is following:

$$s_s = R_0 \widetilde{s}_s, \tag{53}$$

$$\widetilde{s}_s = \frac{t_1}{\int_0^1 \sin\left(\frac{\pi}{2}t^{1+k}\right)dt}. \tag{54}$$

Dimensionless meridional curvature $\widetilde{K}_{1s}$ in a function of dimensionless length of the curve is presented in Fig. 10.

To calculate the membrane stress resultants (Eq. (3)), circumferential radius R_{2s} is necessary (Eqs. (48), (50)), thus it is inevitable to numerically resolve Eq. (45). Relative equivalent stress (Eq. (6)) for clothoidal heads $\widetilde{\sigma}_s$ is presented in Fig. 11.
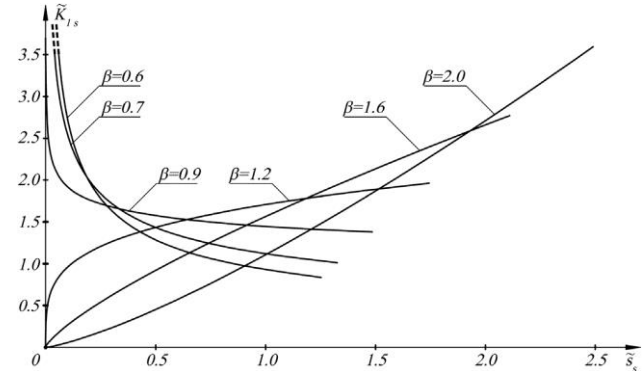
Fig. 10. Dimensionless meridional curvature for generalized clothoids with different exponential coefficient k.
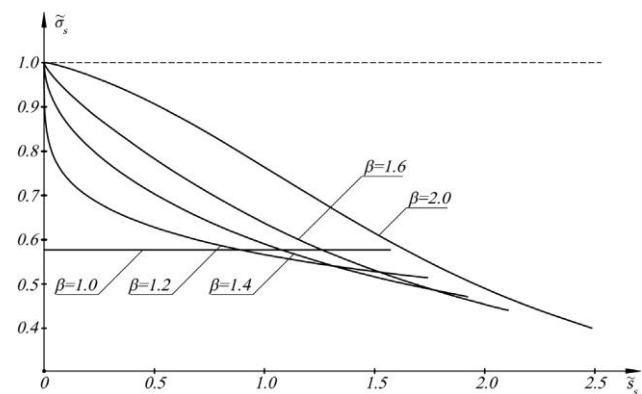
Fig. 11. Relative equivalent von Mises stress for clothoidal heads with diverse exponential coefficient k.

3. Numerical FEM study

3.1. Description of numerical analysis

From the membrane stress state it stands both bending and shear forces are neglected to simplify the problem. Such approach is justified for the structures with relatively low values of shell thickness and smooth geometry. Edge effect cannot be studied referring to the membrane stress state, therefore numerical FEM study is performed to obtain stress concentration factors for previously presented dished heads. Equivalent von Mises stress is analysed in the middle, inner and outer surface of the pressure vessel. It is expected that analytical description must be compatible with FEM solution in the middle surface,

excluding the area of the joint. Additionally elimination of the edge effect implies absolute unity of analytical and numerical approach.

To study the edge effect, static structural analysis in Ansys 18 software is performed. Analysis is limited to some specific values of the relative depth $\beta = 0.1, 0.2, \ldots, 2.5$. Additionally since generalized clothoid does not fulfil the geometry consistency condition for $\beta < 1$ (Eq. (11)), the relative depth of clothoidal dished heads must be equal to or greater than unity ($\beta \geq 1$). To achieve similar length of the pressure vessels meridians, constant volume is assumed. Due to that the length of the cylindrical shell is variable. The following geometrical dimensions are taken into account: radius of the cylindrical shell $R_0 = 1000$ mm, shell thickness $t_s = 2$ mm, volume $V = 12.5$ m^3. The mechanical properties of the material are: Young's modulus $E = 205$ GPa, Poisson's ratio $\nu = 0.3$.

Three symmetry planes are used to simplify the model, thus one-eighth of the pressure vessel geometry is analysed. Those planes are two mutually orthogonal, meridional planes and the plane dividing the model in half along its length. Symmetry conditions on the three edges are sufficient to support the structure. The model is loaded with internal uniform pressure which translates into nodal forces at each node of the mesh. Digital surface model of the pressure vessel is split into second order, quadrilateral and triangular shell elements SHELL281. Each node of the finite element has six degrees of freedom. Equivalent von Mises stress is analysed on the middle, inner and outer surface of the pressure vessel along its meridian. The FE model of the pressure vessel is presented in Fig. 12. Assumed finite elements size is 15 mm which ensures smooth stress distribution along the meridian. Importantly such size can be considered excessive to provide negligible values of discretization error, therefore mesh convergence analysis is not presented.

3.2. FEM results

Numerous FE models are solved to investigate the problem of the edge effect. Stress distribution along the pressure vessel meridian for three different types of heads are presented in Figs. 13–15. Numerical solution is compatible with the analytical solution in the membrane stress state in the middle surface, except the area of joint. Reason of such discrepancy is the membrane stress state disturbance due to the edge effect. Analytical solution is not presented on Figs. 13–15 to maintain good readability, however those can be compared with Figs. 5, 8, 11.

Presented solutions show that for all types of dished heads the edge effect decreases with an increase of parameter β. Such structural behaviour is related with the change of the meridional curvature distribution in the joint area. Intensity of the edge effect varies depending on the type of dished head. Comparing Figs. 13 and 14, for $\beta = 0.6$ and $\beta = 0.7$ it can be seen that the edge effect intensity is lower for Cassini
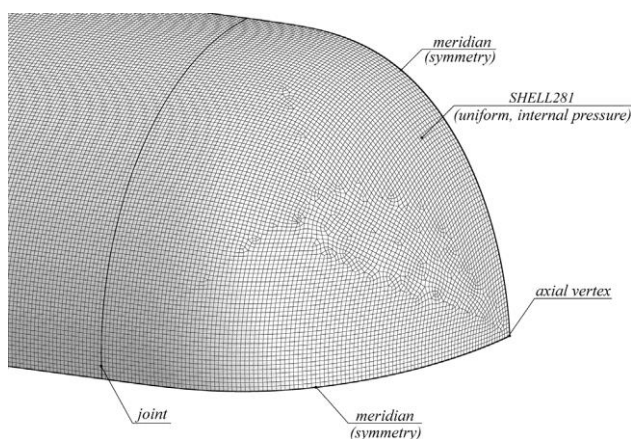
Fig. 12. FE model of the pressure vessel.

oval, similarly to its curvature growth. Therefore, performed study shows that the edge effect is characterised not only by the curvature in the joint, but also by its distribution in the area of joint. To fully eliminate the edge effect the meridional curvature must change smoothly, with suitably moderate tempo. Importantly, for all of the analysed curves peak stress value in the area of joint is observed in the outer surface of the cylindrical shell. This is not a general tendency for all cylindrical pressure vessels, since for some of the normalised dished heads peak stress occurs beyond the cylindrical shell.

Additionally for both ovaloidal heads, for relatively low values of relative depth β peak equivalent stress arises beyond the joint area. For those cases, presented in Figs. 13, 14 stress values significantly vary in the outer, middle and inner surfaces. It is essential that membrane stress state describes precisely stress in the middle surface. However, despite assuming particularly low value of shell thickness t_s comparing to the other geometrical dimensions, from numerical solution it stands stress may vary considerably across the thickness due to bending. Reason for that is a significant change in the meridional curvature. Such issue undoubtedly increases peak stress in the structure, therefore membrane stress state is insufficient to analyse stress in those cases.

To summarize obtained results maximum values of the stress in the cylindrical shell and dished heads is compared to the membrane stress in cylindrical shell $\sigma_{eq\,0}$ (Eq. (5)). Following relative equivalent stresses are introduced:

$$\tilde{\sigma}_{c\,c} = \frac{\sigma_{c\,c}}{\sigma_{eq\,0}}, \quad \tilde{\sigma}_{c\,b} = \frac{\sigma_{c\,b}}{\sigma_{eq\,0}}, \quad \tilde{\sigma}_{c\,s} = \frac{\sigma_{c\,s}}{\sigma_{eq\,0}}, \tag{55}$$

where: $\sigma_{c\,c}, \sigma_{c\,b}, \sigma_{c\,s}$ are maximum values of the equivalent stress in the cylindrical shell in the pressure vessel based on Cassini oval, Booth lemniscate and clothoid correspondingly,

$$\tilde{\sigma}_{h\,c} = \frac{\sigma_{h\,c}}{\sigma_{eq\,0}}, \quad \tilde{\sigma}_{h\,b} = \frac{\sigma_{h\,b}}{\sigma_{eq\,0}}, \quad \tilde{\sigma}_{h\,s} = \frac{\sigma_{h\,s}}{\sigma_{eq\,0}}, \tag{56}$$

where: $\sigma_{h\,c}, \sigma_{h\,b}, \sigma_{h\,s}$ are maximum values of the equivalent stress in the dished head in the pressure vessel based on Cassini oval, Booth lemniscate and clothoid correspondingly.

From Fig. 16 it stands stress concentration factor in the area of joint has certainly lower values for the ovaloidal dished heads. Those geometries fulfil introduced condition of continuity of meridional curvature (Eq. (15)). It can be observed that all relative maximum stress values converge to a value greater than unity. Reason for that is stress variability across shell thickness in FEM solution. In fact presented results converge to the relative stress value in the inner surface of the cylindrical shell. Such negligible stress differences are omitted in membrane stress theory by assuming stress is constant across the thickness. Observed convergence is much faster for Cassini oval and Booth lemniscate.

4. Conclusions – final remarks

Presented work focused on achieving the membrane stress state in a cylindrical pressure vessel with three nonstandard dished heads in Cassini oval, Booth lemniscate and clothoid form. Membrane stress state implies elimination of the edge effect. Such phenomenon is caused by the bending moments and shearing forces in the meridional plane of a shell. The problem of elimination of the edge effect is important particularly in designing pressure vessels. Many papers revealed that achieving negligibly intensity of the edge effect is possible for dished heads with relatively high values of relative depth β. Similarly, in presented study the edge effect was gradually reducing while increasing parameter β, which eventually leads to the membrane stress state. Depth of a dished head has great meaning in terms of practical importance, therefore normalised ellipsoidal and torispherical heads are suitably shallow. Elimination of the edge effect referring to dished heads must be considered maintaining possibly low value of the relative depth.
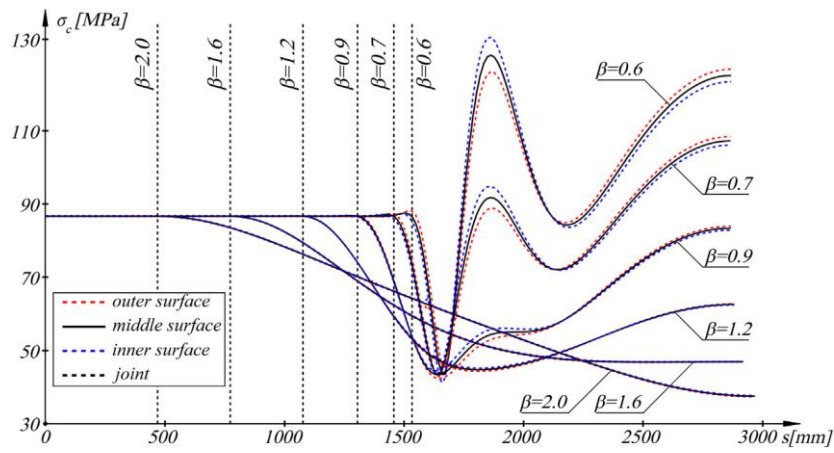
Fig. 13. Equivalent stress along tank meridian with Cassini ovaloidal heads with variable parameter β.
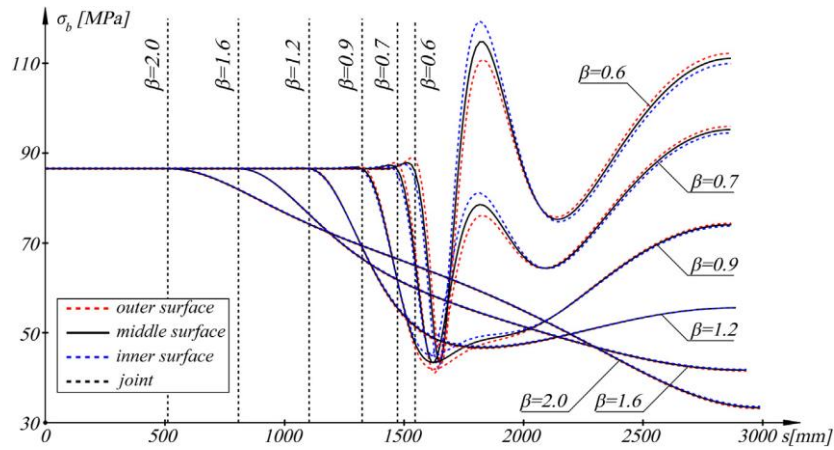

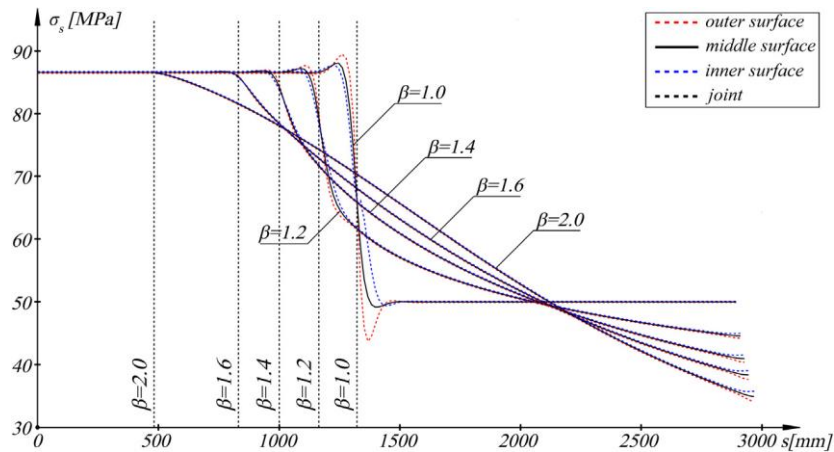Fig. 14. Equivalent stress along tank meridian with Booth ovaloidal heads with variable parameter β.

Fig. 15. Equivalent stress along tank meridian with clothoidal heads with variable parameter β.

Study shows that curves meeting the necessary condition of the edge effect elimination can still be prone to stress concentration in the area of joint. The problem is especially evident for clothoidal heads, which meet such condition for $\beta > 1$. Ovaloidal dished heads fulfil proposed condition of the continuity of the meridional curvature, which ensures considerably lower values of stress concentration factor in the area of joint. Moreover, dished heads based on Cassini oval and Booth lemniscate are characterised by substantially higher convergence ratio (Fig. 16). Consequently membrane stress state is achieved for lower values of relative depth. However, such geometries are susceptible to significantly greater values of stress beyond the area of joint for relatively low values of relative depth β due to bending. Reason for that is sudden change in meridional curvature. However, to define relatively shallow dished heads, meridional curvature must change at
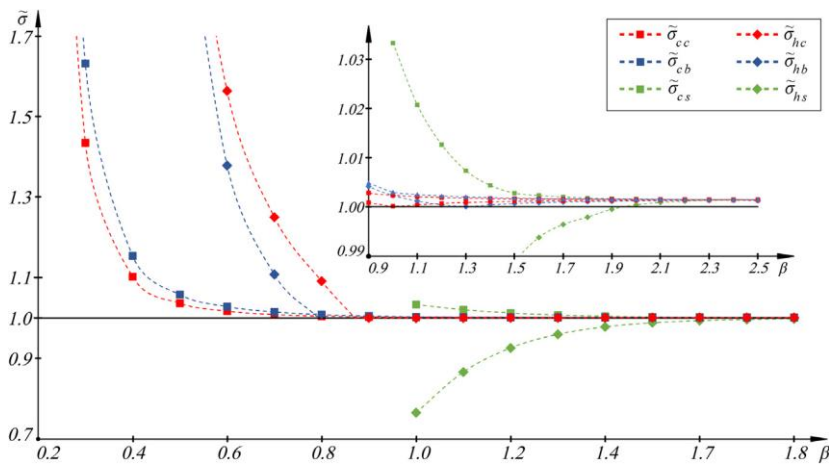
Fig. 16. Relative maximum values of the equivalent stress $\tilde{\sigma}$ described by Eqs. (55), (56).

considerably high rate. Having that in mind reducing both relative depth and the edge effect intensity is contradictory in some measure. Importantly, presented results show that elimination of the edge effect is not possible, however shaping of the dished heads allows to achieve negligible intensity of the investigated phenomenon.

Introduced condition (Eq. (15)) has significant meaning in terms of shaping the dished heads. Fundamental problem in shaping the dished heads is to ensure that maximum stress in the structure is not higher than in a cylindrical shell in the membrane stress state. Therefore, it is crucial that the edge effect must be primarily diminished in the area of joint. Presence of the edge effect beyond the joint does not necessarily imply excessive values of the stress, which can be observed in Figs. 13, 14. Additionally to achieve a desired geometry of the meridional curve, its curvature distribution must be undoubtedly taken into account. Curvature shall meet the introduced condition, and have possibly smoothest distribution along curve length.

Acknowledgement

References

[1] E. Ventsel, T. Krauthammer, Thin Plates and Shells. Theory, Analysis, and Applications, Marcel Dekker, Inc., New York, Basel, 2001.

[2] K. Magnucki, J. Lewiński, Fully stressed head of a pressure vessel, Thin-Walled Struct. 38 (2) (2000) 167–178.

[3] A. Zingoni, Shell Structures in Civil and Mechanical Engineering, ICE Publishing, 2017.

[4] K. Magnucki, W. Szyc, J. Lewiński, Minimization of stress concentration factor in cylindrical pressure vessels with ellipsoidal heads, Int. J. Press. Vessel Pip. 79 (12) (2002) 841–846.

[5] N. Ortega, S. Robles, Form finding of revolution shells by analyzing mechanical behaviour by means of the finite element method, J. Strain Anal. Eng. Des. 40 (8) (2005) 775–784.

[6] N. Banichuk, Optimization of axisymmetric membrane shells, J. Appl. Math. Mech.

71 (4) (2007) 527–535.

[7] Y. Kisioglu, J.R. Brevick, G.L. Kinzel, Minimum material design for propane cylinder end closures, J. Press. Vessel Technol., Trans. ASME 130 (2008) 015001-1–015001-9.

[8] J. Błachut, K. Magnucki, Strength, stability, and optimization of pressure vessels: review of selected problems, Appl. Mech. Rev. Trans. ASME 61 (6) (2008) (Ar 060801).

[9] A. Zingoni, Simplification of the derivation of influence coefficients for symmetric frusta of shells of revolution, Thin-Walled Struct. 47 (2009) 912–918.

[10] J. Lewiński, K. Magnucki, Shaping of a middle surface of a dished head of a circular cylindrical pressure vessel, J. Theor. Appl. Mech. 48 (2) (2010) 297–307.

[11] J. Kruzelecki, R. Proszowski, Shape optimization of thin-walled pressure vessel end closures, Struct. Multidisc. Optim. 46 (2012) 739–754.

[12] A. Zingoni, B. Mokhothu, N. Enoma, A theoretical formulation for the stress analysis of multi-segmented spherical shells for high-volume liquid containment, Eng. Struct. 87 (2015) 21–31.

[13] A. Zingoni, Stresses and deformations in egg-shaped sludge digesters: discontinuity effects, Thin-Walled Struct. 23 (2001) 1373–1382.

[14] A. Zingoni, Parametric stress distribution in shell-of-revolution sludge digesters of parabolic ogival form, Thin-Walled Struct. 40 (2002) 691–702.

[15] A. Zingoni, Discontinuity effect at cone-cone axisymmetric shell junctions, Thin-Walled Struct. 40 (2002) 877–891.

[16] W. Pietraszkiewicz, V. Konopińska, Junctions in shell structures: a review, Thin-Walled Struc. 95 (2015) 310–334.

[17] K. Magnucki, M. Rodak, P. Jasion, Strength and buckling of an untypical dished head of a cylindrical pressure vessels, Int. J. Press. Vessel Pip. 161 (2018) 17–21.

[18] A. Zingoni, Liquid-containment shells of revolution: a review of recent studies on strength, stability and dynamics, Thin-Walled Struct. 87 (2015) 102–114.

[19] J. Błachut, Buckling of externally pressurized shallow spherical caps from composites, Mech. Adv. Mat. Struct. 18 (2011) 96–105.

[20] J. Błachut, Experimental perspective on the buckling of pressure vessel components, Appl. Mech. Rev., Trans. ASME 66 (2013) 010803-1–010803-24.

[21] J. Błachut, Locally flattened or dented domes under external pressure, Thin-Walled Struct. 97 (2015) 44–52.

[22] P. Jasion, K. Magnucki, Elastic buckling of Cassini ovaloidal shells under external pressure – theoretical study, Arch. Mech. 67 (2) (2015) 179–192.

[23] P. Jasion, K. Magnucki, Elastic buckling of clothoidal-spherical shells under external pressure – theoretical study, Thin–Walled Struct. 86 (2015) 18–23.

[24] J. Błachut, Composite spheroidal shells under external pressure, Int. J. Comp. Methods Eng. Sci. Mech. 18 (1) (2017) 2–12.

[25] J. Zhang, M. Wang, W. Wang, W. Tang, Buckling of egg-shaped shell subjected to external pressure, Thin-Walled Struct. 113 (2017) 122–128.

[26] J. Zhang, M. Wang, F. Wang, W. Tang, W. Cui, W. Wang, Elastic buckling of Cassini oval shells with various shape indices, Thin-Walled Struct. 122 (2018) 83–89.

[27] E. Zeidler, W. Hackbusch, H.R. Schwarz, Oxford Users' Guide to Mathematics, Oxford University Press Inc., New York, 2004.

Appendix A3. Stress distribution optimization in dished ends of cylindrical pressure vessels

Full length article

Stress distribution optimization in dished ends of cylindrical pressure vessels

Krzysztof Sowiński *

Faculty of Mechanical Engineering, Institute of Applied Mechanics, Poznan University of Technology, ul. Jana Pawła II 24, 60-965 Poznan, Poland

ARTICLE INFO

ABSTRACT

The standard geometries of dished ends of cylindrical pressure vessels were developed at the beginning of the last century. Among them, there are ellipsoidal and torispherical geometries characterized by disadvantageous stress distribution, which is the primary determinant when designing shell structures. This paper focuses on shape optimization of dished ends with the depth equivalent to the standard ones, with the intent to minimize the maximum von Mises stress in a cylindrical pressure vessel. Referring to the Bézier curve (BC), a unique geometry of arbitrary order is developed to describe the parametric shape of the dished end. The optimization is implemented using two approaches. Initially, the fitness function is obtained analytically through the membrane theory (MT). A deterministic optimization algorithm is adopted to complete the procedure. Further, the optimization method is modified to obtain the fitness function using the finite element method (FEM). To process the solution, a genetic algorithm (GA) is employed. The obtained improvement of stress distribution is compelling while maintaining the manufacturability of the shell structure.

1. Introduction

Shell structures are widely used in numerous applications in engineering. The fundamental theories concerning thin-walled shells are discussed by Mazurkiewicz and Nagórski [1], Magnucki [2], Ventsel and Krauthammer [3] and Zingoni [4]. The most common types of such structures are cylindrical pressure vessels. Their purpose is mainly to store and transport gases and liquids, which can be considered a basic need of many industries. Typically, cylindrical pressure vessels consist of a cylindrical shell and two convex dished ends manufactured in plastic forming processes. Their design and shapes are described within consistent European and American standards, i.e. EN 13445 [5] and ASME Section VIII, Division 1, 2 [6,7].

A comprehensive review of dished ends, including standard geometries and untypical shapes, was performed by Magnucki et al. [8]. The standard dished ends are ellipsoidal, torispherical and hemispherical. The first two types are primarily used for the manufacturing of cylindrical pressure vessels. Notably, technical standards also allow to design and manufacture ellipsoidal dished ends as equivalent torispherical shells in terms of their relative depth, often referred to as semi-ellipsoidal dished ends. This approach is proven to be debatable due to severe discrepancies in stress distributions in the elastic range [9,10]. The hemispherical shape is characterized by a higher cost of production and the decrease in volume of the pressure vessel compared to other geometries due to its significant depth. For those reasons, this type of dished end is not common in industrial pressure vessels.

The stress distribution is usually the fundamental factor in designing various structures, including pressure vessels. Peak stress value can be viewed as the primary determinant of shell thickness considering structural analyses. This implies that minimizing the maximum stress can result in a diminishing of the thickness, which is desired from an economic standpoint. Assuming the thickness remains unchanged, pressure vessels can be loaded with higher pressure to increase the stored energy density. This topic became a severe issue due to the recent development in hydrogen energy, requiring efficient storage and transportation systems [11].

Despite well-known drawbacks of hemispherical ends, those are characterized by favourable equivalent von-Mises stress distribution. The dished ends with smaller relative depth, e.g. torispherical, ellipsoidal or semi-ellipsoidal, are characterized by significant disturbance in the stress near the junction of dished end and cylindrical shell [9,12,13]. Such phenomenon, referred to as the edge effect described in the literature [1–3], is the result of interaction between joined shells, introducing transverse force and bending moment in the junction. The described phenomenon significantly increases the maximum stress value in the structure.

Interestingly, there is no apparent justification for the shapes of dished ends presented in technical standards [5–7]. Those geometries were supposedly arbitrarily assumed due to their simplicity and manufacturability, which is understandable, especially considering the first version of the ASME Boiler and Pressure Vessel Code was published in 1915 [14]. Despite the progress in science and technology, which has

---

a tremendous effect on the industry, the shapes of dished ends remain unchanged throughout the last century.

Performing stress and deformation analyses of shell structures require insight into the possible methods for solving such problems. Literature concerning shell structures [1–4] describes two theories that enable to study of stress and deformation in shell structures, i.e. membrane theory (MT) and moment theory. The first of them neglect the bending phenomenon and restrains the internal loads only to normal forces. Such an approach is only justified for shells for which thickness to radii of curvature ratio is sufficiently low, and the changes in principal radii are smooth. The analyses based on the MT are satisfactory merely for shells with constant radii of curvature, i.e. hemispherical or cylindrical shells.

The moment theory assumes internal forces in a shell in the form of normal and transverse forces as well as bending and twisting moments. Unfortunately, the governing differential equations of moment theory are currently impossible to solve for shells with variable radii of curvature. To study the bending phenomenon in shell structures, one may refer to the edge effect theory, which constitutes a simplification of the moment theory. The edge effect theory can be considered accurate [15] when the shell is sufficiently thin, the change of curvature is moderate for the joined shells and the relative height of the shells is considerable. One must note, however, that in the case of the structures with discontinuous radii of curvature e.g. most the cylindrical pressure vessels, the edge loads are initially unknown. Those can be calculated only by defining displacements and rotations compatibility equations. Such an approach implies the displacements and rotations caused by surface loads e.g. pressure, are resolved according to MT. For the shells with variable radii of curvature MT can become inaccurate, even for relatively thin shells. This yields inexact values of the edge loads, which in consequence directly reduces the accuracy of the edge-effect-approach solution, regardless of the accuracy of the edge effect theory itself.

Numerous authors have studied the optimization of pressure vessels and dished ends themselves. Magnucki et al. [16] focused on reducing the peak stress in a cylindrical pressure vessel by introducing the dished end based on a composite curve of a circular arc and a polynomial of the fifth degree. Magnucki and Lewiński [17] aimed at finding a shape of a dished end that ensures its full charge with stress. Banichuk [18] presented the optimization of a shell structure of revolution, including both shape and thickness distribution. Lewiński and Magnucki [19] developed the shape of the dished end described by the trigonometric series and optimized its geometry by applying the condition of continuity of the curvatures in the joint. Krużelecki and Proszowski [20] proposed the two- and one-arc dished ends described by different functions, including Bézier polynomial and optimized their shapes using simulated annealing algorithm. Błachut [21] considered parabolic and cubic splines together with circular arcs to approximate the meridional shape of externally pressurized domes in the process of maximizing the collapse pressure.

The primary issue with the optimization procedure is the lack of accurate analytical methods for solving the structural problems of shells. The researches provided in papers [16–21] are based on the MT. Despite a significant reduction of the stress concentration factor due to optimization, the verification using FEM resulted in an elevated peak stress value compared to the membrane state solution [16,20]. The reason for that is simply neglection of the bending phenomenon in the analysed shell structures. It is necessary to consider more accurate theories or methods to achieve a better outcome of the optimization.

Carbonari et al. [22] performed a more complex analysis and studied shape sequential linear programming optimization of axisymmetric pressure vessel, intending to reduce von Mises stress. Within the study framework, the fitness function was obtained utilizing FEM, where the pressure vessel was modelled using 2D-axisymmetric shell finite elements. Błachut and Ramachandra [23] considered the problem of internally pressurized torispherical domes and proposed to optimize its shape using genetic algorithms (GAs) and FEM.
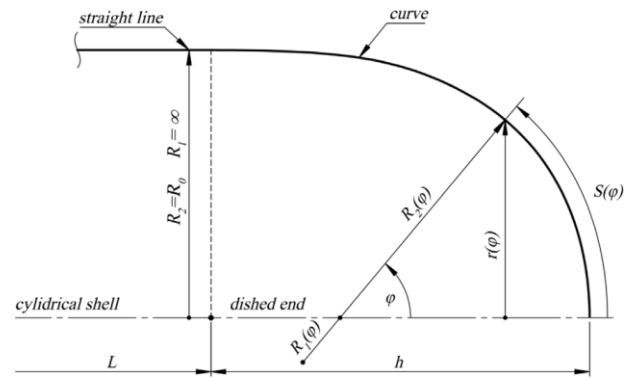

Fig. 1. The general geometry of the cylindrical pressure vessel.

The application of GAs, as the derivative-free method, gained significant attention throughout recent years in structural optimization [24]. It is most likely connected with their ability to operate on discontinuous fitness functions present throughout any numerical analysis, where the relationship between input parameters and output result is undeterminable. There are numerous recently developed papers to justify the given statement. Firlik et al. [25] focused on tram wheel profile optimization using a biologically-inspired optimization algorithm. Yang et al. [26] designed the novel corrugated hierarchical truncated conical shells by adopting a surrogate model and GA. Kumar et al. [27] presented an isogeometric shape optimization to design 2D auxetic structures with a prescribed Poisson ratio. Liang and Li [28] developed an optimization scheme to design the postbuckling behaviour of composite laminates. Imran et al. [29] carried out design optimization of composite submerged pressure hull under hydrostatic pressure. The authors analysed the effect of orientation angles and the number of layers on the load-carrying capacity of a submersible. Eshani and Dalir [30] focused on optimum design to maximize the critical buckling load and minimize the structural weight of an angle grid plate. Zhu et al. [31] investigated the optimal shapes of reticulated shell structures with the intent to maximize non-linear buckling load. Dias and Mahendran [32] carried out the optimization of cold-formed steel framed wall studs with sheathing restraints. Karimi and Kani [33] studied finding the worst imperfection pattern in shallow lattice domes using GAs.

In this paper, the parametric shape of the dished end is described using a Bézier curve (BC) of arbitrary order. Some particular restrains are proposed and applied on its control points to satisfy numerous geometrical conditions, including non-negative curvature. The shape optimization of the dished end aims to minimize maximum equivalent von Mises stress in a cylindrical vessel loaded with uniform internal pressure.

The procedure is performed using two methods. Initially, equivalent stress is solved analytically according to the MT, while the sequential quadratic programming (SQP) algorithm seeks the maximum stress along the meridian of the dished end and attempts to minimize it. Further, numerical FEM calculations are conducted to validate the outcome of the analysis. Realizing the simplified character of the MT and the impact of the bending phenomena in shell structures, the procedure is further changed. The stress distribution is resolved using FEM in ANSYS software, where its peak value constitutes the fitness function. Due to its discontinuous character, the optimization is performed using GA in MATLAB software. A significant improvement in the maximum stress over the standard dished ends is achieved.

2. Cylindrical pressure vessel geometry

Cylindrical pressure vessels consist of cylindrical shell enclosed by two convex dished ends. The general geometry of the cylindrical pressure vessel is presented in Fig. 1.
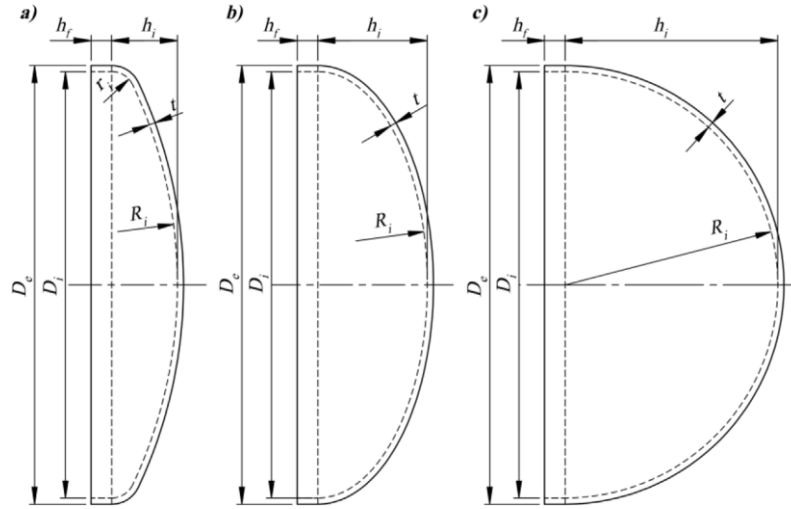
Fig. 2. Dished ends according to EN 13445; (a) - torispherical, (b) - ellipsoidal, (c) - hemispherical.

Most of the pressure vessels are thin-walled shell structures which can be described by the parameters referred to their middle surface (Fig. 1), i.e. φ – meridional angle, R_1, R_2 – meridional and circumferential radii, r – parallel radius, S - meridian length. The relative depth of a dished end is defined as

$$\beta = \frac{h}{R_0}. \tag{1}$$

The standard dished ends are ellipsoidal, torispherical and hemispherical. Those are described and manufactured according to coherent European and American standards, i.e. EN 13445 [5] and ASME Section VIII, Division 1, 2 [6,7]. The description of parameters of those shell structures can also be found in [9] (see Fig. 2).

It is convenient to formulate relative equivalent stress to study the stress distribution in pressure vessels

$$\tilde{\sigma}_r = \frac{\sigma_r}{\sigma_r^{(cyl)}}, \tag{2}$$

where: σ_r – von Mises stress in a pressure vessel, $\sigma_r^{(cyl)}$ – maximum von Mises stress in a cylindrical shell beyond any stress disturbance caused by the edge loads. Such formulation enables to define of the stress concentration factor k, which is the maximum value of $\tilde{\sigma}_r$:

$$k = \frac{\sigma_r^{(max)}}{\sigma_r^{(cyl)}}, \tag{3}$$

where: $\sigma_r^{(max)}$ – maximum von Mises stress in a pressure vessel. The definition of stress concentration factor is similar to the one presented in [8]; however, the denominator does not always refer to the result of the membrane state analysis. For the FEM analysis, the value in the internal surface is slightly higher than in the middle surface in case of internal pressure or external under-pressure. This is due to the stress component normal to the middle surface which leads to a change of stress across the thickness. Such component is omitted in thin-walled shells theories.

The dished ends with smaller relative depth, i.e. torispherical, ellipsoidal or semi-ellipsoidal, are characterized by significant disturbance in the stress near the junction of dished end and cylindrical shell. Such phenomenon, referred to as the edge effect described in the literature [1,3] is the result of interaction between joined shells, introducing transverse force and bending moment in the junction. The described phenomenon significantly increases the maximum stress value in the shell structure. The stress concentration factors for the cylindrical pressure vessels with standard dished ends are shown in Table 1, [8,9].

Table 1
Stress concentration factor in standard dished ends.

t/R_0 [%]	Stress concentration factor k		
	Hemispherical	Ellipsoidal	Equivalent torispherical (semi-ellipsoidal)
0.5	1.030	1.730	2.752
1.5	1.030	1.738	2.392
3.0	1.030	1.754	2.279

3. The parametric shape of the dished ends

Performing shape optimization of a structure requires defining its geometry in some parametric form. Numerous types of curves have been previously used to describe the parametric shape of such shells, including trigonometric series [19], Bézier polynomials [20] and polynomials [22]. The definition of a parametric curve fulfilling various geometric conditions with a sufficient number of free variables can be considered challenging.

Let us consider some parametric curve describing the meridian of a dished end $x(\zeta), y(\zeta)$ for which $\zeta_0 \leq \zeta \leq \zeta_1$. To obtain an appropriate geometry of dished end, applying adequate restrains on the introduced curve is necessary. Assuming $r \rightarrow y$ (Fig. 1), its initial point must remain coincident with the cylindrical shell, therefore:

$$x(\zeta_0) = 0, \qquad y(\zeta_0) = R. \tag{4}$$

The final point of the curve intersects with the axis of revolution of the cylindrical shell:

$$x(\zeta_1) = \beta R, \qquad y(\zeta_1) = 0. \tag{5}$$

Furthermore, the curve is tangent to the cylindrical shell

$$\left.\frac{dy}{dx}\right|_{x=0} = 0, \tag{6}$$

and perpendicular to the axis of revolution, defined by two equivalent expressions:

$$\left.\frac{dx}{dy}\right|_{y=0} = 0, \qquad \left.\frac{dy}{dx}\right|_{x=\beta R} = -\infty. \tag{7}$$

The conditions described in Eqs. (4)–(6) can be applied to the number of well-known curves. Satisfying the constrain in Eq. (7) is difficult for the functions like polynomials or trigonometric series. In previous studies, i.e.: [16,17,19,20], the authors combined a parametric curve with a circular arc, which resolved this issue. Notably, the results
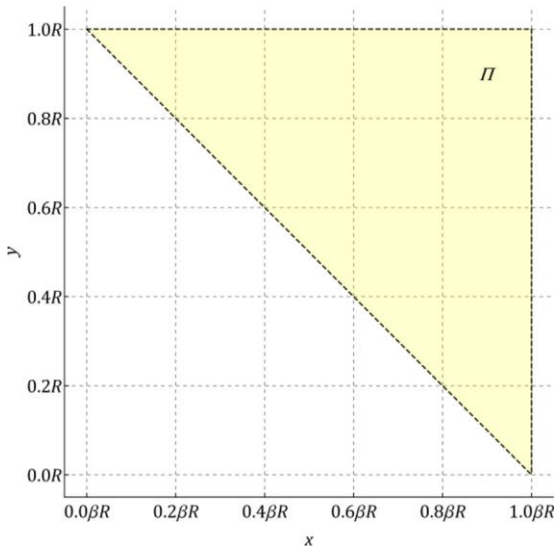
Fig. 3. Triangular feasibility region Π.

obtained in [20] show that complementing the dished end shape with a circular arc generally worsens the optimization results.

To diminish the bending phenomena and to take into consideration the manufacturability of dished ends with conventional methods, its meridian should maintain non-negative meridional curvature in the domain $\zeta_0 \leq \zeta \leq \zeta_1$, therefore:

$$R_1(\zeta) = -\frac{\left[\left(\frac{dx}{d\zeta}\right)^2 + \left(\frac{dy}{d\zeta}\right)^2\right]^{3/2}}{\frac{dx}{d\zeta}\frac{d^2y}{d\zeta^2} - \frac{d^2x}{d\zeta^2}\frac{dy}{d\zeta}} \geq 0. \tag{8}$$

The condition of the non-negative meridional curvature significantly reduces the possibility of obtaining unfeasible curves that are pointless to analyse. The creation of such geometries would drastically hinder the optimization procedure, especially when the fitness function is evaluated using FEM. Unfortunately, its application is complex if the dished end is to be described by one continuous curve characterized by some general form of the functions $x(\zeta), y(\zeta)$. The form of the fifth-order BC considered in [20] enabled to obtain of unfavourable, locally concave dished ends.

Having in mind the restraints applied on the first derivatives of the curve (Eqs. (6), (7)), one can deduce that the functions with non-negative curvature must be contained in triangular feasibility region Π (Fig. 3) defined as

$$y(x) \epsilon \Pi, \tag{9}$$

and described in the following manner (Fig. 1).

$$\Pi = \left\{ (x, y) \in \mathbb{R}^2 : 0 \leq x \leq \beta R; -\frac{1}{\beta}x + R \leq y \leq R \right\}. \tag{10}$$

The restraint in Eq. (9) can be considered the necessary condition of non-negative curvature, i.e. all of the curves fulfilling the condition in Eq. (8) can be found in the region Π. Importantly, the expression in Eq. (9) is not sufficient condition of non-negative curvature as many curves in the region Π can violate the prescribed restrain.

It is challenging to limit the parametric shape described by polynomials or trigonometric functions in the region Π. The authors of [19] and [20] cleverly reduced the number of independent parameters in the functions describing the shape of the dished end, which enabled to achieve geometrically feasible shapes for all possible values of independent parameters. Notably, the more free parameters, the more "flexible" the shape is, therefore the better solution can be obtained in

the optimization process as presented in [20]. It proves that reducing the number of independent variables limits the optimal solution.

Within the framework of this research, BC is selected to describe the parametric shape of the dished end. The general form of the curve is as follows:

$$\begin{aligned} x(\zeta) &= \sum_{i=1}^{n} \frac{n!}{i!(n-1)!} \zeta^i (1-\zeta)^{n-i} x_{ci}, \\ y(\zeta) &= \sum_{i=1}^{n} \frac{n!}{i!(n-1)!} \zeta^i (1-\zeta)^{n-i} y_{ci}, \end{aligned} \tag{11}$$

where: x_{ci}, y_{ci} are coordinates of the control points denoted as c_i, n — number of control points. Let us consider a BC of an arbitrary degree $n-1$ defined by the set of n control points

$$c = \{c_1, \ldots, c_n\}, \tag{12}$$

while

$$c_i = (x_{ci}, y_{ci}), \quad i = 1, \ldots, n. \tag{13}$$

The convex hull property of BC implies the curve is always contained within a convex hull of its control points. Following such property, if the control points are defined in the triangular feasibility region Π, then the curve is also contained in this region

$$c \epsilon \Pi \Rightarrow y(x) \epsilon \Pi, \tag{14}$$

which satisfies the necessary condition of non-negative curvature (Eq. (9)). Moreover, the curve starts and ends in the first and last control point correspondingly, therefore:

$$\begin{aligned} x_{c1} &= 0, & y_{c1} &= R \\ x_{cn} &= \beta R, & y_{cn} &= 0. \end{aligned} \tag{15}$$

The BC is tangent to the line intersecting the first two and the last two control points. The constrain of tangency (Eq. (6)) and perpendicularity (Eq. (7)) is satisfied by assuming:

$$y_{c2} = y_{c1}, \qquad x_{c(n-1)} = x_{cn}. \tag{16}$$

Depending on the selection of the remaining control points, one may obtain the curves that do not meet the condition of non-negative curvature (Eq. (8)). The assumption of some additional restraints can resolve this issue. The BCs are characterized by the variation diminishing property, which implies no line can intersect the curve more times than it intersects the polygon defined by its control points, i.e. control polygon. Notably, any curve with non-negative or non-positive curvature cannot be intersected by any line more than twice. Having those properties in mind, if the control polygon of a BC is convex, then it has non-negative or non-positive curvature, as any line cannot intersect such a curve more than twice.

It is necessary to introduce a method for selecting the control points coordinates to obtain a convex control polygon. In the presented paper following procedure is adopted. The location of the first and last control point is selected according to Eq. (15) in the region $\Pi_1 = \Pi$ (Eq. (10)). To parametrize the described curve, auxiliary points $k_i = (x_{ki}, y_{ki})$, $l_i = (x_{li}, y_{li})$ are provided, where the coordinates of initial auxiliary points are (Fig. 4):

$$x_{k1} = 0, \qquad y_{l1} = R. \tag{17}$$

For each of the auxiliary points, one of their coordinates remains constant:

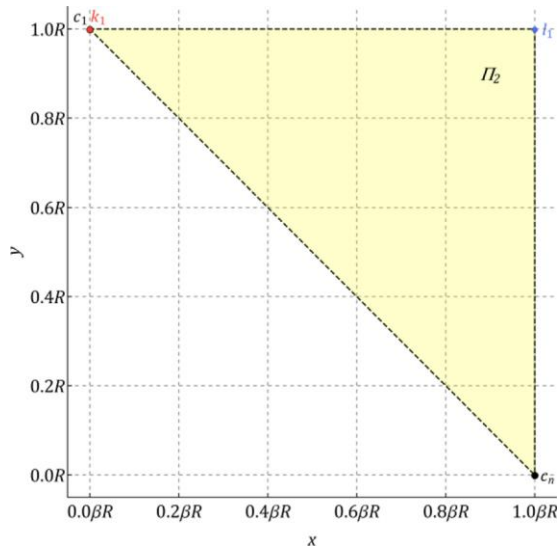$$y_{ki} = R, \qquad x_{li} = \beta R. \tag{18}$$
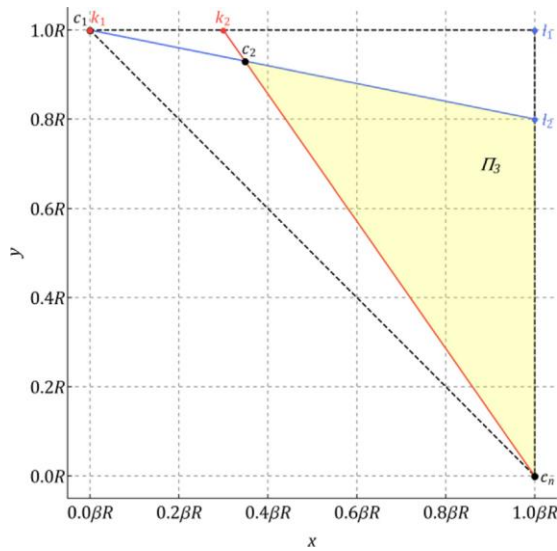
Fig. 4. Position of the initial auxiliary points.

Fig. 5. Creation of the control point c_2.

The feasibility regions for the following control points are defined as follows:

$$c_i \in \Pi_i,$$

$$\Pi_i = \left\{ (x, y) \in \mathbb{R}^2 : x_{c(i-1)} \leq x \leq x_{cn}; \right.$$

$$\frac{y_{cn} - y_{c(i-1)}}{x_{cn} - x_{c(i-1)}} \left(x - x_{c(i-1)} \right) + y_{c(i-1)}$$ (19)

$$\left. \leq y \leq \frac{y_{l(i-1)} - y_{c(i-1)}}{x_{cn} - x_{c(i-1)}} \left(x - x_{c(i-1)} \right) + y_{c(i-1)} \right\},$$

therefore $\Pi_2 = \Pi_1 = \Pi$ (Fig. 4).

To obtain the coordinates of control points $c_2, \ldots, c_{n-1}$, the auxiliary points are defined in the parametric form:

$$x_{ki} = x_{k(i-1)} + \kappa_i \left(x_{cn} - x_{k(i-1)} \right), \qquad y_{li} = \lambda_i y_{l(i-1)}, \quad i = 2, \ldots, n-1, \quad (20)$$

where:

$$0 \leq \kappa_i \leq 1, \qquad 0 \leq \lambda_i \leq 1,$$ (21)

Table 2
Arbitrary parameters of an exemplary BC of order four.

κ_2	κ_3	κ_4	λ_2	λ_3	λ_4
0.3	0.4	0.5	0.8	0.7	0.6

which implies:

$$x_{ki} \geq x_{k(i-1)}, \qquad y_{li} \leq y_{l(i-1)}.$$ (22)

The position of $c_2, \ldots, c_{n-1}$ is defined as the intersection of two lines passing through the points $\{k_i, c_n\}$ and $\{l_i, c_{i-1}\}$ correspondingly, as shown in Fig. 5, therefore formulae describing the considered control points are as follows:

$$x_{ci} = \frac{\left(x_{ki} y_{cn} - y_{ki} x_{cn} \right) \left(x_{li} - x_{c(i-1)} \right) - \left(x_{li} y_{c(i-1)} - y_{li} x_{cn} \right) \left(x_{ki} - x_{cn} \right)}{\left(x_{ki} - x_{cn} \right) \left(y_{li} - y_{c(i-1)} \right) - \left(y_{ki} - y_{cn} \right) \left(x_{li} - x_{c(i-1)} \right)},$$

$$y_{ci} = \frac{\left(x_{ki} y_{cn} - y_{ki} x_{cn} \right) \left(y_{li} - y_{c(i-1)} \right) - \left(x_{li} y_{c(i-1)} - y_{li} x_{cn} \right) \left(y_{ki} - y_{cn} \right)}{\left(x_{ki} - x_{cn} \right) \left(y_{li} - y_{c(i-1)} \right) - \left(y_{ki} - y_{cn} \right) \left(x_{li} - x_{c(i-1)} \right)}.$$ (23)

Despite the structure of Eq. (23) referring to the coordinates of control points seem cumbersome due to its recurrent character, it can be rewritten to a very convenient form:

$$x_{ci} = \beta R \frac{\chi_{ci}}{a_{ci}}, \qquad y_{ci} = R \frac{\gamma_{ci}}{a_{ci}},$$ (24)

where:

$$\chi_{ci} = \kappa_i - \lambda_i \left(\kappa_i - 1 \right) \chi_{c(i-1)},$$ (25)

$$\gamma_{ci} = \lambda_i \gamma_{c(i-1)},$$ (26)

$$a_{ci} = \kappa_i - \lambda_i \left(\kappa_i - 1 \right) a_{c(i-1)}.$$ (27)

The following assumption is necessary to include the constraints in Eq. (15):

$$\chi_{c1} = 0, \qquad \gamma_{c1} = 1, \qquad a_{c1} = 1,$$

$$\chi_{cn} = 1, \qquad \gamma_{cn} = 0, \qquad a_{cn} = 1.$$ (28)

Following Eq. (24), it is possible to express the control points in a dimensionless manner assuming:

$$x_{ci} = \beta R \tilde{x}_{ci}, \qquad y_{ci} = R \tilde{y}_{ci}$$ (29)

and further obtaining:

$$\tilde{x}_{ci} = \frac{\chi_{ci}}{a_{ci}}, \qquad \tilde{y}_{ci} = \frac{\gamma_{ci}}{a_{ci}}.$$ (30)

Similarly, one can describe BC (Eq. (11)) in the dimensionless form:

$$x(\zeta) = \beta R \tilde{x}(\zeta), \qquad y(\zeta) = R \tilde{y}(\zeta)$$ (31)

where:

$$\tilde{x}(\zeta) = \sum_{i=1}^{n} \frac{n!}{i!(n-1)!} \zeta^i (1-\zeta)^{n-i} \tilde{x}_{ci},$$

$$\tilde{y}(\zeta) = \sum_{i=1}^{n} \frac{n!}{i!(n-1)!} \zeta^i (1-\zeta)^{n-i} \tilde{y}_{ci}.$$ (32)

Let us further consider an exemplary BC of order four, i.e. $n = 5$ and apply the arbitrary values of parameters κ_i, λ_i, shown in Table 2 to create the curve. The position of the remaining points c_3, c_4 is resolved according to Eq. (24), which is presented in Figs. 6 and 7.

The BC based on the control points $c_1, \ldots, c_5$ shown in Fig. 7 is presented in Fig. 8, where the light green area shows the convex control polygon.

To satisfy the tangency and perpendicularity condition in Eqs. (6), (7), it is applied:
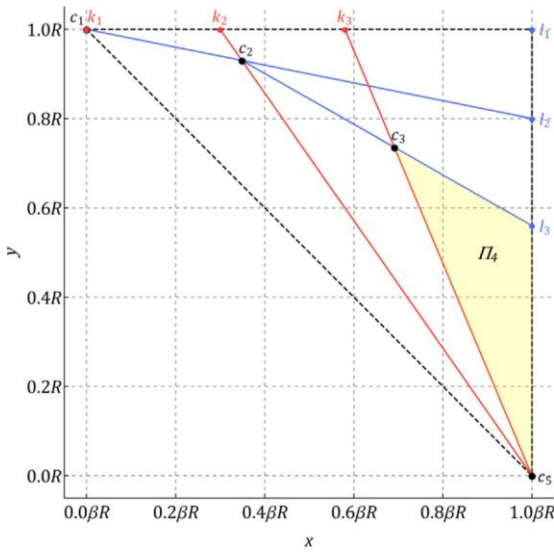
$$\kappa_{n-1} = 1, \qquad \lambda_2 = 1,$$ (33)

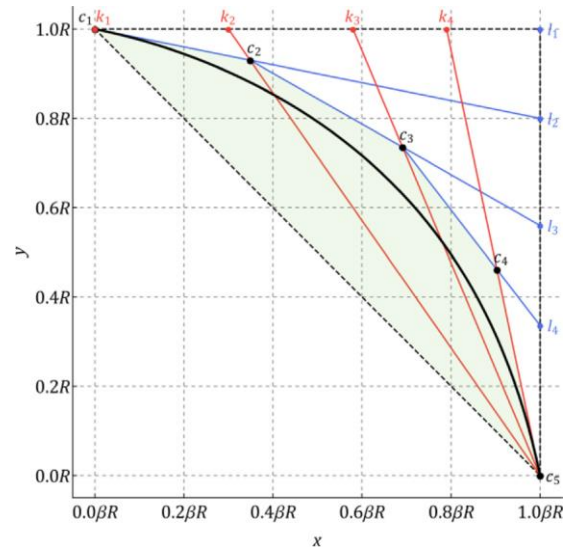**Fig. 6.** Creation of the control point c_3.

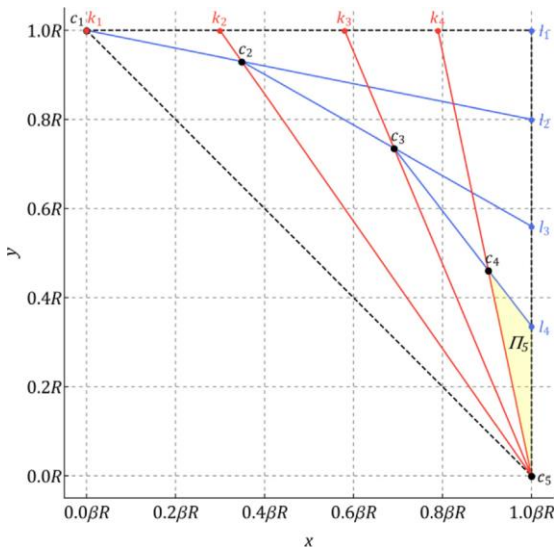**Fig. 8.** Control polygon for the exemplary BC.
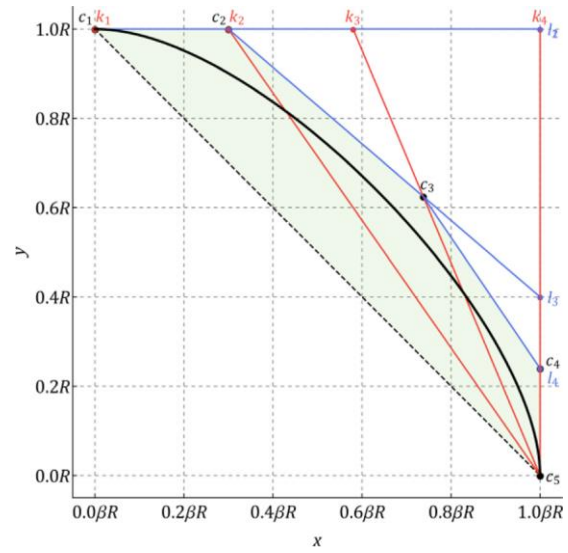

Fig. 7. Creation of the control point c_4.

Fig. 9. Application of tangency and perpendicularity conditions.

regardless of the order of BC, which result is shown in Fig. 9. Independent parameters are further described as a vector V in the following form

$$V = \left\{ \kappa_2, \dots, \kappa_{n-2}, \lambda_3, \dots, \lambda_{n-1} \right\}. \tag{34}$$

Components of the variables vector are referred to as V_i, where $i = 1, 2, \dots, 2n - 6$.

According to the formulation of the proposed geometry, the parametric curve always fits the initially defined feasibility region Π and satisfies all of the constraints, including non-negative curvature. Its shape is defined by $2n - 6$ parameters κ_i, λ_i, which values are simply within the range of $0 \leq V_i \leq 1$. The order of the curve must be at least three ($n = 4$) due to the constraints; however, it can be increased indefinitely. This property is critical for optimization as it enables arbitrarily assuming the number of independent parameters controlling the shape. The increase of the curve order increases the number of its degrees of freedom which potentially enables to obtain better solution due to optimization. Interestingly, the geometry is proportional to the

parameter R, implying that the optimized shape can be adapted to the cylindrical pressure vessels with any diameter. The mentioned properties show that the curve is excellent for optimization as it is unnecessary to introduce any other constraints aside from the value range of the parameters $0 \leq V_i \leq 1$ to the optimization algorithm.

To visualize the possible shapes of dished ends based on the provided description, a couple of BC of order seven are presented in Fig. 10, for which the parameters κ_i, λ_i are selected randomly.

4. Membrane state optimization

As discussed in previous sections, using the MT to evaluate stress and deformation in dished ends of pressure vessels with variable radii of curvature can lead to inaccurate results. Despite that, the optimization in membrane stress state is considered within this paper mainly to evaluate the impact of the number of control points n on the optimization outcome.
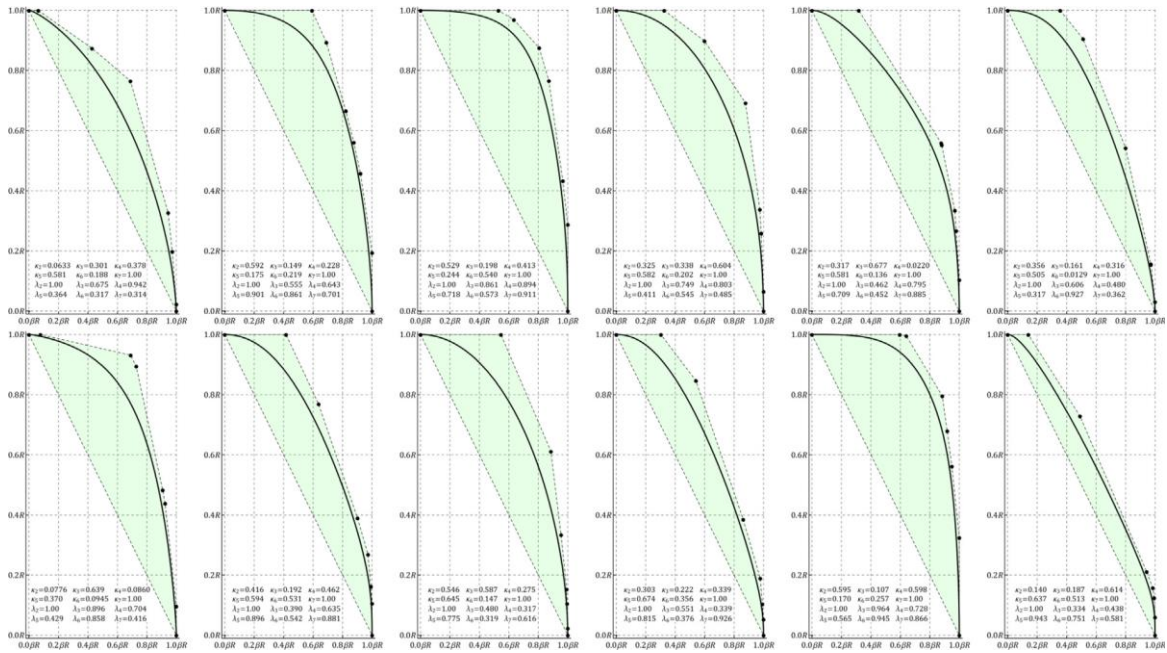
Fig. 10. Shapes of dished ends based on the derived curve of order seven for random values of the parameters κ_i, λ_i.

The definition of principal radii of curvature R_1, R_2 in meridional and circumferential directions correspondingly is critical for calculating stress distribution. In the case of a curve given in the parametric form (Eq. (11)), principal radii of curvature can be resolved from the following formulae:

$$R_1 = -\frac{\left[\left(\frac{dx}{d\zeta}\right)^2 + \left(\frac{dy}{d\zeta}\right)^2\right]^{3/2}}{\frac{dx}{d\zeta}\frac{d^2y}{d\zeta^2} - \frac{d^2x}{d\zeta^2}\frac{dy}{d\zeta}}, \qquad R_2 = y\frac{\left[\left(\frac{dx}{d\zeta}\right)^2 + \left(\frac{dy}{d\zeta}\right)^2\right]^{1/2}}{\frac{dx}{d\zeta}}. \tag{35}$$

Using Eqs. (31) and (32), and applying the following relation:

$$R_1 = R\tilde{R}_1, \qquad R_2 = R\tilde{R}_2, \tag{36}$$

dimensionless radii of curvature are obtained:

$$\tilde{R}_1 = -\frac{1}{\beta}\frac{\left[\left(\beta\frac{d\tilde{x}}{d\zeta}\right)^2 + \left(\frac{d\tilde{y}}{d\zeta}\right)^2\right]^{3/2}}{\frac{d\tilde{x}}{d\zeta}\frac{d^2\tilde{y}}{d\zeta^2} - \frac{d^2\tilde{x}}{d\zeta^2}\frac{d\tilde{y}}{d\zeta}}, \qquad \tilde{R}_2 = \frac{1}{\beta}\tilde{y}\frac{\left[\left(\beta\frac{d\tilde{x}}{d\zeta}\right)^2 + \left(\frac{d\tilde{y}}{d\zeta}\right)^2\right]^{1/2}}{\frac{d\tilde{x}}{d\zeta}}. \tag{37}$$

Internal forces in the membrane state depend solely on the applied pressure and principal radii of curvature:

$$N_1 = -\frac{1}{2}pR_2, \qquad N_2 = -\frac{1}{2}pR_2\left(2 - \frac{R_2}{R_1}\right). \tag{38}$$

The normal stress components are in linear relation with internal forces:

$$\sigma_1 = \frac{N_1}{t}, \qquad \sigma_2 = \frac{N_2}{t}. \tag{39}$$

The equivalent von Mises stress is further calculated according to the plane stress state to analyse the stress distribution

$$\sigma_{eq} = \sqrt{\sigma_1^2 - \sigma_1\sigma_2 + \sigma_2^2}. \tag{40}$$

Applying Eqs. (38) and (39) to Eq. (40) yields

$$\sigma_r = \frac{1}{2}\frac{p}{t}R_2\sqrt{3 + \frac{R_2}{R_1}\left(\frac{R_2}{R_1} - 3\right)}. \tag{41}$$

The stress in the cylinder is calculated by substituting: $R_2 = R, R_1 \rightarrow \infty$ into Eq. (41)

$$\sigma_r^{(cyl)} = \frac{\sqrt{3}}{2}\frac{p}{t}R. \tag{42}$$

Referring to Eq. (2), one can define relative equivalent stress $\tilde{\sigma}$ in the membrane state

$$\tilde{\sigma}_r = \frac{\sqrt{3}}{3}\tilde{R}_2\sqrt{3 + \frac{\tilde{R}_2}{\tilde{R}_1}\left(\frac{\tilde{R}_2}{\tilde{R}_1} - 3\right)}. \tag{43}$$

The optimization problem in membrane stress state is defined as

$$\min_{V} \max_{\zeta} \tilde{\sigma}_r(\zeta, V), \tag{44}$$

subject to:

$$0 \leq V_i \leq 1, \qquad 0 \leq \zeta \leq 1. \tag{45}$$

The optimization is conducted in MATLAB 17 software. To find the global minimum of the fitness function, *GlobalSearch* – MATLAB embedded algorithm is used, which details are discussed in [34]. The algorithm is set to run sequential quadratic programming (SQP) solver [35] from multiple start points to sample numerous basins of attraction. A positive definite approximation of the Hessian matrix in SQP is calculated using Broyden–Fletcher–Goldfarb–Shanno method. MATLAB uses the finite-difference method for calculating derivatives to obtain gradients. The stopping criteria are defined as finishing the analysis for all of the generated trial points.

Initially, the optimization is performed for four control points ($n = 4$), i.e. for BC of order three. Further, the number of control points is being increased, and the result is compared to the previous one. The process is repeated until the relative difference in the maximum value $\tilde{\sigma}_r$ i.e. stress concentration factor k (Eq. (3)) does not exceed 0.5%. Such state is achieved when applying $n = 8$, i.e. for the BC of order seven, characterized by 10 independent variables (Eq. (34)). The optimized relative stress $\tilde{\sigma}_r$ distribution for the BC of order five ($n = 6$), six ($n = 7$) and seven ($n = 8$) is presented in Fig. 11. As expected, the increase in the number of degrees of freedom enables obtaining a more satisfactory solution indicated by the decreasing value of stress concentration factor k.
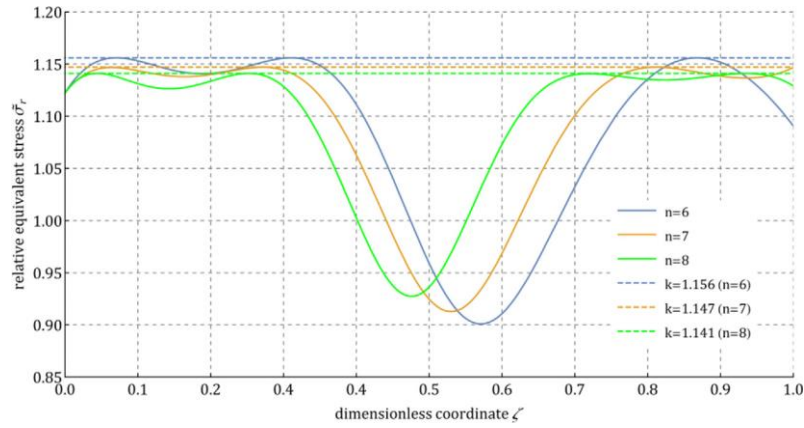
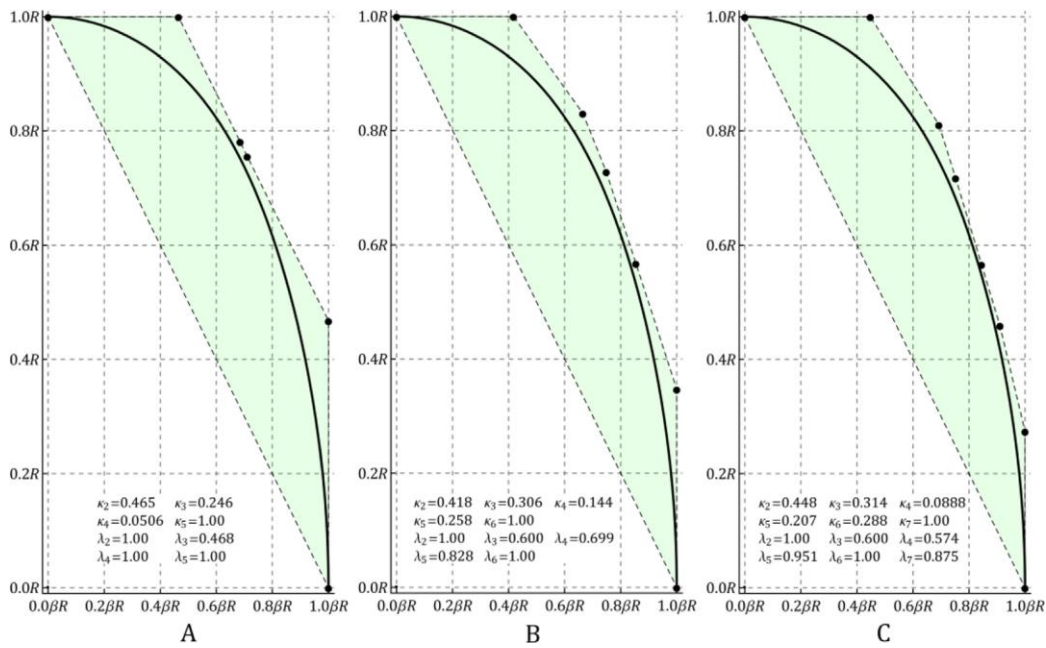**Fig. 11.** The optimized relative equivalent stress distributions for selected BCs.

Fig. 12. The optimized shapes of dished ends based on BC of order: A — five, B — six, C — seven.

The shapes of the optimized dished ends and the corresponding independent variables are presented in Fig. 12. One may notice the similarity between shapes, which indicates the consistency of the performed optimization.

The obtained solution is further validated by performing numerical FEM analyses with the use of ANSYS 2018 software. A necessary description of those is provided in Section 5.2 of the paper. Such procedure is conducted for the pressure vessel with the dished end based on the BC of order seven, where $n = 8$ (Fig. 12-C) characterized by the most favourable stress distribution. During the FEM study, the shell structure is benchmarked for the thickness $t = 5, 10, 15$ mm, consistent with typical liquid petroleum gas pressure vessels with the cylindrical shell radius $R_0 = 1000$ mm. Each of the pressure vessels is loaded with internal pressure causing the equivalent stress of 70 MPa in the cylindrical shell using MT (Eq. (46)). The results of the study are shown in Fig. 13. The detailed stress distributions in the inner and outer surfaces are compared with the MT solutions in the middle surface in Figs. 14–16.

As expected, the stress occurring in the limiting surfaces of the shells is significantly higher than in the middle surface. Its peak value occurs in the outer surface regardless of the thickness. The increase of the thickness yields in the increase of the peak stress expressed as the stress concentration factor k. The relative difference between the parameter k using both calculation methods reaches nearly 20%, which severely decreases the achieved improvement of the optimized dished ends over the standard shapes. To potentially improve the optimization outcome one could refer to more complex shell theories, however, those are significantly limited. The only available theory enabling for analytical evaluation of the stress including the bending phenomenon is the edge effect theory. Due to its simplified character, its adaptation could not necessarily be successful, similarly to MT, which is also justified by lack of the papers using the edge effect theory in the optimization problems.

5. Finite element method optimization

5.1. The procedure description

Regarding the shell structures, the lack of accurate analytical methods for solving the problems of stress and displacements makes it necessary to use numerical calculations while considering the bending
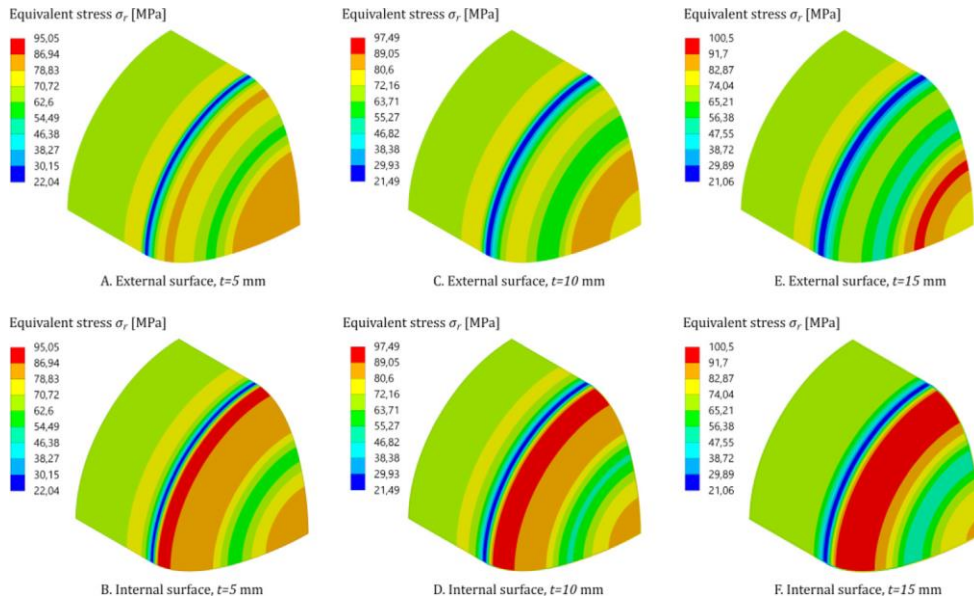
Fig. 13. FEM study results for the optimized dished end of order seven.
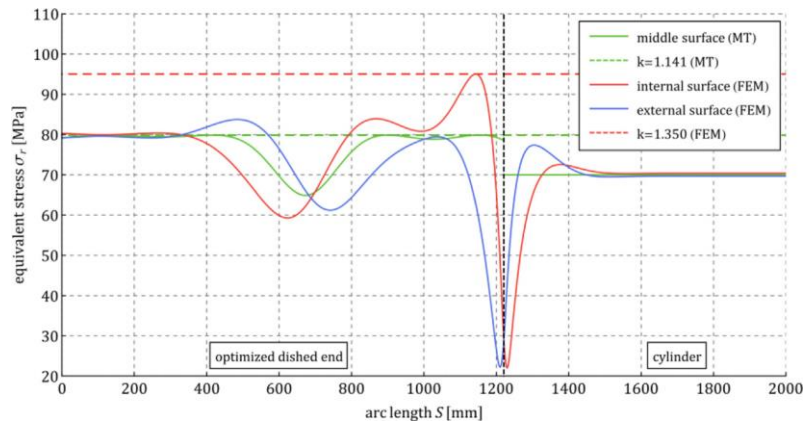

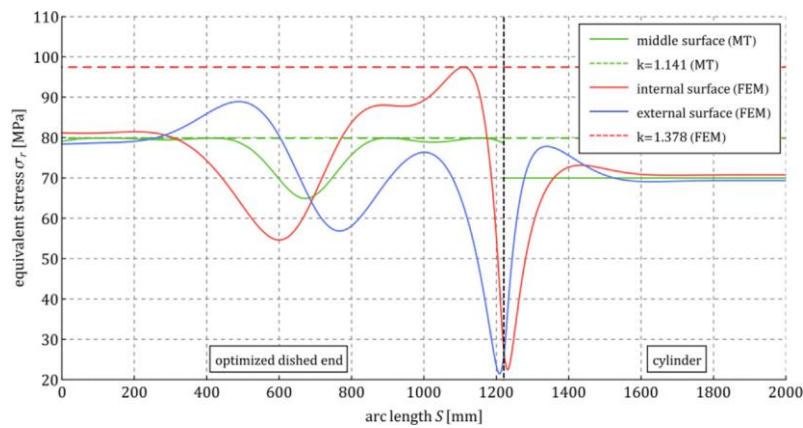Fig. 14. The comparison of equivalent stress distribution for $t = 5$ mm.

Fig. 15. The comparison of equivalent stress distribution for $t = 10$ mm.

phenomenon. The application of FEM for obtaining the fitness function in the optimization procedure is expected to lead to a more satisfactory solution to the analysed problem. Although the idea itself is simple, its utilization requires considerable effort. Foremost, the availability of
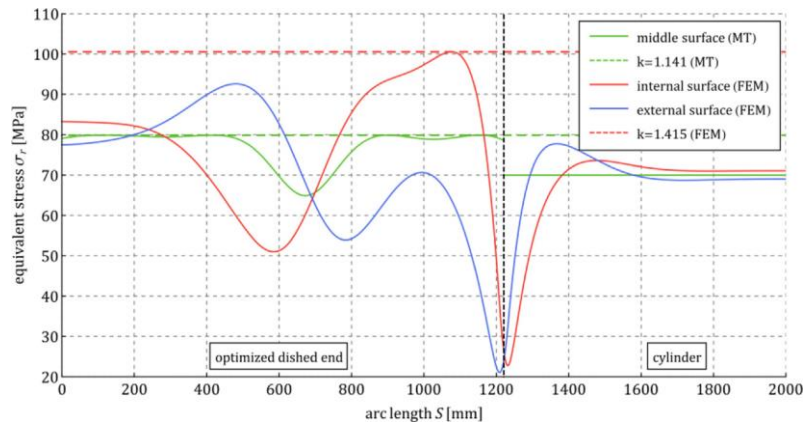
Fig. 16. The comparison of equivalent stress distribution for $t = 15$ mm.
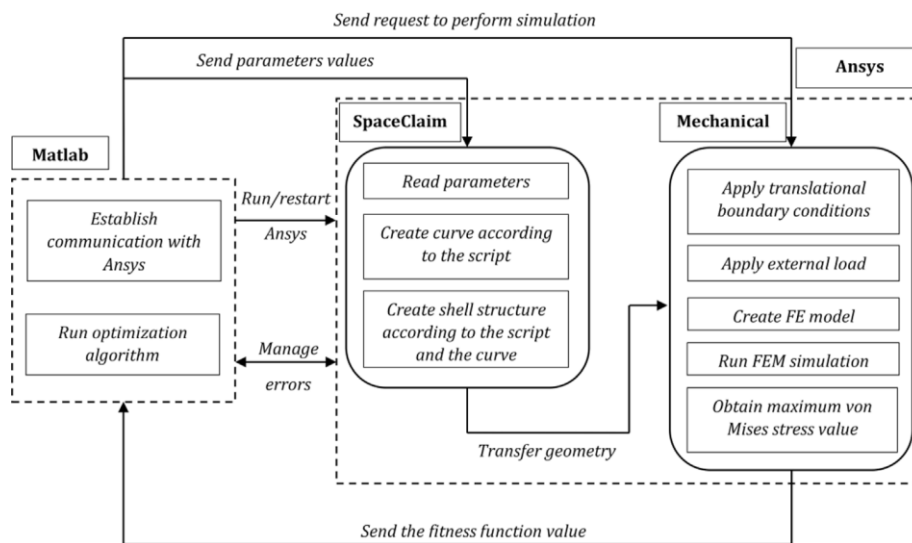
Fig. 17. The optimization procedure flowchart.

optimization algorithms in commercial FEM software is quite limited; therefore, one cannot rely solely on its code to perform the optimization. It creates the need to write an original code for a selected problem. One must also consider that the use of FEM enables to obtain the solution for discrete values of variables, which restrains the possible optimization algorithms that can be adopted due to the discontinuous character of the fitness function.

In the presented analysis, MATLAB 2017 software is coupled with ANSYS 2018 to perform the optimization procedure, as shown in Fig. 17. The prepared MATLAB code uses PYTHON programming language interface to communicate with ANSYS. Initially, MATLAB starts ANSYS software, establishes the connection, opens predefined ANSYS project file and applies values of the parameters (Eq. (34)). The project consists of two components. The first is responsible for creating geometrical models using SpaceClaim software, while the other utilizes Mechanical application for performing FEM analyses over the geometrical models. Using scripting capabilities in SpaceClaim, the prepared code creates the geometry of the dished end based on the BC of order seven, according to the formulae in Eqs. (31), (32). The project file in Mechanical creates an FE model with necessary boundary conditions and performs the analysis. After sending the request to perform the calculations, the fitness function value is calculated according to the peak equivalent stress value retrieved by MATLAB.

During the process, MATLAB is additionally responsible for managing errors that inevitably emerge during FEM calculations. Those issues mainly correspond to incorrect geometry created in SpaceClaim, Mechanical inability to obtain the solution or software errors resulting in unexpected shutdowns or hangs. To resolve such problems, MATLAB closes ANSYS applications and makes a second attempt to solve the previously failed simulation. When the problem persists, MATLAB applies a penalty on the corresponding geometry in the form of a relatively high fitness function value.

The optimization is performed with the use of a build-in MATLAB GA. Notably, the solutions achieved by such algorithms should to referred to as "suboptimal" due to their nature. On account of simplicity, an exception is made, and the term "optimal" is used within this paper. Each of the populations processed by the algorithm consists of 200 unique shapes of the dished ends. The first population for the initially analysed problem, i.e. $t = 5$ mm, is based on the membrane state solution (Fig. 12-C), while the remaining 199 geometries are represented by random values in the range $0 \leq V_i \leq 1$ (Eq. (21)). In the case of the pressure vessels of different thicknesses, instead of using the solution from the optimization, the solution from $t = 5$ mm is introduced to the first population. Subsequent populations are based on 10% elite individuals, 45% crossover children, and 45% mutated entities. The crossover type is single point, while the mutation is carried out by MATLAB function, which randomly generates directions that are
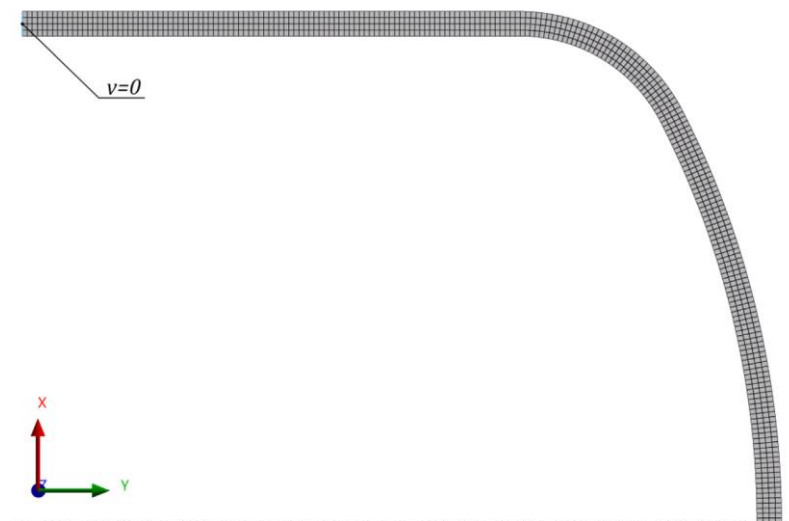
Fig. 18. An exemplary FE model of the analysed pressure vessels.

adaptive concerning the last generation. There are two stopping criteria of the GA. The first of them implies that the optimization is terminated when 200 populations are processed. Another condition assumes halting the optimization when the minimum fitness function value did not change throughout 30 consecutive populations, eliminating unnecessary stalling of the algorithm.

It is important to note that the developed procedure is exceptionally time demanding. Although numerous successful attempts were made to reduce the evaluation time, the final version of the code requires 27 to 33 s for obtaining a single fitness function value on the Intel i5-7500 CPU and SATA III solid-state drive. The most crucial operations in terms of time consumption are geometry creation and communication between ANSYS systems, i.e. SpaceClaim and Mechanical. After the geometry is transferred to Mechanical, it takes about 6 s to prepare the FE model and perform the numerical calculations. Considering that finishing the optimization procedure assumes 40 000 evaluations of the fitness function, the procedure requires nearly two weeks of uninterrupted operation to achieve the solution. Unfortunately, this issue cannot be solved using the hardware with greater computational power, as the evaluation time comes from the software limitations and not computational time. The only seemingly possible method to reduce the time is to solve the problem parallelly using multiple instances of ANSYS processes. This idea brings numerous problems, including ANSYS licensing and coupling of the software.

Considering the challenges mentioned above, the effect of the GA parameters on its performance is not studied in this paper. The selected parameters are established during the observations of numerous unsuccessful optimization attempts performed during the code development.

5.2. Finite element model

The axisymmetrical static structural analysis in ANSYS 2018 software is used to obtain the fitness function value in the form of the stress concentration factor. The analysis includes geometrical nonlinearity. The material model is perfectly elastic and isotropic with Young's modulus $E = 200$ GPa and Poisson's ratio $v = 0.3$. Following geometrical parameters are considered (Fig. 1): $R_0 = 1000$ mm, $L = 1500$ mm, $h = 500$ mm i.e. $\beta = 0.5$. Length of the pressure vessel ensures avoiding the possible interaction between disturbances in the areas of shell junctions due to the edge effect. A quarter of the axisymmetric cross-section of the pressure vessel is studied to reduce the computational time of the analysis. The symmetry condition is applied by restraining the displacements towards y axis i.e. $v = 0$ (Fig. 18).

The geometry of the pressure is divided into two-dimensional, second-order, quadrilateral PLANE183 finite elements with three degrees of freedom at each node. The mesh parameters are justified by the previously performed mesh convergence study for the standard dished ends in [9]. It is assumed that the stress gradient for the optimized dished ends should be lower, which makes the mesh applicable for the analysed problem. All of the FE models are divided so that there are four finite elements across the thickness. The creation of the mesh prioritizes equilaterality of the finite elements, which implies that the thickness determines the number of finite elements along the meridian. An exemplary FE model is shown in Fig. 18, where the thickness is increased to $t = 50$ mm for better readability.

During the numerical calculations, the pressure vessel is loaded with internal pressure causing the equivalent stress of 70 MPa in the cylindrical shell in the membrane state:

$$p = \frac{140\sqrt{3}}{3} \frac{t}{R_0}. \tag{46}$$

The relation between the pressure and thickness ensures the comparability of the results. The fitness function value in the form of stress concentration factor k (Eq. (3)) is calculated directly in ANSYS, where the stress in the cylindrical shell is probed in the internal surface at the location where the translational boundary condition $v = 0$ is applied.

5.3. The results

During the optimization, two factors are monitored (Fig. 19) to evaluate the progress of the procedure i.e. k_{min} and k_{avg}. The first refers to the individual with the minimum value of the stress concentration factor k in the population, while the latter is the mean value for all entities. Initially, both of the parameters are characterized by relatively high values. As expected, they reduce asymptotically throughout the subsequent populations. Both parameters show no significant changes beyond 140 populations, justifying the applied stopping criteria referred to the maximum number of the analysed populations.

Some deviations from the asymptotic character of the studied parameters require further discussion. The fluctuations of k_{avg} are observed for the thickness $t = 5, 10$ mm, which are initiated by the abrupt change of k_{min}. Such a phenomenon occurs when the algorithm suddenly finds the more satisfactory solution, which is significantly different in terms of the variables that describe the dished end geometry. As a result of the crossover operator, the individuals in the successive populations are based on two significantly diverse groups of
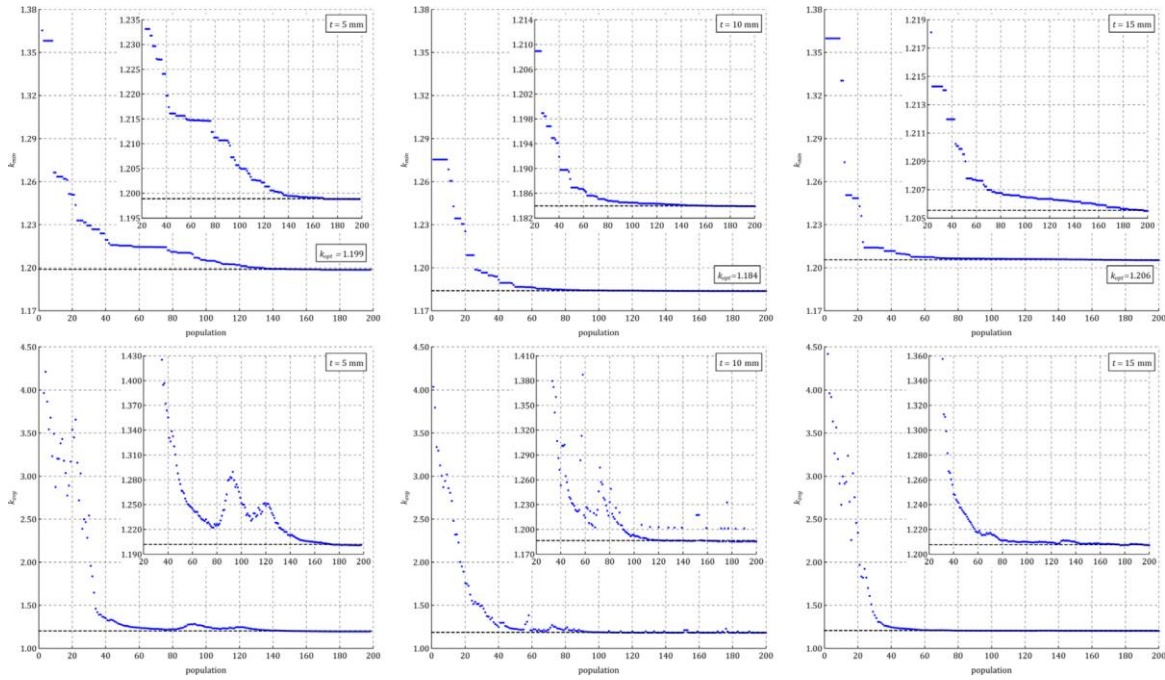
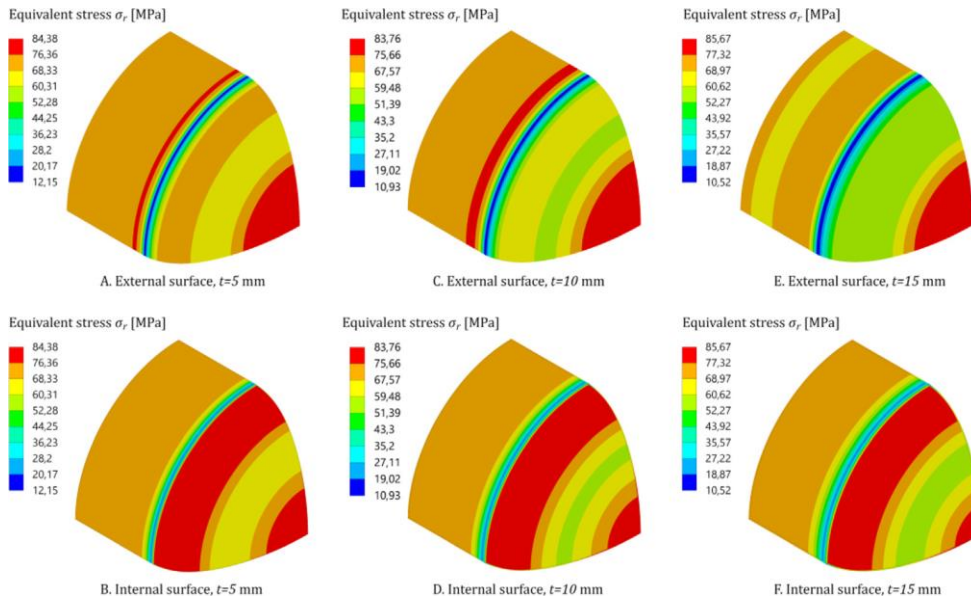**Fig. 19.** Summary of the FEM and GA optimization.

Fig. 20. The stress distribution for the optimized dished ends with the use of FEM.

solutions. The mean value of k parameter increases, while the trend of k_{min} remains unchanged due to the elite individuals.

Another issue with the mean value of the stress concentration factor k_{avg} is observed for the pressure vessel of the thickness $t = 10$ mm. When the algorithm processes about 100 populations, the parameter tends to increase for a single population suddenly. By studying the results closely, it has been noted that such problems are the effect of the algorithm applying the penalty for one or two solutions in the population due to the erroneous geometries created by SpaceClaim software.

The final results of the FEM calculations processed by the GA are shown in Fig. 20. Comparing them to those presented in Fig. 13, one

can note a significant decrease in the peak stress and a more uniform distribution.

The optimized shapes of dished ends, including their convex polygon, are presented in Fig. 21. The parameters (Eq. (34)) describing all three curves are similar in their values, which implies the shapes of the optimized dished ends are alike. The stress distributions for these shells in the internal and external surfaces are presented in Figs. 22–24. For each of them, the optimal solution is achieved when the stress in the inner surface near the juncture with the cylindrical shell equalizes with the stress in the external surface for $S = 0$ mm. According to the convex polygons in Fig. 21, the control points for the BCs are located precisely in the mentioned areas. This phenomenon is not observed
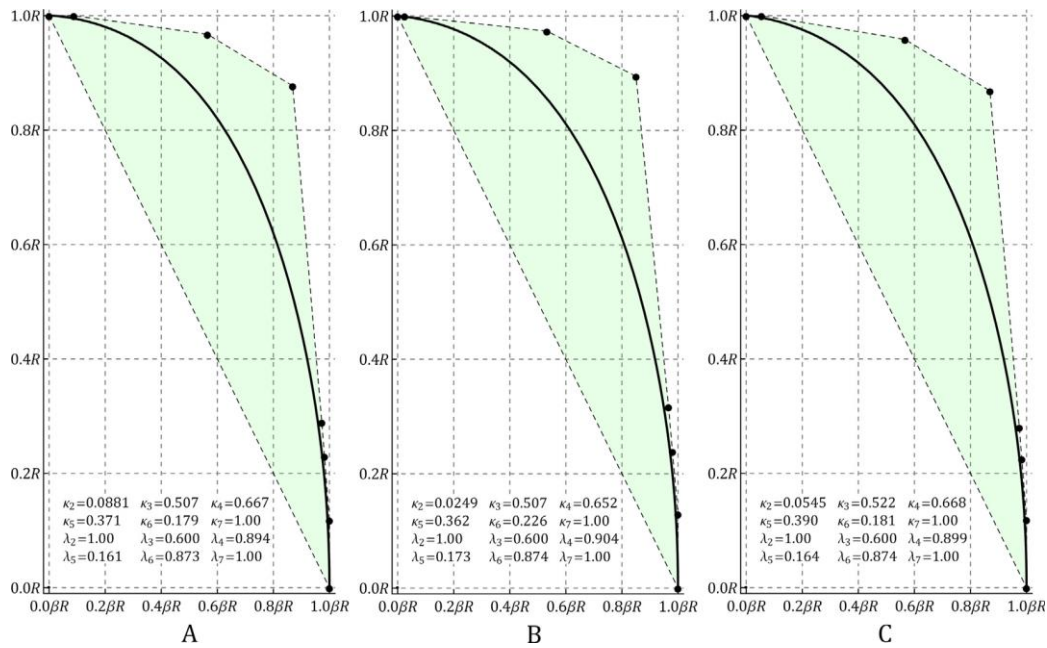
Fig. 21. The optimized shapes of dished ends based on BC of order seven: A − 5 mm, B − 10 mm, C − 15 mm.
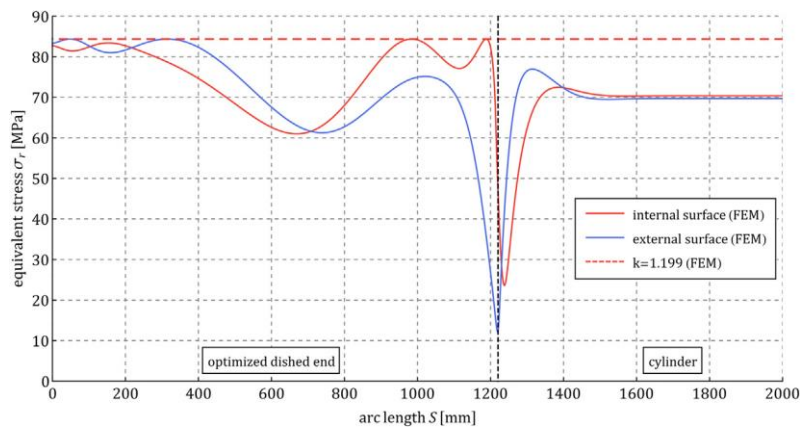

Fig. 22. The equivalent stress distribution for $t = 5$ mm.

in the optimization using the MT (Fig. 12), where the control points are distributed evenly along the curve regardless of its order. It shows that those areas of the structure are the most important in optimizing the shapes of the dished ends when the bending phenomenon is not neglected.

Interestingly, the solution using MT implies that the slope of the curve should remain low at the beginning and the end of the curve. Analogously, the edge effect theory implies the curvature change near the shells junction should be moderate to reduce the bending phenomenon. This observation does not agree with the shapes obtained using FEM and GA, where a considerable bending effect occurs in the optimized geometries. However, in the latter case, the bending phenomenon is distributed somewhat evenly throughout the meridian of the dished end.

6. Summary of the optimization

To provide more insight into the optimized shapes of the dished ends, one must compare their geometries directly with each other

and the standard geometries. The summary of the stress concentration factors is provided in Table 3. The improvement of the peak stress in the developed dished ends is remarkable. It is important to note that the values are slightly different than in Table 1 since the stress in the cylindrical shell is obtained through FEM calculations in the internal surface, where its value is higher than in the middle surface. Instead of performing the comparison for the selected thickness values, the results are generalized concerning t/R_0 ratio. As initially expected it has been found that there is a linear relationship between the magnitude of the applied pressure and the stress distribution. Additionally, the shape of the dished end is proportional to the radius of the cylindrical shell R_0; therefore the forementioned generalization is justified.

The differences in the stress concentration factor k retrieved in MT and FEM must be further discussed. One must note that any disturbance of the membrane state increases the peak stress value in a shell structure. For that reason, it is supposed that the optimization using FEM and GA must yield a worse outcome than MT and SQP optimization. This remark is even more evident when one considers the
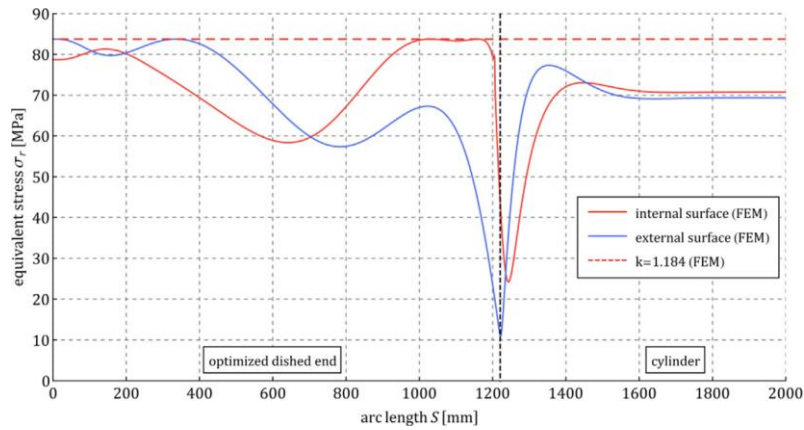
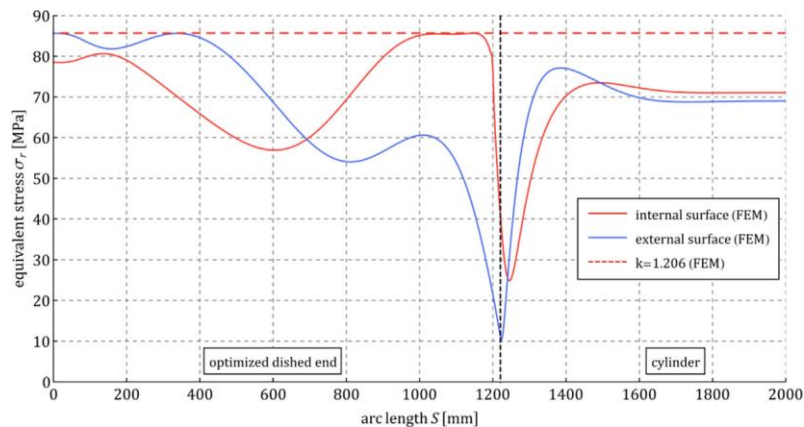**Fig. 23.** The equivalent stress distribution for $t = 10$ mm.

Fig. 24. The equivalent stress distribution for $t = 15$ mm.

Table 3
Summary of the stress concentration factors for the analysed dished ends.

t/R_0 [%]	Stress concentration factor k			
	Standard dished ends		MT optimization	FEM optimization
	Ellipsoidal	Equivalent torispherical (semi-ellipsoidal)		
0.5	1.746	2.738	1.350	1.199
1.0	1.727	2.476	1.378	1.184
1.5	1.712	2.356	1.415	1.206

character of the employed optimization algorithms. The deterministic SQP algorithm is highly efficient at finding the global minimum of the fitness function, whereas GA can be limited to local minima when the fitness function is complex, implying the solution might be suboptimal. To prove this point, the previously shown data for $t = 5$ mm is further compared with the outcome of other optimization attempts with the same conditions. According to Fig. 25, all three solutions converged to different results, despite k_{min} reached an asymptote and the individuals in the final populations became nearly identical in each of them separately. One can conclude the further increase in the number of processed populations is futile.

To evaluate the optimality of the results provided in the previous section, one should consider the magnitude of the differences in the results using both approaches. Those appear to be insignificant; MT and SQP optimization lead to $k = 1.141$ in membrane state, and the maximum stress concentration factor using the other optimization method is $k = 1.206$ for $t = 15$ mm (Table 3). The absolute difference for the least

favourable case is then 6.5%. To properly compare these values, the stress in the middle surface from GA optimization should be considered, which would decrease the aforementioned absolute difference. For that reason, is it assumed that the application of GA and FEM is successful.

The above observations imply that the further potential decrease of the stress concentration factor k when including the bending phenomenon can be minimal and technically meaningless. This conclusion only applies to the type of the developed curve, its parameters, the considered restraints and the material model. Nevertheless, it is unclear what particular changes in these conditions could lead to more favourable stress distribution. Interestingly, no correlation between the thickness t and the solution can be defined. It could be predicted that the increase in thickness can reduce the potential optimality, which is coherent with the shell theories. All of the shapes are further juxtaposed in Fig. 26, where the axis order is changed to ensure better readability of the figure. The comparison of the analysed shapes immediately brings attention to their similarity. The most crucial difference between
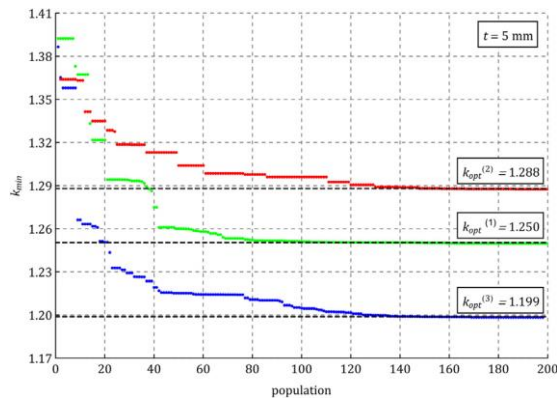
Fig. 25. The comparison of converged optimization results for $t = 5$ mm.

the standard and optimized shapes is the more evident convexity of the latter. The optimized shape for $t = 5$ mm shows a remarkable resemblance to the geometry optimized using MT, whereas such similarity vanishes for the thicker shells. This observation is expected and can be explained by the insignificant effect of the bending phenomenon for a relatively thin shell.

The more noticeable differences can be observed in the principal radii of curvature comparison in Figs. 27 and 28, which explicitly describe the shapes of the considered shell structures. The ellipsoidal dished end, as well as the geometry optimized using MT, are characterized by an asymptotic decrease of the meridional radius of curvature $\tilde{R}_1$ towards the edge, i.e. $\varphi = \pi/2$. The shapes optimized using FEM, where the bending phenomenon is considered, only partially share the same behaviour. An abrupt change is observed in the area of the shells edge, where $\tilde{R}_1$ reaches nearly zero. The rate of change of this parameter depends on thickness. With the increase of thickness, the rate of the mentioned change decreases. It is worth mentioning that the radius of curvature for the cylindrical shell is also zero; therefore, its decrease leads to the diminishing of the edge effect. This condition was previously studied and successfully applied in [13] as such behaviour is expected according to the edge effect theory.

7. Conclusions

In the presented paper, the problem of dished end shape optimization was considered. The research aimed to minimize the maximum stress in the dished end of a cylindrical pressure vessel. A unique shape based on the Bézier curve (BC) of arbitrary order was developed, which satisfies numerous constraints, including non-negative meridional radius of curvature. Regardless of the parameters describing its shape, the geometry maintains manufacturability and the relative depth (Eq. (1)) as the standard dished ends.

Initially, the optimization assumed analytically evaluating the fitness function using membrane theory (MT) and employing sequential quadratic programming (SQP) algorithm. Different curve orders were considered to evaluate sufficient numbers of the independent variables describing the dished end geometry. It has been concluded that the BC of order seven, described by $n = 8$ control points and ten free parameters, is satisfactory for the optimization. The applied geometrical parameters and material model were selected to be coherent with typical technical applications.

The MT optimization enabled the reduction of stress concentration factor to $k = 1.141$. The corresponding value for the standard geometries is $k = 1.712$ to $k = 1.746$ for ellipsoidal shape and $k = 2.356$ to $k = 2.738$ for equivalent torispherical, depending on the thickness (Table 3). The verification of the developed geometry was performed using FEM, which led to an increase in k parameter to 1.350, 1.378, 1.415, depending

on thickness to cylinder radius ratio t/R_0. Such an issue is the effect of the bending phenomenon neglection in the MT, which significantly reduces the optimality of the stress distribution.

As the final step, the optimization was conducted using a more complex approach. The commercial software MATLAB and ANSYS were coupled to perform the procedure by evaluating the fitness function in the latter. A genetic algorithm (GA) has been used to optimize the stress concentration factor. Despite substantial computational time needed to process the calculations, the results can be considered satisfying. The analysed parameter was reduced to 1.199, 1.184, 1.206 for the t/R_0 ratio 0.5, 1.0, 1.5% correspondingly.

Despite the formulated BC-based shape enabled to achieve a satisfactory outcome of the study, the optimization required significant computational time due to the number of fitness function evaluations in the GA optimization approach. This could be connected with one of the properties of BCs. A modification to a single control point i.e. one of the optimization variables results in the global change of geometry. The ability to change the shape locally could be beneficial. Such property is consistent with nonuniform rational b-splines (NURBS), where the changes to a single control point can affect shape only in its neighbourhood. This is connected with the weights of the control points, which can be introduced as another variable in the optimization.

Summarizing the findings of the analysis, the stress in the standard dished ends is 71.2% to 173.8% higher than in the cylindrical shell beyond any disturbance. The developed shapes are characterized merely by 18.4% to 20.6% greater equivalent von Mises stress. The proposed geometries constitute a significant improvement over the shapes described by the current technical standards.

Importantly, the optimized geometries do not necessarily constitute the shapes of the least mass. The decrease of the mass could be obtained by reducing the meridian length of a dished end. This would lead to an increase of the peak stress and result in the necessity of proportional increase of the thickness, and finally increase of the mass. It is difficult to evaluate if the decrease of the meridian length could at least compensate for the increase of the thickness in terms of mass. According to the shapes comparison provided in the paper, supposedly insignificant changes to geometry can result in a severe increase in peak stress. As the differences in length of the compared dished ends can be considered minor, then reducing the meridian length could contradictory result in the increase of the mass. One should also note the reduction of meridian length would most definitively lead to an undesirable shrink in the volume of the pressure vessel.

Realizing the similarities between the studied geometries, it is interesting to what extent the obtained results can be replicated in an experimental study. Further research is necessary to evaluate the imperfection sensitivity of the developed structures.

CRediT authorship contribution statement

Krzysztof Sowiński: Conceptualization, Methodology, Validation, Formal analysis, Investigation, Writing – original data, Writing – review & editing, Visualisation, Supervision, Project administration, Funding acquisition.

Declaration of competing interest

The authors declare that they have no known competing financial interests or personal relationships that could have appeared to influence the work reported in this paper.

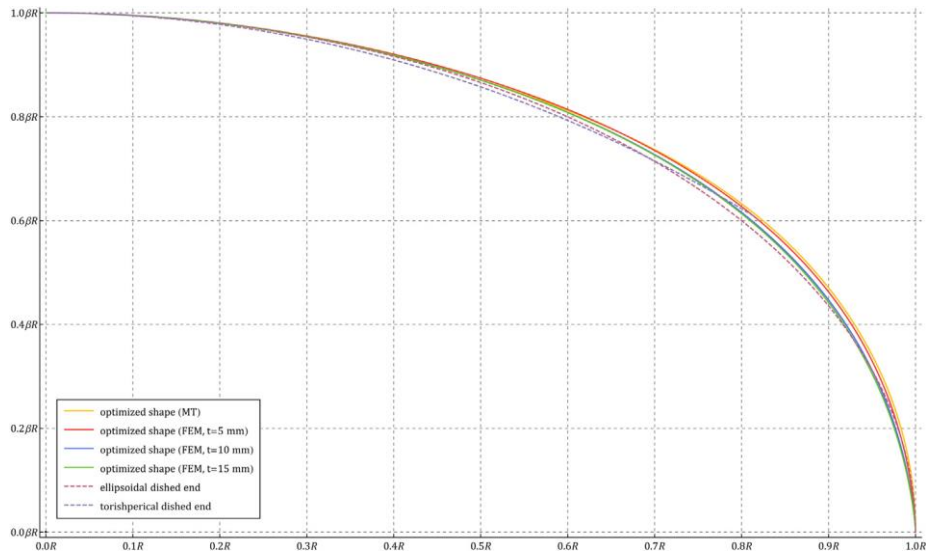**Acknowledgement**

Funding

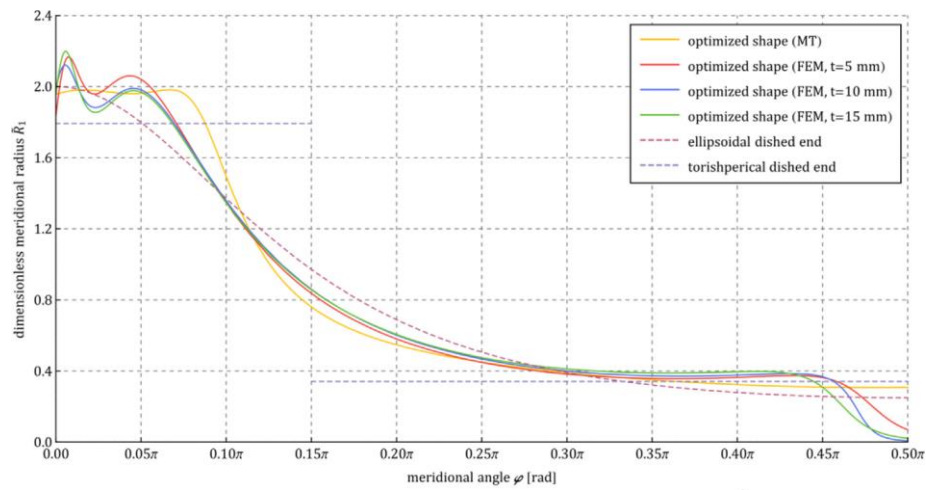**Fig. 26.** The comparison of the analysed shapes (axis order is changed).

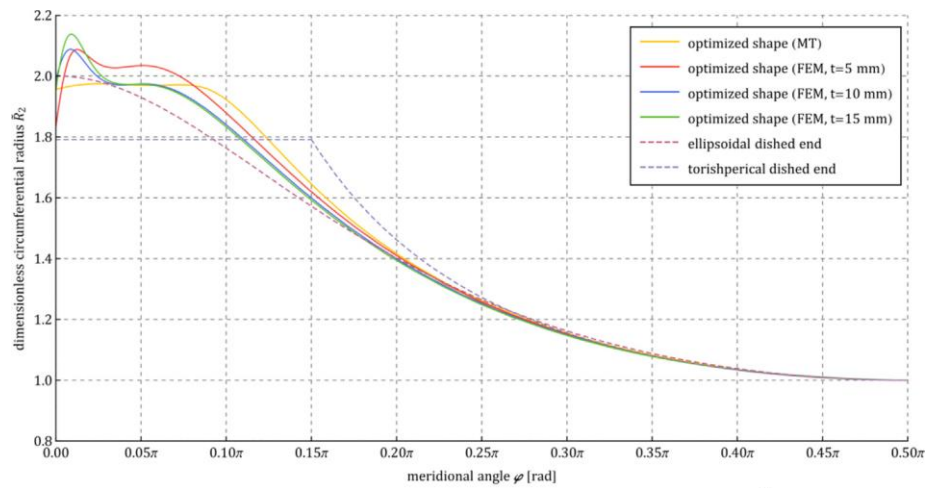**Fig. 27.** The comparison of the dimensionless meridional radius $\bar{R}_1$.

Fig. 28. The comparison of the dimensionless circumferential radius $\bar{R}_2$.

References

[1] Z.E. Mazurkiewicz, R.T. Nagórski, Powłoki Obrotowe Sprężyste (in Polish), Państwowe Wydawnictwo Naukowe, Warsaw, 1987.

[2] K. Magnucki, Strength and Optimization of Thin-Walled Vessels (in Polish), Science Publishers PWN, Warsaw/Poznan, 1998.

[3] E. Ventsel, T. Krauthammer, Thin Plates and Shells. Theory, Analysis, and Applications, Marcel Dekker, Inc., New York, Basel, 2001.

[4] A. Zingoni, Shell Structures in Civil and Mechanical Engineering, ICE Publishing, 2017.

[5] EN 13445-3:2002 Unfired pressure vessels – Part 3: Design, European Committee for Standardization.

[6] A. SME, Asme boiler and pressure vessel code, section viii, division 1, 2015, American Society of Mechanical Engineers, New York, NY.

[7] A. SME, Asme boiler and pressure vessel code, section viii, division 2, 2015, American Society of Mechanical Engineers, New York, NY.

[8] K. Magnucki, J. Lewiński, R. Cichy, Strength and buckling problems of dished heads of pressure vessels – contemporary look, J. Press. Vessel Technol. 140 (4) (2018) 041201.

[9] K. Sowiński, The ritz method application for stress and deformation analyses of standard orthotropic pressure vessels, Thin-Walled Struct. 162 (2021) 107585.

[10] T.G. Seipp, N. Barkley, C. Wright, Ellipsoidal Head Rules: A Comparison Between ASME Section VIII, Divisions 1 and 2, in: Proceedings of the ASME 2017 Pressure Vessels and Piping Conference, PVP, 2017, pp. 65858.

[11] R. Moradi, K.M. Groth, Hydrogen storage and delivery: Review of the state of the art technologies and risk and reliability analysis, Int. J. Hydrogen Energy 44 (23) (2019) 12254–12269.

[12] K. Magnucki, W. Szyc, J. Lewiński, Minimization of stress concentration factor in cylindrical pressure vessels with ellipsoidal heads, Int. J. Press. Vessels Pip. 79 (2002) 841–846.

[13] K. Sowiński, K. Magnucki, Shaping of dished heads of the cylindrical pressure vessel for diminishing of the edge effect, Thin-Walled Struct. 131 (2018) 746–754.

[14] D. Canonico, The history of ASME's boiler and pressure vessel code, 2010, https://www.asme.org/topics-resources/content/the-history-of-asmes-boiler-and-pressure.

[15] A. Zingoni, N. Enoma, N. Govender, Equatorial bending of an elliptic toroidal shell, Thin-Walled Struct. 96 (2015) 286–294.

[16] K. Magnucki, P. Jasion, M. Rodak, Strength and buckling of an untypical dished head of a cylindrical pressure vessel, Int. J. Press. Vessels Pip. 161 (2018) 17–21.

[17] K. Magnucki, J. Lewiński, Fully stressed head of a pressure vessel, Thin-Walled Struct. 38 (2000) 167–178.

[18] N.V. Banichuk, Optimization of axisymmetric membrane shells, J. Appl. Math. Mech. 71 (2007) 527–535.

[19] J. Lewiński, K. Magnucki, Shaping of a middle surface of a dished head of a circular cylindrical pressure vessel, J. Theoret. Appl. Mech. 48 (2) (2010) 297–307.

[20] J. Kruzelecki, R. Proszowski, Shape optimization of thin-walled pressure vessel end closures, Struct. Multidiscip. Optim. 46 (2012) 739–754.

[21] J. Błachut, Influence of meridional shaping of the collapse strength of FRP domes, Eng. Optim. 19 (1992) 65–80.

[22] R.C. Carbonari, P.A. Muñoz Rojas, E.Q. Andrade, G.H. Paulino, K. Nishimoto, E.C.N. Silva, Design of pressure vessels using shape optimization: An integrated approach, Int. J. Press. Vessels Pip. 88 (2011) 198–212.

[23] J. Błachut, L.S. Ramachandra, Optimization of internally pressurized torispheres subject to shakedown via gas, Eng. Optim. 29 (1997) 1–4.

[24] Z. Wang, A. Sobey, A comparative review between genetic algorithm use in composite optimisation and state-of-the-art in evolutionary computation, Compos. Struct. 223 (2020) 111739.

[25] B. Firlik, T. Staśkiewicz, W. Jaśkowski, L. Wittenbeck, Optimisation of a tram wheel profile using a biologically inspired algorithm, Wear 430–431 (2019) 12–24.

[26] M. Yang, B. Han, P. Su, Q. Zhang, Q. Zhang, Z. Zhao, C. Ni, T.J. Lu, Crashworthiness of hierarchial truncated conical shells with corrugated cores, Int. J. Mech. Sci. 193 (2020) 106171.

[27] D. Kumar, L.H. Poh, S.T. Quek, Isogeometric shape optimization of missing rib auxetics with prescribed negative Poisson's ratio over large strains using genetic algorithm, Int. J. Mech. Sci. 193 (2021) 106169.

[28] K. Liang, Z. Li, Postbuckling analysis and optimization of composite laminated panels using a novel perturbation-based approximation FE method, Thin-Walled Struct. 160 (2021) 107398.

[29] M. Imran, D. Shi, L. Tong, H.M. Waqas, Design optimization of composite submerged cylindrical pressure hull using genetic algorithm and finite element analysis, Ocean Eng. 190 (2019) 106443.

[30] A. Eshani, H. Dalir, Multi-objective optimization of composite angle grid plates for maximum buckling load and minimum weight using genetic algorithms and neural networks, Compos. Struct. 229 (2019) 111450.

[31] S. Zhu, M. Ohsaki, X. Guo, Q. Zeng, Shape optimization for non-linear buckling load od aluminum alloy reticulated shells with gausset joints, Thin-Walled Struct. 154 (2020) 106830.

[32] Y. Dias, M. Mahendran, Shape optimisation of cold-formed steel framed wall studs with sheathing restraints, Thin-Walled Struct. 158 (2021) 107135.

[33] H. Karimi, I.M. Kani, Finding the worst imperfection pattern in shallow lattice domes using genetic algorithms, J. Build. Eng. 23 (2019) 107–113.

[34] Z. Ugray, L. Lasdon, J. Plummer, J. Kelly, R. Martí, Scatter search and local NLP solvers: A multistart framework for global optimization, INFORMS J. Comput. 19 (3) (2007) 313–484.

[35] J. Nocedal, S.J. Wright, Numerical Optimization, second ed., in: Springer Series in Operations Research, Springer Verlag, 2006.

Extended Abstract in Polish

Działalność człowieka w dziedzinie inżynierii sięga starożytności. Osiągnięcia w tym obszarze nauki bezpośrednio przyczyniły się do daleko idącego rozwoju cywilizacyjnego. Obecnie rozwój technologii koncentruje się na zaawansowanych rozwiązaniach w zakresie projektowania konstrukcji w celu poprawy ich szeroko rozumianych właściwości.

Podstawowym wyznacznikiem w projektowaniu konstrukcji jest bez wątpienia ich nośność, zapewniająca bezpieczną eksploatację i zapobiegająca nieoptymalnemu wykorzystaniu biorąc pod uwagę czynniki ekonomiczne. W celu odniesienia się do tego problemu konieczne jest zapewnienie specjalnych metod i narzędzi umożliwiających badania wytrzymałościowe. Prezentowane zagadnienia są poświęcone analizie i optymalizacji rozkładu naprężeń w złożonych konstrukcjach powłokowych. Struktury te służą jako elementy nośne wielu istotnych konstrukcji znajdujących zastosowanie przemyśle. Przedstawione rozważania są zawężone do problemów walcowych zbiorników ciśnieniowych, jednakże podobna metodologia może być zaadaptowana do niemal każdego problemu liniowego z obszaru powłok.

Na podstawie analizy literatury sformułowano następujące tezy w rozprawie.

(1) Rozwiązania analityczne oparte na teorii powłok problemów naprężeń i deformacji konstrukcji powłokowych mogą prowadzić do niedokładnych wyników.

(2) Rozkład naprężeń w znormalizowanych dennicach ciśnieniowych zbiorników walcowych jest niekorzystny.

Celem odniesienia się do powyższych problemów z zakresu konstrukcji powłokowych, sformułowano następujące hipotezy.

(1) Zastosowanie metody Ritza do rozwiązywania problemów naprężeń i deformacji powłok może prowadzić do otrzymywania wyników o większej dokładności niż w przypadku rozwiązań analitycznych.

(2) Optymalizacja kształtu dennicy walcowego zbiornika ciśnieniowego może doprowadzić do znaczącej poprawy rozkładu naprężeń przy zachowaniu znormalizowanych wymiarów.

W pracy podejmowane są badania analityczne, semi-analityczne, numeryczne i eksperymentalne celem pogłębienia wiedzy i zaproponowania poprawy w świetle analizowanej problematyki naukowej.

Pierwsza część badań jest oparta na teoriach oraz metodach zawartych w literaturze. Naprężenia oraz deformacje ciśnieniowych zbiorników walcowych ze znormalizowanymi

dennicami elipsoidalnymi i toroidalno-sferycznymi są analizowane z zastosowaniem teorii bezmomenowej oraz teorii zaburzeń brzegowych. Dwa sformułowania teorii zaburzeń brzegowych są rozważane, zastosowane i porównane. Wyprowadzenia są przedstawione dla liniowego, ortotropowego modelu materiałowego. Otrzymane wyniki pokazują, że superpozycja rozwiązania w ramach teorii bezmomentowej oraz zaburzeń brzegowych może prowadzić do otrzymania niezadowalających wyników w związku z uproszczeniami w teorii bezmomentowej oraz pominięciu wpływu obciążeń powierzchniowych w zjawiskach zgięciowych.

Te same konstrukcje są poddawane analizie semi-analitycznej z zastosowaniem metody Ritza. Funkcje opisujące przemieszczenia w metodzie Ritza przyjmują postać wielomianów, szeregów trygonometrycznych oraz funkcji przypominających rozwiązania otrzymywane w teorii zaburzeń brzegowych. Badany jest wpływ stopnia owych funkcji na uzyskiwane wyniki. Rezultaty badania pokazują, że zgodność wyników z metodą elementów skończonych jest otrzymywana dla relatywnie dużego zakresu grubości, co potwierdzają niemal identyczne wartości naprężeń, przemieszczeń oraz energii odkształcenia sprężystego.

W przeprowadzonych obliczeniach walcowych zbiorników ciśnieniowych, uwagę zwraca się na niekorzystny rozkład naprężeń. Maksymalne wartości naprężeń zredukowanych w dennicach znormalizowanych znacząco przekraczają te, które powstają w części walcowej. Taki stan rzeczy powodowany jest nadmiernymi obciążeniami brzegowymi w połączeniu powłok, doprowadzając do zjawisk zgięciowych. Kształty den zostały w dalszych rozważaniach opisane za pomocą trzech krzywych analitycznych tj. owalu Cassiniego i Bootha oraz uogólnionej postaci klotoidy. Zdefiniowane zostały pewne warunki geometryczne celem zmniejszenia intensywności efektu brzegowego. Doprowadziły do zamierzonej poprawy rozkładu naprężeń w obszarze połączenia powłok, jednakże sprawiły, że doszło do ich wzrostu poza tym miejscem. Zaproponowane powłoki nie stanowią znaczącej poprawy w odniesieniu do kształtów znormalizowanych, jednak ich badania przyczyniły się do sformułowania istotnych wniosków dla dalszych prac.

Zdolność do przenoszenia relatywnie wysokich obciążeń przez konstrukcje powłokowe wynika z ich postaci geometrycznej. Poszukiwanie bardziej korzystnych rozwiązań związane jest zatem z odwołaniem się do zagadnień optymalizacji ich kształtu. W ramach ogólnych rozważań na ten temat, dość można do wniosku, że wybór arbitralnych rozwiązań z nieskończonego zbioru możliwości zazwyczaj prowadzi do niezadowalających wyników. W niniejszej pracy optymalizacja prowadzona jest w dwóch

oddzielnych procesach. Opracowana została krzywa parametryczna opisująca geometrię dennicy. Początkowo funkcja celu jest wyznaczana przy odwołaniu do teorii bezmomentowej powłok, a optymalizacja prowadzona jest z zastosowaniem deterministycznego algorytmu. W związku z uproszczoną naturą rozwiązania analitycznego, procedura zostaje następnie zmodyfikowana. Wartość funkcji przystosowania obliczana jest za pomocą metody elementów skończonych, natomiast optymalizacja jest realizowana za pomocą algorytmu genetycznego. Otrzymana poprawa rozkładu naprężeń jest znacząca przy możliwości wytwarzania dennic metodami konwencjonalnymi i zachowaniu znormalizowanych wymiarów ogólnych.

Ostatecznie wyniki optymalizacji są weryfikowane w ramach badania eksperymentalnego. Zbiornik ciśnieniowy ze zoptymalizowaną dennicą jest otrzymany za pomocą technologii wytwarzania przyrostowego Multi Jet Fusion. Pomiary wymiarów modelu realizowane są przy użyciu skanera optycznego, celem weryfikacji imperfekcji geometrycznych oraz utworzenia modelu CAD rzeczywistej konstrukcji. Geometria ta jest poddana badaniom numerycznym metodą elementów skończonych. Wytworzony zbiornik zostaje zbadany na zaprojektowanym stanowisku laboratoryjnym pozwalającym na obciążenie go wewnętrznym ciśnieniem. Analiza polega na zastosowaniu tensometrów do wyznaczenia rzeczywistego rozkładu naprężeń. Wyniki zostają porównane dla geometrii zoptymalizowanej i rzeczywistej w ramach obliczeń metodą elementów skończonych, a następnie zestawione z rezultatem badań eksperymentalnych. Osiągnięta zostaje zadowalająca zgodność, potwierdzająca korzystną charakterystykę opracowanych kształtów dennic.

Declarations